A vertex centred finite volume method for solid dynamics.

Aguirre Font, Miquel

Swansea University
Prifysgol Abertawe

A vertex centred Finite Volume Method for solid dynamics

by

Miquel Aguirre Font

Submitted to the College of Engineering
in partial fulfillment of the requirements for the degree of

Doctor of Philosophy

at

Swansea University

August 18, 2014

Acknowledgements

It is now time to conclude this thesis and I would like to express my gratitude to all the people who have made it possible. I will try to make an exhaustive list, hopefully I will succeed, but my apologies in advance if I miss somebody!

First of all, I would like to thank my two supervisors, Javier and Antonio, for their excellent guidance and support during these almost four years. Despite both being tremendously busy, they have always found the time to meet me and have extended talks about the technical and non technical problems encountered during the preparation of this thesis. They have been two great teachers from whom I have learned, and I'm learning, so many things.

I also want to thank the Mathematics Department of Swansea University, and specifically Prof. Niels Jacob, for offering me the opportunity of teaching in the department during this last semester. It has been a very exciting and interesting experience.

I would also like to thank all my colleagues in the ZC2E department, for the time spent together inside and outside the university. Specifically, Hean, for helping me in the technical issues with the formulation, your experience and dedication has been of great help. Aurelio, for all your pieces of advice in mathematics, computation and engineering. Rubén, also for all your help and extended talks we've had during these years (we agree in so many things but football!). I would also like to thank Oubay, Rogelio, Alejandro, Mauro, Guillermo, Esteban, Isaías, José, Clare, Paul, Ben and Sean.

I want to thank the whole team of the ATCoMe project. Specifically Prof. Antonio Huerta and Dr. Sonia Fernández from UPC for their excellent organisation of the project and also for my secondment at LaCàN. Many thanks also to Prof. Nicolas Moes and Prof. Laurent Stainier for welcoming me at Ecole Centrale de Nantes during my secondment there. Also, many thanks to the rest of the ESR's: Aleksandar, Omid, Augusto, Vladimir, César, Clement, Sudhar and Sudhakar for all the great time spent together at the different ATCoMe meetings and conferences. I also want to express my gratitude to all the people in LaCàN, where I started learning in Computational Mechanics, and specifically to Prof. Antonio Rodríguez, who encouraged me to start this PhD.

I also want to thank all the rest of friends I have made in Swansea: Beth, Charlotte, Pablo, Núria, Rhiannon, Adam, Bea, Adriana and Cal. And also all the friends back home who, despite the distance, have been of great support during these

years: Ramon, Josep, Andrea, Lluís, Agus, Joan, Berta, Felipe, Pere Alfaras, Pere Marc, Emma, Lluc, Elena, Josep, Meri, Jeroni, Maialen, Núria and Pablo. Also many thanks to my former colleagues in SENER, for all their support.

Finally, I would like to thank all my family, specifically my parents, my brother and my sister in law (and my niece and nephew!) for all their continuous unconditional support. Special thanks also to my uncle Pere, who was always so supportive and who would have loved to see this thesis finished. You are really missed. Last but not least, I want to thank Amaia for all her understanding, love and support during these last two years, and specially during these last six hectic months.

This thesis is dedicated to you all.

Als nostres pares i al nostre tiet Pere.

Abstract

With the increase of the computational power over the last decades, computational solid dynamics has become a major field of interest in many industrial applications (as for example aerospace, automotive industry, biomedical engineering or manufacturing). Traditionally, these types of simulations have been carried out using the Finite Element Method (FEM) in conjunction with displacement based formulations, where the displacements are treated as the main problem variables.

In the context of solid mechanics, the use of low order (linear) tetrahedral (or triangular) elements is always preferred, primarily due to the complexity of the constitutive models involved (i.e., the number of evaluations needs to be kept as low as possible) as well as the automatic tetrahedral (or triangular) mesh generators available. However, the combination of low order elements with FEM displacement based formulations presents a series of shortcomings, namely: one order of accuracy less for stresses (or strains) than for displacements (or velocities), poor behaviour in bending dominated scenarios, volumetric and shear locking or the appearance of spurious pressure modes. Furthermore, the time integration is usually performed using Newmark integrators, which tend to introduce high frequency noise in the vicinity of sharp gradients.

Recently, a new Lagrangian mixed methodology [1–4] has been presented for the simulation of fast transient dynamics problems. This methodology is in the form of a system of first order conservation laws, where the linear momentum, $\boldsymbol{p}$, and the deformation gradient tensor, $\boldsymbol{F}$, are regarded as the two main conservation variables. When thermo-mechanical constitutive models are involved, the formulation is complemented with the first law of thermodynamics (conservation of energy). It has been proven [1–3] that this formulation circumvents the drawbacks of the low order displacement based FEM methodologies mentioned above.

The formulation, presented as a set of conservation laws, allows for standard Computational Fluid Dynamcis (CFD) spatial discretisations. So far, successful implementations have been carried out using cell centred upwind Finite Volume method [1], two-step Taylor Galerkin [3], Finite Element Petrov Galerkin (PG) [2] and Hybridizable Discontinuous Galerkin (HDG) [4].

The objective of this thesis is to present a new spatial discretisation in order to solve large scale real life problems. To do so, the Jameson-Schmidt-Turkel (JST) scheme [5], widely know within the CFD community, will be chosen. The JST scheme is a vertex centred finite volume, that combines the use of central differ-

ences with an artificial dissipation term. The scheme obtains second order spatial accuracy without the need of linear reconstruction. Furthermore, the artificial dissipation term includes a shock capturing sensor, very suitable in the context of fast dynamics. The scheme can be implemented in an edge-based framework, which combined with the vertex centred storage of the variables results into a computationally efficient scheme. The JST spatial discretisation will be combined with a Total Variation Diminishing (TVD) two-stage Runge-Kutta time integrator. These spatial and temporal discretisations will be adapted to the problem at hand. Specifically, compatibility conditions (involutions) will have to be satisfied by the discrete scheme. Furthermore, numerical corrections will be introduced in order to ensure the conservation of linear and angular momenta. The framework results in a low order computationally efficient solver for solid dynamics, which proves to be very competitive in nearly incompressible scenarios and bending dominated applications.

The thesis will present numerical results for one dimension, two dimensions (triangular meshes) and three dimensions (tetrahedral meshes). The problems are chosen in order to prove the order of accuracy, robustness and conservation properties of the algorithm.

"More is lost by indecision than by wrong decision".

Carmela Soprano (played by Edie Falco)
to Tony Soprano (played by Michael Gandolfini)
in the TV series *The Sopranos*, episode 52, 2002.

Contents

List of Figures

List of Tables

Nomenclature

$\boldsymbol{x}, x_i$	Spatial or Eulerian coordinates
$\boldsymbol{X}, X_I$	Material or Lagrangian coordinates
$\boldsymbol{F}, F_{iI}$	Deformation gradient tensor, $F_{iI} = \partial x_i / \partial X_I$
v	Spatial or current volume
V	Material or reference volume
J	Jacobian of the deformation, $J = \det(\partial x_i / \partial X_I)$
dv	Differential of volume in the current configuration
dV	Differential of volume in the reference configuration
$\boldsymbol{H}, H_{iI}$	Cofactor of the deformation gradient, $\boldsymbol{H} = J\boldsymbol{F}^{-T}$, $H_{iI} = JF_{iI}^{-T}$
$\boldsymbol{N}, N_I$	Material outward-pointing unit normal vector
$\boldsymbol{n}, n_i$	Spatial outward-pointing unit normal vector
dA	Differential of area in the reference configuration
da	Differential of area in the current configuration
$\boldsymbol{u}$	Displacement field, $\boldsymbol{u} = \boldsymbol{x} - \boldsymbol{X}$
$\boldsymbol{v}, v_i$	Velocity field
$\boldsymbol{p}, p_i$	Linear momentum per unit of undeformed volume, $p_i = \rho_0 v_i$
ρ_0	Material density
$\boldsymbol{\mathcal{U}}$	General conservation variable, variable of the mixed system of conservation laws
ξ	General reference space
V_ξ	Control volume in a reference space ξ
$\boldsymbol{\mathcal{F}}_{N_\xi}$	Normal flux of the variable $\boldsymbol{\mathcal{U}}$ with corresponding normal $\boldsymbol{N}_\xi$
$\boldsymbol{s}$	General source term
$\boldsymbol{N}_\xi$	Normal vector in the reference space ξ
DIV	Divergence operator in the reference configuration
$\boldsymbol{\mathcal{U}}_\alpha^R$	Right eigenvector of the eigenvalue system
c_α	Wave speed of the eigenvalue system
ρ	Spatial density
$\boldsymbol{b}, b_i$	Body force per unit mass
$\boldsymbol{t}, t_i$	Surface traction vector, $t_i = P_{iI} N_I$
$\boldsymbol{P}, P_{iI}$	First Piola-Kirchhoff stress tensor
$\boldsymbol{\mathcal{E}}$	Alternating tensor
$\boldsymbol{S}, S_{iI}$	Second Piola-Kirchhoff stress tensor
E	Total energy

$\boldsymbol{Q}$	Heat flux
∇_0	Gradient operator in the undeformed space
e	Internal energy
s	Heat source
θ	Temperature
η	Entropy
ψ	Helmholtz free energy function, $\psi = e - \theta\eta$
CURL	Curl operator in the reference configuration
div	Divergence operator in the current configuration
p	Pressure
μ	Shear modulus
κ	Bulk modulus
λ	Lamé constant
E	Young's modulus
ν	Poisson's ratio
$\boldsymbol{F}_e$	Elastic component of the deformation gradient tensor
$\boldsymbol{F}_p$	Plastic component of the deformation gradient tensor
$\lambda_{e,\alpha}$	Elastic principle stretches
$\tau_{\alpha\alpha}$	Principal component of Kirchhoff stress tensor, $\tau_{\alpha\alpha} = J\sigma_{\alpha\alpha}$
f	Yield function of elasto-plastic constitutive model
H	Hardening modulus
$\bar{\varepsilon}_p$	Hardening variable
τ_y^0	Initial yield stress
$\boldsymbol{b}_e$	Elastic left Cauchy-Green deformation tensor
$\boldsymbol{C}_p$	Plastic right Cauchy-Green deformation tensor
C_F	Heat coefficient at constant deformation
e_0	Internal energy at reference temperature
η_0	Entropy at reference temperature
e_{0K}	Internal energy at the absolute zero
p_{0K}	Pressure at the absolute zero
Γ	Grüneisen coefficient
v_H	Velocity behind the Hugoniot
p_H	Pressure behind the Hugoniot
e_H	Internal energy behind the Hugoniot
$\boldsymbol{\mathcal{F}}$	Flux of the mixed system of conservation laws
$\boldsymbol{\mathcal{S}}$	Source term of the mixed system of conservation laws
$\boldsymbol{\mathcal{C}}, \mathcal{C}_{iIjJ}$	Material fourth-order constitutive tensor, $\mathcal{C}_{iIjJ} = \partial P_{iI}/\partial F_{jJ}$
c_p	Volumetric wave speed
c_s	Shear wave speed
V_a	Control volume associated to a node a
$\boldsymbol{\mathcal{U}}_a$	Cell averaged value of the variable $\boldsymbol{\mathcal{U}}$ at node a
$(\boldsymbol{\mathcal{F}}_N^C)_k$	Numerical contact flux at facet k
A_k	Area of the facet k

$\boldsymbol{C}^{ab}$	Area vector of the edge connecting nodes a and b
$\boldsymbol{N}_k$	Normal vector of the facet k
$\boldsymbol{\mathcal{F}}_a$	Cell averaged value of the flux $\boldsymbol{\mathcal{F}}$ at node a
h	Mesh size (regular meshes)
$\kappa^{(4)}$	JST dissipation coefficient corresponding to the fourth order differences
$\kappa^{(2)}$	JST dissipation coefficient corresponding to the second order differences
$\varepsilon^{(4)}_{ab}$	JST pressure switch for the fourth order differences at edge ab
$\varepsilon^{(2)}_{ab}$	JST pressure switch for the second order differences at edge ab
Ψ_{ab}	Spectral radius at edge ab
α_{CFL}	Courant-Friedrichs-Lewy number
$\boldsymbol{A}$	Total angular momentum of a system, $\boldsymbol{A} = \int_V \boldsymbol{x} \times \boldsymbol{p}\, dV$
$\boldsymbol{L}$	Linear momentum of a system, $\boldsymbol{L} = \int_V \boldsymbol{p}\, dV$

Chapter 1

Introduction

1.1 Motivation and state of the art

1.1.1 Computational solid dynamics

Many processes in engineering take place in small periods of time. Furthermore, many of these processes involve large deformations and important material non-linearities. At this point, the engineer cannot use the conventional static linear analysis for the design or verification of structures. Therefore, a choice has to be made between the use of physical models or computer simulations. While there is a large experience behind physical models, it is well known that they suffer from physical and economical limitations. On the other hand, the use of computational solid dynamics simulations is still an open field, with not as much experience behind, but with the potential to model any complex physical phenomena at a significant lower cost. Therefore, and with the increase of computer power of the last decades, computational solid dynamics is becoming the predominant choice in many industrial applications such as aerospace, automotion, civil engineering, biomedical engineering or manufacturing (see Figure 1.1).

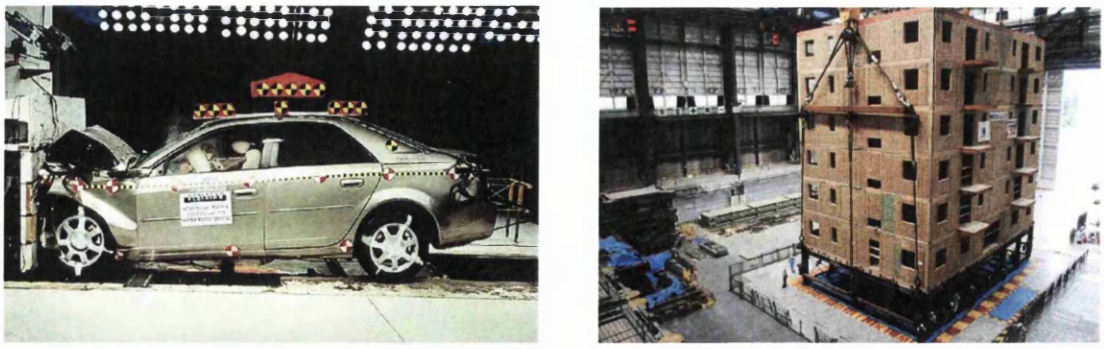

(a) (b)

Figure 1.1: Two possible applications fields for computational solid dynamics: automotive industry (a) and earthquake engineering (b).

1.1.2 Low order Finite Element displacement based formulations in solid dynamics

Traditionally, the Finite Element Method (FEM) displacement based formulation has been used for solid dynamics simulations [6, 7]. In this type of formulations, the linear momentum equation is solved using the displacement as the main problem variable. The equations are integrated in time by using a family of Newmark time integrators [8]. Modern commercial finite element codes, such as LS-DYNA3D [7] or ABAQUS/Explicit [9] use this type of discretisations.

In the context of solid dynamics, the simulation of many materials requires the use of complex constitutive models [10–12]. The evaluation of these constitutive models become a bottleneck in terms of the computational cost of the numerical codes. Therefore, the use of low order elements is always preferred, since the number of evaluations (Gauss points) is reduced drastically as compared to higher order interpolations. Furthermore, solid dynamics problems often involve contact at the boundary surfaces. This contact is always easier to detect using low order elements as compared to high order elements [13]. Finally, the combination of high order elements and explicit codes has also an added cost due to limitations in the time step size [14].[1]

Furthermore, many automotive components, aerospace components or, for example, human body parts have complex geometries. Therefore, precise and fast meshing techniques are required for the design process such that they can cope with any type of geometry without a significant added cost. In this matter, there is a significant difference between tetrahedral (or triangular) mesh generators and hexahedral (or quadrilateral) mesh generators. While hexahedral meshing is still an open field, the automatic tetrahedral mesh generators are well developed thanks to the Delaunay and advancing front techniques [15, 16].

It is now well known that the combination of low order (linear) finite element displacement based formulations with tetrahedral (or triangular) meshes suffers from a series of shortcomings. First of all, the displacements and linear momentum (or velocities) are obtained with second order accuracy, while the strains and stresses with first order accuracy, that is, they are constant in the elements. This results, firstly, in a lower accuracy for the stresses and therefore mesh refinement may be required before a required tolerance is met. Secondly, and perhaps more importantly, the use of constant stress elements has detrimental effects in the behaviour of the numerical solution. Specifically, in bending dominated scenarios the numerical solution tends to stiffen and is not able to capture accurately the deformation process [17]. Furthermore, for nearly incompressible materials, this ill-behaviour is accentuated through the appearance of pressure modes and locking. This all may lead to too optimistic conclusions in the design or verification process, which can

[1] In theory, for the same spatial accuracy, larger elements could be used for higher order methods, which would increase the minimum time step size. Even though, this is limited to simple geometries. In real life problems, the size of the elements is usually dictated by the geometry of the solid.

have disastrous consequences.

Finally, from the time discretisation point of view, the Newmark method has a tendency to introduce high frequency noise in the solution field, especially in the vicinity of sharp gradients. This can be circumvented by the addition of numerical damping, which, on the other hand, affects the overall numerical accuracy [8]. In [18–21] minor modifications were introduced to improve the effect of the numerical dissipation without including a discontinuity sensor, which makes the scheme unsuitable for shock dominated problems.

There are different numerical techniques to circumvent the locking phenomena and poor bending behaviour described above. One of the approaches is the $h-$refinement, which consists of a continuous refinement of the mesh size. This approach is far from optimum due to cost reasons. Furthermore, it can alleviate the shear locking phenomenon in the FEM but it has no effect on the volumetric locking in the nearly incompressible regime [22]. On the other hand, $p-$refinement can be used, where higher order interpolating functions are preferred at the expense of increasing the computational cost.

Another approach is to introduce a multi-field de Veubeke-Hu-Washizu(dVHW) type variational principle [23], which enables the use of independent kinematic descriptions for the volumetric and deviatoric components of the deformation and, next, the volumetric term is underintegrated. A specific case of this approach is the mean dilatation formulation, where constant interpolation is used for the volumetric part [10]. Unfortunately, in three dimensional tetrahedrons and two dimensional triangles for FEM, the mean dilatation cannot be used since these elements already employ the simplest Gaussian quadrature rule. To overcome this difficulty, in reference [24] the volumetric strain energy functional is approximated by evaluating averaged nodal pressures in terms of tributary nodal volumes. However, it was proved that this formulation suffered from poor behaviour in bending dominated scenarios [25]. In reference [26], an alternative technique uses a nodal averaging process to the whole small strain tensor. This idea was then extended to finite deformations in reference [27]. It was later reported [28–30] that this formulation suffers from artificial modes similar to hourglassing.

1.1.3 A new mixed formulation for solid dynamics

A new Lagrangian mixed formulation [1–4] has been recently developed for the simulation of fast transient dynamics problems. The methodology is presented in the form of a system of first order conservation laws where the linear momentum and the deformation gradient tensor are regarded as the two main conservation variables. An additional conservation equation can also be formulated for the total energy of the system which, in the case of reversible elastodynamics, decouples from the rest of the conservation equations. The use of physical equations written in the form of conservation laws enables the use of traditional Computational Fluid Dynamics (CFD) discretisations within the solid dynamics context.

In contrast to displacement based formulations, references [1–3, 31] have demonstrated that the same order of accuracy can be obtained for both strains (or stresses) and velocities (or displacements once integrated in time) if the new mixed formulation is employed. This formulation enables the use of low order elements without exhibiting volumetric locking in nearly incompressible situations and, therefore, it is proposed as an alternative to nodal Finite Element formulations [24–28, 32–37]. Furthermore, by using CFD discretisations, a large wealth of shock capturing techniques becomes available.

In reference [1], the proposed formulation was implemented using a two-dimensional Finite Volume cell centred upwind technique, where a Riemann solvers use the wave characteristics information in order to advance the solution in time (see for example references [38]). The solution was obtained with second order accuracy by using linear reconstruction and limiters, which preserve the solution monotonicity in the vicinity of sharp gradients [39, 40].

In reference [3], the authors present an alternative two-dimensional implementation of the mixed formulation in the form a Two-step Taylor-Galerkin algorithm, where results are compared against those of [1] for a series of benchmark examples. Reference [2] introduces a new Petrov Galerkin (PG) Finite Element Method [41] as an alternative form of stabilisation for the set of mixed conservation equations. Moreover, in the same work [2] the stabilised spatial discretisation is also re-written in the form of the Variational Multiscale Method (VMS) initially introduced in [42] and later extended to Lagrangian shock hydrodynamics in [33–37]. Both references [2, 3] provide two- and three-dimensional results where velocities and strains (stresses) converge at the same rate with excellent behaviour in bending dominated scenarios. Recently, in reference [43], this formulation has been extended with an additional conservation equation for the Jacobian of the deformation. The system of equations is discretised using a Petrov-Galerkin Finite Element Method with an adapted fractional step method. This allows extending the range of use to nearly incompressible and truly incompressible materials.

In parallel, since the formulation is written in the form of a system of conservation laws, it is very suitable for spatial discretisation using Discontinuous Galerkin Methods [44]. This approach was chosen in [4] for a high order implementation using Hybridizable Discontinuous Galerkin (HDG).

1.1.4 The Jameson-Schmidt-Turkel (JST) scheme

The objective of the current thesis is the implementation of the above mentioned system of conservation laws in a general low cost framework for large scale problems. To do so, the well known Jameson-Schmidt-Turkel (JST) scheme [5] is used. The scheme was first introduced in reference [5] for the solution of the Euler equations for rectangular structured meshes, and later extended to unstructured meshes in references [45–48]. The scheme uses a central differences approach, equivalent to a Galerkin Finite Element discretisation with linear elements [45, 49–52] plus a blend

of a non divided Laplacian and a biharmonic operator in order to add artificial diffusion [5, 45, 46, 53–56].

The attractiveness of this scheme relies mainly on computational cost aspects. First of all, it is a nodal based Finite Volume scheme and therefore, the number of evaluations of the stress tensor (constitutive model) is reduced drastically as compared to a cell centred scheme since, as stated in [56,57], the number of elements is from 5 to 7 times the number of nodes in a tetrahedral mesh. Secondly, the computational effort when evaluating the flux gradients is reduced by half in a vertex centred scheme since the loops are performed on edges instead of faces (as in a cell centred scheme), being the ratio between the number of faces and the number of edges approximately 2 to 1 [57]. Furthermore, the combination of the artificial dissipation term and the shock capturing switch gives a second order monotonicity preserving algorithm without the use of linear reconstruction and slope limiters. Finally, since the JST scheme is present in a large amount of available CFD software [58,59], its implementation into a solid dynamics framework can ease the adaptation of existing codes. Nevertheless, it is well known that the JST scheme suffers from excessive dissipative solutions [50] since it does not use wave information to advance the solution in time. Therefore, mesh refinements have to be performed in order to obtain accuracies comparable to those of other methodologies (such as PG or upwind FVM with linear reconstruction).

Apart from [1], there have been other attempts at applying the Finite Volume Method (FVM) in the context of solid dynamics. References [60–64] used displacement based formulations for linear elasticity. Eulerian Finite Volume Godunov methods, classically used for modelling compressible gas dynamics, have been also adapted to model plastic flows in solid dynamics [65–68]. Subsequently, and perhaps more significantly to the current thesis, this work was adapted to a Lagrangian framework by several authors [68–70]. Specifically, in [69], a Lagrangian Godunov method was presented for hyperelastic materials.

1.2 Scope of the thesis and outline

This thesis aims to establish a robust framework for adapting the JST formulation to solid dynamics. In order to adapt the original JST scheme to the problem at hand, dissipation will only be added to the linear momentum equation, which will provide the necessary stability to the hyperbolic system. The update of the deformation gradient tensor will be left as a numerical gradient of the velocities with the use of no additional dissipation. This will enable the discrete satisfaction of the compatibility conditions of the deformation mapping (i.e. curl-free) [1, 3]. Special attention must be paid to the numerical quadrature of the boundary fluxes through the use of a weighted nodal flux average carried out at the boundary faces. The spatial discretisation will be combined with a two-stage Total Variation Diminishing (TVD) Runge-Kutta time integrator [71]. The displacements are integrated in time

using a trapezoidal rule which is combined with a Lagrange multiplier minimisation procedure to ensure the conservation of angular momentum. An additional correction of the numerical dissipation to ensure the conservation of the linear momentum, whilst preserving the order of accuracy, is also presented.

For the above purposes, the thesis is broken down in the following chapters:

- Chapter 2: introduces the classical Lagrangian conservation laws in physics (conservation of linear momentum, conservation of energy and conservation of angular momentum) and the additional conservation laws (conservation of deformation gradient, conservation of the Jacobian of the deformation and conservation of the cofactor of the deformation gradient) used in this thesis.

- Chapter 3: presents constitutive models for isothermal elastic solids, elastic-plastic solids and thermo-elastic solids.

- Chapter 4: introduces the mixed system of conservation laws based in the equations presented in chapter 2. The boundary and initial conditions of the system are also introduced in this chapter. With the objective of discretising this sytem of equations using CFD techniques, the hyperbolicity of this system combined with the constitutive models (presented in chapter 3) is analysed using an eigenvalue analysis.

- Chapter 5: in this chapter the different types of Finite Volume schemes are introduced and classified according to the discretisation of the fluxes and the control volume definition. Next, the JST scheme is introduced, first for one dimensional structured grids and then, for two and three dimensional unstructured grids. Finally, the JST scheme is used for the semi-discretisation of the mixed system of conservation laws.

- Chapter 6: presents the time discretisation of the governing equations, by using a two stage Total Variation Diminishing (TVD) Runge-Kutta scheme. Next, the chapter explains the numerical corrections necessary fo the preservation of the angular and linear momenta. The chapter concludes with a flux summarising the numerical algorithm.

- Chapter 7: the chapter presents a linear analysis of the order of accuracy and numerical stability of the numerical scheme.

- Chapter 8: a set of numerical examples are presented and discussed. These examples are in one, two and three dimensions, and prove the convergence, robustness and conservation properties of the formulation.

- Chapter 9: provides an overall discussion and conclusions of the work done. The chapter also discusses the potential future lines of work.

1.3 Publication list

The following publications were produced during the preparation of this thesis

1.3.1 Journal papers

- M. Aguirre, A. J. Gil and J. Bonet. A vertex centred Finite Volume Jameson-Schmidt-Turkel (JST) algorithm for a mixed conservation formulation in solid dynamics. Journal of Computational Physics, 2014. DOI: 10.1108/EC-12-2012-0319.

- A.J. Gil, C.H. Lee, J. Bonet and M. Aguirre. A stabilised Petrov-Galerkin formulation for linear tetrahedral elements in compressible, nearly incompressible and truly incompressible fast dynamics. Computer Methods in Applied Mechanics and Engineering, 2014. DOI: 10.1016/J.CMA.2014.04.006.

- J. Bonet, A.J. Gil, C.H. Lee and M. Aguirre. A first order hyperbolic framework for large strain computational solid dynamics Part I Total Lagrangian Isothermal Elasticity. Computer Methods in Applied Mechanics and Engineering, 2014. Submitted.

- M. Aguirre, A.J. Gil, J. Bonet and C.H. Lee. An upwind vertex centred finite volume solver for Lagrangian solid dynamics. In preparation. To be submitted to the Journal of Computational Physics, 2014.

1.3.2 Refereed conference papers

- D. Mukherjee, A.J. Gil, J. Bonet, C.H. Lee and M. Aguirre. On alternative numerical frameworks for a new conservation law formulation in structural dynamics. In: Proceedings of the 20^{th} UK Conference of the Association of Computational Mechanics in Engineering, Manchester, 27-28 March 2012.

- D. Mukherjee, A.J. Gil, J. Bonet, C.H. Lee and M. Aguirre. Streamline Upwind Petrov-Galerkin solution of Lagrangian explicit dynamic solid mechanics. In: Proceedings of the 8^{th} European Solid Mechanics Conference (ESMC), Graz, Austria, July 9-13, 2012.

- M. Aguirre, A. J. Gil, J. Bonet and C. H. Lee. Implementation of the Jameson-Schmidt-Turkel (JST) scheme for a new conservation law formulation in fast structural dynamics. In: Proceedings of the 21^{st} UK Conference of the Association of Computational Mechanics in Engineering, Durham, March 25-27, 2013.

- J. Bonet, A. J. Gil, A. Arranz and M. Aguirre, C. H. Lee. Computational simulation of solid dynamics using Computational Fluid Dynamics (CFD) tech-

nologies. In: Proceedings of the 21^{st} UK Conference of the Association of Computational Mechanics in Engineering, Durham, March 25-27, 2013.

- M. Aguirre, A. J. Gil, J. Bonet and C. H. Lee. An unstructured finite volume solver for a new conservation law in fast transient dynamics. In: Proceedings of the International Conference on Adaptive Modelling and Simulation, Lisbon, Portugal, June 3-5, 2013.

- M. Aguirre, A. J. Gil, J. Bonet and C. H. Lee. Development of an efficient unstructured finite volume solver for a new conservation law in fast structural dynamics. In: Proceedings of the 4^{th} International Conference on Computational Methods in Structural Dynamics and Earthquake Engineering, Kos Island, Greece, June 12-14, 2013.

- M. Aguirre, A. J. Gil, J. Bonet and C. H. Lee. An adapted Jameson-Schmidt-Turkel (JST) scheme for fast solid dynamics. In: Proceedings of the 12^{th} US National Congress on Computational Mechanics (USNCCM), Raleigh, North Carolina, July 22-25, 2013.

- C. H. Lee, A. J. Gil, J. Bonet and M. Aguirre. Development of a stabilised SUPG formulation for a new conservation law formulation in Lagrangian fast solid dynamics. In: Proceedings of the 12^{th} US National Congress on Computational Mechanics (USNCCM), Raleigh, North Carolina, July 22-25, 2013.

- C. H. Lee, M. Aguirre, A. J. Gil and J. Bonet. Development of a stabilised Petrov-Galerkin formulation for low-order tetrahedral meshes in Lagrangian fast solid dynamics. In: Proceedings of the YIC2013 Second ECCOMAS Young Investigators Conference, Bordeaux, France, September 2-6, 2013.

- M. Aguirre, A. J. Gil, J. Bonet and C. H. Lee. An edge based vertex centred upwind finite volume method for Lagrangian solid dynamics. In: Proceedings of the 11th World Congress on Computational Mechanics (WCCM XI), Barcelona, 20-25 July 2014.

- J. Bonet, A. J. Gil, C. H. Lee and M. Aguirre. A first order conservation law framework for solid dynamics. In: Proceedings of the 11th World Congress on Computational Mechanics (WCCM XI), Barcelona, 20-25 July 2014.

- C. H. Lee, A.J. Gil, J. Bonet and M. Aguirre. A stabilised Petrov-Galerkin formulation for linear tetrahedral elements in compressible, nearly incompressible and truly incompressible fast dynamics. In: Proceedings of the 11th World Congress on Computational Mechanics (WCCM XI), Barcelona, 20-25 July 2014.

Chapter 2

Conservation laws in solid dynamics

2.1 Preliminaries

The current chapter will introduce the formulation and governing equations used for the problem at hand. Firstly, some preliminaries regarding the kinematical description of the motion will be introduced in section 2.2. Next, in section 2.3 the general concept of a conservation law in physics will be explained. Section 2.4 and 2.5 will give a brief review of the standard balance laws and thermodynamics of solids. This will be complemented with the additional balance laws presented in section 2.6.

2.2 Kinematics

Consider the motion of a continuum body between a reference domain V and a spatial or deformed configuration v. The deformation is defined by a mapping $\boldsymbol{x} = \boldsymbol{x}(\boldsymbol{X}, t)$, where $\boldsymbol{X}$ denotes the material position of a particle and $\boldsymbol{x}$ its position at the deformed configuration (see figure 2.1).

The Jacobian of the transformation is the deformation gradient tensor, $\boldsymbol{F}$ and is given by

$$\boldsymbol{F} = \frac{\partial \boldsymbol{x}(\boldsymbol{X}, t)}{\partial \boldsymbol{X}}, \quad \text{or} \quad F_{iI} = \frac{\partial x_i}{\partial X_I}, \tag{2.1}$$

which is a two point tensor that maps an elemental material vector $d\boldsymbol{X}$ into the corresponding spatial vector $d\boldsymbol{x}$ as

$$d\boldsymbol{x} = \boldsymbol{F} d\boldsymbol{X}. \tag{2.2}$$

The volume elements in the reference and current configurations are related through the determinant of $\boldsymbol{F}$, denoted as J. That is,

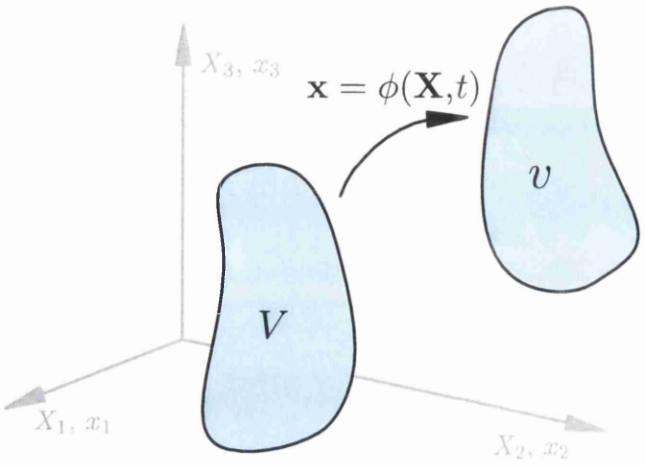

Figure 2.1: Deformation mapping

$$dv = JdV, \quad J = \det(\boldsymbol{F}). \tag{2.3}$$

The cofactor of $\boldsymbol{F}$, denoted here by $\boldsymbol{H}$, expresses the relation between an area vector in the reference domain, $d\boldsymbol{A} = \boldsymbol{N}dA$, and an area vector in the spatial domain, $d\boldsymbol{a} = \boldsymbol{n}da$, as

$$d\boldsymbol{a} = \boldsymbol{H}d\boldsymbol{A}, \quad \boldsymbol{H} = J\boldsymbol{F}^{-T}. \tag{2.4}$$

The material velocity, $\boldsymbol{v}(\boldsymbol{X},t)$, and the linear momentum per unit of reference volume, $\boldsymbol{p}$, are given as:

$$\boldsymbol{v}(\boldsymbol{X},t) = \frac{\partial \boldsymbol{x}(\boldsymbol{X},t)}{\partial t}, \quad \boldsymbol{p} = \rho_0 \boldsymbol{v}, \tag{2.5}$$

where ρ_0 is the density at the reference configuration.

2.3 Conservation laws

Given a variable $\boldsymbol{\mathcal{U}}$ which may be, in general, a scalar, a vector or a tensor and which is a function of a position $\boldsymbol{\xi} = (\xi_1, \xi_2, \xi_3)^T$, in a general reference space, and time t, a conservation law is an equation expressing the variation of such quantity within an enclosed region in that reference space, V_ξ, known as the *control volume* [39], given by

$$\frac{d}{dt}\int_{V_\xi} \boldsymbol{\mathcal{U}}(\boldsymbol{\xi},t)\, dV + \int_{\partial V_\xi} \boldsymbol{\mathcal{F}}_{N_\xi}(\boldsymbol{\mathcal{U}}(\boldsymbol{\xi},t))\, dA = \int_{V_\xi} \boldsymbol{s}\, dV_\xi, \tag{2.6}$$

where ∂V_ξ denotes the boundary of the control volume, $\boldsymbol{s}$ is the source term and $\boldsymbol{\mathcal{F}}_{N_\xi}$ is the *normal flux vector* along this boundary, which can be expressed as

$$\boldsymbol{\mathcal{F}}_{N_\xi} = \boldsymbol{\mathcal{F}} \boldsymbol{N}_\xi, \tag{2.7}$$

where $\boldsymbol{N}_\xi$ is the normal vector along the boundary of the control volume and $\boldsymbol{\mathcal{F}} = \boldsymbol{\mathcal{F}}(\boldsymbol{\mathcal{U}}(\boldsymbol{\xi}, t))$ is the *flux matrix*. Equation (2.6) can be understood more intuitively for a scalar variable ϕ in a one dimensional case with no source term,

$$\frac{d}{dt} \int_{x_a}^{x_b} \phi(x,t)\, dX = f(\phi(x_b,t)) - f(\phi(x_a,t)), \tag{2.8}$$

where the control volume is the region $V = \{x, x \in [x_a, x_b]\}$ and f is the flux function. It can be seen that the variation in time of the variable inside the control volume is equal to the flux "entering" the control volume minus the flux "leaving" the control volume.

2.3.1 Conservation laws in Lagrangian form

This thesis presents the solution of solid dynamics problems using a *Lagrangian* description of the motion, which implies that the variables are expressed in the reference or material configuration. Specifically, a *total Lagrangian* description will be used, which implies that all the fluxes are also referred to the initial configuration. This is a very attractive approach in solid mechanics since the evolution of any particle (and all the physical quantities related to it) can be followed at any instant of the deformation, which can be critical when modelling history dependent materials. Furthermore, the use of Lagrangian meshes eases the treatment of geometrically complex boundaries (see [72]). For this reason, only this approach will be considered in what follows. Two other approaches, namely the *Eulerian* or *Updated Lagrangian* description of the motion are explained in Appendix B and applied to the conservation laws used in the thesis.

Defining a general variable, $\boldsymbol{\mathcal{U}}$, which is a function of the material particles $\boldsymbol{X}$ and time t, that is $\boldsymbol{\mathcal{U}} = \boldsymbol{\mathcal{U}}(\boldsymbol{X}, t)$, a flux $\boldsymbol{\mathcal{F}}$ depending on such variable, $\boldsymbol{\mathcal{F}} = \boldsymbol{\mathcal{F}}(\boldsymbol{\mathcal{U}})$, a source term (which in general may depend on the position and time), $\boldsymbol{\mathcal{S}}(\boldsymbol{X}, t)$, and a control volume placed in the reference domain, V, a Lagrangian conservation law reads

$$\frac{d}{dt} \int_V \boldsymbol{\mathcal{U}}(\boldsymbol{X}, t)\, dV + \int_{\partial V} \boldsymbol{\mathcal{F}}_N(\boldsymbol{\mathcal{U}}(\boldsymbol{X}, t))\, dA = \int_V \boldsymbol{\mathcal{S}}(\boldsymbol{X}, t)\, dV. \tag{2.9}$$

By assuming a smooth solution and absence of discontinuities, the divergence theorem can be applied to the equation above (see Figure 2.2). Since V is a fixed region in the reference domain, the following is obtained

$$\int_V \left(\frac{\partial \boldsymbol{\mathcal{U}}}{\partial t} + \mathrm{DIV}\, \boldsymbol{\mathcal{F}} - \boldsymbol{\mathcal{S}} \right) dV = \boldsymbol{0} \tag{2.10}$$

where the dependence on $\boldsymbol{X}$ and t has been omitted for simplicity. Since the above equation has to be satisfied for any control volume, V, it can be rewritten as (see Appendix A for notation)

$$\frac{\partial \boldsymbol{\mathcal{U}}}{\partial t} + \mathrm{DIV}\,\boldsymbol{\mathcal{F}} = \boldsymbol{\mathcal{S}}, \tag{2.11}$$

which is the local form of the conservation law (2.9).

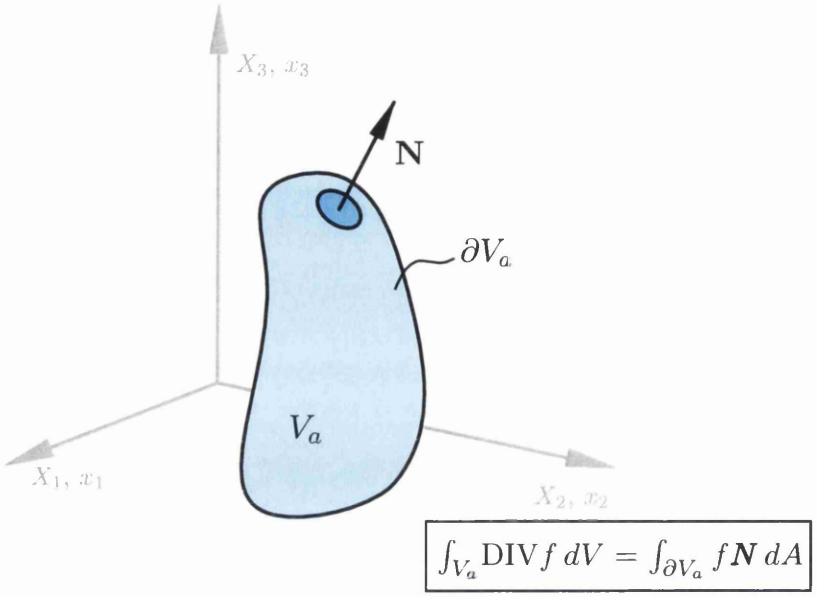

Figure 2.2: Divergence theorem

2.3.2 Hyperbolicity

The system given by the conservation law (2.11) is considered *hyperbolic* if, in the absence of source terms, there exist plane wave solutions of the form [38, 39]

$$\boldsymbol{\mathcal{U}} = \boldsymbol{\mathcal{U}}_\alpha^R f(\boldsymbol{X} \cdot \boldsymbol{N} - c_\alpha t), \tag{2.12}$$

with both c_α and $\boldsymbol{\mathcal{U}}_\alpha^R$ reals. The vectors $\boldsymbol{\mathcal{U}}_\alpha^R$ are the right eigenvectors of the system whereas c_α are the eigenvalues or wave speed associated to those eigenvectors. Replacing (2.12) in (2.11) and setting $\boldsymbol{\mathcal{S}} = \boldsymbol{0}$ gives

$$-c_\alpha \boldsymbol{\mathcal{U}}_\alpha^R f'(\boldsymbol{X} \cdot \boldsymbol{N} - c_\alpha t) + N_I \frac{\partial \boldsymbol{\mathcal{F}}_I}{\partial \boldsymbol{\mathcal{U}}} \boldsymbol{\mathcal{U}}_\alpha^R f'(\boldsymbol{X} \cdot \boldsymbol{N} - c_\alpha t) = \boldsymbol{0}, \tag{2.13}$$

therefore,

$$\frac{\partial \boldsymbol{\mathcal{F}}_N}{\partial \boldsymbol{\mathcal{U}}} \boldsymbol{\mathcal{U}}_\alpha^R = c_\alpha \boldsymbol{\mathcal{U}}_\alpha^R. \tag{2.14}$$

Using the definition of directional derivative this can be rewritten as

$$D\boldsymbol{\mathcal{F}}_N \left[\boldsymbol{\mathcal{U}}_\alpha^R\right] = c_\alpha \boldsymbol{\mathcal{U}}_\alpha^R, \tag{2.15}$$

which is the characteristic equation of the system.

2.3.3 Discontinuous solutions

A general conservation law in integral form as in equation (2.9) can accept discontinuities of the solution. For linear hyperbolic equations, these discontinuities may arise due to the presence of discontinuities on the variables, due to geometric discontinuities or due to the use of a discontinuous numerical approximation. For nonlinear hyperbolic equations, these discontinuities can also appear due to the physics of the problem and are known as *shocks* [38,39]. When such discontinuities arise, an additional equation needs to be solved on top of the integral form (2.9). These equations are the *Rankine-Hugoniot jump conditions* and give the propagation speed of the discontinuity U in terms of the variables and fluxes at both sides of it.

Take a fixed region in space (control volume) V with a discontinuity within it of the variables $[\![\boldsymbol{\mathcal{U}}]\!] = \boldsymbol{\mathcal{U}}^R - \boldsymbol{\mathcal{U}}^L$ given by a surface Γ with normal vector $\boldsymbol{N}^\Gamma$ traveling at speed $\boldsymbol{v}$. The surface divides the control volume V into two material volumes V^L and V^R, such that

$$V = V^L \cup V^R; \quad V^L \cap V^R = \varnothing; \tag{2.16a}$$

$$\partial V = (\partial V^L \backslash \Gamma) \cup (\partial V^R \backslash \Gamma); \quad \partial V^L \cap \partial V^R = \Gamma. \tag{2.16b}$$

Using the Reynold's Transport Theorem (see equation (B.1) in appendix B) for the left material volume yields

$$\begin{aligned} \frac{d}{dt}\int_{V^L} \boldsymbol{\mathcal{U}}\, dV &= \int_{V^L} \frac{\partial \boldsymbol{\mathcal{U}}}{\partial t}\, dV + \int_{(\partial V^L \backslash \Gamma)} \boldsymbol{\mathcal{U}}\boldsymbol{v}\cdot\boldsymbol{N}\, dA + \int_\Gamma \boldsymbol{\mathcal{U}}^L \boldsymbol{v}\cdot(\boldsymbol{N}^\Gamma)\, dA \\ &= \int_{V^L} \frac{\partial \boldsymbol{\mathcal{U}}}{\partial t}\, dV + \int_\Gamma U\boldsymbol{\mathcal{U}}^L\, dA, \end{aligned} \tag{2.17}$$

where $U = \boldsymbol{v}\cdot\boldsymbol{N}^\Gamma$. Proceeding in the same fashion for the right one and adding up the two equations gives,

$$\frac{d}{dt}\int_V \boldsymbol{\mathcal{U}}\, dV = \int_V \frac{\partial \boldsymbol{\mathcal{U}}}{\partial t}\, dV - \int_\Gamma U[\![\boldsymbol{\mathcal{U}}]\!]\, dA. \tag{2.18}$$

The jump in variables will in general produce a jump in the fluxes $[\![\boldsymbol{\mathcal{F}}_N]\!] = \boldsymbol{\mathcal{F}}_N^R - \boldsymbol{\mathcal{F}}_N^L$. The boundary integral of these fluxes for the left material volume is written as

$$\int_{V^L} \frac{\partial \boldsymbol{\mathcal{F}}_I}{\partial X_I}\, dV = \int_{(\partial V^L \backslash \Gamma)} \boldsymbol{\mathcal{F}}_N\, dA + \int_\Gamma \boldsymbol{\mathcal{F}}_N^L\, dA. \tag{2.19}$$

Proceeding in the same manner for the right material volume and adding up these two expressions gives

$$\int_V \frac{\partial \boldsymbol{\mathcal{F}}_I}{\partial X_I}\, dV = \int_{\partial V} \boldsymbol{\mathcal{F}}_N\, dA - \int_\Gamma [\![\boldsymbol{\mathcal{F}}_N]\!]\, dA. \tag{2.20}$$

Finally, replacing equations (2.18) and (2.20) in equation (2.9) renders

$$\int_V \left(\frac{\partial \boldsymbol{\mathcal{U}}}{\partial t} + \frac{\partial \boldsymbol{\mathcal{F}}_I}{\partial X_I} \right) dV - \int_\Gamma \left(U [\![\boldsymbol{\mathcal{U}}]\!] - [\![\boldsymbol{\mathcal{F}}_N]\!] \right) dA = \mathbf{0}. \tag{2.21}$$

A sufficient condition for the equation above to hold is turning both terms to zero, that is

$$\int_V \left(\frac{\partial \boldsymbol{\mathcal{U}}}{\partial t} + \frac{\partial \boldsymbol{\mathcal{F}}_I}{\partial X_I} \right) dV = \mathbf{0}, \tag{2.22a}$$

$$\int_\Gamma \left(U [\![\boldsymbol{\mathcal{U}}]\!] - [\![\boldsymbol{\mathcal{F}}_N]\!] \right) dA = \mathbf{0}. \tag{2.22b}$$

Since the equations above hold for any control volume V and any surface Γ containing the discontinuity, they can be rewritten in strong form as

$$\frac{\partial \boldsymbol{\mathcal{U}}}{\partial t} + \frac{\partial \boldsymbol{\mathcal{F}}_I}{\partial X_I} = \mathbf{0}, \tag{2.23a}$$

$$U [\![\boldsymbol{\mathcal{U}}]\!] = [\![\boldsymbol{\mathcal{F}}_N]\!], \tag{2.23b}$$

and both equations constitute a more general form of equation (2.11) when discontinuities arise.

2.4 Standard balance laws in Lagrangian solid dynamics

In this section, the standard equations for the total Lagrangian description of the solid motion are summarized. These are the conservation of mass, conservation of linear momentum and conservation of angular momentum. They can be found in more detail in standard text books such as [10–12, 72–77].

2.4.1 Conservation of mass

The conservation of mass in material form is written, in integral form, as

$$\int_V \rho_0\, dV = \int_v \rho\, dv, \tag{2.24}$$

which can be transformed using equation (2.3) into

$$\int_V \rho_0 \, dV = \int_V \rho J \, dV, \tag{2.25}$$

with the following equivalent local form

$$\rho_0 = \rho J. \tag{2.26}$$

2.4.2 Conservation of linear momentum

The conservation of linear momentum for an arbitrary reference volume V is expressed in integral form as:

$$\frac{d}{dt} \int_V \boldsymbol{p} \, dV = \int_V \rho_0 \boldsymbol{b} \, dV + \int_{\partial V} \boldsymbol{t} \, dA, \tag{2.27}$$

where $\boldsymbol{b}$ denotes external volume forces per unit mass and $\boldsymbol{t}$ denotes the traction vector in the current configuration. The stress tensor that relates this traction vector to the unit normal $\boldsymbol{N}$ in the reference configuration is the first Piola-Kirchhoff stress tensor $\boldsymbol{P}$ which verifies

$$\boldsymbol{t} = \boldsymbol{P}\boldsymbol{N}. \tag{2.28}$$

Replacing equation (2.28) into (2.27) and using the divergence theorem, leads to the following expression

$$\int_V \left(\frac{\partial \boldsymbol{p}}{\partial t} - \mathrm{DIV}\, \boldsymbol{P} - \rho_0 \boldsymbol{b} \right) dV = \boldsymbol{0} \tag{2.29}$$

and, since the above integral holds for any volume V, the following strong form can be obtained

$$\frac{\partial \boldsymbol{p}}{\partial t} - \mathrm{DIV}\, \boldsymbol{P} = \rho_0 \boldsymbol{b}. \tag{2.30}$$

2.4.3 Conservation of angular momentum

The conservation of angular momentum about a fixed point $\boldsymbol{x}_0$ is written as

$$\int_V \boldsymbol{r} \times \frac{\partial \boldsymbol{p}}{\partial t} \, dV = \int_V \boldsymbol{r} \times \rho_0 \boldsymbol{b} \, dV + \int_{\partial V} \boldsymbol{r} \times \boldsymbol{t} \, dA, \tag{2.31}$$

where $\boldsymbol{r} = \boldsymbol{x} - \boldsymbol{x}_0$, and the right hand side of the equation corresponds to the moments generated by the surface tractions, $\boldsymbol{t}$, and the body forces, $\boldsymbol{b}$. The surface integral on the right hand side can be rewritten as

$$\int_{\partial V} \boldsymbol{r} \times \boldsymbol{t}\, dA = \int_{\partial V} \boldsymbol{\mathcal{E}} : (\boldsymbol{r} \otimes \boldsymbol{t})\, dA = \int_{\partial V} \boldsymbol{\mathcal{E}} : (\boldsymbol{r} \otimes \boldsymbol{P}\boldsymbol{N})\, dA$$
$$= \int_V \left(\boldsymbol{\mathcal{E}} : \left(\boldsymbol{F}\boldsymbol{P}^T\right) + \boldsymbol{r} \times \mathrm{DIV}\, \boldsymbol{P}\right) dV, \tag{2.32}$$

where $\boldsymbol{\mathcal{E}}$ is the alternating tensor[1]. Replacing the above result into equation (2.31) renders

$$\int_V \boldsymbol{r} \times \left(\frac{\partial \boldsymbol{p}}{\partial t} - \rho_0 \boldsymbol{b} - \mathrm{DIV}\, \boldsymbol{P}\right) dV - \int_V \boldsymbol{\mathcal{E}} : \left(\boldsymbol{F}\boldsymbol{P}^T\right) dV = \boldsymbol{0} \tag{2.33}$$

and using the conservation of linear momentum (equation 2.30), the following equation is obtained

$$\int_V \boldsymbol{\mathcal{E}} : \left(\boldsymbol{F}\boldsymbol{P}^T\right) dV = \boldsymbol{0}. \tag{2.34}$$

Equation (2.34) has to be fulfilled for any control volume V, therefore

$$\boldsymbol{\mathcal{E}} : \left(\boldsymbol{F}\boldsymbol{P}^T\right) = \boldsymbol{0}, \tag{2.35}$$

which in turn requires

$$\boldsymbol{F}\boldsymbol{P}^T = \boldsymbol{P}\boldsymbol{F}^T \tag{2.36}$$

and which is the local form of the equation of conservation of angular momentum. Using the relation between the first and the second Piola-Kirchhoff stress tensors

$$\boldsymbol{P} = \boldsymbol{F}\boldsymbol{S}, \tag{2.37}$$

it can be concluded that the conservation of angular momentum requires the symmetry of the second Piola-Kirchhoff stress tensor

$$\boldsymbol{S} = \boldsymbol{S}^T. \tag{2.38}$$

Angular momentum conservation law

A first order conservation law can be obtained for the angular momentum. Defining

$$\boldsymbol{w} = \boldsymbol{r} \times \boldsymbol{p}, \tag{2.39}$$

and considering

$$\int_{\partial V} [\boldsymbol{r} \times \boldsymbol{t}]_i\, dA = \int_{\partial V} \mathcal{E}_{ijk} r_j P_{kM} N_M\, dA = \int_V \frac{\partial}{\partial X_M} \left(\mathcal{E}_{ijk} r_j P_{kM}\right) dV, \tag{2.40}$$

[1]The components of the alternating tensor are defined as $\mathcal{E}_{ijk} = \boldsymbol{e}_i \cdot (\boldsymbol{e}_j \times \boldsymbol{e}_k)$

together with equation (2.31), the following integral form is obtained

$$\frac{d}{dt}\int_V \boldsymbol{w}\, dV = \int_V \mathrm{DIV}\,(\boldsymbol{r}\times\boldsymbol{P})\, dV + \int_V \boldsymbol{r}\times\rho_0\boldsymbol{b}\, dV, \tag{2.41}$$

where the product $\times$ is defined in Appendix A. The above expression can be rewritten in local form as

$$\frac{\partial \boldsymbol{w}}{\partial t} = \mathrm{DIV}\,(\boldsymbol{r}\times\boldsymbol{P}) + \boldsymbol{r}\times\rho_0\boldsymbol{b}. \tag{2.42}$$

Despite being a first order conservation law, this equation will not be useful for the problem formulation, since the numerical fluxes require the use of the position $\boldsymbol{r}$, a variable that cannot be directly solved using another conservation law.

2.5 Thermodynamics

The balance equations provided in the previous section, complemented with an adequate constitutive model, can describe the motion of a reversible process. However, when irreversible processes are taken into account, additional relations and variables are needed. These relations are given by the first law of thermodynamics, which describes the evolution of the total energy, and the second law of thermodynamics, which gives a measure of the irreversibility of the process through the production of entropy.

2.5.1 Conservation of Energy (First Law of Thermodynamics)

Assuming absence of electromagnetic fields or chemical reactions, the evolution of the total energy per unit of undeformed volume of a continuum, E, is due to the rate of work exerted on that body (through body forces $\boldsymbol{b}$ and tractions $\boldsymbol{t}$) plus the rate of increase of heat energy (through the heat source s and heat flux $\boldsymbol{Q}$)

$$\frac{d}{dt}\int_V E\, dV = \int_{\partial V} \boldsymbol{t}\cdot\boldsymbol{v}\, dA + \int_V \rho_0\boldsymbol{b}\cdot\boldsymbol{v}\, dV - \int_{\partial V} \boldsymbol{Q}\cdot\boldsymbol{N}\, dA + \int_V s\, dV, \tag{2.43}$$

where the heat flux $\boldsymbol{Q}$ is normally defined using the Fourier's law (see for example reference [76]), which, for the isotropic case reads

$$\boldsymbol{Q} = -h\nabla_0\theta, \tag{2.44}$$

where θ is the temperature and h a material constant defined as the thermal conductivity[2]. The corresponding local balance law is the first law of thermodynamics given by

[2]In the more general case (anisotropic material) the thermal conductivity is defined through a positive semidefinite tensor $\boldsymbol{h}$.

$$\frac{\partial E}{\partial t} - \text{DIV}\left(\frac{1}{\rho_0}\boldsymbol{P}^T\boldsymbol{p} - \boldsymbol{Q}\right) = s + \rho_0 \boldsymbol{b}\cdot\boldsymbol{v}. \tag{2.45}$$

The energy of a body that is not associated with kinetic energy is named internal energy. The internal energy per unit initial volume, e, is defined as,

$$e = E - \frac{1}{2}\rho_0 \boldsymbol{v}\cdot\boldsymbol{v}, \tag{2.46}$$

and by combining this definition with the first law of thermodynamics and the conservation of linear momentum, equation (2.30), an equation for the conservation of the internal energy per unit initial volume can be written as

$$\frac{\partial e}{\partial t} = \boldsymbol{P} : \frac{\partial \boldsymbol{F}}{\partial t} - \text{DIV}\,\boldsymbol{Q} + s. \tag{2.47}$$

2.5.2 Second Law of Thermodynamics

The second law of thermodynamics, or Clausius-Duhem inequality, states that the rate of the total entropy of a system must be greater than or equal to the transfer of entropy into the system. In Lagrangian form that reads,

$$\frac{d}{dt}\int_V \eta\, dV + \int_{\partial V}\frac{1}{\theta}\boldsymbol{Q}\cdot\boldsymbol{N}\, dA - \int_V \frac{s}{\theta}\, dV \geq 0, \tag{2.48}$$

where η is the entropy and θ the temperature. The entropy is defined as the work conjugate to the temperature, that is,

$$\theta = \frac{\partial e(\boldsymbol{F},\eta)}{\partial \eta}. \tag{2.49}$$

By using the divergence theorem, equation (2.48) can be rewritten as

$$\int_V \left(\frac{\partial \eta}{\partial t} + \text{DIV}\left(\frac{\boldsymbol{Q}}{\theta}\right) - \frac{s}{\theta}\right) dV \geq 0 \tag{2.50}$$

and, since it is valid for any volume V, the local form of equation (2.48) is

$$\frac{\partial \eta}{\partial t} + \text{DIV}\left(\frac{\boldsymbol{Q}}{\theta}\right) - \frac{s}{\theta} \geq 0, \tag{2.51}$$

which is the local form of the Clausius-Duhem inequality or second law of thermodynamics. Substituting equation (2.47) into equation (2.51), the following alternative inequality is obtained

$$\theta\frac{\partial \eta}{\partial t} - \frac{1}{\theta}\boldsymbol{Q}\cdot\nabla_0\theta + \boldsymbol{P} : \frac{\partial \boldsymbol{F}}{\partial t} - \frac{\partial e}{\partial t} \geq 0. \tag{2.52}$$

In addition, the definition of η as work conjugate of the temperature (equation (2.49)), makes it possible to define the Helmholtz free energy potential, $\psi(\boldsymbol{F},\theta)$, using the Legendre transform as:

$$\psi(\boldsymbol{F}, \theta) = e(\boldsymbol{F}, \eta) - \eta\theta, \tag{2.53}$$

where "free energy" is the portion of internal energy available for performing work at constant temperature (see, for example, [74, 75]). It is clear that ψ does not depend on the entropy since

$$\frac{\partial \psi}{\partial \eta} = \frac{\partial e}{\partial \eta} - \theta = \theta - \theta = 0. \tag{2.54}$$

The Clausius-Duhem inequality (equation (2.51)) can now be rewritten using the Helmholtz free energy potential as

$$-\frac{\partial \psi}{\partial t} - \eta \frac{\partial \theta}{\partial t} - \frac{1}{\theta} \boldsymbol{Q} \cdot \nabla_0 \theta + \boldsymbol{P} : \dot{\boldsymbol{F}} \geq 0. \tag{2.55}$$

2.6 Additional balance laws in Lagrangian solid dynamics

The system of conservation laws presented so far, complemented with the adequate constitutive models describes the motion of a continuum. However, the use of this system of equations entails a series of shortcomings when resolved numerically, specially with low order methods. First of all, the constitutive models depend on kinematic variables not resolved directly in the system, such as $\boldsymbol{F}$, J or even $\boldsymbol{H}$ when polyconvex materials are used. Therefore, the deformation gradient $\boldsymbol{F}$ has to be obtained as a "numerical" gradient of the displacements $\boldsymbol{x}$, with the resulting loss of order of accuracy both for the strains and the stresses. This implies difficulties in bending dominated situations, or locking phenomena (see fore example [8]). This issue is more accentuated in nearly-incompressible situations, where an accurate representation of the determinant of $\boldsymbol{F}$, J, is required.

Secondly, the use of the conservation law (2.30) together with the kinematic relation (2.5) form a second order system of hyperbolic equations. The numerical solution of such systems presents oscillations in the vicinity of sharp gradients.

An interesting solution was presented in [1] and later implemented in [2,4,31]. In [1], a mixed system of conservation laws is proposed, where the conservation of linear momentum (equation (2.30) or equation (2.27) in its integral form) together with the conservation of energy (equation (2.45) or equation (2.43) in its integral form) are solved alongside a conservation law for the deformation gradient, $\boldsymbol{F}$. This allows obtaining the same order of accuracy for both strains and stresses, and therefore alleviating the bending difficulties. Furthermore, treating $\boldsymbol{F}$ as a separate variable, results in not needing to solve the conservation of linear momentum in terms of displacements [3]. This leads to a first order hyperbolic system, which can be solved using standard Computational Fluid Dynamics (CFD) techniques [56, 78].

[3] Displacements are solved only for post-process purposes and for the angular momentum correction algorithm as it will be explained in chapter 6.

In the current section, the evolution law for the deformation gradient, $\boldsymbol{F}$ will be presented. Additionally, two more evolution laws will be presented for the determinant of $\boldsymbol{F}$, J, and for the cofactor of $\boldsymbol{F}$, $\boldsymbol{H}$. These additional variables will not be used in the thesis, but an interesting application for polyconvex materials was presented in references [79,80] and briefly summarised in Appendix C.

2.6.1 Conservation of deformation gradient

Expressing the evolution of the deformation gradient as

$$\frac{\partial \boldsymbol{F}}{\partial t} = \frac{\partial}{\partial t}\left(\frac{\partial \boldsymbol{x}}{\boldsymbol{X}}\right) = \frac{\partial \boldsymbol{v}}{\partial \boldsymbol{X}} = \nabla_0 \boldsymbol{v} \tag{2.56}$$

and noting that

$$\nabla_0 \boldsymbol{v} = \mathrm{DIV}\left(\frac{1}{\rho_0}\boldsymbol{p} \otimes \boldsymbol{I}\right), \tag{2.57}$$

the following local conservation law is obtained

$$\frac{\partial \boldsymbol{F}}{\partial t} - \mathrm{DIV}\left(\frac{1}{\rho_0}\boldsymbol{p} \otimes \boldsymbol{I}\right) = \boldsymbol{0}, \tag{2.58}$$

which, by using the divergence theorem, can be written in integral form as

$$\frac{d}{dt}\int_V \boldsymbol{F}\, dV = \int_{\partial V} \frac{1}{\rho_0}\boldsymbol{p} \otimes \boldsymbol{N}\, dA. \tag{2.59}$$

When solving the deformation gradient as a separate variable, a series of compatibility conditions have to be fulfilled [17,65]. These conditions ensure that the deformation gradient corresponds to the gradient of a real mapping and are written as

$$\mathrm{CURL}(\boldsymbol{F}) = \boldsymbol{0}. \tag{2.60}$$

2.6.2 Conservation of J

By using the Reynold's Transport Theorem (see Appendix B) for a constant scalar variable $u = 1$, the rate of change of a spatial volume v is obtained as

$$\frac{d}{dt}\int_v dv = \int_{\partial v} \boldsymbol{v} \cdot \boldsymbol{n}\, da \tag{2.61}$$

and this can be pulled back into the reference domain by using relations (2.3) and (2.4) as

$$\frac{d}{dt}\int_V J\, dV = \int_{\partial V} \boldsymbol{v} \cdot (\boldsymbol{H}\boldsymbol{N})\, dA, \tag{2.62}$$

which is the conservation law for J in integral form. The correspondent local conservation law is written as

$$\frac{\partial J}{\partial t} - \mathrm{DIV}(\boldsymbol{H}^T \boldsymbol{v}) = 0. \tag{2.63}$$

2.6.3 Conservation of $\boldsymbol{H}$

The cofactor of $\boldsymbol{F}$, $\boldsymbol{H}$, can be rewritten as (see appendix A)

$$\boldsymbol{H} = \frac{1}{2}\boldsymbol{F} \times \boldsymbol{F}, \tag{2.64}$$

and its time derivative,

$$\dot{\boldsymbol{H}} = \boldsymbol{F} \times \nabla_0 \boldsymbol{v}. \tag{2.65}$$

Using the definition of CURL of a second order tensor (see Appendix A), the following identity is derived

$$\begin{aligned}
[\mathrm{CURL}(\boldsymbol{v} \times \boldsymbol{F})]_{iI} &= \varepsilon_{IJK} \frac{\partial [\boldsymbol{v} \times \boldsymbol{F}]_{iK}}{\partial X_J} = \varepsilon_{IJK} \frac{\partial}{\partial X_J} (\varepsilon_{ijk} v_j F_{kK}) \\
&= \varepsilon_{IJK} \varepsilon_{ijk} \frac{\partial v_j}{\partial X_J} F_{kK} + \varepsilon_{IJK} \varepsilon_{ijk} v_j \frac{\partial F_{kK}}{\partial X_J} \\
&= [\nabla_0 \boldsymbol{v} \times \boldsymbol{F}]_{iI} = [\boldsymbol{F} \times \nabla_0 \boldsymbol{v}]_{iI},
\end{aligned} \tag{2.66}$$

where the involution given by equation (2.60) has been taken into account. Replacing the result above into equation (2.65), a conservation law for $\boldsymbol{H}$ is obtained as

$$\frac{\partial \boldsymbol{H}}{\partial t} = \mathrm{CURL}(\boldsymbol{v} \times \boldsymbol{F}). \tag{2.67}$$

On the other hand

$$\begin{aligned}
\int_V [\mathrm{CURL}(\boldsymbol{v} \times \boldsymbol{F})]_{iI}\, dV &= \int_V \varepsilon_{IJK} \frac{\partial [\boldsymbol{v} \times \boldsymbol{F}]_{iK}}{\partial X_J}\, dV = \int_{\partial V} \varepsilon_{IJK} [\boldsymbol{v} \times \boldsymbol{F}]_{iK} N_J\, dA \\
&= -\int_{\partial V} \varepsilon_{IKJ} [\boldsymbol{v} \times \boldsymbol{F}]_{iK} N_J\, dA = -\int_{\partial V} [\boldsymbol{v} \times \boldsymbol{F} \times \boldsymbol{N}]_{iI}\, dA
\end{aligned} \tag{2.68}$$

integrating (2.67) within a control volume V and replacing the above result gives finally the integral form of the conservation law (2.67)

$$\frac{d}{dt} \int_V \boldsymbol{H}\, dV = -\int_{\partial V} (\boldsymbol{v} \times \boldsymbol{F} \times \boldsymbol{N}) dA. \tag{2.69}$$

As in the case for the deformation gradient, if $\boldsymbol{H}$ is solved separately, certain compatibility conditions need to be fulfilled. In this particular case, these are given by the following equation

$$\mathrm{DIV}(\boldsymbol{H}) = \boldsymbol{0}. \tag{2.70}$$

Chapter 3

Constitutive models

3.1 Preliminaries

The balance laws presented thus far represent a system of equations with more unknowns than equations. Therefore, additional relationships need to be provided. These relationships stem from the constitutive model, relating stresses to strains and to internal variables in the case of thermo-mechanical materials. This constitutive model has to satisfy the objectivity requirements which state that the stress components do not fundamentally change due to rigid body motions (rotations and translations). A further consequence of the objectivity requirement for thermoelastic materials is the symmetry of the second Piola-Kirchhoff stress tensor [75, 81]. Furthermore, the constitutive model has to satisfy the second law of thermodynamics through the dissipation inequality (2.55) [10, 12, 75, 76]. This chapter will present constitutive models for three different cases: isothermal elastic solids (section 3.2), elasto-plastic solids (section 3.3) and thermo-elastic solids (section 3.4).

3.2 Isothermal elastic solids

In the case of reversible isothermal elasticity, the first Piola-Kirchhoff tensor is defined as a function of the deformation gradient derived from an elastic energy potential $\psi(\boldsymbol{F})$ as (see for example [10, 11, 75])

$$\boldsymbol{P}(\boldsymbol{F}) = \frac{\partial \psi}{\partial \boldsymbol{F}}. \tag{3.1}$$

For instance, the compressible neo-Hookean constitutive model is defined by the following strain energy function

$$\psi(\boldsymbol{F}) = \frac{1}{2}(\boldsymbol{F} : \boldsymbol{F} - 3) - \mu \ln J + \frac{1}{2}\lambda(\ln J)^2, \tag{3.2}$$

where λ and μ are positive material constants with a similar interpretation to the

classical Lamé coefficients of the linear case [1]. The first Piola-Kirchhoff stress tensor is then given as

$$\boldsymbol{P} = \mu(\boldsymbol{F} - \boldsymbol{F}^{-T}) + \lambda(\ln J)\boldsymbol{F}^{-T}. \tag{3.3}$$

For nearly incompressible applications, it is often convenient to split this strain energy $\psi(\boldsymbol{F})$ into isochoric and volumetric components $\psi(\boldsymbol{F}) = \psi_{iso}(\hat{\boldsymbol{F}}) + \psi_{vol}(J)$, with $\hat{\boldsymbol{F}} = J^{-1/3}\boldsymbol{F}$, which in turn leads to the deviatoric and pressure components of $\boldsymbol{P}$ as,

$$\boldsymbol{P} = \boldsymbol{P}_{dev} + \boldsymbol{P}_{vol}; \quad \boldsymbol{P}_{dev} = \frac{\partial \psi_{iso}}{\partial \boldsymbol{F}}, \quad \boldsymbol{P}_{vol} = \frac{\partial \psi_{vol}}{\partial \boldsymbol{F}}. \tag{3.4}$$

In particular, the volumetric term can be further developed by introducing the pressure p as

$$\boldsymbol{P}_{vol} = pJ\boldsymbol{F}^{-T}; \quad p = \frac{d\psi_{vol}(J)}{dJ}. \tag{3.5}$$

Note that the sign convention used here is p positive in tension and negative in compression. The simplest example of a constitutive model which satisfies the above form is given by the nearly incompressible extension of the neo-Hookean model (3.3) defined by

$$\psi_{dev} = \frac{\mu}{2}\left[J^{-2/3}(\boldsymbol{F} : \boldsymbol{F}) - 3\right]; \quad \psi_{vol} = \frac{1}{2}\kappa(J-1)^2, \tag{3.6}$$

where μ and κ are the shear and bulk modulus, respectively. The resulting components of the first Piola-Kirchhoff stress tensor read

$$\boldsymbol{P} = \mu J^{-2/3}\left[\boldsymbol{F} - \frac{1}{3}(\boldsymbol{F} : \boldsymbol{F})\boldsymbol{F}^{-T}\right] + pJ\boldsymbol{F}^{-T}; \quad p = \kappa(J-1). \tag{3.7}$$

3.3 Elastic-plastic solids

In order to model plastic behaviour, a rate-independent von Mises plasticity model with isotropic hardening, such as that presented in [10,82], is used. The deformation gradient tensor $\boldsymbol{F}$ is multiplicatively decomposed into an elastic component $\boldsymbol{F}_e$ and a plastic component $\boldsymbol{F}_p$ as

$$\boldsymbol{F} = \boldsymbol{F}_e\boldsymbol{F}_p; \quad \boldsymbol{b}_e = \boldsymbol{F}\boldsymbol{C}_p^{-1}\boldsymbol{F}^T; \quad \boldsymbol{C}_p = \boldsymbol{F}_p^T\boldsymbol{F}_p. \tag{3.8}$$

In addition, a strain energy functional in terms of the elastic principal stretches $(\lambda_{e,1}, \lambda_{e,2}, \lambda_{e,3})$ is defined as

$$\psi(\lambda_{e,1}, \lambda_{e,2}, \lambda_{e,3}, J) = \psi_{dev}(J^{-1/3}\lambda_{e,1}, J^{-1/3}\lambda_{e,2}, J^{-1/3}\lambda_{e,3}) + \psi_{vol}(J), \tag{3.9}$$

[1] In specific cases such as plane strain, the deformation gradient $\boldsymbol{F}$ is defined as $\boldsymbol{F} = \begin{pmatrix} F_{11} & F_{12} & 0 \\ F_{21} & F_{22} & 0 \\ 0 & 0 & 1 \end{pmatrix}$

where

$$\psi_{dev} = \mu\left[(\ln\lambda_{e,1})^2 + (\ln\lambda_{e,2})^2 + (\ln\lambda_{e,3})^2\right] - \frac{1}{3}\mu(\ln J)^2 \tag{3.10}$$

and

$$\psi_{vol} = \frac{1}{2}\kappa(\ln J)^2; \quad \ln J = \ln\lambda_{e,1} + \ln\lambda_{e,2} + \ln\lambda_{e,3}. \tag{3.11}$$

The algorithm to update the plastic strain $\boldsymbol{C}_p$ is summarised in Algorithm 3.3.1 [10].

Algorithm 3.3.1: EVALUATION OF $\boldsymbol{P}_{n+1}(\boldsymbol{F}_{n+1}, \boldsymbol{C}_{p,n}^{-1}, \bar{\varepsilon}_{p,n})$

(1) Given $\boldsymbol{F}_{n+1}$, $\boldsymbol{C}_{p,n}^{-1}$ and $\bar{\varepsilon}_{p,n}$
(2) Initiate $\Delta\gamma = \nu_\alpha^{n+1} = 0$
(3) Evaluate $J_{n+1} = \det \boldsymbol{F}_{n+1}$
(4) Solve pressure $p = \kappa \frac{\ln J_{n+1}}{J_{n+1}}$
(5) Compute trial left strain tensor $\boldsymbol{b}_{e,n+1}^{trial} = \boldsymbol{F}_{n+1}\boldsymbol{C}_{p,n}^{-1}\boldsymbol{F}_{n+1}^T$
(6) Spectral decomposition: $\boldsymbol{b}_{e,n+1}^{trial} = \sum_{\alpha=1}^{3}(\lambda_{e,\alpha}^{trial})^2\, \boldsymbol{n}_\alpha^{trial} \otimes \boldsymbol{n}_\alpha^{trial}$
(7) Set $\boldsymbol{n}_\alpha^{n+1} = \boldsymbol{n}_\alpha^{trial}$
(8) Trial Kirchhoff stress: $\tau_{\alpha\alpha}^{\prime\, trial} = 2\mu \ln\lambda_{e,\alpha}^{trial} - \frac{2}{3}\mu \ln J_{n+1}$
if $(f(\boldsymbol{\tau}^{\prime\, trial}, \bar{\varepsilon}_{p,n}) > 0)$
then
(9) Direction vector: $\nu_\alpha^{n+1} = \frac{\tau_{\alpha\alpha}^{\prime\, trial}}{\sqrt{\frac{2}{3}}\|\boldsymbol{\tau}^{\prime\, trial}\|}$
(10) Incremental plastic multiplier: $\Delta\gamma = \frac{f(\boldsymbol{\tau}^{\prime\, trial}, \bar{\varepsilon}_{p,n})}{3\mu + H}$
(11) Elastic stretch: $\lambda_{e,\alpha}^{n+1} = \mathrm{Exp}\,(\ln\lambda_{e,\alpha}^{trial} - \Delta\gamma\nu_\alpha^{n+1})$
(12) Return map: $\tau_{\alpha\alpha}^{\prime} = \left(1 - \frac{2\mu\Delta\gamma}{\sqrt{2/3}\|\boldsymbol{\tau}^{\prime\, trial}\|}\right)\tau_{\alpha\alpha}^{\prime\, trial}$
(13) Update stress: $\tau_{\alpha\alpha} = \tau_{\alpha\alpha}^{\prime} + Jp; \quad \boldsymbol{\tau} = \sum_{\alpha=1}^{3}\tau_{\alpha\alpha}\boldsymbol{n}_\alpha^{n+1} \otimes \boldsymbol{n}_\alpha^{n+1}$
(14) First Piola-Kirchhoff stress tensor: $\boldsymbol{P} = \boldsymbol{\tau}\boldsymbol{F}^{-T}$
(15) Update $\boldsymbol{b}_{e,n+1} = \sum_{\alpha=1}^{3}(\lambda_{e,\alpha}^{n+1})^2\, \boldsymbol{n}_\alpha^{n+1} \otimes \boldsymbol{n}_\alpha^{n+1}$
(16) Update $\boldsymbol{C}_{p,n+1}^{-1} = \boldsymbol{F}_{n+1}^{-1}\boldsymbol{b}_{e,n+1}\boldsymbol{F}_{n+1}^{-T}; \quad \bar{\varepsilon}_{p,n+1} = \bar{\varepsilon}_{p,n} + \Delta\gamma$
return $(\boldsymbol{P}_{n+1})$

3.4 Thermo-elastic solids

There are many applications in engineering where thermal effects need to be taken into account. In these processes the constitutive equations are more complex than the ones for isothermal elasticity, since the stress tensor is not only related to the deformation but as well to some internal varible, such as the temperature or the internal energy. For these applications, the first law of thermodynamics (equation (2.43)) needs to be solved, while the second law of thermodynamics (equation (2.48)) needs to be satisfied by the constitutive relationship. In order to give a detailed

explanation of the thermo-mechanical constitutive relationships, new relations need to be provided. The internal energy e is related to the temperature θ through the heat coefficient at constant deformation, C_F as

$$\rho_0 C_F = \left.\frac{\partial e}{\partial \theta}\right|_{\boldsymbol{F}}, \tag{3.12}$$

therefore, the internal energy can be expressed as

$$e(\boldsymbol{F},\theta) = e_0(\boldsymbol{F}) + \int_{\theta_0}^{\theta} \rho_0 C_F(\theta)\, d\theta, \tag{3.13}$$

where e_0 is the internal energy at the reference temperature, that is

$$e_0(\boldsymbol{F}) = e(\boldsymbol{F},\theta_0). \tag{3.14}$$

Alternatively, using the definition of entropy as work conjugate of the temperature (equation (2.49)), equation (3.12) can be rewritten as

$$\rho_0 C_F = \left.\frac{\partial e(\boldsymbol{F},\theta)}{\partial \theta}\right|_{\boldsymbol{F}} = \left.\frac{\partial e(\boldsymbol{F},\eta)}{\partial \eta}\right|_{\boldsymbol{F}} \left.\frac{\partial \eta(\boldsymbol{F},\theta)}{\partial \theta}\right|_{\boldsymbol{F}} = \theta \left.\frac{\partial \eta(\boldsymbol{F},\theta)}{\partial \theta}\right|_{\boldsymbol{F}} \tag{3.15}$$

which gives

$$\eta(\boldsymbol{F},\theta) = \eta_0(\boldsymbol{F}) + \int_{\theta_0}^{\theta} \frac{\rho_0 C_F(\theta)}{\theta}\, d\theta, \tag{3.16}$$

where η_0 is the entropy at the reference temperature

$$\eta_0(\boldsymbol{F}) = \eta(\boldsymbol{F},\theta_0). \tag{3.17}$$

Expressing the internal energy as a function of $\boldsymbol{F}$ and η can lead to additional relations, for example

$$\frac{\partial e(\boldsymbol{F},\eta)}{\partial t} = \frac{\partial e(\boldsymbol{F},\eta)}{\partial \boldsymbol{F}} : \frac{\partial \boldsymbol{F}}{\partial t} + \frac{\partial e(\boldsymbol{F},\eta)}{\partial \eta}\frac{\partial \eta}{\partial t}, \tag{3.18}$$

which compared to the balance of internal energy in the absence of heat sources (see equation (2.47)) and considering $\theta = \partial e(\boldsymbol{F},\eta)/\partial\eta$ gives

$$\boldsymbol{P} = \frac{\partial e(\boldsymbol{F},\eta)}{\partial \boldsymbol{F}} \tag{3.19}$$

$$\frac{\partial \eta}{\partial t}, = -\frac{1}{\theta}\,\mathrm{DIV}\,\boldsymbol{Q}. \tag{3.20}$$

Since the elastic relations are obtained from free energy potentials, it would be more interesting to obtain a thermoelastic constitutive relation using such functionals. By using the Legendre transform (equation (2.53)) the following two relations are obtained

$$\frac{\partial \psi(\boldsymbol{F},\theta)}{\partial \boldsymbol{F}} = \frac{\partial e(\boldsymbol{F},\eta)}{\partial \boldsymbol{F}} = \boldsymbol{P}, \tag{3.21}$$

$$\frac{\partial \psi(\boldsymbol{F},\theta)}{\partial \theta} = -\eta. \tag{3.22}$$

Using equations (2.53), (3.13) and (3.16) and supposing that C_F does not change with temperature, the Helmholtz free energy can be written, for a particular deformation $\boldsymbol{F}$ and temperature θ as

$$\psi(\boldsymbol{F},\theta) = e(\boldsymbol{F},\theta) - \theta\eta(\boldsymbol{F},\theta) = \psi_0(\boldsymbol{F}) - \eta_0(\boldsymbol{F})\Delta\theta + T(\theta), \tag{3.23}$$

where

$$T(\theta) = \rho_0 C_F \left(\Delta\theta - \theta \ln \frac{\theta}{\theta_0}\right), \tag{3.24}$$

$$\psi_0(\boldsymbol{F}) = \psi(\boldsymbol{F},\theta_0). \tag{3.25}$$

Finally, the constitutive equation is now expressed as

$$\boldsymbol{P} = \boldsymbol{P}_0 - \frac{\partial \eta_0}{\partial \boldsymbol{F}} \frac{(e - e_0(\boldsymbol{F}))}{\rho_0 C_F}, \quad \boldsymbol{P}_0 = \frac{\partial \psi_0}{\partial \boldsymbol{F}} \tag{3.26}$$

It is clear from the above equation that the term $\eta_0(\boldsymbol{F})$ couples the thermal and mechanical effects. In its simplest form it can be assumed to depend only on the Jacobian of the motion J, that is $\eta_0(\boldsymbol{F}) = \eta_0(J)$, which will be the case for the Mie-Grüneisen equation of state explained in the next section. The stress tensor would then be computed as,

$$\boldsymbol{P} = \boldsymbol{P}_0 - \frac{\partial \eta_0(J)}{\partial J}\frac{\partial J}{\partial \boldsymbol{F}}\frac{(e - e_0(\boldsymbol{F}))}{\rho_0 C_F} = \boldsymbol{P}_0 - \eta_0'(J) J \boldsymbol{F}^{-T}\frac{(e - e_0(\boldsymbol{F}))}{\rho_0 C_F} \tag{3.27}$$

or, by virtue of equation (3.13),

$$\boldsymbol{P} = \boldsymbol{P}_{0,dev} + (p_0 - \eta_0'(J)\Delta\theta) J \boldsymbol{F}^{-T} \tag{3.28}$$

Mie-Grüneisen equation of state

According to Grüneisen theory, the total internal energy of a solid state or a dense fluid regime is comprised by a cold component, emerging from the intermolecular repulsive and attractive forces, e_{0K}, (at temperature $\theta = 0$ K), and a thermal component, associated with the random motion of atoms and molecules, e_{th}, (see [83–86]). This is

$$e = e_{0K}(J) + e_{th}(J,\theta). \tag{3.29}$$

Furthermore, also according to the Grüneisen theory, the related pressure is again comprised of a cold component p_{0K} and a thermal component p_{th}, that is

$$p(J,\theta) = p_{0K}(J) + p_{th}(J,\theta) \tag{3.30}$$

and the thermal component can be written as

$$p_{th}(J,\theta) = -\frac{\Gamma(J)}{J} e_{th}(J,\theta) \tag{3.31}$$

where $\Gamma(J)$ is the dimensionless Grüneisen coefficient that takes into account the random vibration of the atoms. Combining equations (3.29), (3.30) and (3.31) results into a linear relation between the pressure and the internal energy,

$$p(e,J) = p_{0K}(J) - \frac{\Gamma(J)}{J}(e - e_{0K}(J)), \tag{3.32}$$

From the macroscopic point of view, the Grüneisen coefficient can be defined from thermodynamic considerations as (see reference [86] and equations (3.12) and (3.15))

$$\Gamma = -J \left.\frac{\partial p}{\partial e}\right|_J = -\frac{J}{\rho_0 C_F} \left.\frac{\partial p}{\partial \theta}\right|_J = \frac{J\eta_0'}{\rho_0 C_F}. \tag{3.33}$$

In general, it is assumed that Γ varies according to the equation

$$\Gamma = \Gamma_0 J^q, \tag{3.34}$$

where Γ_0 is a material parameter and the coefficient q is usually taken to be 1 for solids and 0 for fluids. This parameter has to be obtained from physical experiments or molecular dynamics simulations [84].

The Mie-Grüneisen equation (3.35) can be extended to other reference states, as for example a general reference temperature θ_0 (which can be different to $\theta = 0$ K) to give

$$p(e,J) = p_0(J) - \frac{\Gamma(J)}{J}(e - e_0(J)), \tag{3.35}$$

which can now be combined with equation (3.27) to give the stress tensor as

$$\boldsymbol{P} = \boldsymbol{P}_0 - \rho_0 C_F \Gamma_0 J^q \Delta\theta \boldsymbol{F}^{-T}, \tag{3.36}$$

with (see equation (3.13))

$$\Delta\theta = \frac{1}{\rho_0 C_F}(e - e_0(\boldsymbol{F})), \tag{3.37}$$

where it has been considered that C_F does not change with temperature.

Instead of a reference temperature θ_0, a reference entropy (normally $\eta = 0$) could have been chosen. Another possible reference state is the locus of states behind a shock, named the *Hugoniot* locus. This locus is obtained by taking the conservation

of mass, linear momentum and energy in Eulerian form (see Appendix B) and using the Rankine-Hugoniot jump conditions (see section 2.3.3) in the direction of the shock (see [66, 83–85])[2], which yields

$$v_S(\rho_0 - \rho_H) = \rho_0 v_0 - \rho_H v_H \tag{3.38}$$

$$v_S(\rho_0 v_0 - \rho_H v_H) = \rho_0 v_0^2 - \rho_H v_H^2 + p_0 - p_H \tag{3.39}$$

$$v_S(J_0^{-1}E_0 - J_H^{-1}E_H) = v_0(J_0^{-1}E_0 + p_0) - v_H(J_H^{-1}E_H + p_H) \tag{3.40}$$

where v_S is the shock velocity, the subscript 0 stands for the reference state and the subscript H for the state behind the shock. The reference state is usually considered as uncompressed and at rest, therefore it has null internal energy, velocity and pressure $v_0 = 0$, $e_0 = 0$ and $p_0 = 0$. After some algebra it is found that,

$$v_H = v_S\,(1 - J)\,, \tag{3.41}$$

$$p_H = -\rho_0 v_S v_H, \tag{3.42}$$

$$e_H = \frac{1}{2}\frac{\rho_0}{J} v_H^2. \tag{3.43}$$

These equations are usually complemented with experimental data that relates the shock velocity v_S to the particle velocity v_H behind the shock in the form $v_S = v_S(v_H)$. For metals in the absence of phase transitions, it is proved that this relation is linear [66, 83] and given by

$$v_S = c_{p,0} + s v_H, \tag{3.44}$$

where s is a material parameter (to be found in experiments) and $c_{p,0}$ is the bulk sound speed of the uncompressed material. Combining this equation with equations (3.41), (3.42) and (3.43) gives

$$p_H(J) = \frac{\rho_0 c_{p,0}^2 (J-1)}{(1 - s(1-J))^2}, \tag{3.45}$$

$$e_H(J) = \frac{1}{2}\frac{\rho_0 c_{p,0}^2 (J-1)^2}{(1 - s(1-J))^2}. \tag{3.46}$$

Using p_H and e_H as reference presssure and energy, the Mie-Grüneisen formalism (equation (3.35)) can now be used to describe states off the Hugoniot as

$$p(e, J) = \frac{\rho_0 c_{p,0}^2 (J-1)}{(1 - s(1-J))^2} - \frac{\Gamma(J)}{J}\left[e - \frac{1}{2}\rho_0 c_{p,0}^2 \left(\frac{(J-1)}{1 - s(1-J)}\right)^2\right], \tag{3.47}$$

[2]The Eulerian form is used because in the physical experiments the spatial velocity is measured

which is an equation of state valid for those solids satisfying the relation given by equation (3.44). In such cases, an equation of state as the one given by equation (3.47) can be obtained by uniquely using shock wave data. In these particular cases, the first Piola-Kirchhoff stress tensor would be obtained as,

$$\boldsymbol{P} = \boldsymbol{P}_{0,dev} + p(e, J)J\boldsymbol{F}^{-T}, \tag{3.48}$$

with $p(e, J)$ obtained using equation (3.47).

Chapter 4

Combined conservation law formulation for solid dynamics

4.1 Preliminaries

The combination of the balance laws provided in section 2.4, the first and second laws of thermodynamics presented in section 2.5 and an adequate constitutive model as presented in chapter 3, together with adequate initial conditions and boundary conditions, can establish a well-posed problem. Specifically, in Lagrangian dynamics, the solution of the conservation of linear momentum and total energy equations (2.30) and (2.45) is enough given that the constitutive model satisfies the production of entropy and symmetry of the second Piola-Kirchhoff stress tensor (the conservation of mass is not necessary since the spatial density is an escalation of the material density trough the Jacobian of the deformation J). From a discrete point of view, this solution would traditionally be obtained on displacements $\boldsymbol{x} = \boldsymbol{x}(\boldsymbol{X}, t)$ using a kinematic relation of the type $\boldsymbol{v}(\boldsymbol{X}, t) = \frac{d}{dt}(\boldsymbol{x}(\boldsymbol{X}, t))$. The constitutive model would be evaluated using the gradient of the displacements, $\nabla_0 \boldsymbol{x}$, and, if a thermomechanical constitutive model is used, an internal variable such as the entropy η, i.e. $\boldsymbol{P} = \boldsymbol{P}(\nabla_0 \boldsymbol{x}, \eta)$.

In the current thesis, instead, a mixed system of conservation laws is presented as in [1,2,17,31]. The conservation of linear momentum, equation (2.30) will be solved along with the conservation of deformation gradient, equation (2.58) and the first law of thermodynamics, equation (2.45). In this case, the discrete solution will be in terms of linear momentum, $\boldsymbol{p}$, deformation gradient, $\boldsymbol{F}$ and total energy, E. The constitutive model will be evaluated using the deformation gradient as a variable, i.e. $\boldsymbol{P} = \boldsymbol{P}(\boldsymbol{F}, \eta)$. The displacements, $\boldsymbol{x}$ will be obtained integrating the velocity in time $\boldsymbol{v} = \boldsymbol{p}/\rho_0$. As a result, the discrete deformation gradient will not be linked to the discrete displacements, i.e. $\boldsymbol{F} \neq \nabla_0 \boldsymbol{x}$. Therefore, despite the constitutive model satisfying the symmetry of the discrete second Piola-Kirchhoff stress tensor, the conservation of angular momentum is not fulfilled (see proof in section 2.4.3). This issue will be addressed in detail in section 6.3.

The current chapter will introduce this new mixed system of conservation laws (section 4.2) and the boundary conditions and initial conditions necessary to close the system (sections 4.3 and 4.4). The chapter will be closed with an analysis of the eigenvalue structure of the problem (section 4.5).

4.2 Mixed system of conservation laws

The problem formulation is given using equations (2.30), (2.58) and (2.45) which form a mixed system of equations as follows

$$\frac{\partial \boldsymbol{p}}{\partial t} - \mathrm{DIV}\,\boldsymbol{P} = \rho_0 \boldsymbol{b}, \tag{4.1a}$$

$$\frac{\partial \boldsymbol{F}}{\partial t} - \mathrm{DIV}\,(\boldsymbol{v} \otimes \boldsymbol{I}) = \boldsymbol{0}, \tag{4.1b}$$

$$\frac{\partial E_T}{\partial t} - \mathrm{DIV}\left(\boldsymbol{P}^T \boldsymbol{v} - \boldsymbol{Q}\right) = s. \tag{4.1c}$$

The above system of equations can be rewritten in a more compact form, describing a first order hyperbolic system as

$$\frac{\partial \boldsymbol{\mathcal{U}}}{\partial t} + \frac{\partial \boldsymbol{\mathcal{F}}_I}{\partial X_I} = \boldsymbol{\mathcal{S}}, \tag{4.2}$$

where $\boldsymbol{\mathcal{U}}$, $\boldsymbol{\mathcal{F}}_I$ and $\boldsymbol{\mathcal{S}}$ are written in indicial notation as

$$\boldsymbol{\mathcal{U}} = \begin{pmatrix} p_1 \\ p_2 \\ p_3 \\ F_{11} \\ F_{12} \\ F_{13} \\ F_{21} \\ F_{22} \\ F_{23} \\ F_{31} \\ F_{32} \\ F_{33} \\ E_T \end{pmatrix}, \quad \boldsymbol{\mathcal{F}}_I = \begin{pmatrix} -P_{1I}(\boldsymbol{F}) \\ -P_{2I}(\boldsymbol{F}) \\ -P_{3I}(\boldsymbol{F}) \\ -\delta_{I1} v_1 \\ -\delta_{I2} v_1 \\ -\delta_{I3} v_1 \\ -\delta_{I1} v_2 \\ -\delta_{I2} v_2 \\ -\delta_{I3} v_2 \\ -\delta_{I1} v_3 \\ -\delta_{I2} v_3 \\ -\delta_{I3} v_3 \\ Q_I - P_{iI} v_i \end{pmatrix}, \quad \boldsymbol{\mathcal{S}} = \begin{pmatrix} \rho_0 b_1 \\ \rho_0 b_2 \\ \rho_0 b_3 \\ 0 \\ 0 \\ 0 \\ 0 \\ 0 \\ 0 \\ 0 \\ 0 \\ 0 \\ s \end{pmatrix}, \quad \forall I = 1, 2, 3. \tag{4.3}$$

The equivalent integral form of the system of equations (4.1a), (4.1b) and (4.1c)

is given by

$$\frac{d}{dt}\int_V \boldsymbol{p}\,dV = \int_{\partial V} \boldsymbol{t}\,dA + \int_V \rho_0 \boldsymbol{b}\,dV, \tag{4.4a}$$

$$\frac{d}{dt}\int_V \boldsymbol{F}\,dV = \int_{\partial V} \frac{1}{\rho_0}\boldsymbol{p}\otimes\boldsymbol{N}\,dA, \tag{4.4b}$$

$$\frac{d}{dt}\int_V E\,dV = \int_{\partial V} \boldsymbol{t}\cdot\boldsymbol{v}\,dA - \int_{\partial V} \boldsymbol{Q}\cdot\boldsymbol{N}\,dA + \int_V s\,dV, \tag{4.4c}$$

with the equivalent compact form

$$\frac{d}{dt}\int_V \boldsymbol{\mathcal{U}}\,dV = -\int_{\partial V} \boldsymbol{\mathcal{F}}_N\,dA + \int_V \boldsymbol{\mathcal{S}}\,dV, \tag{4.5}$$

where

$$\boldsymbol{\mathcal{U}} = \begin{pmatrix} \boldsymbol{p} \\ \boldsymbol{F} \\ E_T \end{pmatrix}, \quad \boldsymbol{\mathcal{F}}_N = \begin{pmatrix} -\boldsymbol{t} \\ -\boldsymbol{v}\otimes\boldsymbol{N} \\ -\boldsymbol{t}\cdot\boldsymbol{v} + \boldsymbol{Q}\cdot\boldsymbol{N} \end{pmatrix}, \quad \boldsymbol{\mathcal{S}} = \begin{pmatrix} \rho_0\boldsymbol{b} \\ \boldsymbol{0} \\ s \end{pmatrix}. \tag{4.6}$$

4.3 Boundary conditions

The boundary conditions will have to be imposed on each of the equations of the mixed system of conservation laws (4.5). For clarity purposes, only the case where no heat fluxes are present (adiabatic process) will be considered. In this particular case, the fluxes of the three equations can be uniquely defined using the traction, $\boldsymbol{t}$, and the linear momentum, $\boldsymbol{p}$ (see equation (4.6)). It is important to notice that the linear momentum, $\boldsymbol{p}$, acts as a variable in equation (4.1a) and as a flux in equations (4.1b) and (4.1c). On the other hand, the traction, $\boldsymbol{t}$, acts as a flux in equations (4.1a) and (4.1c). This means that the linear momentum will be used as a weak or Neumann boundary condition (for equations (4.1b) and (4.1c)) and also as a strong or Dirichlet boundary condition (for equation (4.1a)). The traction will only be used as a Neumann boundary condition for equations (4.1a) and (4.1c).

Four different types of boundary conditions have been considered: clamped boundary (displacement not allowed in any direction), free boundary (displacement allowed in all directions and imposed traction), symmetric boundary (displacement restricted to the normal direction and imposed normal traction) and skew-symmetric boundary (displacement restricted to the tangential direction and imposed tangential traction). Figure 4.1 represents these boundary conditions. Table 4.1 shows the set of weak boundary conditions, where the notation a_n represents the normal component of a given spatial vector $\boldsymbol{a}$, that is $a_n = \boldsymbol{a}\cdot\boldsymbol{n}$, and where $\boldsymbol{n}$ is the mapping of the normal vector $\boldsymbol{N}$ from the material to the deformed configuration, given by the following push forward operation

$$\boldsymbol{n} = \frac{\boldsymbol{F}^{-T}\boldsymbol{N}}{\|\boldsymbol{F}^{-T}\boldsymbol{N}\|}. \tag{4.7}$$

Table 4.2 shows the strong boundary conditions as imposed to the linear momentum, $\boldsymbol{p}$.[1]

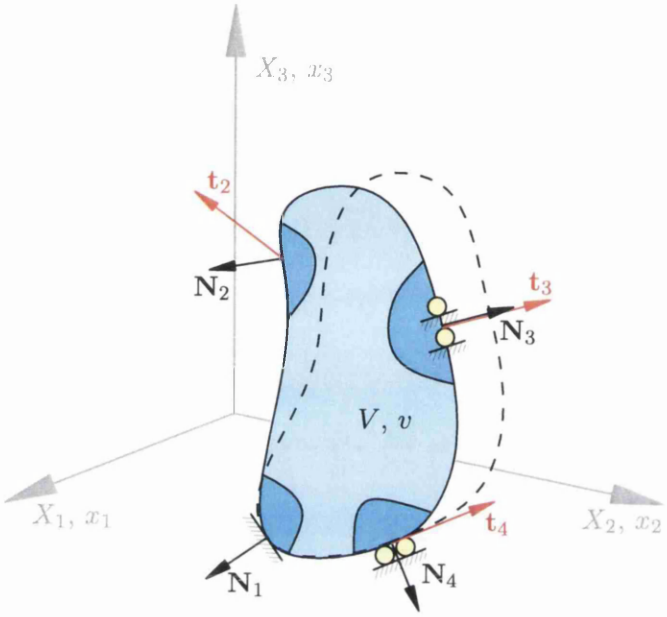

Figure 4.1: The boundary conditions are imposed at the reference configuration. The continuous line represents the body at the reference (undeformed) configuration, while the discontinuous line the body at the spatial (deformed) configuration. Four different types of boundary conditions are considered: clamped boundary (condition 1), free boundary (condition 2), normally sliding boundary (condition 3) and tangentially sliding boundary (condition 4).

4.4 Initial conditions

The dynamic equations proposed in this thesis require establishing a set of initial conditions. These can be imposed either setting an initial linear momentum, $\boldsymbol{p}(\boldsymbol{X}, t = 0) = \boldsymbol{p}_0(\boldsymbol{X})$ and/or an initial deformation gradient $\boldsymbol{F}(\boldsymbol{X}, t = 0) = \boldsymbol{F}_0(\boldsymbol{X})$ such that they are compatible with the prescribed boundary conditions. If an initial deformation gradient, $\boldsymbol{F}_0$ is prescribed, this has to be obtained from an initial deformed configuration, that is

[1] It is important to notice that no rotations are allowed for the two sliding boundary conditions. Therefore, in these cases the normal vector, $\boldsymbol{n}$, remains unchanged from the material configuration, that is $\boldsymbol{n} = \boldsymbol{N}$.

	Traction	Linear momentum
Clamped	-	$\boldsymbol{p}(\boldsymbol{X}) = \boldsymbol{0}$
Free	$\boldsymbol{t}(\boldsymbol{X}) = \boldsymbol{t}^B(\boldsymbol{X}, t)$	-
Normally sliding	$t_n(\boldsymbol{X}) = t_n^B(\boldsymbol{X}, t)$	$\boldsymbol{p}(\boldsymbol{X}) - p_n(\boldsymbol{X})\boldsymbol{n} = \boldsymbol{0}$
Tangentially sliding	$\boldsymbol{t}(\boldsymbol{X}) - t_n(\boldsymbol{X})\boldsymbol{n} = \boldsymbol{t}_t^B(\boldsymbol{X}, t)$	$p_n(\boldsymbol{X}) = 0$

Table 4.1: Continuum weak boundary conditions on traction and velocity for a material particle $\boldsymbol{X} \in \partial\Omega$.

	Linear momentum
Clamped	$\boldsymbol{p}(\boldsymbol{X}) = \boldsymbol{0}$
Free	-
Normally sliding	$\boldsymbol{p}(\boldsymbol{X}) - p_n(\boldsymbol{X})\boldsymbol{n}(\boldsymbol{X}) = \boldsymbol{0}$
Tangentially sliding	$p_n(\boldsymbol{X}) = 0$

Table 4.2: Continuum strong boundary conditions on linear momentum for a material particle $\boldsymbol{X} \in \partial\Omega$.

$$\boldsymbol{F}_0 = \frac{\partial \boldsymbol{x}_0}{\partial \boldsymbol{X}}, \quad \boldsymbol{x}_0 = \boldsymbol{X} + \boldsymbol{u}_0 \tag{4.8}$$

ensuring therefore that the compatibility conditions (2.60) are satisfied at the initial state.

4.5 Eigenvalue structure

In order to solve the system of equations (4.5) by using standard CFD techniques (as the Finite Volume Method), a necessary step is to prove its hyperbolicity. In this section, the hyperbolicity of the system (4.5) will be proved for two different cases. First, the isothermal processes will be analised. In this case the energy equation will be omitted and an isothermal constitutive model similar to those presented in section 3.2 will be used. Next, the thermo-elastic processes will be taken into account, using the energy equation in the system (4.6) and considering a thermo-elastic constitutive relationship as presented in section 3.4.

4.5.1 Isothermal processes

Omitting thermal effects (and therefore the energy equation) and replacing $\boldsymbol{\mathcal{U}}$ and $\boldsymbol{\mathcal{F}}_N$ from equation (4.6) into equation (2.15) gives

$$\begin{pmatrix} Dt\left[\boldsymbol{F}_\alpha^R\right] \\ \boldsymbol{v}_\alpha^R \otimes \boldsymbol{N} \end{pmatrix} = c_\alpha \begin{pmatrix} -\rho_0 \boldsymbol{v}_\alpha^R \\ -\boldsymbol{F}_\alpha^R \end{pmatrix}. \tag{4.9}$$

Considering only the cases where $c_\alpha \neq 0$, the second equation of the system (4.9) results in

$$\boldsymbol{F}_\alpha^R = -\frac{1}{c_\alpha} \boldsymbol{v}_\alpha^R \otimes \boldsymbol{N}, \tag{4.10}$$

which used in the first equation of (4.9) renders

$$Dt\left[\boldsymbol{v}_\alpha^R \otimes \boldsymbol{N}\right] = \rho_0 c_\alpha^2 \boldsymbol{v}_\alpha^R. \tag{4.11}$$

The above equation can be rewritten in a scalar manner premultiplying it by a generic virtual velocity $\delta\boldsymbol{v}$ to obtain

$$(\delta\boldsymbol{v} \otimes \boldsymbol{N}) : D\boldsymbol{P}\left[\boldsymbol{v}_\alpha^R \otimes \boldsymbol{N}\right] = \rho_0 c_\alpha^2 \delta\boldsymbol{v} \cdot \boldsymbol{v}_\alpha^R, \tag{4.12}$$

which has to be fulfilled for any value of $\delta\boldsymbol{v}$. By using the relation between $\boldsymbol{P}$, $\boldsymbol{F}$ and the strain function ψ (see equation (3.1)), the above equation is reassembled as

$$(\delta\boldsymbol{v} \otimes \boldsymbol{N}) : \frac{\partial^2 \psi}{\partial \boldsymbol{F} \partial \boldsymbol{F}} : (\boldsymbol{v}_\alpha^R \otimes \boldsymbol{N}) = \rho_0 c_\alpha^2 \delta\boldsymbol{v} \cdot \boldsymbol{v}_\alpha^R, \tag{4.13}$$

or

$$(\delta\boldsymbol{v} \otimes \boldsymbol{N}) : \boldsymbol{\mathcal{C}} : (\boldsymbol{v}_\alpha^R \otimes \boldsymbol{N}) = \rho_0 c_\alpha^2 \delta\boldsymbol{v} \cdot \boldsymbol{v}_\alpha^R. \tag{4.14}$$

By taking the particular case $\delta\boldsymbol{v} = \boldsymbol{v}_\alpha^R$ the above equation shows that the existence of real eigenvalues is ensured by the ellipticity of the elasticity tensor (see [75])[2]. Equation (4.14) can be rewritten as

$$\delta\boldsymbol{v} \cdot (\boldsymbol{\mathcal{C}}_{NN} \boldsymbol{v}_\alpha^R) = \rho_0 c_\alpha^2 \delta\boldsymbol{v} \cdot \boldsymbol{v}_\alpha^R, \quad , \tag{4.15}$$

where $[\boldsymbol{\mathcal{C}}_{NN}]_{ij} = [\boldsymbol{\mathcal{C}}_{NN}]_{iIjJ} N_I N_J$. Since the above equation has to hold for any $\delta\boldsymbol{v}$, the following is obtained

$$\boldsymbol{\mathcal{C}}_{NN} \boldsymbol{v}_\alpha^R = \rho_0 c_\alpha^2 \boldsymbol{v}_\alpha^R. \tag{4.16}$$

[2]The ellipticity of the elastic tensor implies that

$$(\boldsymbol{a} \otimes \boldsymbol{N}) : \boldsymbol{\mathcal{C}} : (\boldsymbol{a} \otimes \boldsymbol{N}) \geq 0 \quad \forall \boldsymbol{a}, \boldsymbol{N}$$

Compressible Neo-Hookean material

For the compressible neo-Hookean model, the strain function is written as (see section 3.2),

$$\psi(\boldsymbol{F}) = \frac{\mu}{2}(\boldsymbol{F} : \boldsymbol{F} - 3) - \mu \ln J + \frac{\lambda}{2}(\ln J)^2. \tag{4.17}$$

The corresponding elasticity tensor is

$$\boldsymbol{\mathcal{C}} = \mu\boldsymbol{\mathcal{I}} + (\mu - \lambda \ln J)\boldsymbol{\mathcal{H}} + \lambda \boldsymbol{F}^{-T} \otimes \boldsymbol{F}^{-T}, \tag{4.18}$$

with $[\boldsymbol{\mathcal{I}}]_{iIjJ} = \delta_{ij}\delta_{IJ}$, $[\boldsymbol{\mathcal{H}}]_{iIjJ} = \left[\boldsymbol{F}^{-T}\right]_{iJ}\left[\boldsymbol{F}^{-T}\right]_{jI}$ and $[\boldsymbol{F}^{-T} \otimes \boldsymbol{F}^{-T}]_{iIjJ} = [\boldsymbol{F}^{-T}]_{iI}[\boldsymbol{F}^{-T}]_{jJ}$. Replacing the elasticity tensor in equation (4.14) the following is obtained,

$$\mu \delta\boldsymbol{v} \cdot \boldsymbol{v}_\alpha^R + (\mu + \lambda(1 - \ln J))(\delta\boldsymbol{v} \cdot \boldsymbol{F}^{-T}\boldsymbol{N})(\boldsymbol{v}_\alpha^R \cdot \boldsymbol{F}^{-T}\boldsymbol{N}) = \rho_0 c_\alpha^2 \delta\boldsymbol{v} \cdot \boldsymbol{v}_\alpha^R. \tag{4.19}$$

The first two eigenvalues (and corresponding eigenvectors) are obtained using $\boldsymbol{v}_\alpha^R = \boldsymbol{n}$. Replacing in the above equation gives

$$\rho_0 c_\alpha^2 = \mu + \frac{h^2}{J^2}(\mu + \lambda(1 - \ln J)), \tag{4.20}$$

where $h = J\|\boldsymbol{F}^{-T}\boldsymbol{N}\|$. Therefore, the 1 and 2 waves are given by

$$c_{1,2} = \pm c_p, \quad c_p = \sqrt{\frac{\mu\left(1 + \frac{h^2}{J^2}\right) + \frac{h^2}{J^2}\lambda(1 - \ln J)}{\rho_0}} \tag{4.21}$$

where c_p is known as the pressure wave speed. By taking the particular, and extremest case, $\mu = 0$ it can be seen that the 1 and 2 waves will be real if

$$\ln J < 1. \tag{4.22}$$

The remaining set of eigenvalues and eigenvectors will be obtained using two arbitrary vectors $\boldsymbol{t}_1, \boldsymbol{t}_2$ orthogonal to $\boldsymbol{n}$. For a general vector t_i, with $i \in \{1, 2\}$, the following is obtained

$$\mu \delta\boldsymbol{v} \cdot \boldsymbol{t}_i + \frac{h^2}{J^2}(\mu + \lambda(1 - \ln J))(\delta\boldsymbol{v} \cdot \boldsymbol{n})(\boldsymbol{t}_i \cdot \boldsymbol{n}) = \rho_0 c_\alpha^2 \delta\boldsymbol{v} \cdot \boldsymbol{t}_i, \tag{4.23}$$

which gives the 3, 4, 5 and 6 waves as

$$c_{3,4} = c_{5,6} = \pm c_s, \quad c_s = \sqrt{\frac{\mu}{\rho_0}} \tag{4.24}$$

and c_s is the shear wave speed. In this case, since $\mu \geq 0$, the 3, 4, 5 and 6 waves will always be real and, therefore, the hyperbolicity of the problem will be limited by the condition (4.22).

Finally, the non-zero eigenvectors are given by

$$\boldsymbol{\mathcal{U}}^R_{1,2} = \begin{pmatrix} \boldsymbol{n} \\ \mp\frac{1}{c_p}\boldsymbol{n}\otimes\boldsymbol{N} \end{pmatrix}, \quad \boldsymbol{\mathcal{U}}^R_{3,4} = \begin{pmatrix} \boldsymbol{t}_1 \\ \mp\frac{1}{c_s}\boldsymbol{t}_1\otimes\boldsymbol{N} \end{pmatrix}, \quad \boldsymbol{\mathcal{U}}^R_{5,6} = \begin{pmatrix} \boldsymbol{t}_2 \\ \mp\frac{1}{c_s}\boldsymbol{t}_2\otimes\boldsymbol{N} \end{pmatrix}. \tag{4.25}$$

Nearly incompressible Neo-Hookean material

For nearly incompressible materials the strain energy functional is written as a sum of the volumetric and deviatoric parts as (see section 3.2)

$$\psi = \frac{\mu}{2}\left[J^{-2/3}(\boldsymbol{F}:\boldsymbol{F}) - 3\right] + \frac{1}{2}\kappa(J-1)^2,, \tag{4.26}$$

with the corresponding elasticity tensor

$$\boldsymbol{\mathcal{C}} = -\frac{2}{3}\mu J^{-2/3}\boldsymbol{F}\otimes\boldsymbol{F}^{-T} + \frac{2}{9}\mu J^{-2/3}(\boldsymbol{F}:\boldsymbol{F})\boldsymbol{F}^{-T}\otimes\boldsymbol{F}^{-T} \tag{4.27}$$

$$+ \mu J^{-2/3}\boldsymbol{\mathcal{I}} - \frac{2}{3}\mu J^{-2/3}\boldsymbol{F}^{-T}\otimes\boldsymbol{F} - \frac{1}{3}\mu J^{-2/3}(\boldsymbol{F}:\boldsymbol{F})\boldsymbol{\mathcal{H}} \tag{4.28}$$

$$+ \kappa J(2J-1)\boldsymbol{F}^{-T}\otimes\boldsymbol{F}^{-T} + \kappa J(J-1)\boldsymbol{\mathcal{H}}. \tag{4.29}$$

Using this result in equation (4.14) gives

$$-\frac{2}{3}h\mu J^{-5/3}(\delta\boldsymbol{v}\cdot\boldsymbol{m})(\boldsymbol{v}^R_\alpha\cdot\boldsymbol{n}) + \frac{2}{9}h^2\mu J^{-8/3}(\boldsymbol{F}:\boldsymbol{F})(\delta\boldsymbol{v}\cdot\boldsymbol{n})(\boldsymbol{v}^R_\alpha\cdot\boldsymbol{n})$$
$$+ \mu J^{-2/3}(\delta\boldsymbol{v}\cdot\boldsymbol{v}^R_\alpha) - \frac{2}{3}h\mu J^{-5/3}(\delta\boldsymbol{v}\cdot\boldsymbol{n})(\boldsymbol{v}^R_\alpha\cdot\boldsymbol{m}) + \frac{1}{3}h^2\mu J^{-8/3}(\boldsymbol{F}:\boldsymbol{F})(\delta\boldsymbol{v}\cdot\boldsymbol{n})(\boldsymbol{v}^R_\alpha\cdot\boldsymbol{n})$$
$$+ \kappa h^2(\delta\boldsymbol{v}\cdot\boldsymbol{n})(\boldsymbol{v}^R_\alpha\cdot\boldsymbol{n}) = \rho_0 c_\alpha^2\delta\boldsymbol{v}\cdot\boldsymbol{v}^R_\alpha, \tag{4.30}$$

where $\boldsymbol{m} = \boldsymbol{F}\boldsymbol{N}$. Proceeding identically as before, the first two eigenvalues are obtained setting $\boldsymbol{v}^R_\alpha = \boldsymbol{n}$ to give

$$\delta\boldsymbol{v}\cdot\Big(-\frac{2}{3}h\mu J^{-5/3}\boldsymbol{m} + \frac{2}{9}h^2\mu J^{-8/3}(\boldsymbol{F}:\boldsymbol{F})\boldsymbol{n} \tag{4.31}$$

$$+ \mu J^{-2/3}\boldsymbol{n} - \frac{2}{3}h\mu J^{-5/3}(\boldsymbol{n}\cdot\boldsymbol{m})\boldsymbol{n} + \frac{1}{3}h^2\mu J^{-8/3}(\boldsymbol{F}:\boldsymbol{F})\boldsymbol{n} \tag{4.32}$$

$$+ \kappa h^2\boldsymbol{n} - \rho_0 c_\alpha^2\boldsymbol{n}\Big) = 0, \tag{4.33}$$

therefore,

$$-\frac{2}{3}h\mu J^{-5/3}\boldsymbol{m} + \frac{2}{9}h^2\mu J^{-8/3}(\boldsymbol{F}:\boldsymbol{F})\boldsymbol{n} \tag{4.34}$$

$$+ \mu J^{-2/3}\boldsymbol{n} - \frac{2}{3}h\mu J^{-5/3}(\boldsymbol{n}\cdot\boldsymbol{m})\boldsymbol{n} + \frac{1}{3}h^2\mu J^{-8/3}(\boldsymbol{F}:\boldsymbol{F})\boldsymbol{n} \tag{4.35}$$

$$+ \kappa h^2\boldsymbol{n} = \rho_0 c_\alpha^2\boldsymbol{n}. \tag{4.36}$$

Multiplying the above result by $\boldsymbol{n}$ renders

$$-\frac{4}{3}h\mu J^{-5/3}\boldsymbol{m}\cdot\boldsymbol{n}+\frac{5}{9}h^2\mu J^{-8/3}(\boldsymbol{F}:\boldsymbol{F})+\mu J^{-2/3}+\kappa h^2=\rho_0 c_\alpha^2, \tag{4.37}$$

and this can be reorganized as

$$c_\alpha^2=\frac{1}{\rho_0}\left(-\frac{4}{3}\mu J^{-2/3}+\frac{5}{9}\frac{1}{\Lambda^2}\mu J^{-2/3}(\boldsymbol{F}:\boldsymbol{F})+\mu J^{-2/3}+\kappa\frac{J^2}{\Lambda^2}\right), \tag{4.38}$$

with $\Lambda=(\|\boldsymbol{F}^{-T}\boldsymbol{N}\|)^{-1}$. Consequently, the 1 and 2 eigenvalues are

$$c_{1,2}=\pm c_p;\quad c_p=\sqrt{\frac{\frac{\alpha}{\Lambda^2}+\beta+2\gamma}{\rho_0}}, \tag{4.39}$$

where

$$\alpha=\frac{5}{9}\mu J^{-2/3}(\boldsymbol{F}:\boldsymbol{F})+\kappa J^2, \tag{4.40}$$

$$\beta=\mu J^{-2/3}, \tag{4.41}$$

$$\gamma=-\frac{2}{3}\mu J^{-2/3} \tag{4.42}$$

and c_p will be real if

$$\frac{5}{9}\mu(\boldsymbol{F}:\boldsymbol{F})+\kappa J^{8/3}-\frac{1}{3}\mu\Lambda^2\geq 0. \tag{4.43}$$

The 3 to 6 eigenvalues are obtained using two arbitrary vectors orthogonal to $\boldsymbol{n}$ and given by $\boldsymbol{v}_\alpha^R=\boldsymbol{t}_i$, with $i\in\{1,2\}$. Replacing in equation 4.30 gives

$$\mu J^{-2/3}(\delta\boldsymbol{v}\cdot\boldsymbol{t}_i)-\frac{2}{3}h\mu J^{-5/3}(\delta\boldsymbol{v}\cdot\boldsymbol{n})(\boldsymbol{t}_i\cdot\boldsymbol{m})=\rho_0 c_\alpha^2\delta\boldsymbol{v}\cdot\boldsymbol{t}_i. \tag{4.44}$$

In order to solve the above equation, it will be assumed that $\boldsymbol{N}$ is a principal direction of the deformation, which will give an upper bound of the shear waves speed. With such assumption, $\boldsymbol{m}$ and $\boldsymbol{n}$ are collinear and the following holds

$$\boldsymbol{t}_i\cdot\boldsymbol{m}=0, \tag{4.45}$$

which gives the 3,4,5 and 6 waves speeds are given as

$$c_{3,4}=c_{5,6}=\pm c_s;\quad c_s=\sqrt{\frac{\beta}{\rho_0}} \tag{4.46}$$

where c_s is always real and, therefore, the hyperbolicity of the system is conditioned to the fulfilment of the inequality (4.43).

Finally, the set of 6 eigenvectors is

$$\boldsymbol{\mathcal{U}}_{1,2}^R=\begin{pmatrix}\boldsymbol{n}\\ \mp\frac{1}{c_p}\boldsymbol{n}\otimes\boldsymbol{N}\end{pmatrix},\quad \boldsymbol{\mathcal{U}}_{3,4}^R=\begin{pmatrix}\boldsymbol{t}_1\\ \mp\frac{1}{c_s}\boldsymbol{t}_1\otimes\boldsymbol{N}\end{pmatrix},\quad \boldsymbol{\mathcal{U}}_{5,6}^R=\begin{pmatrix}\boldsymbol{t}_2\\ \mp\frac{1}{c_s}\boldsymbol{t}_2\otimes\boldsymbol{N}\end{pmatrix}. \tag{4.47}$$

4.5.2 Thermo-mechanical processes

According to equation (3.26), the constitutive equation for a thermo-elastic solid is expressed as a function of the deformation gradient, $\boldsymbol{F}$, and the temperature, θ. Rewriting the equation for clarity

$$\boldsymbol{P} = \boldsymbol{P}_0 - \frac{\partial \eta_0(\boldsymbol{F})}{\partial \boldsymbol{F}} \Delta\theta; \quad \boldsymbol{P}_0 = \frac{\partial \psi_0}{\partial \boldsymbol{F}}, \; \Delta\theta = \frac{(e - e_0(\boldsymbol{F}))}{\rho_0 C_F}, \tag{4.48}$$

where

$$e_0(\boldsymbol{F}) = \psi_0(\boldsymbol{F}) + \theta_0 \eta_0(\boldsymbol{F}); \quad \psi_0(\boldsymbol{F}) = \psi(\boldsymbol{F}, \theta_0); \; \eta_0(\boldsymbol{F}) = \eta(\boldsymbol{F}, \theta_0), \tag{4.49}$$

and

$$\Delta\theta = \frac{1}{\rho_0 C_F}\left(e - e_0(\boldsymbol{F})\right) = \frac{1}{\rho_0 C_F}\left(E - \frac{1}{2}\rho_0 \boldsymbol{v}\cdot\boldsymbol{v} - \psi_0(\boldsymbol{F}) - \theta_0\eta_0(\boldsymbol{F})\right), \tag{4.50}$$

where, in the absence of heat sources and body forces, the internal energy is a function of the total energy E and the kinetic velocity $\frac{1}{2}\rho_0 \boldsymbol{v}\cdot\boldsymbol{v}$, therefore

$$e = e(\boldsymbol{v}, E). \tag{4.51}$$

Consequently, the stress tensor can be written as a function of the three conserved variables, i.e.

$$\boldsymbol{P}(\boldsymbol{v}, \boldsymbol{F}, E) = \boldsymbol{P}_0(\boldsymbol{F}) - \frac{\partial \eta_0(\boldsymbol{F})}{\partial \boldsymbol{F}} \Delta\theta(\boldsymbol{v}, \boldsymbol{F}, E) \tag{4.52}$$

and a linearisation of the stress tensor in a specific direction of the variables $[\boldsymbol{v}^*, \boldsymbol{F}^*, E^*]$ can be expressed as

$$\begin{aligned} D\boldsymbol{P}[\boldsymbol{v}^*, \boldsymbol{F}^*, E^*] = {} & \frac{1}{C_F}\frac{\partial \eta_0(\boldsymbol{F})}{\partial \boldsymbol{F}}(\boldsymbol{v}\cdot\boldsymbol{v}^*) \\ & + \boldsymbol{\mathcal{C}} : \boldsymbol{F}^* - \Delta\theta \frac{\partial^2 \eta_0(\boldsymbol{F})}{\partial \boldsymbol{F}\partial \boldsymbol{F}} : \boldsymbol{F}^* + \frac{1}{\rho_0 C_F}\left(\frac{\partial \eta_0(\boldsymbol{F})}{\partial \boldsymbol{F}} \otimes \boldsymbol{P}_0\right) : \boldsymbol{F}^* \\ & + \frac{\theta_0}{\rho_0 C_F}\left(\frac{\partial \eta_0(\boldsymbol{F})}{\partial \boldsymbol{F}} \otimes \frac{\partial \eta_0(\boldsymbol{F})}{\partial \boldsymbol{F}}\right) : \boldsymbol{F}^* - \frac{1}{\rho_0 C_F}\frac{\partial \eta_0(\boldsymbol{F})}{\partial \boldsymbol{F}} E^*. \end{aligned} \tag{4.53}$$

On the other hand, the characteristic system will be given combining the system of equations (4.1a), (4.1b) and (4.1c) with the characteristic equation (2.15). Omitting heat fluxes, the characteristic system is

$$\begin{pmatrix} D\boldsymbol{t}\left[\boldsymbol{v}_\alpha^R, \boldsymbol{F}_\alpha^R, E_\alpha^R\right] \\ \boldsymbol{v}_\alpha^R \otimes \boldsymbol{N} \\ D\boldsymbol{t}\left[\boldsymbol{v}_\alpha^R, \boldsymbol{F}_\alpha^R, E_\alpha^R\right]\cdot\boldsymbol{v} + \boldsymbol{t}\cdot\boldsymbol{v}_\alpha^R \end{pmatrix} = c_\alpha \begin{pmatrix} -\rho_0 \boldsymbol{v}_\alpha^R \\ -\boldsymbol{F}_\alpha^R \\ -E_\alpha^R \end{pmatrix}. \tag{4.54}$$

Considering only the cases when $c_\alpha \neq 0$, the second equation gives,

$$\boldsymbol{F}_\alpha^R = -\frac{1}{c_\alpha}\boldsymbol{v}_\alpha^R \otimes \boldsymbol{N} \tag{4.55}$$

and substituting into the first equation of the system (4.54) renders

$$D\boldsymbol{t}\left[c_\alpha \boldsymbol{v}_\alpha^R, -\boldsymbol{v}_\alpha^R \otimes \boldsymbol{N}, c_\alpha E_\alpha^R\right] = -\rho_0 c_\alpha^2 \boldsymbol{v}_\alpha^R, \tag{4.56}$$

which can be rewritten in a scalar form premultiplying by a virtual velocity $\delta\boldsymbol{v}$,

$$\delta\boldsymbol{v} \otimes \boldsymbol{N} : D\boldsymbol{P}\left[c_\alpha \boldsymbol{v}_\alpha^R, -\boldsymbol{v}_\alpha^R \otimes \boldsymbol{N}, c_\alpha E_\alpha^R\right] = -\rho_0 c_\alpha^2 \delta\boldsymbol{v} \cdot \boldsymbol{v}_\alpha^R. \tag{4.57}$$

The last equation of (4.54) can be rewritten as

$$\begin{aligned} &\boldsymbol{v} \otimes \boldsymbol{N} : D\boldsymbol{P}\left[c_\alpha \boldsymbol{v}_\alpha^R, -\boldsymbol{v}_\alpha^R \otimes \boldsymbol{N}, c_\alpha E_\alpha^R\right] \\ &+ c_\alpha \boldsymbol{P}_0 : (\boldsymbol{v}_\alpha^R \otimes \boldsymbol{N}) - c_\alpha \Delta\theta \frac{\partial \eta_0(\boldsymbol{F})}{\partial \boldsymbol{F}} : (\boldsymbol{v}_\alpha^R \otimes \boldsymbol{N}) = -c_\alpha^2 E_\alpha^R \end{aligned} \tag{4.58}$$

and equations (4.57) and (4.58) are the ones that need to be solved in order to obtain the eigenvalues and corresponding eigenvectors.

Considering the Mie-Grüneisen model, the entropy at the reference temperature, η_0, is only a function of J (see section 3.4) in the following form

$$\eta_0(J) = \rho_0 C_F \Gamma_0 \frac{J^q - 1}{q}, \tag{4.59}$$

$$\eta_0'(J) = \rho_0 C_F \Gamma_0 J^{q-1}, \tag{4.60}$$

therefore

$$\frac{\partial \eta_0(\boldsymbol{F})}{\partial \boldsymbol{F}} = \frac{\partial \eta_0(J)}{\partial J}\frac{\partial J}{\partial \boldsymbol{F}} = \rho_0 C_F \Gamma_0 J^{q-1} J \boldsymbol{F}^{-T} = \rho_0 C_F \Gamma_0 J^q \boldsymbol{F}^{-T}, \tag{4.61}$$

$$\frac{\partial^2 \eta_0(\boldsymbol{F})}{\partial \boldsymbol{F} \partial \boldsymbol{F}} = q\rho_0 C_F \Gamma_0 J^q \boldsymbol{F}^{-T} \otimes \boldsymbol{F}^{-T} + \rho_0 C_F \Gamma_0 J^q \boldsymbol{\mathcal{H}} \tag{4.62}$$

and these results are now combined with the linearisation of the stress tensor, $\boldsymbol{P}$, given by equation (4.53) and with equation (4.57). After some algebra this gives

$$\begin{aligned} &c_\alpha \rho_0 \Gamma_0 J^{q-1} h(\delta\boldsymbol{v} \cdot \boldsymbol{n})(\boldsymbol{v} \cdot \boldsymbol{v}_\alpha^R) - \delta\boldsymbol{v} \cdot \boldsymbol{C}_{NN} \boldsymbol{v}_\alpha^R + \Delta\theta \rho_0 C_F \Gamma_0 J^{q-2} h^2 (\delta\boldsymbol{v} \cdot \boldsymbol{n})(\boldsymbol{v}_\alpha^R \cdot \boldsymbol{n})(q-1) \\ &- \Gamma_0 J^{q-1} h(\delta\boldsymbol{v} \cdot \boldsymbol{n})(\boldsymbol{v}_\alpha^R \cdot \boldsymbol{P}_0 \boldsymbol{N}) - \theta_0 \rho_0 C_F \Gamma_0^2 J^{2q-2} h^2 (\delta\boldsymbol{v} \cdot \boldsymbol{n})(\boldsymbol{v}_\alpha^R \cdot \boldsymbol{n}) \\ &- c_\alpha \Gamma_0 J^{q-1} h(\delta\boldsymbol{v} \cdot \boldsymbol{n}) E_\alpha^R = -\rho_0 c_\alpha^2 \delta\boldsymbol{v} \cdot \boldsymbol{v}_\alpha^R \end{aligned} \tag{4.63}$$

and, since it is valid for any $\delta\boldsymbol{v}$, this can be rewritten as

$$c_\alpha \rho_0 \Gamma_0 J^{q-1} h (\boldsymbol{v}\cdot\boldsymbol{v}_\alpha^R)\boldsymbol{n} - \boldsymbol{C}_{NN}\boldsymbol{v}_\alpha^R + \Delta\theta\rho_0 C_F \Gamma_0 J^{q-2} h^2 (\boldsymbol{v}_\alpha^R\cdot\boldsymbol{n})(q-1)\boldsymbol{n}$$
$$- \Gamma_0 J^{q-1} h (\boldsymbol{v}_\alpha^R\cdot\boldsymbol{P}_0\boldsymbol{N})\boldsymbol{n} - \theta_0\rho_0 C_F \Gamma_0^2 J^{2q-2} h^2 (\boldsymbol{v}_\alpha^R\cdot\boldsymbol{n})\boldsymbol{n}$$
$$- c_\alpha \Gamma_0 J^{q-1} h E_\alpha^R \boldsymbol{n} + \rho_0 c_\alpha^2 \boldsymbol{v}_\alpha^R = \boldsymbol{0}. \tag{4.64}$$

Proceeding equivalently for the linearised third equation (4.58) gives

$$c_\alpha \rho_0 \Gamma_0 J^{q-1} h (\boldsymbol{v}\cdot\boldsymbol{n})(\boldsymbol{v}\cdot\boldsymbol{v}_\alpha^R) - \boldsymbol{v}\cdot\boldsymbol{C}_{NN}\boldsymbol{v}_\alpha^R + \Delta\theta\rho_0 C_F \Gamma_0 J^{q-2} h^2 (\boldsymbol{v}\cdot\boldsymbol{n})(\boldsymbol{v}_\alpha^R\cdot\boldsymbol{n})(q-1)$$
$$- \Gamma_0 J^{q-1} h (\boldsymbol{v}\cdot\boldsymbol{n})(\boldsymbol{v}_\alpha^R\cdot\boldsymbol{P}_0\boldsymbol{N}) - \theta_0\rho_0 C_F \Gamma_0^2 J^{2q-2} h^2 (\boldsymbol{v}\cdot\boldsymbol{n})(\boldsymbol{v}_\alpha^R\cdot\boldsymbol{n})$$
$$- c_\alpha \Gamma_0 J^{q-1} h (\boldsymbol{v}\cdot\boldsymbol{n}) E_\alpha^R + c_\alpha \boldsymbol{v}_\alpha^R\cdot\boldsymbol{P}_0\boldsymbol{N} - c_\alpha \Delta\theta\rho_0 C_F \Gamma_0 J^{q-1} h (\boldsymbol{v}_\alpha^R\cdot\boldsymbol{n}) = -c_\alpha^2 E_\alpha^R. \tag{4.65}$$

As before, the first two waves are obtained using $\boldsymbol{v}_\alpha^R = \boldsymbol{n}$. Replacing in equation (4.64) gives

$$c_\alpha \rho_0 \Gamma_0 J^{q-1} h (\boldsymbol{v}\cdot\boldsymbol{n})\boldsymbol{n} - \rho_0 c_{p,0}^2 \boldsymbol{n} + \Delta\theta\rho_0 C_F \Gamma_0 J^{q-2} h^2 (q-1)\boldsymbol{n}$$
$$- \Gamma_0 J^{q-1} h (\boldsymbol{n}\cdot\boldsymbol{P}_0\boldsymbol{N})\boldsymbol{n} - \theta_0\rho_0 C_F \Gamma_0^2 J^{2q-2} h^2 \boldsymbol{n}$$
$$- c_\alpha \Gamma_0 J^{q-1} h E_\alpha^R \boldsymbol{n} + \rho_0 c_\alpha^2 \boldsymbol{n} = \boldsymbol{0}, \tag{4.66}$$

where, in order to simplify the algebra, the following result from the previous section has been used (see equation (4.16))

$$\boldsymbol{C}_{NN}\boldsymbol{n} = \rho_0 c_{p,0}^2 \boldsymbol{n} \tag{4.67}$$

and the sub-index 0 denotes that the wave speed corresponds to the material at the reference temperature. Multiplying equation (4.66) by $\boldsymbol{n}$ and after some algebra, the following is obtained

$$\frac{1}{\Gamma_0 J^{q-1} h} c_\alpha^2 = \frac{1}{\Gamma_0 J^{q-1} h} c_{p,0}^2 + (\Delta\theta + \theta_0) C_F \Gamma_0 J^{q-1} h - \Delta\theta C_F \frac{h}{J}(q-1). \tag{4.68}$$

Finally, the 1 and 2 waves are

$$c_{1,2} = \pm\, c_p, \quad c_p = \sqrt{c_{p,0}^2 + (\Delta\theta + \theta_0) C_F (\Gamma_0 J^{q-1} h)^2 - \Delta\theta C_F \Gamma_0 J^{q-2} h^2 (q-1)}. \tag{4.69}$$

In the case that $\theta_0 = 0$, then $\Delta\theta \geq 0$ and the 1 and 2 wave speeds are real. If $\theta_0 \neq 0$, then the speeds are real if

$$\theta > \frac{1}{\Gamma_0 J^q + (1-q)} \left[\theta_0 (1-q) - \frac{c_{p,0}^2}{C_F \Gamma_0 J^{q-2} h^2} \right], \tag{4.70}$$

In the specific case of $q = 0$, this condition is given by

$$\theta > \frac{1}{\Gamma_0 + 1}\left[\theta_0 - \frac{c_{p,0}^2}{C_F \Gamma_0 J^{-2} h^2}\right]. \tag{4.71}$$

which, in the case of gas dynamics, there is no elastic constitutive model and $c_{p,0} = 0$ and, therefore, the condition is always fulfilled. If, otherwise $q = 1$, the eigenvalues $c_{1,2}$ will be real if

$$\theta > \frac{1}{\Gamma_0 J}\left[-\frac{c_{p,0}^2}{C_F \Gamma_0 J^{-1} h^2}\right], \tag{4.72}$$

which is always fulfilled since the right hand side is always negative and the temperature θ always positive by definition.

In order to obtain the shear waves, $\boldsymbol{v}_\alpha^R = \boldsymbol{t}_i$, $i \in \{1, 2\}$ is replaced in equation (4.64) to give

$$c_\alpha \rho_0 \Gamma_0 J^{q-1} h (\boldsymbol{v} \cdot \boldsymbol{t}_i)\boldsymbol{n} - \rho_0 c_{s,0}^2 \boldsymbol{t}_i - \Gamma_0 J^{q-1} h (\boldsymbol{t}_i \cdot \boldsymbol{P}_0 \boldsymbol{N})\boldsymbol{n} - c_\alpha \Gamma_0 J^{q-1} h E_\alpha^R \boldsymbol{n} + \rho_0 c_\alpha^2 \boldsymbol{t}_i = \boldsymbol{0}.$$

Multiplying by $\boldsymbol{t}_i$ the above equation the following is obtained

$$-\rho_0 c_{s,0}^2 = -\rho_0 c_\alpha^2,$$

which ends up giving the 3 to 6 eigenvalues as

$$c_{3,4} = c_{5,6} = \pm c_s, \quad c_s = c_{s,0} \tag{4.73}$$

and therefore the 3 to 6 waves speeds are equal to the elastic shear wave at the reference temperature. The corresponding eigenvectors of the 1 to 6 waves are given by,

$$\boldsymbol{\mathcal{U}}_{1,2}^R = \begin{pmatrix} \boldsymbol{n} \\ -\frac{1}{c_\alpha}\boldsymbol{n} \otimes \boldsymbol{N} \\ E_\alpha^R \end{pmatrix}, \tag{4.74}$$

where

$$E_\alpha^R = \rho_0 (\boldsymbol{v} \cdot \boldsymbol{n}) - \frac{1}{c_\alpha}\Big((\boldsymbol{n} \cdot \boldsymbol{P}_0 \boldsymbol{N}) - \frac{\rho_0}{\Gamma_0 J^{q-1} h}(c_\alpha^2 - c_{p,0}^2) \tag{4.75}$$

$$- \rho_0 C_F \frac{h}{J}(\Delta\theta(q-1) - \theta_0 \Gamma_0 J^q)\Big), \tag{4.76}$$

$$\boldsymbol{\mathcal{U}}_{3,4}^R = \begin{pmatrix} \boldsymbol{t}_1 \\ -\frac{1}{c_\alpha}\boldsymbol{t}_1 \otimes \boldsymbol{N} \\ \rho_0(\boldsymbol{v} \cdot \boldsymbol{t}_1) - \frac{1}{c_\alpha}(\boldsymbol{t}_1 \cdot \boldsymbol{P}_0 \boldsymbol{N}) \end{pmatrix}, \quad \boldsymbol{\mathcal{U}}_{5,6}^R = \begin{pmatrix} \boldsymbol{t}_2 \\ -\frac{1}{c_\alpha}\boldsymbol{t}_2 \otimes \boldsymbol{N} \\ \rho_0(\boldsymbol{v} \cdot \boldsymbol{t}_2) - \frac{1}{c_\alpha}(\boldsymbol{t}_2 \cdot \boldsymbol{P}_0 \boldsymbol{N}) \end{pmatrix}. \tag{4.77}$$

Perfect gases

In order to verify the results, the particular case of perfect gases will be analised. It can be seen that the Mie-Grüneisen equation of state with $q = 0$ and $\theta_0 = 0$ is equivalent to the equation of state for perfect gases. Then

$$p = -\rho_0 c_F \Gamma_0 J^{-1} \theta, \tag{4.78}$$

where the reference temperature is set to $\theta_0 = 0$. Furthermore, there is no elastic constitutive relationship at the reference temperature. This results in

$$c_{p,0} = 0 \tag{4.79}$$

and the deformation is reduced to volumetric deformation. Therefore

$$\boldsymbol{F} = J\boldsymbol{I} \Rightarrow h = J\|\boldsymbol{F}^{-T}\boldsymbol{N}\| = J\|J^{-1}\boldsymbol{N}\| = 1. \tag{4.80}$$

The 1 and 2 eigenvalues are reduced to (see equation (4.69))

$$c_{1,2} = \pm c_p, \quad c_p = \sqrt{\theta C_F \Gamma_0 (\Gamma_0 + 1) J^{-2}} = \frac{1}{J}\sqrt{-\frac{1}{\rho_0} p J \gamma}, \tag{4.81}$$

which is the isentropic wave speed for a perfect gas divided by the stretch in the reference undeformed domain. The corresponding eigenvectors are

$$\boldsymbol{\mathcal{U}}^R_{1,2} = \begin{pmatrix} \boldsymbol{n} \\ -\frac{1}{c_\alpha}\boldsymbol{n} \otimes \boldsymbol{N} \\ E^R_\alpha \end{pmatrix}, \tag{4.82}$$

$$E^R_\alpha = \rho_0 v_n + \frac{\rho_0 J}{\Gamma_0} c_\alpha - \frac{1}{J}\frac{1}{c_\alpha} e. \tag{4.83}$$

Chapter 5

Spatial semidiscretisation

5.1 Preliminaries

In the last two chapters the problem formulation was presented as a mixed system of conservation laws (section 4.2) complemented with an adequate constitutive model (chapter 3), boundary conditions (section 4.3) and initial conditions (section 4.4). Furthermore, the hyperbolicity of the system of equations was proved in section 4.5. Therefore, the problem can now be discretised using standard CFD techniques.

The current chapter will present the spatial semidiscretisation of this system of equations. To do so, a Finite Volume Method using central differences and JST type of dissipation will be used. The chapter is organised as follows. Section 5.2 introduces the Finite Volume Method. Section 5.3 explains the construction of the dual mesh. Section 5.4 presents the central differences stencil used in combination with the JST artificial dissipation, which is presented in section 5.5. In section 5.6, the spatial semidiscretisation is used for discretising the governing equations. Finally, section 5.7 presents the discretisation of the boundary conditions.

5.2 The Finite Volume Method

The Finite Volume Method (FVM) is the technique by which the integral formulation of the conservation laws is discretised directly in the physical space [52]. It is a very popular technique among the CFD community due to its flexibility, the easiness of implementation in structured or unstructured grids and its conservative properties [39, 52, 56, 87]. In the FVM, the discretisation of a conservation law is carried out using its integral form (see equation (2.6)). In contrast to the Finite Element Method (FEM), where the stored numerical quantities are the local function values at each mesh point, in the FVM these quantities are cell-averaged values. As a consequence, the FVM can be regarded as a FEM with piecewise constant approximation [52, 56]. The FVM is usually classified according to the discretisation of the fluxes (convective fluxes in fluids) and the control volume definition. This will be summarised in what follows.

5.2.1 Discretisation of the fluxes

The main idea behind the FVM is the division of a given computational domain into a finite number of control volumes where the discretised integral conservation law is going to be solved.

Given a domain Ω, this can be divided into smaller non overlapping control volumes V_a with boundary ∂V_a, where a conservation law can be applied. Specifically, using a Lagrangian conservation law of the form (2.9) and omitting source terms for simplicity, the integral conservation law at the control volume V_a reads

$$\frac{d}{dt}\int_{V_a} \boldsymbol{\mathcal{U}}\, dV = -\int_{\partial V_a} \boldsymbol{\mathcal{F}}_N\, dA, \tag{5.1}$$

and it can be noted that if all the contributions of the control volumes are added up, the conservation law for the whole domain Ω is recovered (see Figure 5.1), this is

$$\sum_a \frac{d}{dt}\int_{V_a} \boldsymbol{\mathcal{U}}\, dV = -\sum_a \int_{\partial V_a} \boldsymbol{\mathcal{F}}_N\, dA, \tag{5.2}$$

which leads to

$$\frac{d}{dt}\int_{\Omega} \boldsymbol{\mathcal{U}}\, dV = -\int_{\partial\Omega} \boldsymbol{\mathcal{F}}_N\, dA, \tag{5.3}$$

where it has been taken into account that the normal flux contribution of two adjacent cells cancel each other ($\boldsymbol{\mathcal{F}}_N = -\boldsymbol{\mathcal{F}}_{-N}$), which is the necessary local conservative property of the FVM. The spatial discretisation chosen will have to satisfy such conservative property. A general spatial discretisation of equation (5.1) is given by (see Figure 5.2)

$$V_a \frac{d\boldsymbol{\mathcal{U}}_a}{dt} = -\sum_k (\boldsymbol{\mathcal{F}}_N^C)_k A_k, \tag{5.4}$$

where the summation is done over all the facets k that conform the boundary of the discrete control volume, $(\boldsymbol{\mathcal{F}}_N^C)_k$ is the contact flux at the midpoint of facet k[1], A_k is the area (or length in the 2D case) of the facet k and $\boldsymbol{\mathcal{U}}_a$ is the cell averaged value of the variable $\boldsymbol{\mathcal{U}}$ at node a defined as

$$\boldsymbol{\mathcal{U}}_a = \frac{1}{V_a}\int_{V_a} \boldsymbol{\mathcal{U}}\, dV. \tag{5.5}$$

Since a unique contact flux $(\boldsymbol{\mathcal{F}}_N^C)_k$ is used per facet and $(\boldsymbol{\mathcal{F}}_N^C)_k = -(\boldsymbol{\mathcal{F}}_{-N}^C)_k$ (see Figure 5.3), the spatial discretisation will be conservative. The definition of this

[1] A unique Gauss point at the midpoint of the facet is enough for integrating the contact fluxes since, at the most, a linear reconstruction of the fluxes is used in the context of FVM.

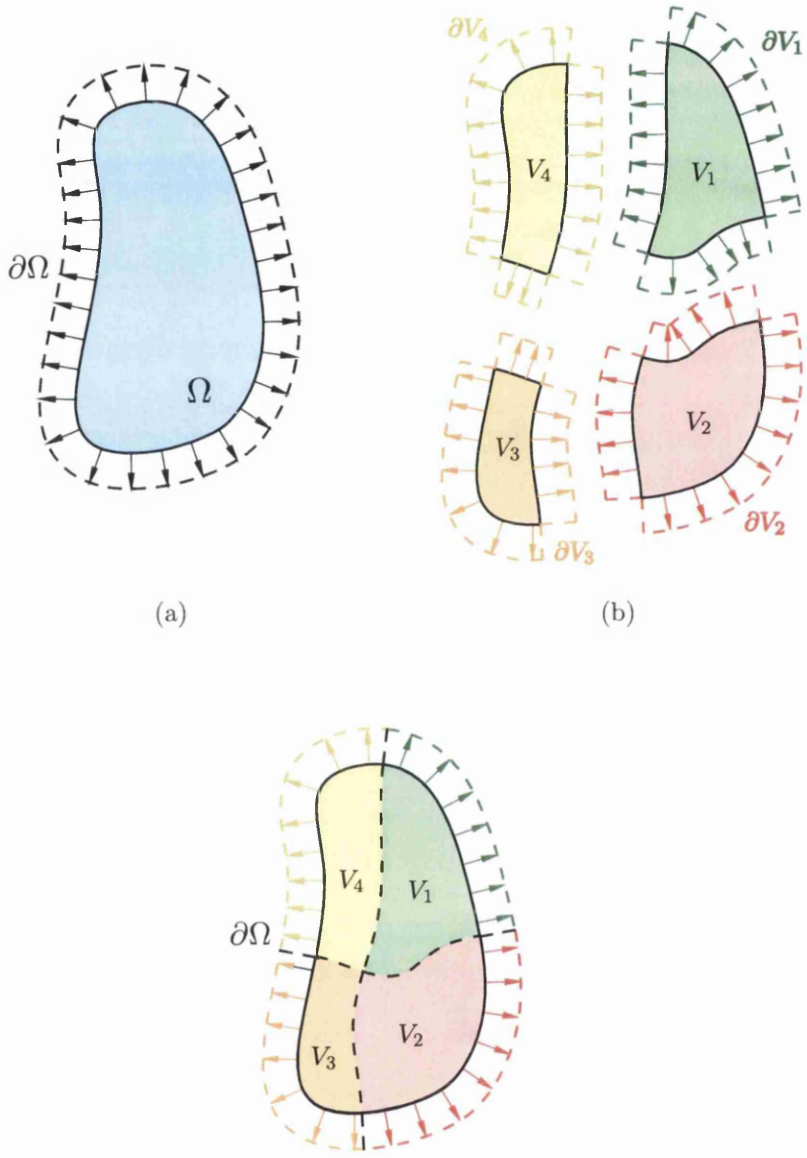

Figure 5.1: Subdivision of a domain Ω in several control volumes in the continuum.

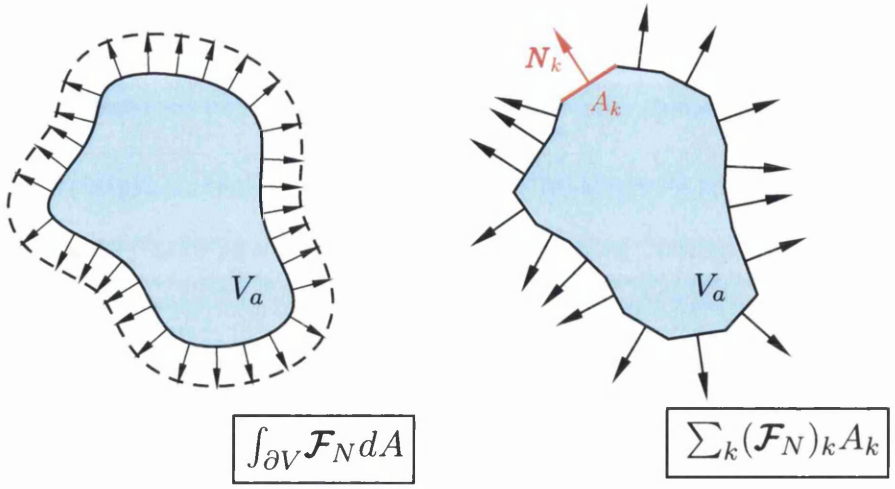

(a) (b)

Figure 5.2: Integral across the boundary of a control volume of the normal fluxes $\mathcal{F}_N$ in the continuum (a) and discrete (b) spaces.

contact flux will be given by the type of FVM used. For this purpose, two main approaches are usually chosen: central fluxes with added artificial dissipation or upwinding techniques.

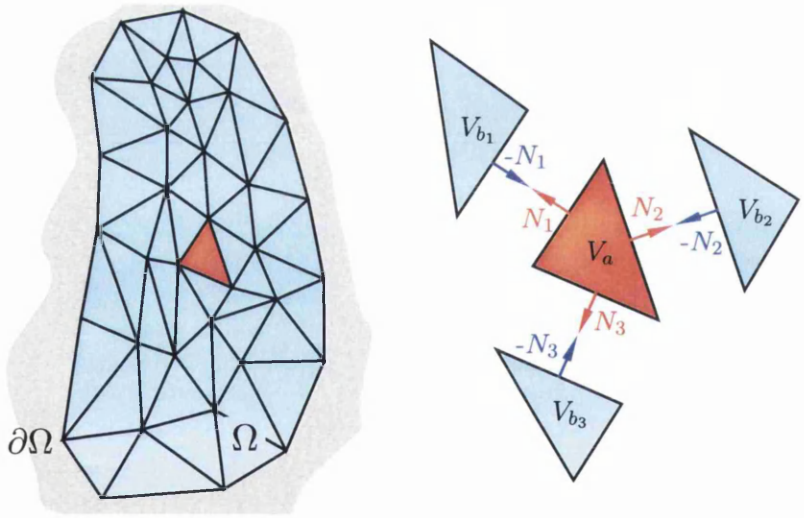

(a) (b)

Figure 5.3: A control volume and its neighbours in the discretised space.

The added artificial dissipation schemes use a centred stencil in order to discretise the numerical fluxes. As it is known [5, 51, 52, 56], the use of central differences in hyperbolic equations leads to solution instability. This is circumvented by adding an artificial dissipation term which prevents the appearance of numerical modes. The method is second order in space which is provided by the central differences

stencil, while the artificial dissipation is designed in order to provide enough diffusion while keeping the accuracy of the method. These schemes are relatively inexpensive though sometimes too dissipative, since the information related to the eigenstructure of the problem is not used in order to propagate the information in time [50].

On the other hand, upwind schemes use the eigenstructure information through approximate Riemann solvers in order to better capture the wave propagation phenomenon. As a result, these methods provide less diffusive solutions. Popular approximated Riemann solvers are those of Roe [88] and Osher [89]. Since the solution is approximated as piecewise constant, a linear reconstruction of the fluxes is required in order to increase the spatial accuracy to second order. Furthermore, when shocks are present, the use of limiters is required in order to reduce the numerical oscillations.

The upwinding schemes are known to be less diffusive than the artificial dissipation schemes [52,56,87]. On the other hand, the use of linear reconstruction and limiters makes the upwinding schemes computationally more expensive. Since the scope of this thesis is the implementation of a fast Finite Volume solver for solid dynamics, the central differences schemes with added dissipation are preferred. A very popular and successful approach in the CFD industry is the Jameson-Schmidt-Turkel scheme (JST), which will be explained in detail in sections 5.4 and 5.5.

5.2.2 Control volume definition

Regarding the type of control volume used, two different approaches can be followed: cell centred discretisations and vertex centred discretisations [50, 52, 56, 90]. In the first approach, each element of the initial mesh corresponds to the control volume of the Finite Volume discretisation (see Figure 5.4a). The variable is then stored at the barycentre of this cell and the edges of the mesh correspond to the edges of the control volumes. In the vertex-centred discretisations (see Figure 5.4b), the mesh vertices are used for storing the numerical values. To do so, a *dual mesh* is built, such that a control volume is associated with each of the nodes.

Comparing between the two, the cell-centred scheme does not require the construction of a dual mesh and therefore no pre-processing is required. Furthermore, for CFD applications, the dual mesh can become quite distorted in boundary layers, making the cell-centred approximation more suitable. On the other hand, the vertex centred scheme allows for a better treatment of the boundary conditions, since the stored variables are placed directly at the boundary and these can be corrected strongly. Furthermore, and perhaps more importantly, the ratio of elements to nodes is between 5 and 7 in a tetrahedral mesh. Therefore, the use of a vertex-centred approach can become significantly cheaper [50, 56] specially in the context of solid mechanics (where there is a significant cost in the evaluation of the stresses via an often complex constitutive model). A cell-centred Finite Volume discretisation of the current formulation was presented in [1]. In contrast, and for the reasons stated above, a vertex-centred approach will be used in the current thesis.

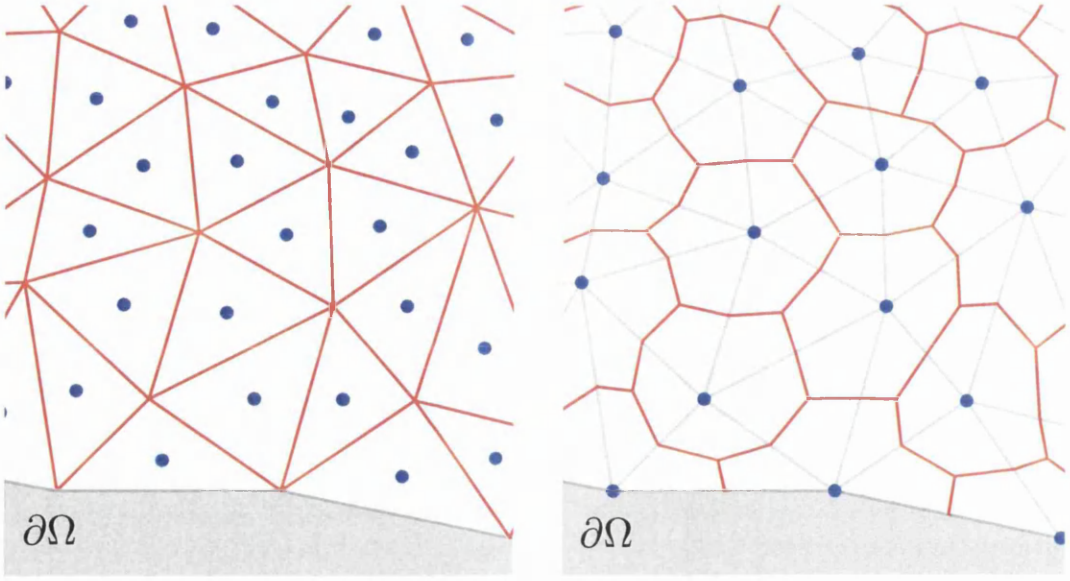

(a) (b)

Figure 5.4: Cell centred (a) and vertex centred (b) control volumes for the same triangular mesh. The red lines are the control volumes of the mesh, while the blue dots represent the point where the problem variables are stored.

5.3 Dual mesh construction

As explained in section 5.2.2, a vertex centred scheme requires the use of a dual mesh. In this thesis, the dual mesh is built using the median dual approach for triangular and tetrahedral meshes, as presented in [55] or [56]. This approach constructs the dual mesh by connecting edge midpoints with element centroids in two dimensions (see Figure 5.5) and edge midpoints with face centroids and element centroids in three dimensions (see Figure 5.6). Such a configuration ensures no overlapping of the control volumes.

For clarity purposes, a notation as the one followed by [55] will be used throughout the thesis. For a given node a, the set of nodes connected to it through an edge is denoted by Λ_a and the subset of nodes connected to a through a boundary edge is written as Λ_a^B (see Figure 5.5). For a given edge connecting nodes a and b, an area vector is defined as

$$\mathbf{C}^{ab} = \sum_{k \in \Gamma_{ab}} A_k \mathbf{N}_k, \tag{5.6}$$

where Γ_{ab} is the set of facets belonging to edge ab, A_k is the area of a given facet k and $\mathbf{N}_k$ its normal. Due to the definition of the dual mesh, the area vectors satisfy $\mathbf{C}^{ab} = -\mathbf{C}^{ba}$. These area vectors enable a substantial reduction in the computational cost when computing the boundary integral used in the Green-Gauss divergence theorem, since they save an additional loop over facets. In the case of a boundary edge, the contribution of the boundary faces to which it belongs, has to be taken

into account as well. This set of faces will be defined as Γ_a^B (see Figures 5.5b and 5.6b).

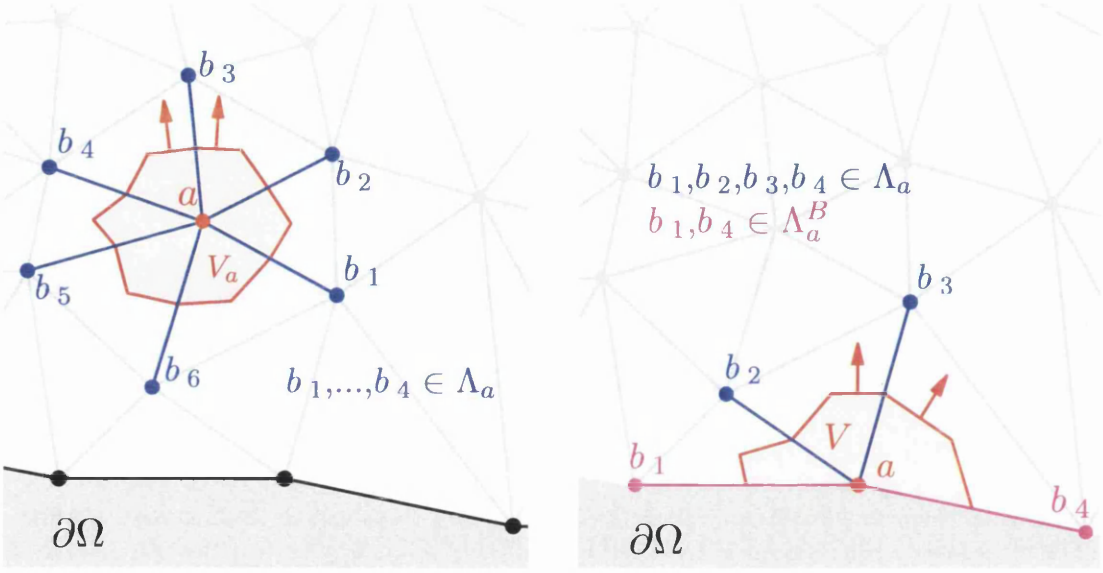

(a) (b)

Figure 5.5: Control volume for an interior node (a) and boundary node (b) using the median dual approach in a triangular mesh. The red shaded area is the control volume associated to node a. The blue lines are the edges connecting node a to its neighbouring nodes b_i, that is, the set Λ_a. The magenta lines in (b) are the boundary edges connecting node a to its neighbouring nodes b_i, that is, the set Λ_a^B.

5.4 Central differences

The central differences term is computed using the area vectors (5.6) as presented in the previous section. Taking this into consideration, equation (5.4) can be written using central differences as

$$V_a \frac{d\boldsymbol{\mathcal{U}}_a}{dt} = \sum_{b \in \Lambda_a} \frac{\boldsymbol{\mathcal{F}}_a + \boldsymbol{\mathcal{F}}_b}{2} \boldsymbol{C}^{ab} + \sum_{\gamma \in \Gamma_a^B} \boldsymbol{\mathcal{F}}_a^{\gamma} \boldsymbol{N}^{\gamma} \frac{A^{\gamma}}{3}, \tag{5.7}$$

where it can be seen that the evaluation is composed of a summation over edges (first term in the parenthesis) and a summation over boundary faces (second term in the parenthesis). In this second term, the weighted average stencil proposed by [91] is employed which gives the the flux over a face γ in three dimensions as (see details in Appendix D),

$$\boldsymbol{\mathcal{F}}_a^{\gamma} = \frac{6\boldsymbol{\mathcal{F}}_a + \boldsymbol{\mathcal{F}}_b + \boldsymbol{\mathcal{F}}_c}{8}, \tag{5.8}$$

where b, c are the two nodes that together with node a define face γ. For the two dimensional case the above expression reads

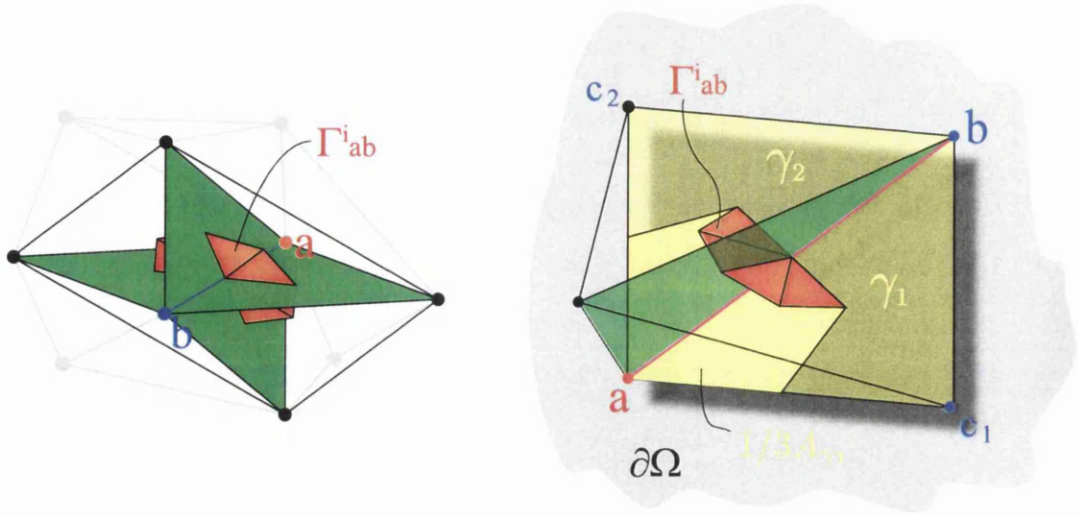

(a) (b)

Figure 5.6: Set of facets related to an interior edge (a) and boundary edge (b) in three dimensions. The green surfaces correspond to the interior faces to which the edge belongs, whereas the dark yellow surfaces correspond to the boundary faces $\gamma_1 = \widehat{abc_1}$ and $\gamma_2 = \widehat{abc_2}$. The red surfaces are the set of interior facets Γ_{ab} corresponding to edge ab. The bright yellow zone is the tributary area of faces γ_1 and γ_2 to node a.

$$\boldsymbol{\mathcal{F}}_a^{\gamma} = \frac{5\boldsymbol{\mathcal{F}}_a + \boldsymbol{\mathcal{F}}_b}{6}. \tag{5.9}$$

As explained in [45, 49–52], the expression (5.7) is equivalent to a Finite Element Galerkin approximation using linear interpolation of fluxes and lumped mass matrix (see prove in Appendix D). Therefore, the central differences term is second order in space but inherently unstable, as explained in the next section.

5.5 Artificial dissipation

The central differences scheme requires of an artificial dissipation term in order to stabilise the solution. Here, the JST artificial dissipation term is chosen, which is a combination of dissipation terms that allow both stabilising the solution and, at the same time, shock capturing in the presence of discontinuities. In order to clarify how this artificial dissipation term is built, firstly, the addition of dissipation into a central differences scheme will be introduced for one dimensional regular meshes (section 5.5.1). Next, the JST scheme will be explained for these same one dimensional regular meshes (section 5.5.2). Finally, the JST artificial dissipation will be extended to triangular (two dimensions) and tetrahedral (three dimensions) unstructured meshes (section 5.5.3).

5.5.1 Explicit addition of diffusion

Consider a one dimensional conservation law of the form

$$\frac{\partial \mathcal{U}}{\partial t} + \frac{\partial \mathcal{F}}{\partial x} = 0, \tag{5.10}$$

which, for an interior node, can be discretised using equation (5.7) in a regular mesh of nodes $i \in \{1, 2, \ldots, N\}$ spaced at an equal distance h as

$$h\frac{d\mathcal{U}_i}{dt} = -(\mathcal{F}_{i+1/2} - \mathcal{F}_{i-1/2}), \tag{5.11}$$

where $i+1/2$ stands for the midpoint of the edge connecting node i and $i+1$. Using $\mathcal{F}_{i+1/2} = \frac{1}{2}(\mathcal{F}(\mathcal{U}_i) + \mathcal{F}(\mathcal{U}_{i+1}))$ the scheme can be written as

$$h\frac{d\mathcal{U}_i}{dt} = -\frac{1}{2}\left(\mathcal{F}(\mathcal{U}_{i+1}) - \mathcal{F}(\mathcal{U}_{i-1})\right). \tag{5.12}$$

To start with, the particular case of the linear advection equation will be considered, which is given by a linear form of the fluxes as,

$$\mathcal{F} = a\mathcal{U}, \tag{5.13}$$

where a is the wave speed. Discretising as in (5.12) gives

$$h\frac{d\mathcal{U}_i}{dt} = -\frac{a}{2}\left(\mathcal{U}_{i+1} - \mathcal{U}_{i-1}\right). \tag{5.14}$$

It can be seen that (5.14) admits solutions of alternate value $+1$ and -1 at successive nodes without altering the left hand side [50, 92]. These are numerical modes, which lead to the phenomenon known as *odd-even decoupling*. The appearance of these modes can be circumvented by the addition of artificial diffusion, which has to be added in a consistent manner, such that it vanishes when $h \to 0$. Furthermore, the order of the original scheme has to be maintained [50–52]. This is accomplished adding a dissipative contribution to the scheme with a truncation error lower than the truncation error of the discretisation. A straightforward way to achieve that for a second order method (such as the central differences) is using a fourth order differences term of the form

$$h^4\left(\frac{\partial^4 \mathcal{U}}{\partial x^4}\right)_i \simeq \mathcal{U}_{i+2} - 4\mathcal{U}_{i+1} + 6\mathcal{U}_i - 4\mathcal{U}_{i-1} + \mathcal{U}_{i-2}, \tag{5.15}$$

where $\left(\frac{\partial^4 \mathcal{U}}{\partial x^4}\right)_i$ stands for $\frac{\partial^4 \mathcal{U}}{\partial x^4}$ evaluated at point $x = x_i$. Equation (5.15) can be added to the right hand side of equation (5.14) in the following manner

$$\frac{d\mathcal{U}_i}{dt} = -\frac{a}{2h}\left(\mathcal{U}_{i+1} - \mathcal{U}_{i-1}\right) - \frac{1}{h}|a|\kappa^{(4)}(\mathcal{U}_{i+2} - 4\mathcal{U}_{i+1} + 6\mathcal{U}_i - 4\mathcal{U}_{i-1} + \mathcal{U}_{i-2}), \tag{5.16}$$

where $\kappa^{(4)}$ is a user defined dissipation factor. This form stabilises the solution and maintains the second order of the central differences scheme (5.14). It can be seen that equation (5.16) is the discrete version of

$$\frac{\partial \mathcal{U}}{\partial t} + \frac{\partial \mathcal{F}}{\partial x} = -\kappa^{(4)} h^3 |a| \left(\frac{\partial^4 \mathcal{U}}{\partial x^4} \right), \tag{5.17}$$

which is the vanishing viscosity equivalent of the homogeneous equation (5.10) and therefore stable by construction [52]. This artificial diffusion scheme can be extended to a general conservation law adding third order differences to the average numerical flux as,

$$\begin{aligned} \mathcal{F}^C_{i+1/2} &= \frac{1}{2}(\mathcal{F}(\mathcal{U}_i) + \mathcal{F}(\mathcal{U}_{i+1})) + \kappa^{(4)} h^3 |\mathcal{A}_{i+1/2}| \left(\frac{\partial^3 \mathcal{U}}{\partial x^3} \right)_{i+1/2} \\ &= \frac{1}{2}(\mathcal{F}(\mathcal{U}_i) + \mathcal{F}(\mathcal{U}_{i+1})) + \kappa^{(4)} |\mathcal{A}_{i+1/2}| \left(\mathcal{U}_{i+2} - 3\mathcal{U}_{i+1} + 3\mathcal{U}_i - \mathcal{U}_{i-1} \right), \end{aligned} \tag{5.18}$$

where $\mathcal{A} = \frac{\partial \mathcal{F}}{\partial \mathcal{U}}$. Finally, the contact flux (5.18) replaces the average flux $\mathcal{F}_{i+1/2}$ in (5.11) to give a stable scheme. Due to the differences between the fluxes at $i+1/2$ and $i-1/2$, a fourth order differences approximation is again achieved, and therefore the scheme discretises a vanishing viscosity equation similar to (5.17).

5.5.2 JST artificial dissipation for structured grids

The JST scheme was first introduced in reference [5] for the solution of the Euler equations for rectangular structured meshes. The idea of the JST dissipation term is to provide background dissipation in the smooth regions (in order to stabilise the central differences equation) and, at the same time, act as a shock capturing operator close to discontinuities. To do so, a blend of fourth order differences, as in equation (5.18), and second order differences is used in combination with a discontinuity switch. As explained before, the fourth order differences avoid the appearance of the odd-even decoupling resulting from the central scheme, while keeping the scheme second order. The second order differences are activated in the vicinity of a sharp gradient in order to smear out the solution while reducing the accuracy to first order locally. For a one dimensional conservation law as (5.10) the JST dissipative flux reads

$$\begin{aligned} \mathcal{F}^C_{i+1/2} = \frac{1}{2}(\mathcal{F}(\mathcal{U}_i) + \mathcal{F}(\mathcal{U}_{i+1})) &- \varepsilon^{(2)}_{i+1/2} |\mathcal{A}_{i+1/2}| (\mathcal{U}_{i+1} - \mathcal{U}_i) \\ &+ \varepsilon^{(4)}_{i+1/2} |\mathcal{A}_{i+1/2}| \left(\mathcal{U}_{i+2} - 3\mathcal{U}_{i+1} + 3\mathcal{U}_i - \mathcal{U}_{i-1} \right), \end{aligned} \tag{5.19}$$

where the second term corresponds to the second order differences and $\varepsilon^{(2)}_{i+1/2}$ and $\varepsilon^{(4)}_{i+1/2}$ are the discontinuity switches. These are defined as

$$\varepsilon^{(2)}_{i+1/2} = \kappa^{(2)} \max(\Upsilon_i, \Upsilon_{i+1}), \tag{5.20}$$

$$\varepsilon^{(4)}_{i+1/2} = \max\left[0, (\kappa^{(4)} - \varepsilon^{(2)}_{i+1/2})\right], \tag{5.21}$$

where $\kappa^{(2)}$ and $\kappa^{(4)}$ are user defined coefficients. The coefficients Υ_i are normalised second order differences of the variable written as

$$\Upsilon_i = \frac{|\mathcal{U}_{i+1} - 2\mathcal{U}_i + \mathcal{U}_{i-1}|}{|\mathcal{U}_{i+1}| + 2|\mathcal{U}_i| + |\mathcal{U}_{i-1}|}. \tag{5.22}$$

which is a normalised second order difference and, therefore, an approximation to a normalised second order derivative. Therefore, in smooth regions, the coefficients Υ_i and Υ_{i+1} are kept small, which in turn makes the coefficient $\varepsilon^{(2)}_{i+1/2}$ small, and therefore keeps the second order differences deactivated (second term in equation (5.19)). This ensures that the second order accuracy of the method is preserved in smooth regions. Conversely, in the vicinity of sharp gradients the second order derivative of a function grows (curvature), which will activate the second order differences and therefore smear the solution. It can also be seen from the definition of the $\varepsilon^{(4)}_{i+1/2}$ discontinuity switch (equation (5.21)), that the fourth order differences are deactivated near sharp gradients. This is due to the fact that the fourth order differences may produce oscillations in the solution when activated close to discontinuities [45].

The extension of this scheme to two dimensional structured grids is straightforward and will not be described. Instead, the JST for unstructured triangular and tetrahedral unstructured grids will be introduced in the next section.

5.5.3 JST for triangular and tetrahedral unstructured grids

The extension of the JST artificial dissipation term to unstructured grids was firstly presented in [45] for the simulation of inviscid flow over a complete aircraft, where the Euler equations were implemented using a tetrahedral mesh. Later on, it has been implemented by many authors as for example [46–48, 93].

The complex stencils resulting from the use of an unstructured grid make impossible the use of a contact JST flux as in equation (5.19). Instead, the dissipation is added at the node in the following manner

$$V_a \frac{d\boldsymbol{\mathcal{U}}_a}{dt} = -\sum_{b\in\Lambda_a} \frac{\boldsymbol{\mathcal{F}}_a + \boldsymbol{\mathcal{F}}_b}{2} \boldsymbol{C}^{ab} - \sum_{\gamma\in\Gamma^B_a} \boldsymbol{\mathcal{F}}^\gamma_a \boldsymbol{N}^\gamma \frac{A^\gamma}{3} + \boldsymbol{\mathcal{D}}(\boldsymbol{\mathcal{U}}_a), \tag{5.23}$$

where the first term are the central differences defined in equation (5.7) and $\boldsymbol{\mathcal{D}}(\boldsymbol{\mathcal{U}}_a)$ is the dissipation added at node a. This dissipation term is defined as

$$\boldsymbol{\mathcal{D}}(\boldsymbol{\mathcal{U}}_a) = \sum_{b\in\Lambda_a} \varepsilon^{(2)}_{ab} \Psi_{ab} \theta_{ab} \left(\boldsymbol{\mathcal{U}}_b - \boldsymbol{\mathcal{U}}_a\right) - \sum_{b\in\Lambda_a} \varepsilon^{(4)}_{ab} \Psi_{ab} \theta_{ab} \left(\boldsymbol{L}(\boldsymbol{\mathcal{U}}_b) - \boldsymbol{L}(\boldsymbol{\mathcal{U}}_a)\right), \tag{5.24}$$

where the second order differences are written as a difference between the value at a given node and its nearest neighbours [45]. The term Ψ_{ab} is the spectral radius which gives the adequate dimension to the dissipation (and replaces $|\mathcal{A}_{i+1/2}|$ in one dimensional problems) and θ_{ab} are geometrical weights that allow maintaining the second order in distorted grids. The fourth order differences are written using a non divided Laplacian, $\boldsymbol{L}$, as

$$\boldsymbol{L}(\boldsymbol{\mathcal{U}}_a) = \sum_{b \in \Lambda_a} \theta_{ab}(\boldsymbol{\mathcal{U}}_b - \boldsymbol{\mathcal{U}}_a). \tag{5.25}$$

The geometrical weights θ_{ab} were proposed by [48] and are constructed in such a way that the non divided Laplacian, $\boldsymbol{L}$, cancels for a linear field (see Appendix E). These are given by

$$\theta_{ab} = 1 - \boldsymbol{\lambda}_a \cdot (\boldsymbol{X}_b - \boldsymbol{X}_a), \tag{5.26}$$

where $\boldsymbol{\lambda}_a$ is the solution to the following system of equations

$$\boldsymbol{K}_a \boldsymbol{\lambda}_a = \boldsymbol{b}_a, \tag{5.27}$$

and

$$\boldsymbol{K}_a = \sum_{b \in \Lambda_a} (\boldsymbol{X}_b - \boldsymbol{X}_a) \otimes (\boldsymbol{X}_b - \boldsymbol{X}_a), \tag{5.28}$$

$$\boldsymbol{b}_a = \sum_{b \in \Lambda_a} (\boldsymbol{X}_b - \boldsymbol{X}_a). \tag{5.29}$$

It is clear from (5.26) that $\theta_{ab} \neq \theta_{ba}$ and, therefore, this will affect the conservation of the variables when adding the artificial dissipation. This issue will be addressed later in the thesis, by using a modified dissipation term such that the satisfaction of the conservation of the primary variables is ensured (see section 6.3). Similar to the one dimensional case, the pressure switches evaluate the jump difference between the two nodes a and b connected by an edge as

$$\varepsilon_{ab}^{(2)} = \kappa^{(2)} \max(\Upsilon_a, \Upsilon_b), \tag{5.30}$$

$$\varepsilon_{ab}^{(4)} = \max\left[0, (\kappa^{(4)} - \varepsilon_{ab}^{(2)})\right]. \tag{5.31}$$

In this case, Υ is the second order difference of some conserved variable. For the discretisation of the Euler equations as in [5, 45], these differences are computed using the fluid pressure, p, as

$$\Upsilon_a = \frac{|\sum_{b \in \Lambda_a} \theta_{ab}(p_b - p_a)|}{\sum_{b \in \Lambda_a}(p_b + p_a)}. \tag{5.32}$$

Finally, the artificial dissipation requires a scaling, which is obtained by using the spectral radius. The spectral radius is defined as

$$\Psi_{ab} = \frac{1}{2}\left[\Psi_a + \Psi_b\right], \quad \Psi_a = \sum_{k\in\partial\Omega_a} |\lambda| A_k, \tag{5.33}$$

where $|\lambda|$ is the maximum eigenvalue of the flux Jacobian matrix of the system of conservation equations to be solved. In the particular case of this thesis, this is simply c_p, the speed of the pressure wave.

5.6 Discretisation of the governing equations

The central differences scheme (5.23) and JST artifical dissipation term (5.24) will now be used for the discretisation of the governing equations (4.1a,4.1b,4.1c). It transpires that dissipation only needs to be added to the first equation in order to stabilise the system. The discretised equations read

$$V_a \frac{d\boldsymbol{p}_a}{dt} = \sum_{\alpha\in\Lambda_a} \frac{1}{2}\left(\boldsymbol{P}_a + \boldsymbol{P}_b\right)\boldsymbol{C}^{ab} + \sum_{\gamma\in\Gamma_a^B} \hat{\boldsymbol{t}}_a^\gamma \frac{A^\gamma}{3} + \frac{1}{V_a}\boldsymbol{\mathcal{D}}(\boldsymbol{p}_a) \tag{5.34}$$

$$V_a \frac{d\boldsymbol{F}_a}{dt} = \sum_{\alpha\in\Lambda_a} \frac{\boldsymbol{v}_a + \boldsymbol{v}_b}{2} \otimes \boldsymbol{C}^{ab} + \sum_{\gamma\in\Gamma_a^B} \left(\hat{\boldsymbol{v}}_a^\gamma \otimes \boldsymbol{N}^\gamma\right) \frac{A^\gamma}{3} \tag{5.35}$$

$$V_a \frac{dE_{Ta}}{dt} = \sum_{a\in\Lambda_a} \frac{1}{2}\left(\boldsymbol{P}_a^T\boldsymbol{v}_a + \boldsymbol{P}_b^T\boldsymbol{v}_b\right)\cdot\boldsymbol{C}^{ab} + \sum_{\gamma\in\Gamma_a^B} \left(\hat{\boldsymbol{v}}_a^\gamma \cdot \hat{\boldsymbol{t}}_a^\gamma\right) \frac{A^\gamma}{3} \tag{5.36}$$

where $\hat{\boldsymbol{t}}_a^\gamma$ and $\hat{\boldsymbol{v}}_a^\gamma$ are the corrected face tractions and velocities that will lead to the imposition of the weak boundary conditions.

The time evolution of the deformation gradient $\boldsymbol{F}$ in equation (5.35) is carried out without the introduction of numerical dissipation. This discrete space-time evolution equation yields a discrete update of $\boldsymbol{F}$ which is curl-free at a discrete level, as the right hand side of equation (5.35) represents a central difference stencil (see equation (2.60)). With this update and provided that the initial conditions are curl free, it is then possible to guarantee the existence of a discrete deformation gradient tensor which satisfies the necessary involutions [1,65,94].

As mentioned above, artificial dissipation is only added in the first equation. Therefore, the artificial dissipation term reads (see equation (5.24))

$$\boldsymbol{\mathcal{D}}(\boldsymbol{p}_a) = \sum_{b\in\Lambda_a} \varepsilon_{ab}^{(2)}\Psi_{ab}\theta_{ab}\left(\boldsymbol{p}_b - \boldsymbol{p}_a\right) - \sum_{b\in\Lambda_a} \varepsilon_{ab}^{(4)}\Psi_{ab}\theta_{ab}\left(\boldsymbol{L}(\boldsymbol{p}_b) - \boldsymbol{L}(\boldsymbol{p}_a)\right). \tag{5.37}$$

Since, in most of the numerical tests, there will be an absence of physical shocks, this dissipation operator will be reduced to the fourth order dissipation term, that is

$$\boldsymbol{\mathcal{D}}(\boldsymbol{p}_a) = -\sum_{b\in\Lambda_a} \kappa^{(4)}\Psi_{ab}\theta_{ab}\left(\boldsymbol{L}(\boldsymbol{p}_b) - \boldsymbol{L}(\boldsymbol{p}_a)\right). \tag{5.38}$$

	Traction	Velocity
Clamped	$\hat{\boldsymbol{t}}_a^\gamma = \boldsymbol{t}_a^\gamma$	$\hat{\boldsymbol{v}}_a^\gamma = \boldsymbol{0}$
Free	$\hat{\boldsymbol{t}}_a^\gamma = \boldsymbol{t}^B$	$\hat{\boldsymbol{v}}_a^\gamma = \boldsymbol{v}_a^\gamma$
Normally sliding	$\hat{\boldsymbol{t}}_a^\gamma = (\boldsymbol{I} - \boldsymbol{N} \otimes \boldsymbol{N})\boldsymbol{t}_a^\gamma + (\boldsymbol{N} \otimes \boldsymbol{N})\boldsymbol{t}^B$	$\hat{\boldsymbol{v}}_a^\gamma = (\boldsymbol{N} \otimes \boldsymbol{N})\boldsymbol{v}_a^\gamma$
Tangentially sliding	$\hat{\boldsymbol{t}}_a^\gamma = (\boldsymbol{N} \otimes \boldsymbol{N})\boldsymbol{t}_a^\gamma + (\boldsymbol{I} - \boldsymbol{N} \otimes \boldsymbol{N})\boldsymbol{t}^B$	$\hat{\boldsymbol{v}}_a^\gamma = (\boldsymbol{I} - \boldsymbol{N} \otimes \boldsymbol{N})\boldsymbol{v}_a^\gamma$

Table 5.1: Discretised weak boundary conditions on traction and velocity for a boundary node a.

	Linear momentum
Clamped	$\hat{\boldsymbol{p}}_a = \boldsymbol{0}$
Free	$\hat{\boldsymbol{p}}_a = \boldsymbol{p}_a$
Normally sliding	$\hat{\boldsymbol{p}}_a = (\boldsymbol{N} \otimes \boldsymbol{N})\boldsymbol{p}_a$
Tangentially sliding	$\hat{\boldsymbol{p}}_a = (\boldsymbol{I} - \boldsymbol{N} \otimes \boldsymbol{N})\boldsymbol{p}_a$

Table 5.2: Discretised strong boundary conditions on traction and velocity for a boundary node a.

5.7 Boundary conditions

Finally, only the discretisation of the boundary conditions (see section 4.3) remains in order to obtain the spatial semidiscretisation. Given the spatial discretisation used, the boundary conditions can be imposed both weakly, using the fluxes of the discretised equations (5.34), (5.35) and (5.36), and strongly, once the value at a specific boundary node has been obtained.

In order to impose the weak boundary conditions, the traction, $\boldsymbol{t}_a^\gamma$, and velocity, $\boldsymbol{v}_a^\gamma$, corresponding to the contribution of face γ to node a and defined as (see equations (5.9) and (5.8))

$$\boldsymbol{t}_a^\gamma = \frac{6\boldsymbol{P}_a + \boldsymbol{P}_b + \boldsymbol{P}_c}{8}\boldsymbol{N}^\gamma, \tag{5.39}$$

$$\boldsymbol{v}_a^\gamma = \frac{6\boldsymbol{v}_a + \boldsymbol{v}_b + \boldsymbol{v}_c}{8}, \tag{5.40}$$

will be corrected depending on the type of boundary conditions. Table 5.1 summarises these weak boundary conditions, where the symbol "$\hat{}$" indicates a corrected flux.[2] On the other hand, the strong boundary conditions will be imposed, when possible on the linear momentum. This is shown in table 5.2.

[2]The fact that $\boldsymbol{n} = \boldsymbol{N}$ for the sliding boundary conditions has been used (see section 4.3)

Chapter 6

Time integration of the semidiscrete system of equations

6.1 Preliminaries

Once the system of equations has been discretised in space, it is necessary to implement a temporal discretisation in order to obtain the complete numerical algorithm. This chapter will present the time integration of both the governing equations and the displacements (section 6.2), a numerical correction in order to satisfy the exact conservation of linear and angular momentum (section 6.3) and the solution procedure that defines the full numerical algorithm (section 6.4).

6.2 Time integration

The spatial semidiscretisation leaves a system of Ordinary Differential Equations (ODE's) in time for each node a written as,

$$V_a \frac{d\boldsymbol{\mathcal{U}}_a}{dt} = -\boldsymbol{\mathcal{R}}_a(\boldsymbol{\mathcal{U}}_a, t) \tag{6.1}$$

where $\boldsymbol{\mathcal{R}}_a(\boldsymbol{\mathcal{U}}_a, t)$ stands for the complete spatial discretisation at node a and time t. This procedure of separating the spatial and time discretisations is known as the *method of lines* [39, 52, 87].

In order to integrate (6.1) in time, the time scale is divided in a sequence of *time steps* $n \in \{0, 1, 2, \ldots, N_{steps}\}$ with associated time instants $t^n \in \{t^0, t^1, t^2, \ldots, t^{end}\}$. At each time step n, the *time step size* is defined as $\Delta t^n = t^{n+1} - t^n$. A general time integrator will give the solution at time step $n+1$ as

$$V_a \frac{\boldsymbol{\mathcal{U}}_a^{n+1} - \boldsymbol{\mathcal{U}}_a^n}{\Delta t^n} = -\sum_j \alpha_j \boldsymbol{\mathcal{R}}(\boldsymbol{\mathcal{U}}_a^j) \tag{6.2}$$

where the number of residuals used on the right hand side will define the type of time integrator used. In general, time integration techniques are classified as explicit or

implicit (see extensive discussion in [50,52,56,77]). In explicit time integrators, only known information, from time steps $n, n-1, n-2, \ldots$, is used on the right hand side of equation (6.2). In implicit methods, information from time step $n+1$ (yet unknown) is also included in the temporal stencil. Therefore, a system of equations needs to be solved when using implicit time integrators and, consequentially, they have a higher computational cost per time step than the explicit ones. In explicit time integrators, the time step size is always limited due to stability reasons which results in a larger number of time steps to be computed for the same final time. Depending on the case, for example very fine meshes, this may counterbalance the added cost of the implicit methods, making explicit methods less competitive.

The decision on choosing either a implicit or a explicit scheme is usually driven by the physics of the problem. In the current thesis, the objective is the simulation of fast dynamics phenomena, which implies that small time steps will be required in order to accurately capture the deformation process. This will be specially critical when time dependent constitutive models are used (e.g. plasticity). Therefore, the small time step size required by an explicit numerical algorithm will be in good agreement with the time scale of the problem. As a consequence, an explicit time integration scheme will be used.

6.2.1 Integration of the problem variables, TVD Runge-Kutta scheme

A very popular family of explicit schemes are the multistage Runge-Kutta time-stepping schemes. In these schemes, the residual of the spatial discretisation is evaluated at different intermediate stages before reaching the time increment [95]. These schemes can be optimised in order to improve the stability properties of the scheme or, alternatively, in order to increase the accuracy of the temporal discretisation. Furthermore, multistage schemes have been traditionally used alongside the JST spatial discretisation [5, 96, 97]. A convinient choice is the two stages Total Variation Diminishing (TVD) Runge-Kutta time integrator as proposed by Shu and Osher [44, 71]. This time integrator is second order in time and, at the same time, ensures the satisfaction of the TVD condition which requires that the monotonicity of the scheme is preserved at each time step [39]. Equation (6.1) is discretised using the two stages TVD Runge-Kutta scheme, from time step t^n to time step t^{n+1}, as

$$\begin{aligned} \boldsymbol{\mathcal{U}}_a^* &= \boldsymbol{\mathcal{U}}_a^n - \Delta t \boldsymbol{\mathcal{R}}_a(\boldsymbol{\mathcal{U}}_a^n, t^n), \\ \boldsymbol{\mathcal{U}}_a^{**} &= \boldsymbol{\mathcal{U}}_a^* - \Delta t \boldsymbol{\mathcal{R}}_a(\boldsymbol{\mathcal{U}}_a^*, t^{n+1}), \\ \boldsymbol{\mathcal{U}}_a^{n+1} &= \frac{1}{2}\left(\boldsymbol{\mathcal{U}}_a^n + \boldsymbol{\mathcal{U}}_a^{**}\right), \end{aligned} \tag{6.3}$$

where the time step is governed by a standard Courant–Friedrichs–Lewy (CFL) condition [98] given as

$$\Delta t \leq \alpha_{CFL} \min_a \left(\frac{h_a}{(c_p)_a^n} \right), \tag{6.4}$$

where h_a is the minimum length across the control volume of node a at the reference domain, $(c_p)_a^n$ is the volumetric wave speed as presented in equations (4.21, 4.39,4.69) and α_{CFL} is the CFL stability number, which depends on the specific time and spatial discretisation used (as it will be explained later in the thesis).

6.2.2 Integration of the displacements, trapezoidal rule

The displacements $\boldsymbol{x}$ are not in the set of equations (4.1a,4.1b,4.1c) of the problem formulation, but still, they are needed for post-processing purposes and in order to compute external magnitudes as the angular momentum (see next section). In principle, any type of temporal integration could be used, such that it has second order accuracy. Here, the trapezoidal rule is chosen, which is written as

$$\boldsymbol{x}_a^{n+1} = \boldsymbol{x}_a^n + \frac{\Delta t}{2} \left(\boldsymbol{v}_a^n + \boldsymbol{v}_a^{n+1} \right). \tag{6.5}$$

This particular choice will ease certain algebraic manipulations in the next section.

6.3 Discrete angular and linear momentum conserving algorithm

Since the conservation variables are linear momentum, deformation gradient and total energy, the proposed scheme does not necessarily preserve the angular momentum of the system. Furthermore, as stated in section 5.5, the artificial dissipation term prevents the exact conservation of linear momentum due to the lack of symmetry of the geometrical weights. The current section presents an adaptation of the angular momentum conservation algorithm presented in [1] that will modify the internal tractions and dissipation in order to preserve both linear and angular momentum.

In the absence of external tractions, the conservation of the discrete angular momentum after a time step can be written as

$$\sum_{a=1}^{N_{nodes}} \boldsymbol{x}_a^{n+1} \times m_a \boldsymbol{v}_a^{n+1} - \sum_{a=1}^{N_{nodes}} \boldsymbol{x}_a^n \times m_a \boldsymbol{v}_a^n = \boldsymbol{0}. \tag{6.6}$$

By taking into account the trapezoidal rule for the time integration of the positions (see equation (6.5)), the above equation can be rewritten as

$$\sum_{a=1}^{N_{nodes}} \boldsymbol{x}_a^{n+1/2} \times m_a \Delta \boldsymbol{v}_a = \boldsymbol{0}; \quad \Delta \boldsymbol{v}_a = \boldsymbol{v}_a^{n+1} - \boldsymbol{v}_a^n; \quad \boldsymbol{x}_a^{n+1/2} = \boldsymbol{x}_a^n + \frac{\Delta t}{2} \boldsymbol{v}_a^n \tag{6.7}$$

Considering the TVD Runge-Kutta time integration as presented in the previous section, the velocity reads

$$\Delta \boldsymbol{v}_a = -\frac{\Delta t}{2\rho_0}(\boldsymbol{\mathcal{R}}_a^n(\boldsymbol{p}_a^n, t^n) + \boldsymbol{\mathcal{R}}_a^*(\boldsymbol{p}_a^*, t^*)), \tag{6.8}$$

where $\boldsymbol{\mathcal{R}}_a(\boldsymbol{p}_a, t)$ corresponds to the right hand side of equation (5.34). Substituting equation (6.8) into (6.7), the following equation is obtained

$$\sum_{e=1}^{N_{nodes}} \boldsymbol{x}_a^{n+1/2} \times m_a \left(-\frac{\Delta t}{2\rho_0}(\boldsymbol{\mathcal{R}}_a^n(\boldsymbol{p}_a^n, t^n) + \boldsymbol{\mathcal{R}}_a^*(\boldsymbol{p}_a^*, t^*)) \right) = \boldsymbol{0}. \tag{6.9}$$

A sufficient condition to satisfy the above equation is given when the following equation

$$\sum_{a=1}^{N_{nodes}} \boldsymbol{x}_a^{n+1/2} \times m_a \boldsymbol{\mathcal{R}}_a^\alpha(\boldsymbol{p}_a^\alpha, t^\alpha) = \boldsymbol{0} \tag{6.10}$$

is satisfied at the two time stages of the Runge-Kutta time integrator (i.e., $\forall \alpha \in \{n, *\}$). Substituting the right hand side of equation (5.34) into (6.10) and omitting the time superindex for simplicity, the following equation is obtained

$$\sum_{a=1}^{N_{nodes}} \boldsymbol{x}_a \times \frac{m_a}{\rho_0 V_a} \left(\sum_{\alpha \in \Lambda_a} \frac{1}{2} (\boldsymbol{P}_a + \boldsymbol{P}_b) \boldsymbol{C}^{ab} + \sum_{\gamma \in \Gamma_a^B} \hat{\boldsymbol{t}}_a^\gamma \frac{A^\gamma}{3} + \boldsymbol{\mathcal{D}}(\boldsymbol{p}_a) \right) = \boldsymbol{0}. \tag{6.11}$$

Assuming a free boundary traction (that could otherwise contribute to an external torque) and rearranging the first term into a summation over edges, the equation above is simplified to

$$\sum_{k=1}^{N_{ed_{int}}} \boldsymbol{f}_k \times (\boldsymbol{x}_b - \boldsymbol{x}_a) + \sum_{a=1}^{N_{nodes}} \boldsymbol{\mathcal{D}}(\boldsymbol{p}_a) \times \boldsymbol{x}_a = \boldsymbol{0}, \tag{6.12}$$

where the fact that $\boldsymbol{C}^{ab} = -\boldsymbol{C}^{ba}$ has been considered and where $\boldsymbol{f}_k = \frac{1}{2}(\boldsymbol{P}_a + \boldsymbol{P}_b)\boldsymbol{C}^{ab}$ is the force related to edge k. A sufficient condition for fulfilling the above equation is satisfied when both terms separately vanish. For the internal forces, this reads

$$\sum_{k=1}^{N_{ed_{int}}} \boldsymbol{f}_k \times \Delta \boldsymbol{x} = \boldsymbol{0}, \tag{6.13}$$

where $\Delta \boldsymbol{x} = \boldsymbol{x}_b^{n+1/2} - \boldsymbol{x}_a^{n+1/2}$. As explained in section 5.5 the geometrical weights are not symmetric and, therefore, the conservation of linear momentum would not be

satisfied. An extra condition has to be added for the satisfaction of such condition which, together with the angular momentum preservation condition, reads

$$\sum_{a=1}^{N_{nodes}} \mathcal{D}(\boldsymbol{p}_a) \times \boldsymbol{x}_a = \boldsymbol{0}, \tag{6.14a}$$

$$\sum_{e=1}^{N_{nodes}} \mathcal{D}(\boldsymbol{p}_a) = \boldsymbol{0}. \tag{6.14b}$$

A Lagrangian minimisation procedure has to be used to obtain a minimally modified set of internal forces, $\hat{\boldsymbol{f}}_k$ that satisfy equation (6.13) and a set of minimally modified dissipation $\hat{\mathcal{D}}(\boldsymbol{p}_e)$ that satisfy both equations (6.14a) and (6.14b). This is achieved by minimising the following two functionals

$$\Pi_f(\hat{\boldsymbol{f}}_k, \boldsymbol{\lambda}_f) = \left(\frac{1}{2} \sum_{k=1}^{N_{ed_{int}}} (\hat{\boldsymbol{f}}_k - \boldsymbol{f}_k) \cdot (\hat{\boldsymbol{f}}_k - \boldsymbol{f}_k) \right) + \boldsymbol{\lambda}_f \cdot \sum_{k=1}^{N_{ed_{int}}} \hat{\boldsymbol{f}}_k \times \Delta \boldsymbol{x}_k, \tag{6.15}$$

$$\begin{aligned} \Pi_D(\hat{\mathcal{D}}(\boldsymbol{p}_a), \boldsymbol{\lambda}_D, \boldsymbol{\mu}_D) &= \left(\frac{1}{2} \sum_{a=1}^{N_{nodes}} (\hat{\mathcal{D}}(\boldsymbol{p}_a) - \mathcal{D}(\boldsymbol{p}_a)) \cdot (\hat{\mathcal{D}}(\boldsymbol{p}_a) - \mathcal{D}(\boldsymbol{p}_a)) \right) \\ &+ \boldsymbol{\lambda}_D \cdot \sum_{a=1}^{N_{nodes}} \hat{\mathcal{D}}(\boldsymbol{p}_a) \times \boldsymbol{x}_a + \boldsymbol{\mu}_D \cdot \sum_{a=1}^{N_{nodes}} \hat{\mathcal{D}}(\boldsymbol{p}_a). \end{aligned} \tag{6.16}$$

After some algebra a modified set of internal forces $\hat{\boldsymbol{f}}_k$ is obtained as

$$\hat{\boldsymbol{f}}_k = \boldsymbol{f}_k + \boldsymbol{\lambda}_f \times \Delta \boldsymbol{x}_k, \tag{6.17}$$

where $\boldsymbol{\lambda}_f$ is the solution to the following system of 3×3 equations

$$\boldsymbol{K}_f \boldsymbol{\lambda}_f = \boldsymbol{b}_f \tag{6.18}$$

and where

$$\boldsymbol{K}_f = \sum_{k=1}^{N_{ed_{int}}} (\Delta \boldsymbol{x}_k \cdot \Delta \boldsymbol{x}_k) \boldsymbol{I} - \Delta \boldsymbol{x}_k \otimes \Delta \boldsymbol{x}_k, \tag{6.19a}$$

$$\boldsymbol{b}_f = \sum_{k=1}^{N_{ed_{int}}} \boldsymbol{f}_k \times \Delta \boldsymbol{x}_k. \tag{6.19b}$$

In a similar fashion, the minimisation of the functional described on equation (6.16) gives a modified set of dissipation at nodes

$$\hat{\mathcal{D}}(\boldsymbol{p}_a) = \mathcal{D}(\boldsymbol{p}_a) + \boldsymbol{\lambda}_D \times \boldsymbol{x}_a - \boldsymbol{\mu}_D, \tag{6.20}$$

where $\boldsymbol{\lambda}_D$ is the solution to

$$\boldsymbol{K}_D \boldsymbol{\lambda}_D = \boldsymbol{b}_D \tag{6.21}$$

and

$$\boldsymbol{K}_D = \sum_{a=1}^{N_{nodes}} \left((\boldsymbol{x}_a \cdot \boldsymbol{x}_a)\boldsymbol{I} - \boldsymbol{x}_a \otimes \boldsymbol{x}_a \right) - \frac{1}{N_{nodes}} \left((\boldsymbol{a} \cdot \boldsymbol{a})\, \boldsymbol{I} - \boldsymbol{a} \otimes \boldsymbol{a} \right), \tag{6.22a}$$

$$\boldsymbol{b}_D = \sum_{a=1}^{N_{nodes}} \boldsymbol{D}(\boldsymbol{p}_a) \times \boldsymbol{x}_a - \frac{1}{N_{nodes}} \boldsymbol{c} \times \boldsymbol{a}, \tag{6.22b}$$

where the notation $\boldsymbol{a} = \sum_{a=1}^{N_{nodes}} \boldsymbol{x}_a$ and $\boldsymbol{c} = \sum_{a=1}^{N_{nodes}} \boldsymbol{D}(\boldsymbol{p}_a)$ has been used. Finally $\boldsymbol{\mu}_D$ is obtained as

$$\boldsymbol{\mu}_D = \frac{1}{N_{nodes}} \left(\sum_{a=1}^{N_{nodes}} \boldsymbol{D}(\boldsymbol{p}_a) + \boldsymbol{\lambda}_D \times \boldsymbol{a} \right). \tag{6.23}$$

This correction requires the computation of three global parameters $\boldsymbol{\lambda}_f$, $\boldsymbol{\lambda}_D$ and $\boldsymbol{\mu}_D$, during the spatial discretisation routines.

6.4 Solution procedure

The algorithm 6.4.1 presents the solution procedure used for the update of the primary variables after a time step. The algorithm requires a preprocessing step for the computation of the geometrical variables (θ_{ab}, $\boldsymbol{C}_{ab}$) related to the dual mesh. Once this is obtained, the algorithm only requires two loops over edges and one loop over boundary faces per time stage.

Algorithm 6.4.1: EVALUATION OF $\mathcal{U}_{n+1}(\mathcal{U}_n)$

(1) GIVEN $\mathcal{U}_a^n = (\boldsymbol{p}_a^n, \boldsymbol{F}_a^n)^T$, $\boldsymbol{x}_a^n$

(2) LOOP over Runge-Kutta stages (to compute $\mathcal{U}_a^*$, $\mathcal{U}_a^{**}$)

(2.1)LOOP over edges $k(ab)$

$\boldsymbol{L}(\boldsymbol{p_a}^n) := \boldsymbol{L}(\boldsymbol{p_a}^n) + \theta_{ab}\,(\boldsymbol{p}_b^n - \boldsymbol{p}_a^n)$

$\boldsymbol{L}(\boldsymbol{p_b}^n) := \boldsymbol{L}(\boldsymbol{p_b}^n) + \theta_{ba}\,(\boldsymbol{p}_a^n - \boldsymbol{p}_b^n)$

$\boldsymbol{b}_f := \boldsymbol{b}_f + \boldsymbol{f}_k^n \times \Delta\boldsymbol{x}_k^{n+1/2}$

$\boldsymbol{K}_f := \boldsymbol{K}_f + (\Delta\boldsymbol{x}_k^{n+1/2} \cdot \Delta\boldsymbol{x}_k^{n+1/2})\boldsymbol{I} - \Delta\boldsymbol{x}_k^{n+1/2} \otimes \Delta\boldsymbol{x}_k^{n+1/2}$

(2.2)COMPUTE $\boldsymbol{\lambda}_f = \boldsymbol{K}_f^{-1}\boldsymbol{b}_f$

(2.3)LOOP over edges $k(ab)$

$\hat{\boldsymbol{f}}_k^n = \boldsymbol{f}_k^n + \boldsymbol{\lambda}_f \times \Delta\boldsymbol{x}_k^{n+1/2}$

$\hat{\boldsymbol{\mathcal{R}}}_{p,a}^n := \hat{\boldsymbol{\mathcal{R}}}_{p,a}^n + \hat{\boldsymbol{f}}_k$

$\boldsymbol{\mathcal{R}}_{F,a}^n := \boldsymbol{\mathcal{R}}_{F,a}^n + \frac{1}{2}(\boldsymbol{v}_a + \boldsymbol{v}_b) \otimes \boldsymbol{C}^{ab}$

$\boldsymbol{\mathcal{D}}(\boldsymbol{p}_a) := \boldsymbol{\mathcal{D}}(\boldsymbol{p}_a) - \kappa^{(4)}\Psi_{ab}\theta_{ab}\,(\boldsymbol{L}(\boldsymbol{p}_b) - \boldsymbol{L}(\boldsymbol{p}_a))$

(repeat for node b)

(2.4)LOOP over boundary faces $\gamma(abc)$

$\hat{\boldsymbol{t}}_a^\gamma, \hat{\boldsymbol{t}}_b^\gamma, \hat{\boldsymbol{t}}_c^\gamma, \hat{\boldsymbol{v}}_a^\gamma, \hat{\boldsymbol{v}}_b^\gamma, \hat{\boldsymbol{v}}_c^\gamma$ according to B.C.

$\hat{\boldsymbol{\mathcal{R}}}_{p,a}^n := \hat{\boldsymbol{\mathcal{R}}}_{p,a}^n + \hat{\boldsymbol{t}}_a^\gamma \frac{A^\gamma}{3}$

$\boldsymbol{\mathcal{R}}_{F,a}^n := \boldsymbol{\mathcal{R}}_{F,a}^n + (\hat{\boldsymbol{v}}_a^\gamma \otimes \boldsymbol{N}^\gamma)\,\frac{A^\gamma}{3}$

(repeat for nodes b, c)

(2.5)COMPUTE $\boldsymbol{\lambda}_D$, $\boldsymbol{\mu}_D$ and modified dissipation

$\hat{\boldsymbol{\mathcal{D}}}(\boldsymbol{p}_a) = \boldsymbol{\mathcal{D}}(\boldsymbol{p}_a) + \boldsymbol{\lambda}_D \times \boldsymbol{x}_a^{n+1} - \boldsymbol{\mu}_D$

(2.6)UPDATE conservation variables at stage

$\boldsymbol{p}_a^* = \boldsymbol{p}_a^n + \frac{1}{V_a}\left(\hat{\boldsymbol{\mathcal{R}}}_{p,a}^n + \hat{\boldsymbol{\mathcal{D}}}(\boldsymbol{p}_a)\right)$

$\boldsymbol{F}_a^* = \boldsymbol{F}_a^n + \frac{1}{V_a}\boldsymbol{\mathcal{R}}_{F,a}^n$

(2.7)EVALUATE $\boldsymbol{P}_a^* = \boldsymbol{P}(\boldsymbol{F}_a^*)$ (only after stage 1)

(2.8)APPLY strong BC

(repeat for stage $**$)

(3) UPDATE conservation variables and positions

$\mathcal{U}_a^{n+1} = \frac{1}{2}\,(\mathcal{U}_a^n + \mathcal{U}_a^{**})$

$\boldsymbol{x}_a^{n+1} = \boldsymbol{x}_a^n + \frac{\Delta t}{2}(\boldsymbol{v}_a^n + \boldsymbol{v}_a^{n+1})$

(4) EVALUATE $\boldsymbol{P}_a^{n+1} = \boldsymbol{P}(\boldsymbol{F}_a^{n+1})$

(5) APPLY strong BC

Chapter 7

Stability and accuracy analysis

7.1 Preliminaries

This section is devoted to an analytical analysis of the convergence of the numerical scheme (spatial discretisation together with the temporal integration). To do so, a very important theorem in numerical analysis will be used. This is the *Lax equivalence theorem* [99], which states that for a well-posed problem, a consistent scheme is convergent if and only if it is stable (see [39,52,87,100,101] for a detailed discussion in the topic).

A drawback of this type of analysis, is that they are limited to simple, linear cases. Still, they are widely used since they can provide a good insight into the behaviour of the numerical algorithm [39]. The one dimension linear advection equation will be used for this purpose. This is written as

$$\frac{\partial \mathcal{U}}{\partial t} + a\frac{\partial \mathcal{U}}{\partial x} = 0, \tag{7.1}$$

where $\mathcal{U}$ is the (scalar) problem variable and a is the wave speed, which will be assumed to be positive. This equation will be discretised using central differences and JST artificial dissipation in space, as presented in chapter 5, and the two stages TVD Runge-Kutta time integrator in time, as presented in chapter 6.

Nevertheless, this type of convergence study entails the use of smooth linear solutions. Therefore, the second order differences of the JST artificial dissipation (5.24) will not be needed, and equation (7.1) will be discretised using only central differences and fourth order dissipation. Considering only the discretisation in space for a one dimensional regular mesh (and using the same notation as in section 5.5), this reads

$$\left(\frac{\partial \mathcal{U}}{\partial t}\right)_i = -a\frac{\mathcal{U}_{i+1} - \mathcal{U}_{i-1}}{2h} - \frac{1}{h}a\kappa^{(4)}(\mathcal{U}_{i+2} - 4\mathcal{U}_{i+1} + 6\mathcal{U}_i - 4\mathcal{U}_{i-1} + \mathcal{U}_{i-2}). \tag{7.2}$$

The results obtained using the artificial dissipation will be compared to those obtained using only the central differences term, written as

$$\left(\frac{\partial \mathcal{U}}{\partial t}\right)_i = -a\frac{\mathcal{U}_{i+1} - \mathcal{U}_{i-1}}{2h}. \tag{7.3}$$

The chapter will be organised as follows. In section 7.2, the consistency of the numerical algorithms will be proved through the truncation error. In section 7.3, the stability will be analysed by means of an eigenvalue analysis and Fourier decomposition of the spatial and temporal discretisations. It will be proved, as required by the Lax equivalence theorem, that the JST algorithm is both consistent (it maintains the second order of the central differences) and stable (the artificial dissipation stabilises the unstable central differences stencil).

7.2 Consistency

In order to prove consistency of the numerical method, the *truncation error* will be used, which is defined as the numerical error introduced by the method to the exact solution after one time step (see [39, 52, 100]). This is normally written as

$$\tau^n = \frac{1}{\Delta t}(\mathcal{N}(\tilde{\mathcal{U}}^n) - \tilde{\mathcal{U}}^{n+1}) \tag{7.4}$$

where $\tilde{\mathcal{U}}$ denotes the exact solution of the partial differential equation (7.1) and $\mathcal{N}$ is the numerical operator that advances the solution from time step n to time step $n+1$ (gathering spatial and temporal discretisations). A spatial discretisation is said to be consistent with the differential equations and boundary conditions if (see [100])

$$\tau^n \to 0 \quad \text{as} \quad h \to 0 \text{ and } \Delta t \to 0. \tag{7.5}$$

Typically, the truncation error can be written as $\tau^n = \mathcal{O}(h^p, \Delta t^q)$, which ensures the consistency of the method. Furthermore, if this is satisfied, the discretisation is said to be of order p in space and q in time. In our case, we want to ensure that the method is second order both in space and in time, that is $p = q = 2$.

7.2.1 Central differences

In order to obtain the truncation error, each term of the stencil of $\mathcal{N}(\tilde{\mathcal{U}}^n)$ will be expanded using Taylor series around $\tilde{\mathcal{U}}_i^n$. Due to the fact that two stages of the Runge-Kutta time integrator are involved, this will be carried out stage by stage. By using the central differences spatial discretisation (7.3), the first stage of the Runge-Kutta time integrator can be written as

$$\tilde{\mathcal{U}}_i^* = \tilde{\mathcal{U}}_i^n - \Delta t a\frac{\tilde{\mathcal{U}}_{i+1}^n - \tilde{\mathcal{U}}_{i-1}^n}{2h}. \tag{7.6}$$

expanding each of the terms around $\tilde{\mathcal{U}}_i^n$ and substituting,

$$\tilde{U}_i^* = \tilde{U}_i^n - \Delta t a \left(\frac{\partial \tilde{U}}{\partial x}\right)_i^n - \frac{\Delta t h^2}{6} a \left(\frac{\partial^3 \tilde{U}}{\partial x^3}\right)_i^n + \mathcal{O}(h^4). \tag{7.7}$$

The second stage has an identical structure to the first stage,

$$\tilde{U}_i^{**} = \tilde{U}_i^* - \Delta t a \frac{\tilde{U}_{i+1}^* - \tilde{U}_{i-1}^*}{2h}, \tag{7.8}$$

and, therefore, using equation (7.7) it can be rewritten as

$$\tilde{U}_i^{**} = \tilde{U}_i^* - \Delta t a \left(\frac{\partial \tilde{U}}{\partial x}\right)_i^* - \frac{\Delta t h^2}{6} a \left(\frac{\partial^3 \tilde{U}}{\partial x^3}\right)_i^* + \mathcal{O}(h^4). \tag{7.9}$$

The terms $\left(\frac{\partial \tilde{U}}{\partial x}\right)_i^*$ and $\left(\frac{\partial^3 \tilde{U}}{\partial x^3}\right)_i^*$ can be obtained deriving from equation (7.7). Substituting into (7.9) gives

$$\begin{aligned}\tilde{U}_i^{**} = \tilde{U}_i^n &- 2\Delta t a \left(\frac{\partial \tilde{U}}{\partial x}\right)_i^n - 2\frac{\Delta t h^2}{6} a \left(\frac{\partial^3 \tilde{U}}{\partial x^3}\right)_i^n + (\Delta t a)^2 \left(\frac{\partial^2 \tilde{U}}{\partial x^2}\right)_i^n \\ &+ 2\frac{(\Delta t a h)^2}{6} \left(\frac{\partial^4 \tilde{U}}{\partial x^4}\right)_i^n + \mathcal{O}(h^4),\end{aligned} \tag{7.10}$$

which yields

$$\begin{aligned}\mathcal{N}(\tilde{U}_i^n) = \tilde{U}_i^n &- \Delta t a \left(\frac{\partial \tilde{U}}{\partial x}\right)_i^n - \frac{\Delta t h^2}{6} a \left(\frac{\partial^3 \tilde{U}}{\partial x^3}\right)_i^n + \frac{(\Delta t a)^2}{2} \left(\frac{\partial^2 \tilde{U}}{\partial x^2}\right)_i^n \\ &+ \frac{(\Delta t a h)^2}{6} \left(\frac{\partial^4 \tilde{U}}{\partial x^4}\right)_i^n + \mathcal{O}(h^4).\end{aligned} \tag{7.11}$$

Substituting the above result in equation (7.4) and expanding $\tilde{U}_i^{n+1}$ around $\tilde{U}_i^n$, the truncation error can be obtained as

$$\begin{aligned}\tau^n = &-a \left(\frac{\partial \tilde{U}}{\partial x}\right)_i^n - \frac{h^2}{6} a \left(\frac{\partial^3 \tilde{U}}{\partial x^3}\right)_i^n + \frac{\Delta t a^2}{2} \left(\frac{\partial^2 \tilde{U}}{\partial x^2}\right)_i^n \\ &- \left(\frac{\partial \tilde{U}}{\partial t}\right)_i^n - \frac{\Delta t}{2} \left(\frac{\partial^2 \tilde{U}}{\partial t^2}\right)_i^n - \frac{\Delta t^2}{6} \left(\frac{\partial^3 \tilde{U}}{\partial t^3}\right)_i^n + \mathcal{O}(h^3, \Delta t^3)\end{aligned} \tag{7.12}$$

and since $\tilde{U}$ satisfies the exact solution, the following holds

$$\left(\frac{\partial^2\tilde{u}}{\partial t^2}\right)_i^n - a^2\left(\frac{\partial^2\tilde{u}}{\partial x^2}\right)_i^n = 0. \tag{7.13}$$

Substituting into (7.12) gives

$$\tau^n = -\frac{h^2}{6}a\left(\frac{\partial^3\tilde{u}}{\partial x^3}\right)_i^n - \frac{\Delta t^2}{6}\left(\frac{\partial^3\tilde{u}}{\partial t^3}\right)_i^n + \mathcal{O}(h^3, \Delta t^3) \tag{7.14}$$

and therefore,

$$\tau^n = \mathcal{O}(h^2, \Delta t^2). \tag{7.15}$$

Which proves, as expected, that the method is second order in space and time.

7.2.2 Central differences and fourth order dissipation

Proceeding in an identical fashion as before, the truncation error for the central differences scheme with added fourth order differences will be obtained. Using Taylor series expansion, the first stage of the Runge-Kutta integrator can be written as

$$\begin{aligned}\tilde{u}_i^* &= \tilde{u}_i^n - \Delta t a\frac{\tilde{u}_{i+1}^n - \tilde{u}_{i-1}^n}{2h} - \frac{\Delta t}{h}a\kappa^{(4)}(\tilde{u}_{i+2}^n - 4\tilde{u}_{i+1}^n + 6\tilde{u}_i^n - 4\tilde{u}_{i-1}^n + \tilde{u}_{i-2}^n)\\ &= \tilde{u}_i^n - \Delta t a\left(\frac{\partial\tilde{u}}{\partial x}\right)_i^n - \frac{\Delta t h^2}{6}a\left(\frac{\partial^3\tilde{u}}{\partial x^3}\right)_i^n - \Delta t h^3 a\kappa^{(4)}\left(\frac{\partial^4\tilde{u}}{\partial x^4}\right)_i^n + \mathcal{O}(h^4)\end{aligned} \tag{7.16}$$

and using this result for the second stage, the following is obtained

$$\begin{aligned}\tilde{u}_i^{**} &= \tilde{u}_i^* - \Delta t a\left(\frac{\partial\tilde{u}}{\partial x}\right)_i^* - \frac{\Delta t h^2}{6}a\left(\frac{\partial^3\tilde{u}}{\partial x^3}\right)_i^* - \Delta t h^3 a\kappa^{(4)}\left(\frac{\partial^4\tilde{u}}{\partial x^4}\right)_i^* + \mathcal{O}(h^4)\\ &= \tilde{u}_i^n - 2\Delta t a\left(\frac{\partial\tilde{u}}{\partial x}\right)_i^n + (\Delta t a)^2\left(\frac{\partial^2\tilde{u}}{\partial x^2}\right)_i^n - \frac{2\Delta t h^2}{6}a\left(\frac{\partial^3\tilde{u}}{\partial x^3}\right)_i^n\\ &\quad - 2\Delta t h^3 a\kappa^{(4)}\left(\frac{\partial^4\tilde{u}}{\partial x^4}\right)_i^n + \frac{2(\Delta t h a)^2}{6}\left(\frac{\partial^4\tilde{u}}{\partial x^4}\right)_i^n + \mathcal{O}(\Delta t^2 h^3),\end{aligned} \tag{7.17}$$

which renders the numerical operator $\mathcal{N}$ as

$$\begin{aligned}\mathcal{N}(\tilde{u}_i^n) &= \tilde{u}_i^n - \Delta t a\left(\frac{\partial\tilde{u}}{\partial x}\right)_i^n + \frac{(\Delta t a)^2}{2}\left(\frac{\partial^2\tilde{u}}{\partial x^2}\right)_i^n - \frac{\Delta t h^2}{6}a\left(\frac{\partial^3\tilde{u}}{\partial x^3}\right)_i^n\\ &\quad - \Delta t h^3 a\kappa^{(4)}\left(\frac{\partial^4\tilde{u}}{\partial x^4}\right)_i^n + \frac{(\Delta t h a)^2}{6}\left(\frac{\partial^4\tilde{u}}{\partial x^4}\right)_i^n + \mathcal{O}(\Delta t^2 h^3).\end{aligned} \tag{7.18}$$

Finally, using this result together with equation (7.13) and replacing into (7.4) gives the truncation error as

$$\tau^n = -\frac{h^2}{6}a\left(\frac{\partial^3\tilde{U}}{\partial x^3}\right)_i^n - \frac{\Delta t^2}{6}\left(\frac{\partial^3\tilde{U}}{\partial t^3}\right)_i^n + \mathcal{O}(h^3, \Delta t^3) \tag{7.19}$$

and therefore,

$$\tau^n = \mathcal{O}(h^2, \Delta t^2) \tag{7.20}$$

which concludes that the artificial dissipation preserves the second order of the central differences scheme.

7.3 Stability analysis

In order to study the stability of the numerical schemes, an eigenvalue analysis obtained through a Fourier decomposition will be used. This will allow the study in a simple manner, firstly of the stability properties of the spatial discretisation alone and, next, the stability of the spatial and temporal discretisations together. As a result, the stability limits of the numerical scheme will be obtained, which will be used for optimising the time step in the numerical simulations.

7.3.1 Stability of the space semidiscretisation

A spatial discretisation as (7.2) or (7.3) can be rewritten in matrix form as (see [39, 52])

$$\frac{\partial \boldsymbol{U}}{\partial t} = \boldsymbol{S}\boldsymbol{U} + \boldsymbol{Q}, \tag{7.21}$$

where $\boldsymbol{U}$ is a vector gathering all the nodal values[1] written as

$$\boldsymbol{U} = (U_1, U_2, \ldots, U_N), \tag{7.22}$$

$\boldsymbol{S}$ is a $N \times N$ matrix representing the spatial discretisation and $\boldsymbol{Q}$ a vector containing the boundary contributions. In general, $\boldsymbol{Q}$ and $\boldsymbol{S}$ will depend on the boundary conditions, making the eigenvalue analysis somewhat troublesome. If periodic boundary conditions are used, the term $\boldsymbol{Q}$ vanishes and the matrix $\boldsymbol{S}$ can be written, for a central differences scheme (7.3) as

[1] It should not be confused with the conserved variable in equation (4.2)

$$\mathcal{S} = \frac{a}{2h}\begin{pmatrix} 0 & -1 & & & & & 1 \\ 1 & 0 & -1 & & & & \\ & \ddots & \ddots & \ddots & & & \\ & & 1 & 0 & -1 & & \\ & & & \ddots & \ddots & \ddots & \\ & & & & 1 & 0 & -1 \\ -1 & & & & & 1 & 0 \end{pmatrix} \tag{7.23}$$

and for the central differences and artificial dissipation (7.2) as

$$\mathcal{S} = \frac{a}{2h}\begin{pmatrix} -12\kappa^{(4)} & -1+8\kappa^{(4)} & -2\kappa^{(4)} & & & & -2\kappa^{(4)} & 1+8\kappa^{(4)} \\ & & \ddots & & & & & \\ & -2\kappa^{(4)} & 1+8\kappa^{(4)} & -12\kappa^{(4)} & -1+8\kappa^{(4)} & -2\kappa^{(4)} & & \\ & & & & \ddots & & & \\ -1+8\kappa^{(4)} & -2\kappa^{(4)} & & & -2\kappa^{(4)} & 1+8\kappa^{(4)} & -12\kappa^{(4)} & \end{pmatrix} \tag{7.24}$$

The matrix $\mathcal{S}$ can be analysed using its eigenvalues Ω_j and associated eigenvectors $\mathcal{V}^j$ obtained from

$$\begin{aligned} &\det(\mathcal{S} - \Omega_j \boldsymbol{I}) = 0, \quad \forall j = 1, \ldots, N \\ &\mathcal{S}\mathcal{V}^j = \Omega_j \mathcal{V}^j, \quad \mathcal{V}^j = (\mathcal{V}_1^j, \mathcal{V}_2^j, \ldots, \mathcal{V}_N^j)^T. \end{aligned} \tag{7.25}$$

Since the matrix $\mathcal{S}$ is of rank N, the vectors $\mathcal{V}^j$ form a complete set of basis vectors in the space of the mesh-point functions. Therefore, the exact solution vector of the space discretisation[2], denoted as $\bar{\mathcal{U}}$, can be expressed as a linear combination of them in the following manner

$$\bar{\mathcal{U}}(t, x) = \sum_{j=1}^{N} \mathcal{W}_j(t)\mathcal{V}^j(x) \tag{7.26}$$

which is a modal decomposition of $\bar{\mathcal{U}}$ and where $\mathcal{W}_j$ are time-dependent components yet to be determined. Substituting equation (7.26) into (7.21) gives

$$\sum_{j=1}^{N} \frac{d\mathcal{W}_j}{dt}\mathcal{V}^j(x) = \sum_{j=1}^{N} \Omega_j \mathcal{W}_j \mathcal{V}^j, \tag{7.27}$$

which results in what is known as the *modal equation*

$$\frac{d\mathcal{W}_j}{dt} = \Omega_j \mathcal{W}_j. \tag{7.28}$$

[2]This is the solution satisfying exactly the discrete system of equations which should not be confused with the analytical solution, $\tilde{\mathcal{U}}$, of the partial differential equation.

Equation (7.28) has the following exact solution

$$\mathcal{W}_j(t) = \mathcal{W}_j^0 e^{\Omega_j t} \tag{7.29}$$

where $\mathcal{W}_j^0$ are the initial conditions, which will not be needed for the stability analysis. In order to ensure that the system (7.21) is stable, its exact solution (7.26) has to remain bounded, which in turn implies that all the components have also to remain bounded. Therefore, the exponential term cannot grow indefinitely. This can only be achieved through the following requirement

$$\mathrm{Re}(\Omega_j) \leq 0, \quad \forall j = 1, \ldots, n. \tag{7.30}$$

Once the temporal components $\bar{\mathcal{W}}_j(t)$ have been found, the eigenvectors are now needed. Given the fact that periodic boundary conditions are used, the solution at a specific time instant can be decomposed using Fourier series. Consequently, the Fourier modes make up a valid set of eigenvectors of the spatial discretisation, this is

$$\mathcal{V}_i^j = e^{Ik_j x_i} = e^{Ii\phi_j}, \tag{7.31}$$

where $I = \sqrt{-1}$, k_j is the wave number given by

$$k_j = \frac{j\pi}{Nh}, \quad j = 0, \ldots, N, \tag{7.32}$$

and ϕ_j is the phase angle defined as

$$\phi_j = k_j h, \quad j = 0, \ldots, N, \tag{7.33}$$

which ranges from $-\pi$ to π [3]. It can be seen that there are as many wave numbers as mesh points, since the maximum number of wavelengths representable in a given mesh is limited to the number of nodes. The eigenvalues can be now obtained using the Fourier modes and the characteristic equation (7.25)

$$\mathcal{S}_{ij} e^{Ik_j x_i} = \Omega(\phi_j) e^{Ik_j x_i}, \tag{7.34}$$

where $\Omega(\phi_j)$ is the eigenvalue, also known as the *Fourier symbol*, of the space discretisation matrix $\boldsymbol{\mathcal{S}}$. Applying equation (7.34) to the central differences scheme gives

$$\mathcal{S}_{ij} e^{Ii\phi_j} = -\frac{a}{2h}\left[e^{I(i+1)\phi_j} - e^{I(i-1)\phi_j}\right] = -\frac{a}{2h}\left[e^{I\phi_j} - e^{-I\phi_j}\right] e^{Ii\phi_j} \tag{7.35}$$

[3] In order to use the Fourier decomposition, the domain needs to be mirrored from a domain $(0, L)$ to a new domain $(-L, L)$. This allows having a periodic function of length $2L$, which can now be decomposed by Fourier series (see [52] or standard mathematics textbooks as [102])

and therefore the Fourier symbol is given by

$$\Omega(\phi_j) = -\frac{a}{2h}\left[e^{I\phi_j} - e^{-I\phi_j}\right], \tag{7.36}$$

which has the following real and imaginary parts[4]

$$\mathrm{Re}(\Omega(\phi_j)) = -\frac{a}{2h}\left[\cos(\phi_j) - \cos(\phi_j)\right] = 0, \tag{7.37}$$

$$\mathrm{Im}(\Omega(\phi_j)) = -\frac{a}{h}\sin(\phi_j). \tag{7.38}$$

Consequently, the central differences satisfy the stability condition for the space discretisation (7.30) [5]. The Fourier symbol for the central differences scheme with artificial dissipation can be found in an identical manner. Table 7.1 summarises the real and imaginary parts of Fourier symbol for both schemes. It can be seen that the central differences scheme with artificial dissipation is stable if $\kappa^{(4)} \geq 0$.

Method	$\mathrm{Re}(\Omega(\phi_j))$	$\mathrm{Im}(\Omega(\phi_j))$
CD	0	$-\frac{a}{h}sin(\phi_j)$
CD + AD	$-\frac{a}{h}[2\kappa^{(4)}cos(2\phi_j) - 8\kappa^{(4)}cos(\phi_j) + 6\kappa^{(4)}]$	$-\frac{a}{h}sin(\phi_j)$

Table 7.1: Fourier Symbols for the central differences (CD) and central differences plus artificial dissipation (CD+AD) spatial discretisations

7.3.2 Stability of the combined space and time discretisations

Once the space discretisation has been analysed, the stability of the time discretisation can now be studied. To do so, the time discretisation will be analysed using a general eigenvalue of the space discretisation. Therefore, the modal equation (7.28) can be used which, once dropped the subindexes for the sake of clarity, is rewritten as

$$\frac{d\mathcal{W}}{dt} = \Omega\mathcal{W}. \tag{7.39}$$

This equation can be discretised in time, from time step n to time step $n+1$, using a general time integrator defined by an operator $\mathcal{P}$ written as

[4] $e^{kI} = cos(k) + Isin(k)$, $e^{-kI} = cos(k) - Isin(k)$, $k \in \mathbb{N}$, $k > 0$

[5] The central differences scheme, as such, satisfies the stability requirements of the spatial discretisation. Depending on the temporal discretisation chosen it becomes unstable, as it is the case for the Forward Euler scheme or the Runge-Kutta scheme as it will be shown later in the section. Alternatively, a stable algorithm would be provided combining the central differences with the Leap-frog time integrator [52].

$$\mathcal{W}^{n+1} = \mathcal{P}(\Omega\Delta t)\mathcal{W}^n, \tag{7.40}$$

which is actually the *numerical amplification factor.* In order for the numerical solution to remain bounded, the following condition should be fulfilled

$$|\mathcal{P}(\Omega\Delta t)| \leq 1 \qquad \forall\Omega. \tag{7.41}$$

Equation (7.39) can be discretised using the Forward Euler scheme as

$$\begin{aligned} \mathcal{W}^{n+1} &= \mathcal{W}^n + \Omega\Delta t\mathcal{W}^n \\ &= (1 + \Omega\Delta t)\mathcal{W}^n \end{aligned} \tag{7.42}$$

and therefore, $\mathcal{P} = (1 + \Omega\Delta t)$. An identical proceeding can be performed for the Runge-Kutta scheme. Table 7.2 summarises the amplification factor for these two schemes.

Method	z_P
Forward Euler	$1 + \Omega\Delta t$
Two stages TVD RK	$1 + \Omega\Delta t + \frac{1}{2}(\Omega\Delta t)^2$

Table 7.2: Amplification factor for the Forward Euler and two stages TVD Runge-Kutta time integration methods

Given the eigenvalues of the spatial discretisation, Ω_j, and the amplification factor of the temporal discretisation $\mathcal{P}$, it is now possible to check the compatibility between the spatial and temporal discretisations. This analysis is more clearly done graphically using a representation in the complex $\Omega\Delta t$ space (see [52, 103, 104]). This is shown in Figures 7.1, 7.2 and 7.3. The real component of $\Omega\Delta t$ is represented in the horizontal axis, while the imaginary component in the vertical axis. The thin blue lines correspond to the different eigenvalues of the spatial discretisation (corresponding to all the modes $\phi_j \in [-\pi, \pi]$). The thick red lines represent the set of eigenvalues Ω_j in the stability limit of the numerical scheme (continuous line correspond to the Forward Euler method and discontinuous line to the two stages TVD Runge-Kutta method). A given space discretisation (for a given α_{CFL} or numerical diffusion factor) will be stable if, first, all the eigenvalues lie on the left hand side of the vertical axis ($\text{Re}(\Omega\Delta t) \leq 0$) and, second, if these eigenvalues lie inside the stability limit given by the numerical amplification factor (i.e., the thin blue line has to be contained inside the thick red line). Figure 7.1 shows that, as expected, the Central Differences scheme is unstable if combined with any of the presented time integrators. In Figure 7.2, the central differences scheme with added dissipation is studied for increasing values of the α_{CFL} parameter and for

$\kappa^{(4)} = 1/16$. Figure 7.3 shows the opposite procedure: given a value for α_{CFL} (0.5), the eigenvalues are plotted for different $\kappa^{(4)}$ values. It is shown that all eigenvalues have a negative real component. Furthermore, this spatial discretisation is unstable if combined with the Forward Euler time integration (the lines intersect even for small values of α_{CFL} or $\kappa^{(4)}$). If, instead, the TVD Runge-Kutta scheme is used, the stability will be conditioned by a combination of $\kappa^{(4)}$ and α_{CFL}. This relation has been computed and plotted in Figure 7.4, which illustrates that, given the α_{CFL} number, a minimum and maximum ammount of dissipation is required in order to ensure the stability. According to these results, the optimum value of $\kappa^{(4)}$ is $\kappa^{(4)} = 1/16$, which allows the largest α_{CFL} and, therefore, the largest time step.

In order to verify the results above, a numerical test has been carried out. Results are shown in Figure 7.5. The linear advection equation (7.1) with $a = 1$ is discretised using central differences and the artificial dissipation term (fourth order differences) and the TVD Runge-Kutta time integrator in time. An initial profile formed by a smooth pulse and a rectangular pulse (see discontinuous red line behind any of the plots) is advected one cycle using 6 different dissipation factors, $\kappa^{(4)}$, for $\alpha_{CFL} = 0.5$. It can be seen that, in accordance to the results in Figure 7.5, the solution is unstable for dissipation factors larger than $\kappa^{(4)} = 1/8$. For $\kappa^{(4)} = 1/64$, large wiggles appear near the discontinuity and it can be expected that they would grow and, eventually, provoke instabilities, if the dissipation factor were further reduced.

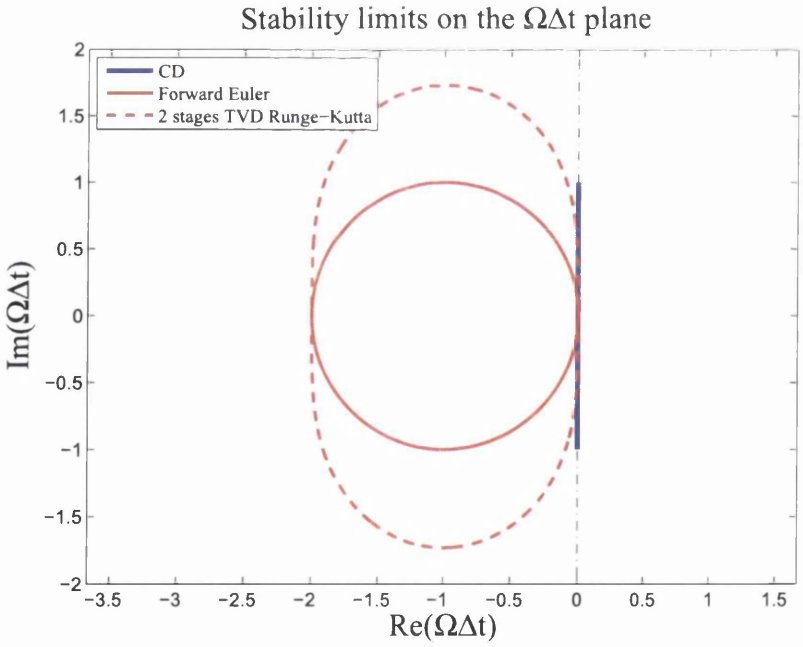

Figure 7.1: Stability limits of the Central differences combined either with the Forward Euler Method or the two stages TVD Runge-Kutta method, $\alpha_{CFL} = 1$

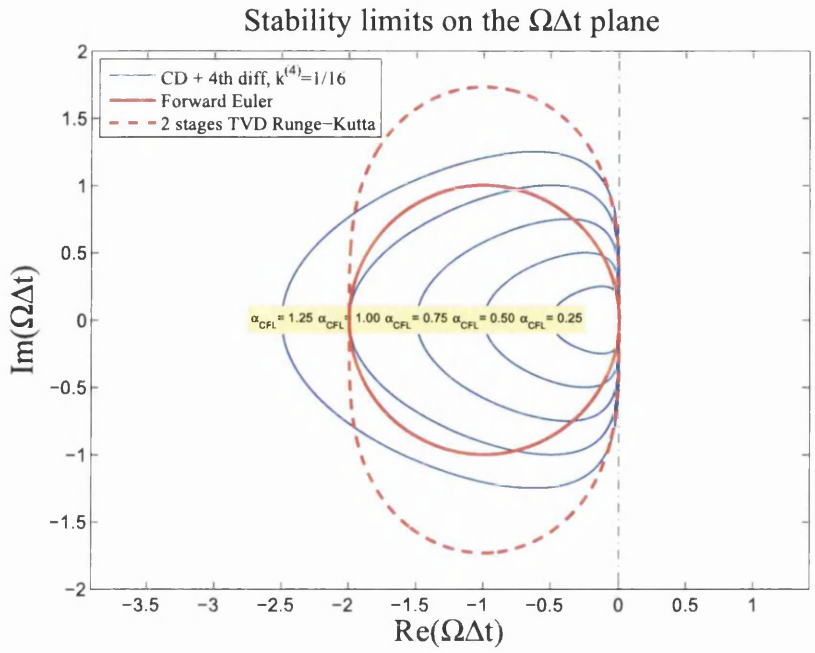

Figure 7.2: Stability limits of the Central differences and fourth order artificial dissipation, as compared to the Forward Euler Method and the two stages TVD Runge-Kutta method, for different values of α_{CFL}, $k^{(4)} = 1/16$

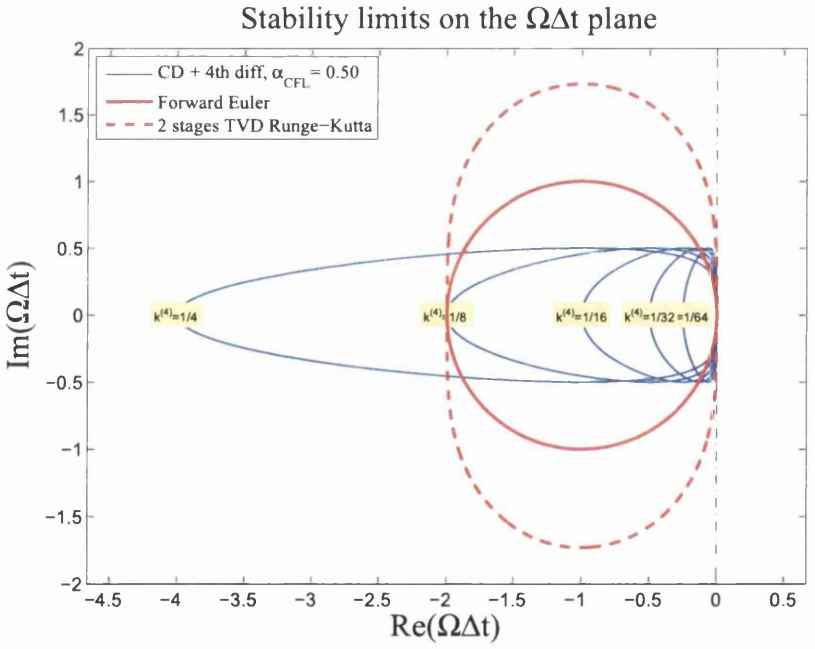

Figure 7.3: Stability limits of the Central differences and fourth order artificial dissipation, as compared to the Forward Euler Method and the two stages TVD Runge-Kutta method, for different values of $k^{(4)}$, $\alpha_{CFL} = 0.5$

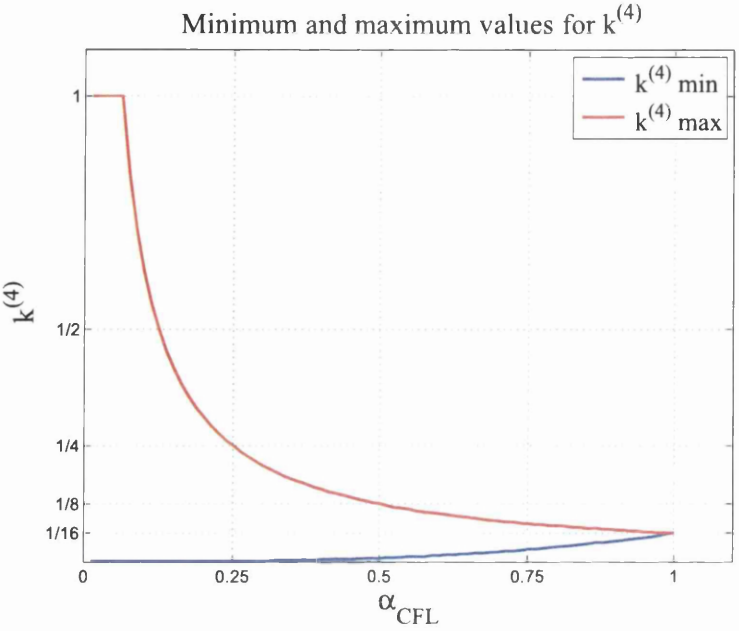

Figure 7.4: Maximum and minimum $k^{(4)}$ per α_{CFL} that ensure the stability of the central differences with fourth order artificial dissipation with the two stages TVD Runge-Kutta time integrator

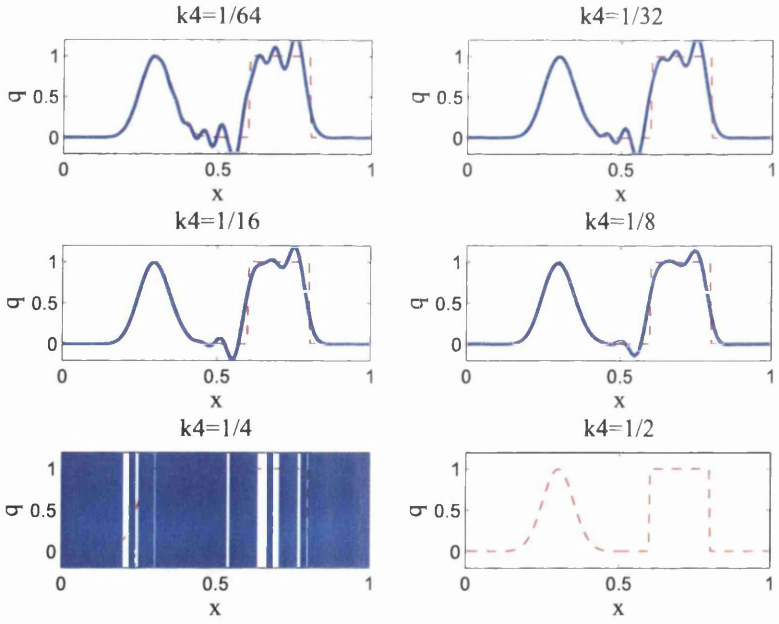

Figure 7.5: Linear advection of a smooth and rectangular pulses. Discretisation using central differences and fourth order artificial dissipation. Comparison of results as the $\kappa^{(4)}$ factor is increased, $\alpha_{CFL} = 0.50$

Chapter 8

Numerical examples

8.1 Preliminaries

In the previous sections, the problem formulation and space and time discretisations have been presented. In this section, this discretisation will be used in order to implement a series of examples. Different problems have been chosen in one, two and three dimensions (presented in sections 8.2, 8.3 and 8.4 respectively) in order to prove the convergence, robustness and conservation properties of the algorithm.

8.2 One dimensional problems

8.2.1 1D convergence analysis

This example is designed to test the accuracy of the method in one dimensional problems. A linear elastic one dimensional cable is subjected to an initial smooth velocity profile. The linear elasticity and small deformations assumption enable an analytical solution to be obtained, which will be used for computing the error in the numerical approximation. The cable has a length $L = 10$ m and its composed of a linear elastic material with density $\rho_0 = 1$ kg/m^3, Young's modulus $E = 1$ Pa and $\nu = 0$. The initial velocity profile is given by

$$v_1(X_1, t = 0) = \frac{k}{2}\left(1 - \sin\left(\frac{2\pi}{10}X_1 + \frac{\pi}{2}\right)\right),$$

where the parameter k is chosen to be $k = 1 \cdot 10^{-3}$ (see Figure 8.1). Assuming small deformations, the solution can be obtained by means of Fourier series and is given by,

$$u_1(X_1,t) == \frac{4kL}{c_p\pi^2}\sum_{n=1}^{\infty}\frac{\cos(n\pi)-1}{n^3-4n}\sin\left(\frac{n\pi}{L}X_1\right)\sin(\lambda_n t)$$

$$v_1(X_1,t) = \frac{4kL}{c_p\pi^2}\sum_{n=1}^{\infty}\frac{\lambda_n(\cos(n\pi)-1)}{n^3-4n}\sin\left(\frac{n\pi}{L}X_1\right)\cos(\lambda_n t)$$

$$F_{11}(X_1,t) = 1+\frac{4kL}{c_p\pi^2}\sum_{n=1}^{\infty}\frac{\pi(\cos(n\pi)-1)}{n^2L-4nL}\cos\left(\frac{n\pi}{L}X_1\right)\sin(\lambda_n t)$$

where $\lambda_n = \frac{c_p n\pi}{L}$ and c_p is the pressure wave speed defined in section 4.5. Since the solution is smooth, the JST scheme is used only with the fourth order dissipation term, with $\kappa^{(4)} = 1/16$. The error convergence analysis is shown in Figures 8.2 and 8.3 for the stress and linear momentum respectively. The error is measured in the L^1 and L^2 norms for different mesh sizes. It can be seen that the solution tends to second order convergence both for the linear momentum and stress and in both L^1 and L^2 norms.

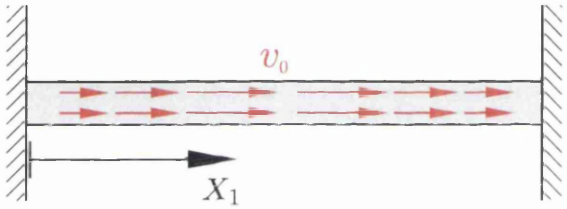

Figure 8.1: 1D cable convergence analysis, initial configuration

8.2.2 1D cable shock

This example is designed to prove the shock capturing capabilities of the method. The configuration consists of a one dimensional cable, of length $L = 10$ m and material properties $E = 2\times10^{11}$ Pa, $\rho_0 = 8\times10^3$ kg/m^3 and $\nu = 0$ (see Figure 8.4). The cable is clamped at the left end and free at the right end. At time $t = 0$, a step function force, $P_0 = -5\times10^7$ Pa is applied at the free end of the cable and left constant from this instant on (see Figure 8.5). This triggers the propagation of a linear momentum and stress square waves along the cable.

For comparison purposes, the problem has been simulated using the averaged fluxes and fourth order differences (with $\kappa^{(4)} = 1/16$), averaged fluxes and second order differences (with $\kappa^{(2)} = 1/4$) and the full JST scheme (with $\kappa^{(2)} = 1/4$ and $\kappa^{(4)} = 1/16$). Figure 8.6 shows these waves at time $t = 1\times10^{-3}$ seconds. The solutions using fourth order difference (blue line), second order differences (green line) and the complete JST scheme with shock capturing (black line) are compared against the analytical solution (red discontinuous line). It can be seen that numeric

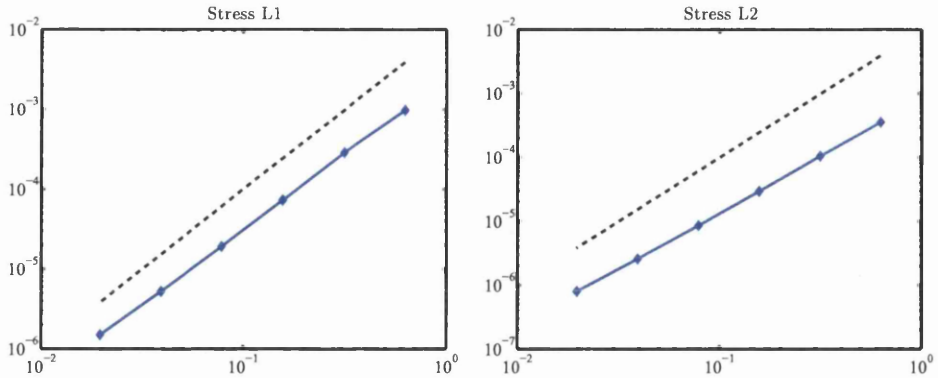

(a) (b)

Figure 8.2: Linear elasticity one dimensional case. Convergence error for the stress component P_{11} in L^1 and L^2 norms at time $t = 15$ s as compared to the analytical solution. Linear elastic material with Poisson's ratio $\nu = 0$, Young's modulus $E = 1$ Pa and density $\rho_0 = 1$ kg/m^3. JST spatial discretisation using fourth order differences, with $\kappa^{(4)} = 1/16$ and $\alpha_{CFL} = 0.5$.

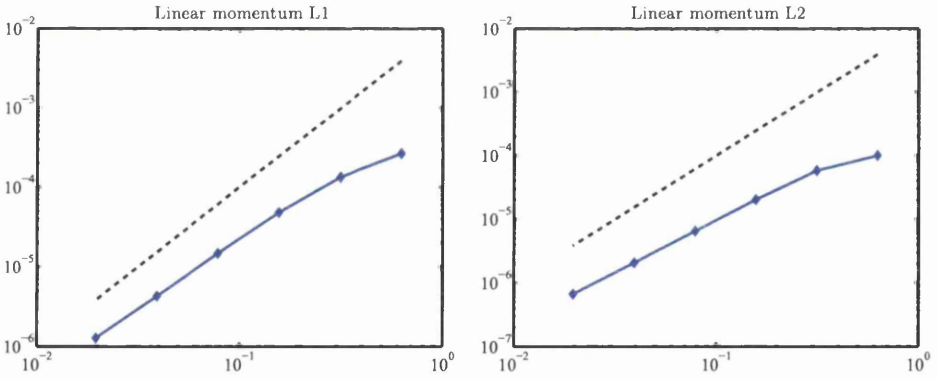

(a) (b)

Figure 8.3: Linear elasticity one dimensional case. Convergence error for the linear momentum component p_1 in L^1 and L^2 norms at time $t = 15$ s as compared to the analytical solution. Linear elastic material with Poisson's ratio $\nu = 0$, Young's modulus $E = 1$ Pa and density $\rho_0 = 1$ kg/m^3. JST spatial discretisation using fourth order differences, with $\kappa^{(4)} = 1/16$ and $\alpha_{CFL} = 0.5$.

oscillations appear behind the shock when only the fourth order differences used. If the second order differences are used, these oscillations disappear at the expense of a significant increase of the diffusion. Finally, if the full JST scheme is used, the shock is well captured with absence of numerical oscillations.

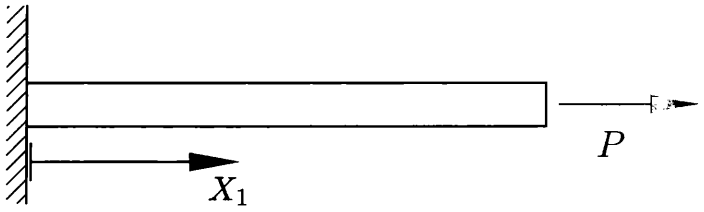

Figure 8.4: 1D cable shock, initial configuration.

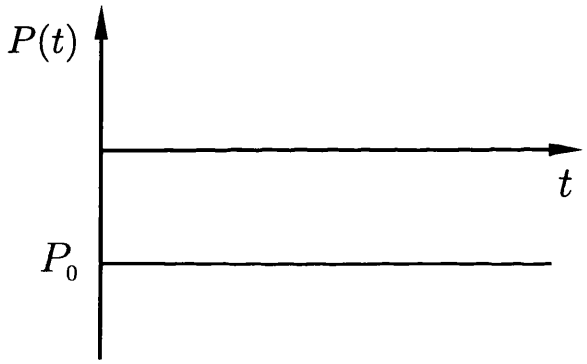

Figure 8.5: 1D cable shock, step forcing function.

8.3 Two dimensional problems

8.3.1 Swinging plate

This example is designed to prove the error convergence of the method in the two dimensional case and it was previously presented in [1]. A linear elastic square plate of unit side length is subjected to an initial deformation in the elastic small strains regime. The plate is subjected to symmetric boundary conditions (restricted normal displacement) at its south and west sides and skew symmetric boundary conditions (restricted tangent displacement) at its north and east sides (see Figure 8.7). In the small strain case, the combination of this set of boundary conditions and specific initial condition gives an analytical solution of the type

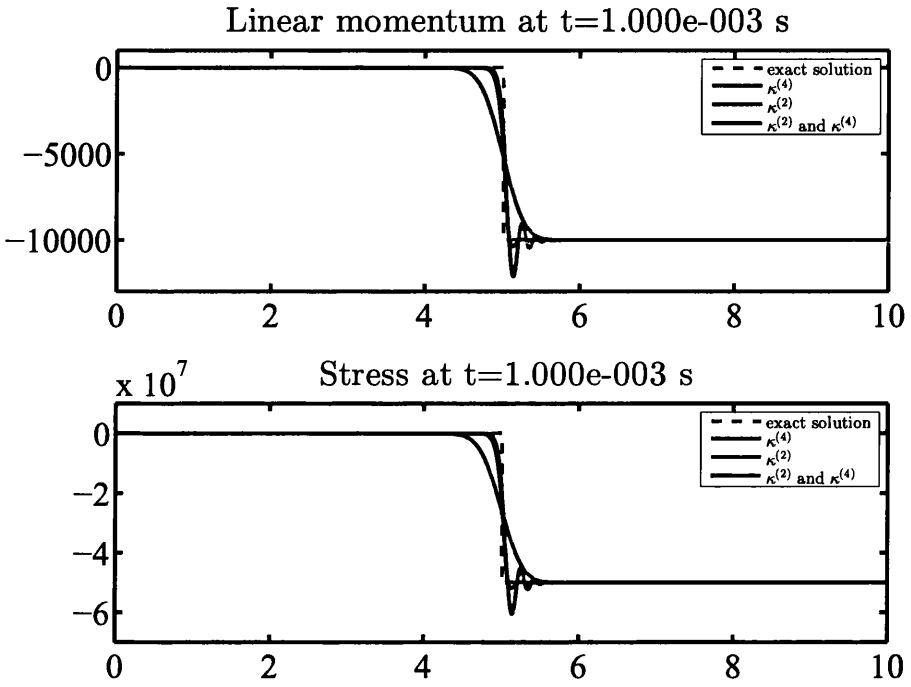

Figure 8.6: One dimensional rod of length $L = 10$ m and material properties $E = 200$ GPa, $\rho_0 = 8 \times 10^3$ kg/m^3 and $\nu = 0$. The rod is clamped at the left end and free at the right end with a step function force $P_0 = 5 \times 10^7$ Pa applied from time $t = 0$. The analytical solution (red discontinuous line) is compared against the numerical solution using average fluxes and fourth order differences (blue line), average fluxes and second order differences (green line) and the full JST scheme with shock capturing (black line).

$$\boldsymbol{u} = U_0 \cos\left(\frac{\sqrt{2}}{2} c_d \pi t\right) \begin{bmatrix} \sin\left(\frac{\pi X_1}{2}\right) \cos\left(\frac{\pi X_2}{2}\right) \\ -\cos\left(\frac{\pi X_1}{2}\right) \sin\left(\frac{\pi X_2}{2}\right) \end{bmatrix}, \quad c_d = \sqrt{\frac{\mu}{\rho_0}}$$

where U_0 is a user defined parameter that determines the amplitude of the oscillation. If U_0 is smaller than $1 \cdot 10^{-3}$, the solution is assumed to be in the linear elastic regime. In this case, it will be chosen as $U_0 = 5 \times 10^{-4}$. The material parameters are Young's modulus $E = 1.7 \times 10^7$ Pa, density $\rho_0 = 1.1 \times 10^3$ kg/m^3 and Poisson's ratio $\nu = 0.45$. A series of solutions are obtained at time $t = 0.02$ s for different mesh sizes and compared to the analytical solution using the L^1 and L^2 norms. The JST method is used only with the fourth order differences term, with $\kappa^{(4)} = 1/64$ and $\alpha_{CFL} = 0.4$. Figures 8.8 and 8.9 show the error convergence for the stress and linear momentum components in the L^1 and L^2 norms. As expected, the solution tends to quadratic convergence for both variables.

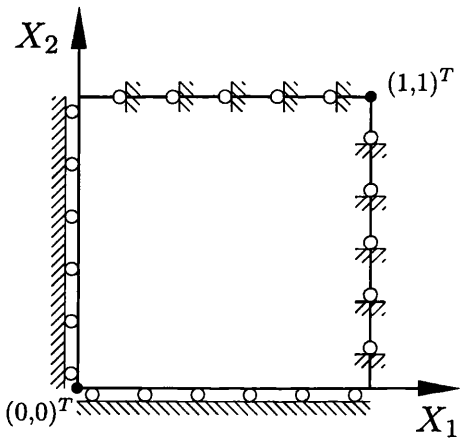

Figure 8.7: Swinging plate, initial setup.

8.3.2 Elastic vibration of a Beryllium plate

This example, designed to evaluate the accuracy of the method in the elastic regime, was previously published in [64, 105]. A Beryllium plate with no supports or constraints, of 6 cm length and 1 cm width, and material properties $\rho_0 = 1.845 \times 10^3$ kg/m^3, $E = 3.1827 \times 10^{11}$ Pa and $\nu = 0.05390$ has an initial velocity of the form (see Figure 8.10),

$$\begin{aligned} \boldsymbol{v}_0 &= (0, v(X_1))^T \text{ m/s} \\ v(X_1) &= A\omega[g_1 (\sinh(\Omega(X_1 + 0.03)) + \sin(\Omega(X_1 + 0.03))) - \\ &\quad g_2 (\cosh(\Omega(X_1 + 0.03)) + \cos(\Omega(X_1 + 0.03)))] \end{aligned}$$

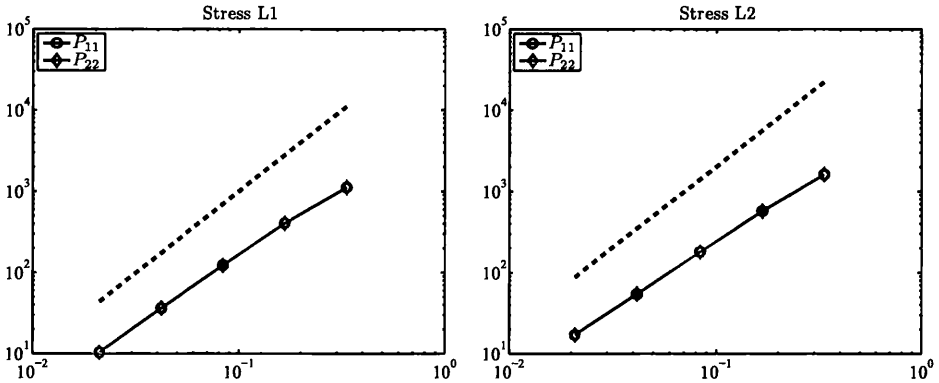

Figure 8.8: Linear elasticity two dimensional case. Convergence error for the stress components P_{11} and P_{22} in L^1 and L^2 norms at time $t = 0.02$ s as compared to the analytical solution. Solution using $U_0 = 5 \times 10^{-4}$ m. Linear elastic material with Poisson's ratio $\nu = 0.45$, Young's modulus $E = 1.7 \times 10^7$Pa and density $\rho_0 = 1.1 \times 10^3$kg/m^3. JST spatial discretisation with $\kappa^{(4)} = 1/64$ and $\alpha_{CFL} = 0.4$.

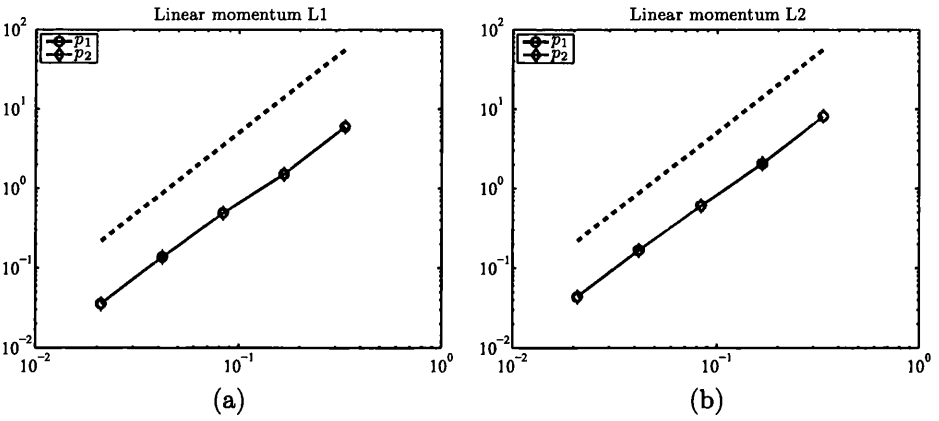

Figure 8.9: Linear elasticity two dimensional case. Convergence error for the linear momentum components p_1 and p_2 in L^1 and L^2 norms at time $t = 0.02$ s as compared to the analytical solution. Solution using $U_0 = 5 \times 10^{-4}$ m. Linear elastic material with Poisson's ratio $\nu = 0.45$, Young's modulus $E = 1.7 \times 10^7$Pa and density $\rho_0 = 1.1 \times 10^3$kg/m^3. JST spatial discretisation with $\kappa^{(4)} = 1/64$ and $\alpha_{CFL} = 0.4$.

where [64, 105]

$$g_1 = 56.637, \quad g_2 = 57.646, \quad \omega = 2.3597 \times 10^5 \text{ s}^{-1}, \quad A = 4.3369 \times 10^{-5} \text{ m}$$
$$\Omega = 78.834 \text{ m}^{-1}$$

which excites its first flexural mode [105]. Figure 8.11 shows the evolution in time of the norm of the velocity vector. Results compare very well with those provided in [64].

In Figure 8.12, the evolution in time of the internal and kinetic energies are compared against the total energy (solution of equation (4.1c) for three different mesh refinements). In the absence of plasticity and heat effects, the difference between the total energy (black discontinuous line) and the summation of the internal and kinetic energies (green line) is the actual dissipation introduced by the numerical scheme. In this particular case, it corresponds to the dissipation of the first flexural mode of the plate, since it is the one predominantly excited. It can be seen that, as the mesh is refined, the dissipation is clearly reduced. The results of the $2 \times (100 \times 25)$ triangular elements mesh compare well against the solution provided in [64]. Finally, Figure 8.13 shows the evolution in time of the vertical displacement and vertical velocity at $\boldsymbol{X} = (0, 0)^T$. It can be seen again the predominance of the first flexural mode, although as the mesh is refined higher modes emerge. Results compare well in terms of amplitude and frequency with the solution presented in [64].

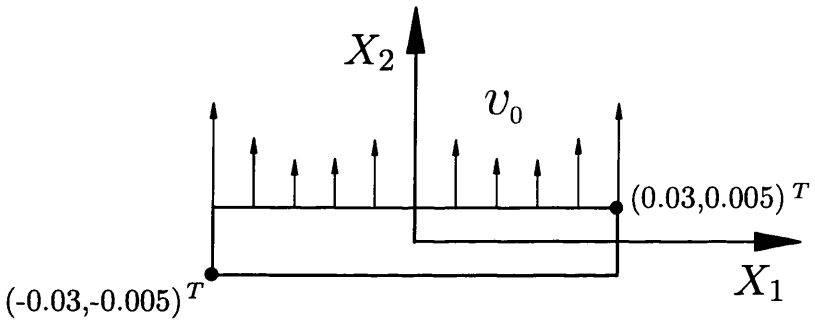

Figure 8.10: Beryllium plate initial configuration.

8.3.3 Spinning plate

This example was previously presented in [1] and is designed to prove the ability of the method to preserve linear and angular momentum in a two dimensional case. A squared rubber plate of side length 1 m is of constraints and has an initial angular momentum of $\boldsymbol{\omega}_0 = (0, 0, 105)^T$ rad/s imposed at its centre of gravity. The rubber is modelled using a neo-Hookean constitutive model with Young's modulus $E = 1.7 \times 10^7$ Pa, density $\rho_0 = 1.1 \times 10^3$ kg/m^3 and Poisson's ratio $\nu = 0.45$. The

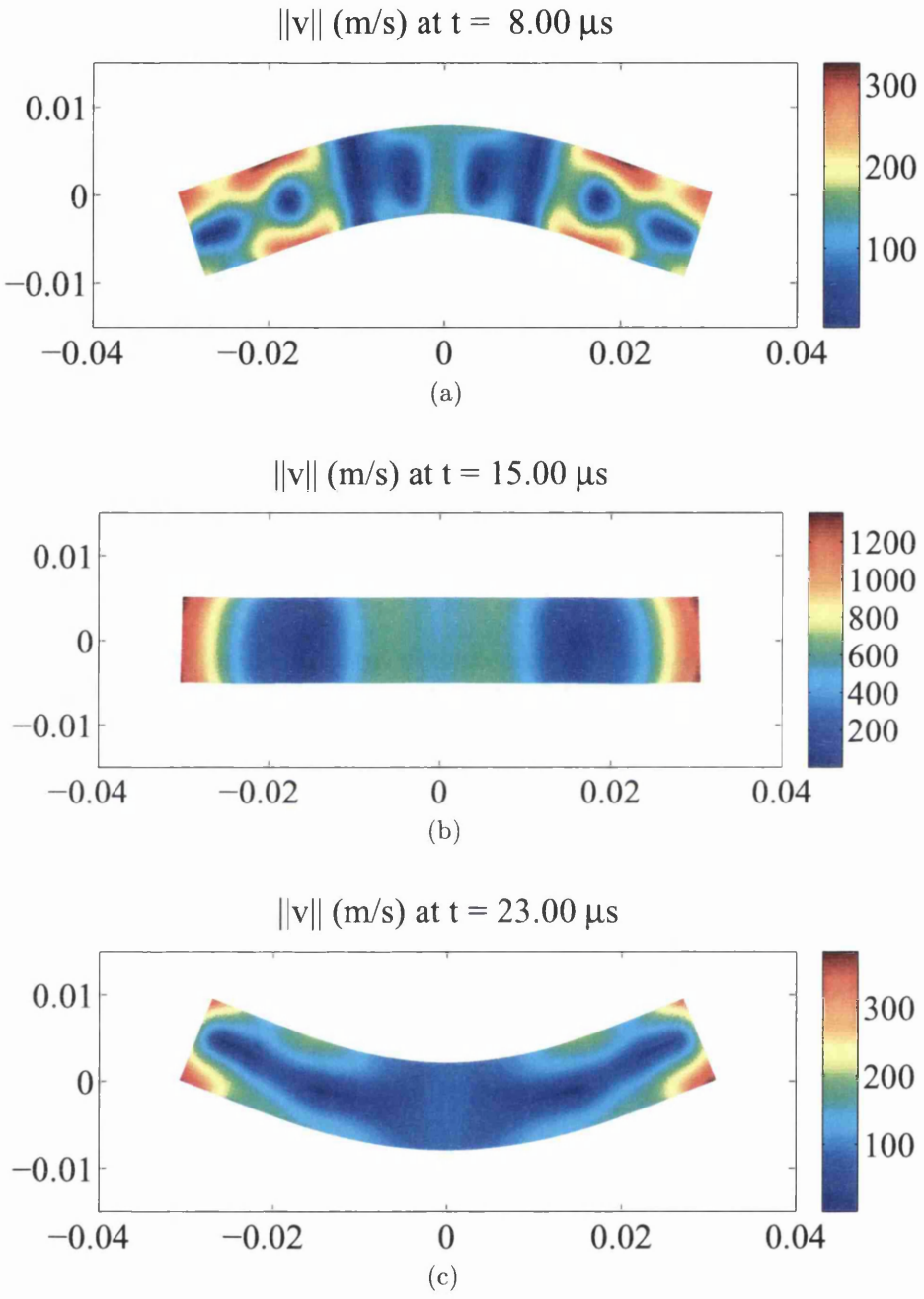

Figure 8.11: Beryllium plate. Material properties $\rho_0 = 1.845 \times 10^3$ kg/m^3, $E = 3.1827 \times 10^{11}$ Pa, $\nu = 0.05390$s, $Y^0 = 1 \times 10^{11}$ Pa. Evolution in time of the deformed shaped. The contour plot represents the norm of the velocity vector. Solution obtained using 2x(100x25) triangular elements and the JST method with $\kappa^{(4)} = 1/64$ and $\alpha_{CFL} = 0.4$.

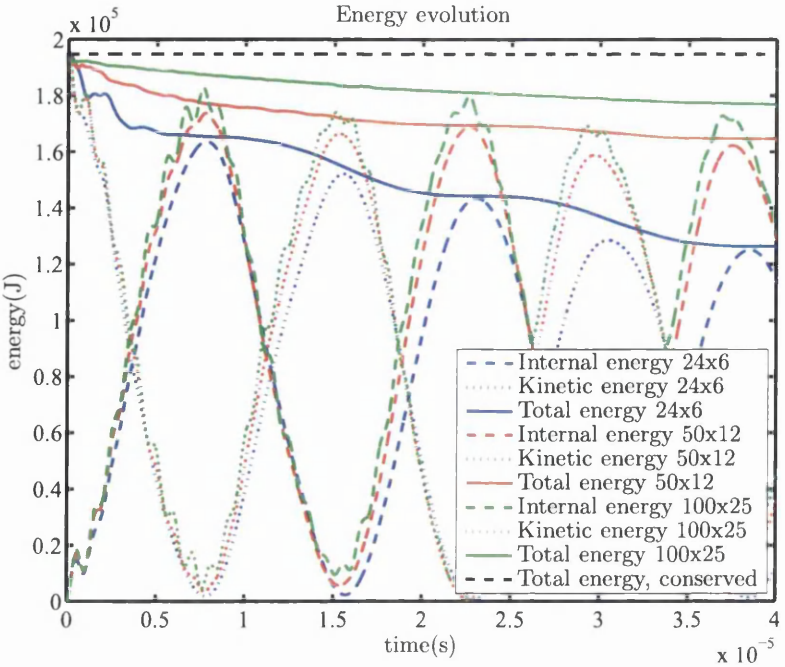

Figure 8.12: Beryllium plate. Material properties $\rho_0 = 1.845 \times 10^3$ kg/m^3, $E = 3.1827 \times 10^{11}$ Pa, $\nu = 0.05390$s, $Y^0 = 1 \times 10^{11}$ Pa. Evolution in time of the internal energy (blue lines), kinetic energy (red lines), summation of both (green lines) against the total conserved energy (black discontinuous line) for three different meshes of 2x(24x6), 2x(50x12) and 2x(100x25) triangular elements. JST method with $\kappa^{(4)} = 1/64$ and $\alpha_{CFL} = 0.4$. The difference between the total conserved energy and the summation of internal and kinetic energy is the numerical dissipation.

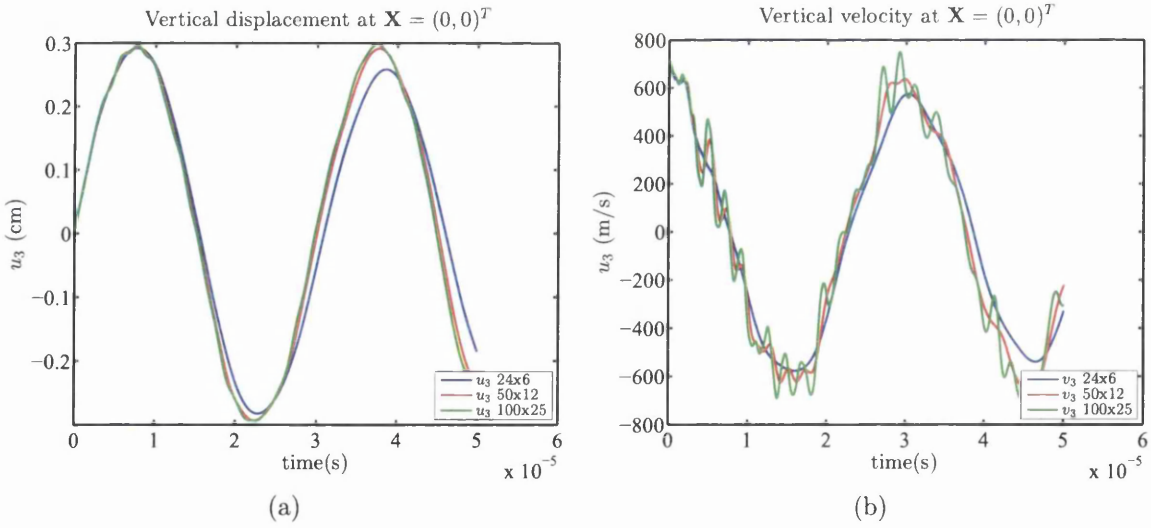

Figure 8.13: Beryllium plate. Material properties $\rho_0 = 1.845 \times 10^3$ kg/m^3, $E = 3.1827 \times 10^{11}$ Pa, $\nu = 0.05390$s, $Y^0 = 1 \times 10^{11}$ Pa. Evolution in time of the vertical displacement (a) and the vertical velocity (b) at $\boldsymbol{X} = (0,0)^T$ for three different meshes of 2x(24x6), 2x(50x12) and 2x(100x25) triangular elements (blue, red and green lines, respectively). JST method with $\kappa^{(4)} = 1/64$ and $\alpha_{CFL} = 0.4$.

problem is simulated using the fourth order differences dissipation with $\kappa^{(4)} = 1/64$, $\alpha_{CFL} = 0.4$ and an unstructured mesh of 121 nodes. Figure 8.15 shows the deformed configuration and pressure distribution for different time instants. In Figure 8.16 shows that, using the numerical corrections presented in section 6.3, the exact conservation of angular and linear momenta is fulfilled. It is also important to note that the corrections performed in the internal tractions are very small, as compared to the actual value of this tractions. This is proved in Figures 8.17 and 8.18. Figure 8.17 shows the distribution of the ratio between the norm of the modification of the edge forces against the norm of the actual edge forces, that is $\frac{||\hat{\boldsymbol{f}}_k - \boldsymbol{f}_k||}{||\boldsymbol{f}_k||}$. Figure 8.18 shows the time history of the L^2 norm of the edge forces, $\boldsymbol{f}_k$, and the modification of the edge forces $\hat{\boldsymbol{f}}_k - \boldsymbol{f}_k$.

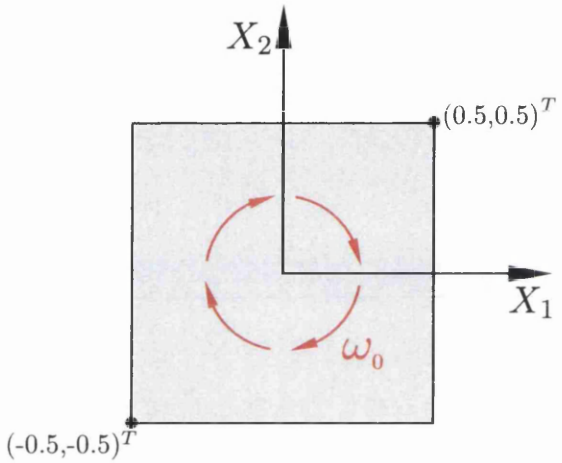

Figure 8.14: Spinning plate, initial configuration.

8.3.4 Bending column (2D)

A rubber-like column of 1 m width and 6 m height is clamped on its bottom end and subjected to an initial uniform horizontal velocity of $V_0 = 10$ m/s (see Figure 8.19). The example shows the performance of the numerical technique in bending dominated scenarios and it has been previously presented in [1, 2, 31]. The material is chosen as neo-Hookean with Young's modulus $E = 1.7 \times 10^7$ Pa, density $\rho_0 = 1.1 \times 10^3$ kg/m^3 and Poisson's ratio $\nu = 0.45$. Figure 8.20 shows the JST solution (column (c)) at different times as compared to the PG solution (column (b)) and the cell centred Finite Volume solution (column (a)). The same mesh of 8×48 quadrilateral elements ($\Delta x_{max} = 0.125$ m) was employed for comparison purposes. All three solutions exhibit very similar deformation patterns with smooth pressure distribution and absence of locking. Comparison of the resolution of the three solutions shows that the JST method offers the most dissipative solution, whereas the

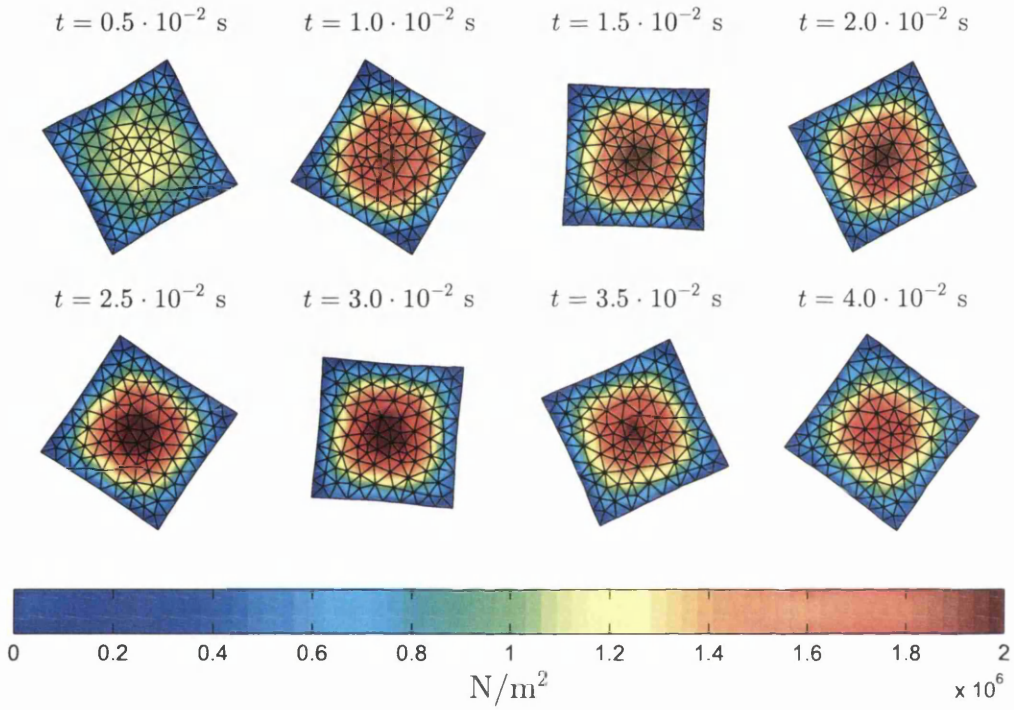

Figure 8.15: Spinning plate, distribution of pressure during the deformation process. Results obtained with initial horizontal angular momentum $\omega_0 = 105$rad/s. The nearly incompressible neo-Hookean constitutive model is used with Poisson's ratio $\nu = 0.45$, Young's modulus $E = 1.7 \times 10^7$Pa, density $\rho_0 = 1.1 \times 10^3$kg/m^3 and $\alpha_{CFL} = 0.4$. Discretisation using the JST method with an unstructured mesh of 121 nodes and $\kappa^{(4)} = 1/64$

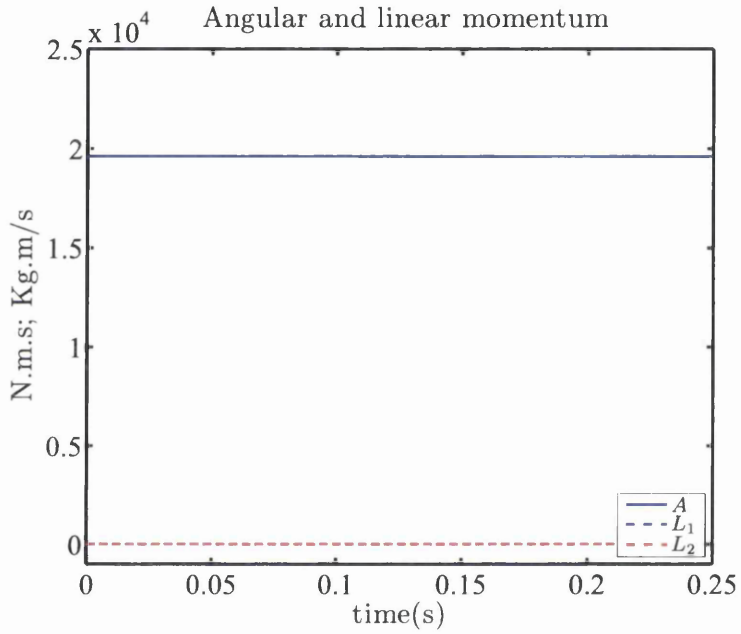

Figure 8.16: Spinning plate, conservation of the total linear momentum $\boldsymbol{L} = [L_1, L_2, L_3]^T$ and angular momentum $\boldsymbol{A} = [A_1, A_2, A_3]^T$. Results obtained with initial horizontal angular momentum $\omega_0 = 105\text{rad/s}$. The nearly incompressible neo-Hookean constitutive model is used with Poisson's ratio $\nu = 0.45$, Young's modulus $E = 1.7 \times 10^7$ Pa, density $\rho_0 = 1.1 \times 10^3$ kg/m^3 and $\alpha_{CFL} = 0.4$. Discretisation using the JST method with an unstructured mesh of 121 nodes and $\kappa^{(4)} = 1/64$.

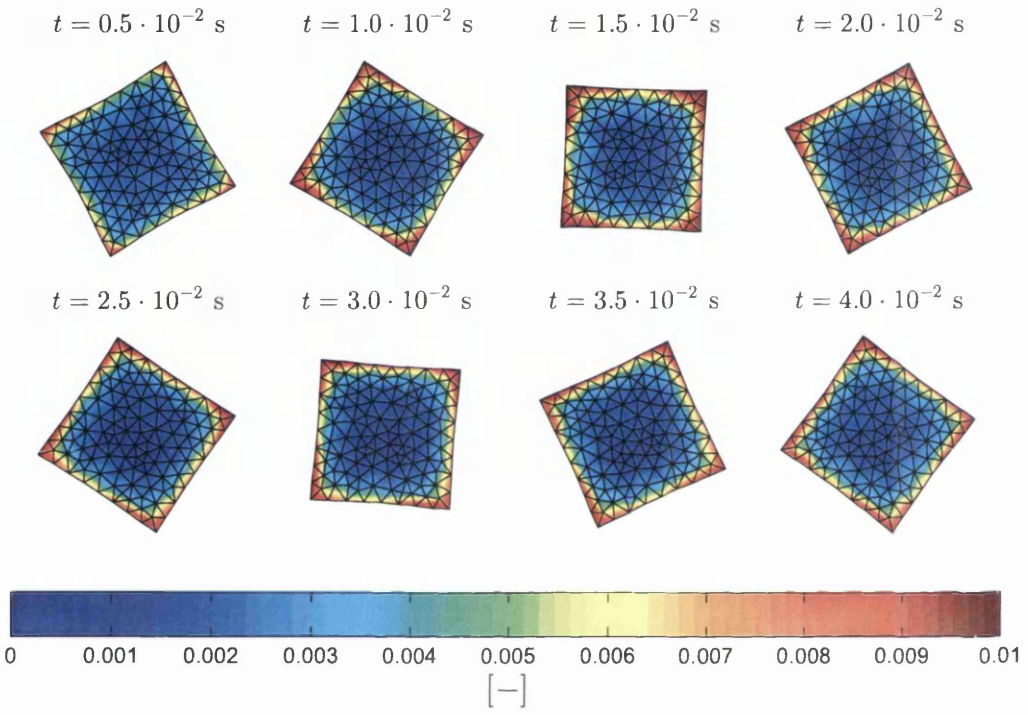

Figure 8.17: Spinning plate, distribution of the normalised norm of the vector resulting from the difference between the modified edge forces, and the original edge forces, $\frac{||(\boldsymbol{f}_k - \hat{\boldsymbol{f}}_k)||}{||\boldsymbol{f}_k||}$. The plot shows the average at the nodes from its surrounding edge values. Results obtained with initial horizontal angular momentum $\omega_0 = 105\text{rad/s}$. The nearly incompressible neo-Hookean constitutive model is used with Poisson's ratio $\nu = 0.45$, Young's modulus $E = 1.7 \times 10^7\text{Pa}$, density $\rho_0 = 1.1 \times 10^3\text{kg/m}^3$ and $\alpha_{CFL} = 0.4$. Discretisation using the JST method with an unstructured mesh of 121 nodes and $\kappa^{(4)} = 1/64$

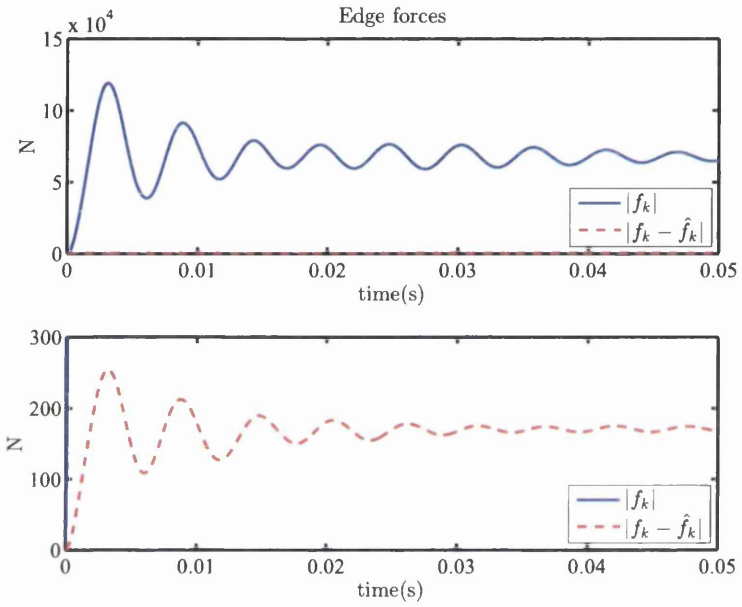

Figure 8.18: Spinning plate, evolution of the L^2 norm of the edge forces (blue) against the L^2 norm of the modification of the edge forces (red). The bottom plot shows a zoomed version of the above plot. Results obtained with initial horizontal angular momentum $\omega_0 = 105$rad/s. The nearly incompressible neo-Hookean constitutive model is used with Poisson's ratio $\nu = 0.45$, Young's modulus $E = 1.7 \times 10^7$ Pa, density $\rho_0 = 1.1 \times 10^3$ kg/m^3 and $\alpha_{CFL} = 0.4$. Discretisation using the JST method with an unstructured mesh of 121 nodes and $\kappa^{(4)} = 1/64$.

PG method provides the most accurate solution (but at a greater computational cost).

Figure 8.21 presents the results for the JST method using a more refined unstructured mesh with $\Delta x_{max} = 0.05$ m, which naturally leads to more accurate results.

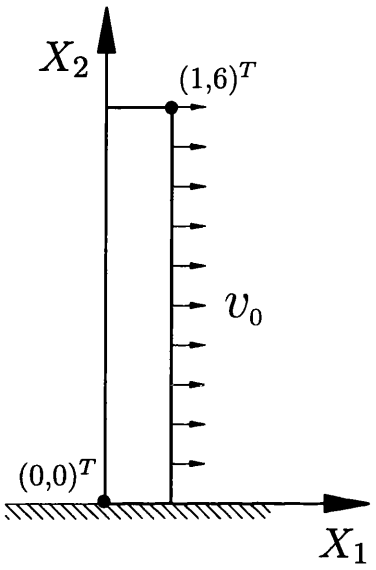

Figure 8.19: Bending column initial configuration

8.3.5 Collapse of a thick-walled cylindrical beryllium shell

This test problem was initially proposed by [68] and later implemented in [69,70,105] in order to assess the ability of a computational method to model plastic flows. A thick-walled cylindrical beryllium shell has an initial radial velocity directed towards its centre. Plane strain conditions are assumed for the shell. After a certain time, all the kinetic energy of the material should be transformed into plastic dissipation. The final interior and exterior radii of the shell are called stopping radii, and a closed form solution for both was provided in [68]. Following, the problem presented in [70] will be modelled.

The shell is centred at $\boldsymbol{X} = (0,0)^T$ m and has an initial interior radius $R_i = 80 \cdot 10^{-3}$ m and an outer radius $R_o = 100 \times 10^{-3}$ m. The material is modelled using a hyperelastic-plastic constitutive model (see algorithm 3.3.1) and a Mie-Grüneisen equation of state (see equation (3.47)). The material parameters are $\rho_0 = 1.845 \times 10^3$ kg/m^3, $\Gamma_0 = 2$, $c_0 = 12870$ m/s and $s = 1.124$. The elastic-plastic constitutive law is characterized by the shear modulus $\mu = 151.9 \times 10^9$ Pa, yield strength $Y^0 = 330 \times 10^6$ Pa and hardening modulus $H = 0$ Pa (perfectly plastic material). The initial velocity field is defined by

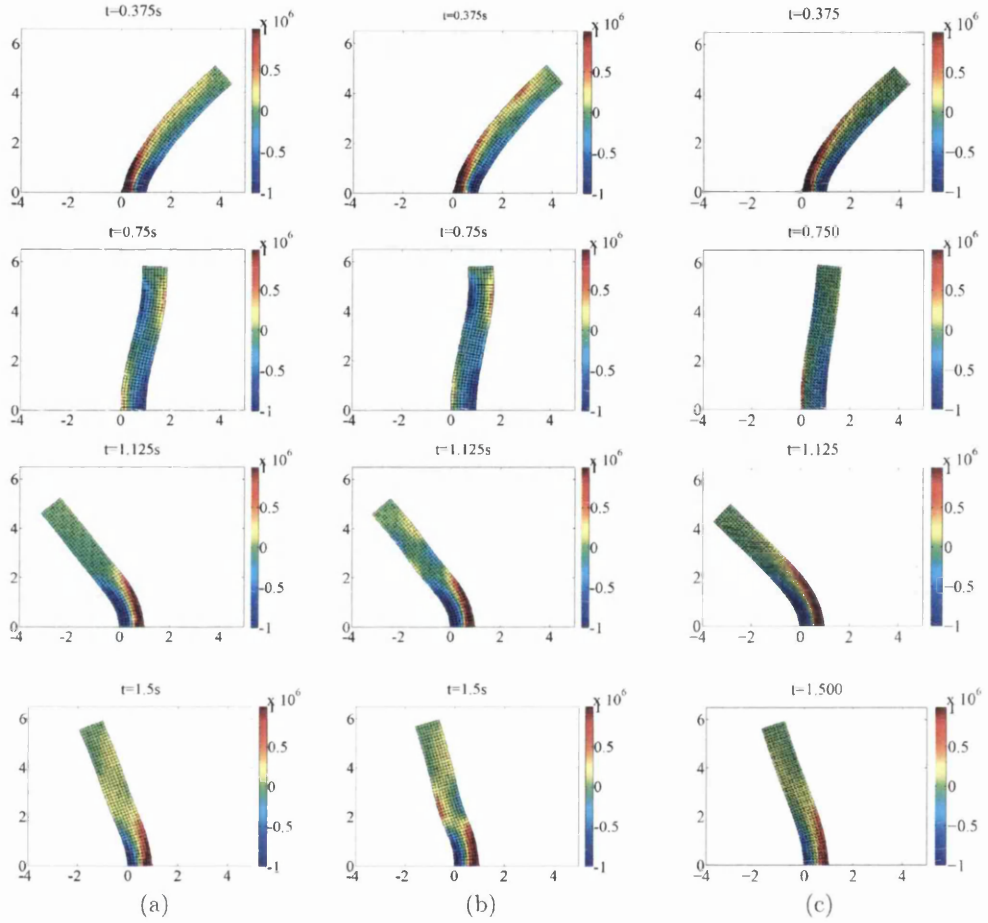

Figure 8.20: Bending column: Sequence of pressure distribution of deformed shapes using: column (a) CCFVM imposing piecewise linear reconstruction; column (b) PG (consistent mass, $\tau_{\boldsymbol{F}} = \Delta t, \tau_{\boldsymbol{p}} = 0, \alpha = 0.05$) and column (c) JST ($\kappa^{(4)} = 1/64$). Results obtained with initial horizontal velocity $V_0 = 10\text{m/s}$. The nearly incompressible neo-Hookean constitutive model is used with Poisson's ratio $\nu = 0.45$, Young's modulus $E = 1.7 \times 10^7\text{Pa}$, density $\rho_0 = 1.1 \times 10^3\text{kg/m}^3$ and $\alpha_{CFL} \approx 0.4$. Discretisation with 8×48 quadrilateral elements with $\Delta x_{max} = 0.125$ m. Time step $\Delta t = 1 \times 10^{-4}\text{s}$.

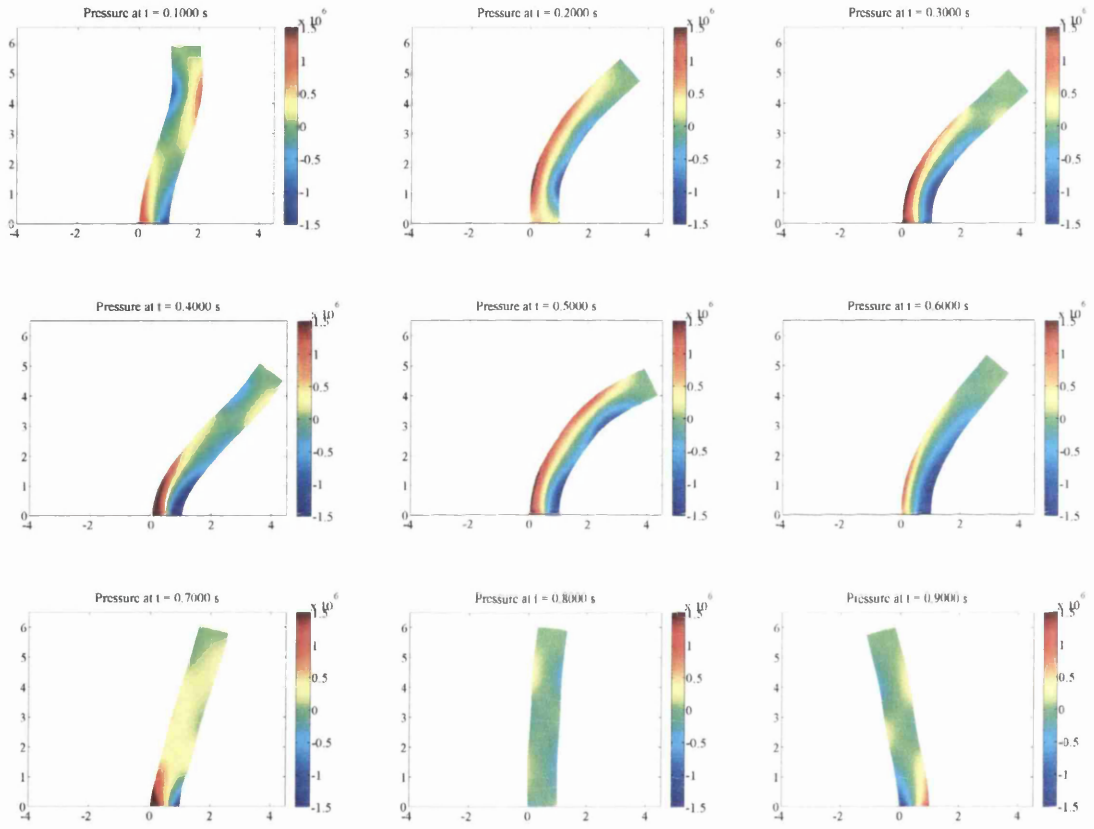

Figure 8.21: Bending column. Results obtained with initial horizontal velocity $V_0 = 10\text{m/s}$. The nearly incompressible neo-Hookean constitutive model is used with Poisson's ratio $\nu = 0.45$, Young's modulus $E = 1.7 \times 10^7\text{Pa}$, density $\rho_0 = 1.1 \times 10^3\text{kg/m}^3$ and $\alpha_{CFL} \approx 0.4$. Discretisation using the JST method with an unstructured mesh and $\kappa^{(4)} = 1/64$, $\Delta t = 2.5 \times 10^{-5}$, $\Delta x_{max} = 0.05$ m.

$$\boldsymbol{v}(\boldsymbol{X}, t_0) = -V_0 \frac{R_i}{\|X_1^2 + X_2^2\|^2} (X_1, X_2)^T \quad \text{m/s}$$

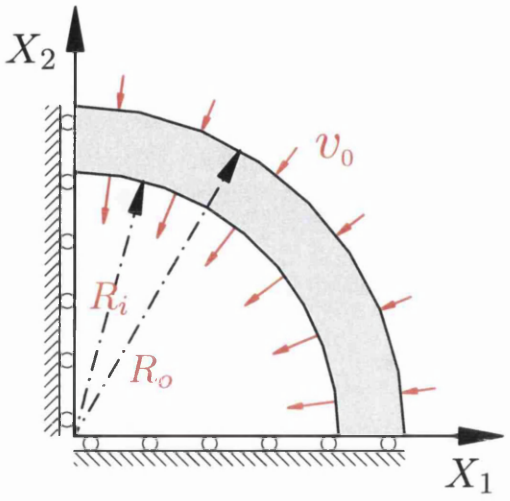

Figure 8.22: Beryllium shell initial configuration

and the exterior pressure is defined as $p = 1 \times 10^{-6}$ Pa. The shell is simulated using relevant boundary conditions. A mesh of $2 \times (20 \times 8)$ triangular elements is used, which has 720 degrees of freedom. The dissipation parameter is set to $\kappa^{(4)} = 1/1024$.

In [68], a closed form solution at the stopping time was obtained considering an incompressible material and that all the energy of the system is dissipated through plasticity. This yields a relationship between the initial velocity $\boldsymbol{v}_0$ and the inner and outer stopping radii. As in [68], the simulation has been performed for three different initial velocities $v_0 = 417.1$ m/s, $v_0 = 454.7$ m/s and $v_0 = 490.2$ m/s, and the analytical results, as presented in Table 8.1, are used for the benchmarking the problem.

Figure 8.23 shows the results for the three cases at the stopping time, where the plastic strain (left) and the initial and final meshes (right) are depicted. The final mesh is compared against the analytical solution. It confirms the axisymmetry of the three solutions. In Table 8.2, the inner and outer stopping radii are compared against the analytical solution. It transpires that there is a good match against the analytical solution, where the maximum error is 0.135 %. The table also shows the stopping time of the solutions. All results are in good agreement with those provided in [68], despite using a much coarser mesh in this thesis.

Next, the axisymmetry of the solutions is quantified as in [68]. Firstly, the mean radius of the 9 different circumferential rings of the mesh is computed as $\bar{R}^i, \quad i = \{1, ..9\}$. Next, the radius deviation is computed per node, comparing the nodal radius against the mean radius of its corresponding layer. This information is used as well for computing the standard deviation. Table 8.3 shows the obtained

v_0 (m/s)	Outer stopping radius (mm)	Inner stopping radius (mm)
417.1	50	78.10
454.7	45	75.00
490.2	40	72.12

Table 8.1: Analytical results for the Beryllium shell problem.

Stopping radius (mm)	Stopping time (ms)	Inner radius error (%)	Outer radius error (%)
50	125.6	+0.135	+0.022
45	131.6	+0.106	-0.012
40	136.2	+0.030	-0.072

Table 8.2: Numerical results for the Beryllium shell problem. Table shows the stopping time, and the error in the inner and outer radius for the three different solutions.

results. It can be seen how the algorithm is capable of preserving an excellent axisymmetry, giving maximum standard deviation of the order 10^{-9}.

Finally, in Figure 8.24, the evolution of the inner and outer radii is shown and compared against the analytical solution. This shows a good convergence of both three results as the shell reaches its stopping time.

8.4 Three dimensional problems

8.4.1 Swinging cube

This example is an extension of the two dimensional swinging plate presented in the previous section. A cube of 1 m side has symmetric boundary conditions (con-

Stopping radius (mm)	Standard deviation σ (%)	Minimum deviation (%)	Maximum deviation (%)
50	$6.74 \cdot 10^{-10}$	$-2.61 \cdot 10^{-11}$	$+2.98 \cdot 10^{-11}$
45	$9.84 \cdot 10^{-10}$	$-5.10 \cdot 10^{-11}$	$4.12 \cdot 10^{-11}$
40	$1.62 \cdot 10^{-9}$	$-9.00 \cdot 10^{-11}$	$+7.98 \cdot 10^{-11}$

Table 8.3: Numerical results for the Beryllium shell problem. The table shows the standard deviation of the radius for each of the layers of the mesh. The minimum and maximum deviation among all the nodes is as well presented.

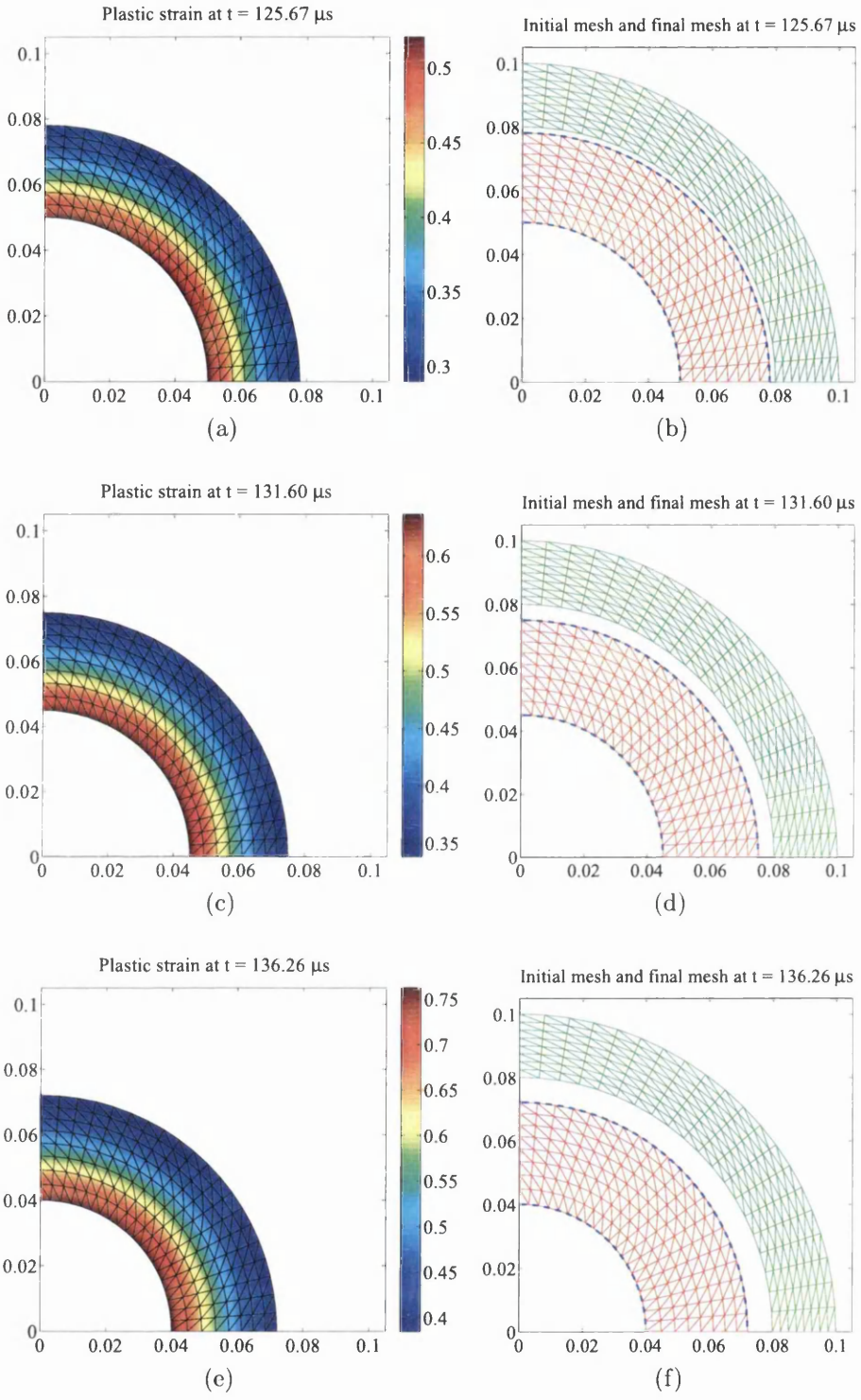

Figure 8.23: Beryllium shell problem. Hyperelastic-plastic constitutive model and Mie-Grüneisen equation of state. Material parameters: $\rho_0 = 1.845 \times 10^3$ kg/m^3, $\Gamma_0 = 2$, $c_0 = 12870$ m/s, $s = 1.124$, $\mu = 151.9 \times 10^9$ Pa, $Y^0 = 330 \times 10^6$ Pa, $H = 0$ Pa. Mesh of $2 \times (40 \times 32)$ triangular elements and 1353 degrees of freedom. Dissipation parameter $\kappa^{(4)} = 1/2048$. From top to bottom rows, results are shown for initial velocities $v_0 = 417.1$ m/s, $v_0 = 454.7$ m/s and $v_0 = 490.2$ m/s at their stopping time. Plastic strain is shown in the left column. Initial mesh (green) and final mesh (red) against the analytical solution (thick blue line) are shown in the right column.

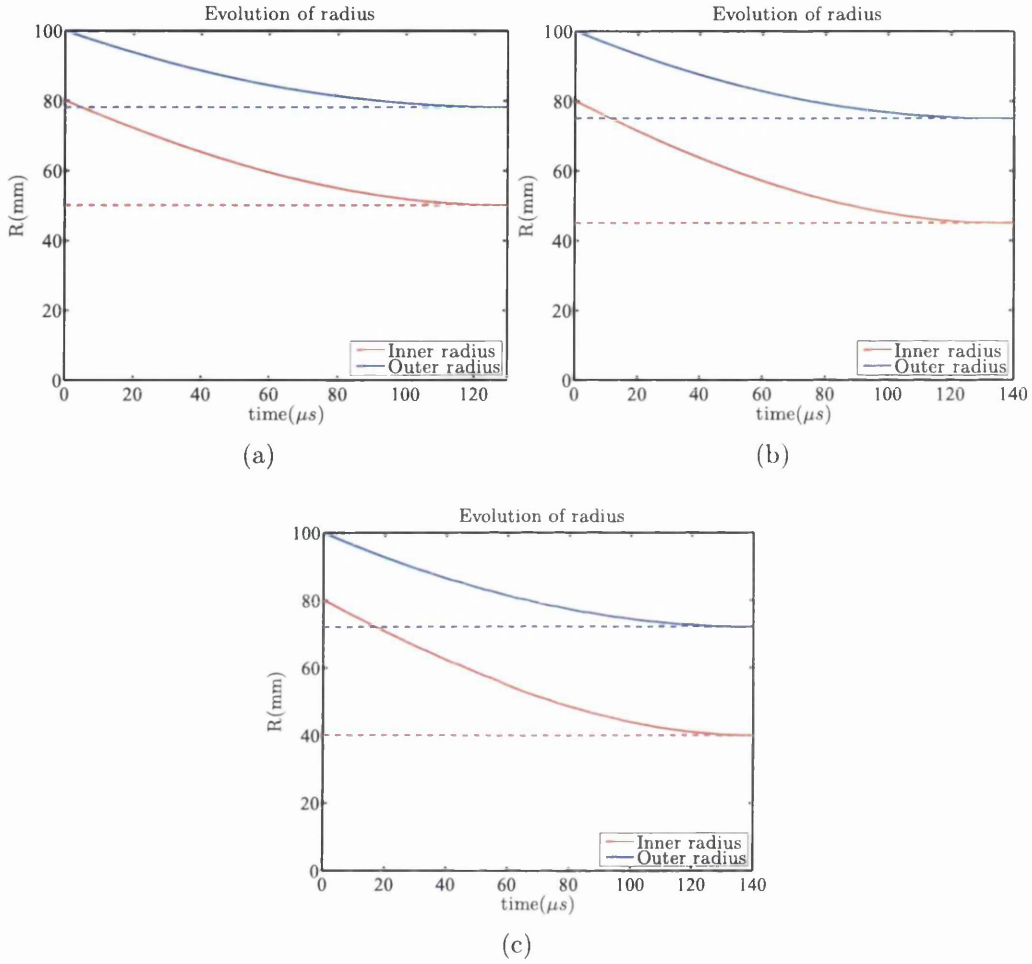

Figure 8.24: Beryllium shell problem. Hyperelastic-plastic constitutive model and Mie-Grüneisen equation of state. Material parameters: $\rho_0 = 1.845 \times 10^3$ kg/m^3, $\Gamma_0 = 2$, $c_0 = 12870$ m/s, $s = 1.124$, $\mu = 151.9 \times 10^9$ Pa, $Y^0 = 330 \times 10^6$ Pa, $H = 0$ Pa. Mesh of $2 \times (40 \times 32)$ triangular elements and 1353 degrees of freedom. Dissipation parameter $\kappa^{(4)} = 1/2048$. The evolution of the radius is shown for the three test cases: $v_0 = 417.1$ m/s (a), $v_0 = 454.7$ m/s (b) and $v_0 = 490.2$ m/s (c). The inner radius (continuous thick red line) and the outer radius (continuous thick blue line) are compared against the analytical solution (discontinuous lines).

strained normal displacement) at the faces $X_1 = 0$ m, $X_2 = 0$ m and $X_3 = 0$ m and skew-symmetric boundary conditions (constrained tangential displacement) at the opposite faces, $X_1 = 1$ m, $X_2 = 1$ m and $X_3 = 1$ m. For the small strain case, the problem has an analytical solution of the type

$$\boldsymbol{u} = U_0 \cos\left(\frac{\sqrt{3}}{2} c_d \pi t\right) \begin{bmatrix} A \sin\left(\frac{\pi X_1}{2}\right) \cos\left(\frac{\pi X_2}{2}\right) \cos\left(\frac{\pi X_3}{2}\right) \\ B \cos\left(\frac{\pi X_1}{2}\right) \sin\left(\frac{\pi X_2}{2}\right) \cos\left(\frac{\pi X_3}{2}\right) \\ C \cos\left(\frac{\pi X_1}{2}\right) \cos\left(\frac{\pi X_2}{2}\right) \sin\left(\frac{\pi X_3}{2}\right) \end{bmatrix}$$

where A, B and C are constants such that $A + B + C = 0$ [1] and $c_d = \sqrt{\frac{\mu}{\rho_0}}$. The problem is considered linear when $U_0 < 1 \times 10^{-3}$ m and, after applying a linear elastic constitutive model and imposing compatible initial conditions, the solution both for stresses and displacements can be computed at any time t. For the current example, a linear elastic material is chosen with a Poisson's ratio of $\nu = 0.45$, Young's modulus $E = 1.7 \times 10^7$Pa and density $\rho_0 = 1.1 \times 10^3$kg/m^3. The solution parameters are set as $A = 1$, $B = 1$ and $C = -2$ and $U_0 = 5 \times 10^{-4}$ m. Figure 8.25 shows the deformed shape of the cube as it evolves in time, and the values of the off-diagonal components of the first Piola-Kirchhoff stress tensor $\boldsymbol{P}$ (which in the linear elastic case is equal to the Cauchy stress tensor, $\boldsymbol{\sigma}$). The convergence error is analysed at time $t = 4 \times 10^{-3}$ s both for the stress and linear momentum components and for the L^1 and L^2 norms. Results are shown in Figure 8.26 and Figure 8.27. Crucially, it can be seen how the solution tends to asymptotic quadratic convergence for both stresses and velocities as the mesh is refined.

8.4.2 L-shaped block

This example was first proposed by Simo et al. in [106] and later implemented by several authors (see for example references [107–109]). In what follows, the results for the example as proposed in [109] for a neo-Hookean material will be shown. A three-dimensional L-shaped block is left free in space and subjected to time varying forces at two of its sides (see Figure 8.28). These forces are described by the equations,

$$\boldsymbol{F}_1(t) = -\boldsymbol{F}_2(t) = (150, 300, 450)p(t), \quad p(t) = \begin{cases} t, & 0 \leq t < 2.5, \\ 5 - t, & 2.5 \leq t < 5, \\ 0, & t \geq 5. \end{cases}$$

The block is made of a neo-Hookean material, with properties $\mu = 1.925 \times 10^4$ Pa, $\lambda = 2.885 \times 10^4$ Pa and $\rho_0 = 1.0 \times 10^3$ kg/m^3. Figure 8.29 shows the evolution in time of the pressure and deformed shape. Figure 8.30a demonstrates the ability of the algorithm to preserve the angular momentum (once the external forces are released) and linear momentum (the external torque is applied at the centre of mass of the block). Figure 8.30b compares the total energy of the system (red line)

[1] When $A + B + C = 0$ the volumetric deformation is zero since $\nabla^2 \boldsymbol{u} = 0$

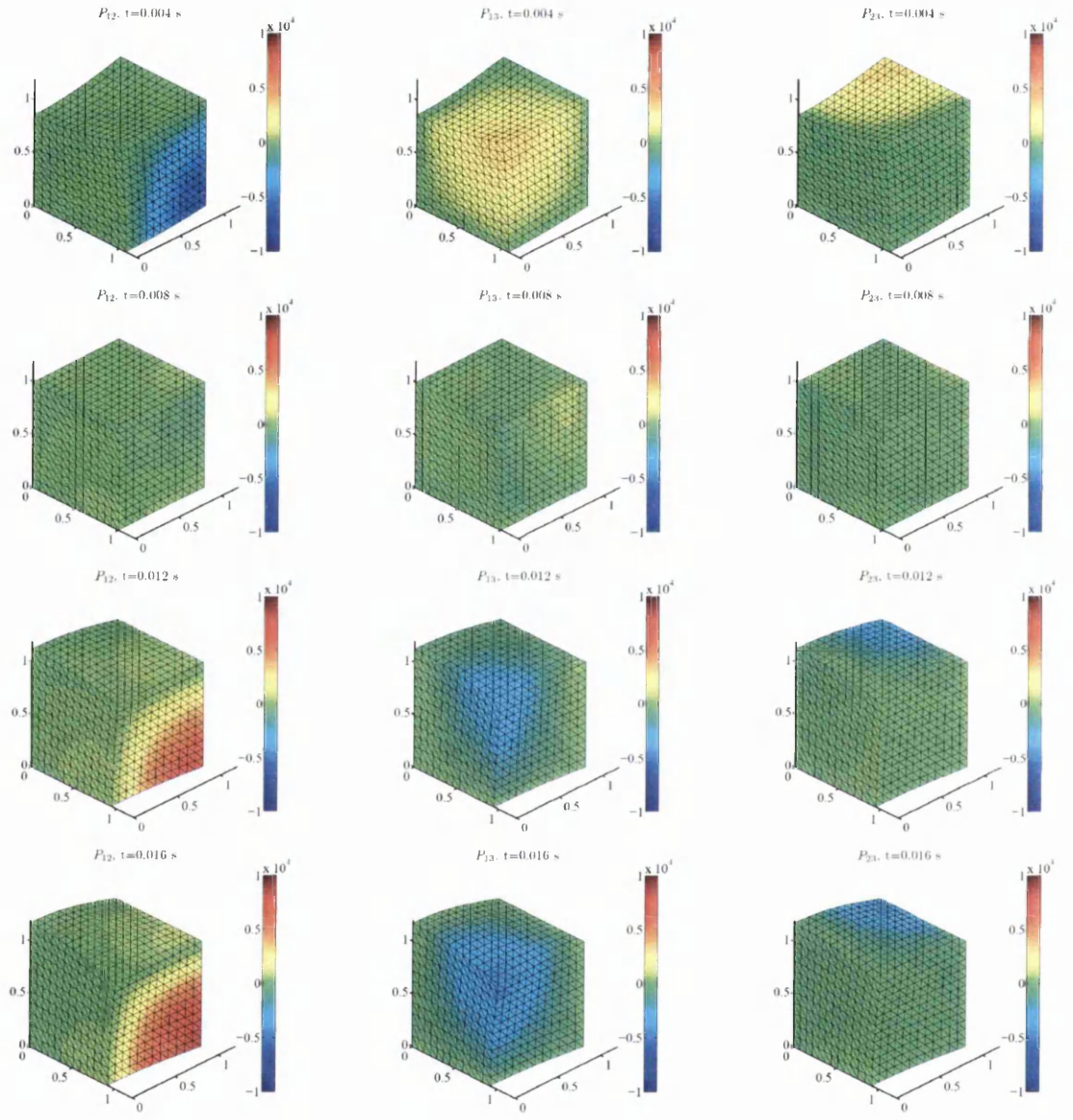

Figure 8.25: Linear elasticity three dimensional case. Snapshots at different times of the off diagonal components of the first Piola Kirchhoff stress tensor. Solution using $A = 1$, $B = 1$ and $C = -2$ and $U_0 = 5 \times 10^{-4}$ m. Linear elastic material with Poisson's ratio $\nu = 0.45$, Young's modulus $E = 1.7 \times 10^7$Pa and density $\rho_0 = 1.1 \times 10^3$kg/m^3. JST spatial discretisation with $h = 1/12$ m, $\kappa^{(4)} = 1/128$ and $\alpha_{CFL} = 0.4$. Displacements scaled 100 times.

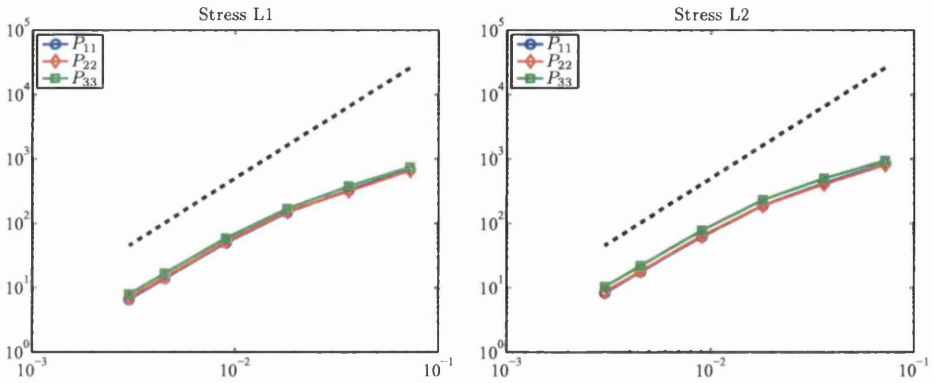

(a) (b)

Figure 8.26: Linear elasticity three dimensional case. Convergence error for the stress components P_{11}, P_{22} and P_{33} in L^1 and L^2 norms at time $t = 0.004$ s as compared to the analytical solution. Solution using $A = 1$, $B = 1$ and $C = -2$ and $U_0 = 5 \times 10^{-4}$ m. Linear elastic material with Poisson's ratio $\nu = 0.45$, Young's modulus $E = 1.7 \times 10^7$Pa and density $\rho_0 = 1.1 \times 10^3$kg/m^3. JST spatial discretisation with $\kappa^{(4)} = 1/128$ and $\alpha_{CFL} = 0.4$.

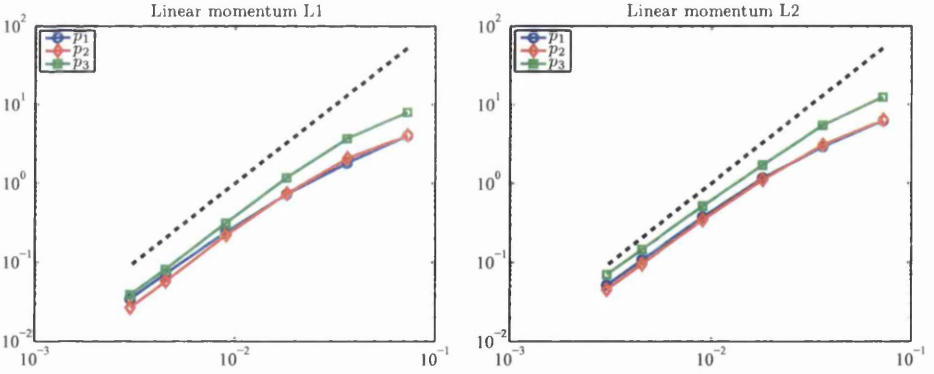

(a) (b)

Figure 8.27: Linear elasticity three dimensional case. Convergence error for the linear momentum components p_1, p_2 and p_3 in L^1 and L^2 norms at time $t = 0.004$ s as compared to the analytical solution. Solution using $A = 1$, $B = 1$ and $C = -2$ and $U_0 = 5 \times 10^{-4}$ m. Linear elastic material with Poisson's ratio $\nu = 0.45$, Young's modulus $E = 1.7 \times 10^7$Pa and density $\rho_0 = 1.1 \times 10^3$kg/m^3. JST spatial discretisation with $\kappa^{(4)} = 1/128$ and $\alpha_{CFL} = 0.4$.

and the summation of kinetic and potential energies (blue lines) when using three different tetrahedral meshes: 388, 1178 and 3546 nodes. It can be seen that, as the mesh is refined, the numerical dissipation (difference between the total energy of the system and the summation of kinetic and potential energies) is reduced, obtaining therefore a more accurate solution. As it was done for the spinning plate test case (section 8.3.3), Figures 8.31 and 8.32 prove that the correction of the internal forces, necessary for the preservation of the angular momentum, are small as compared to the actual internal forces.

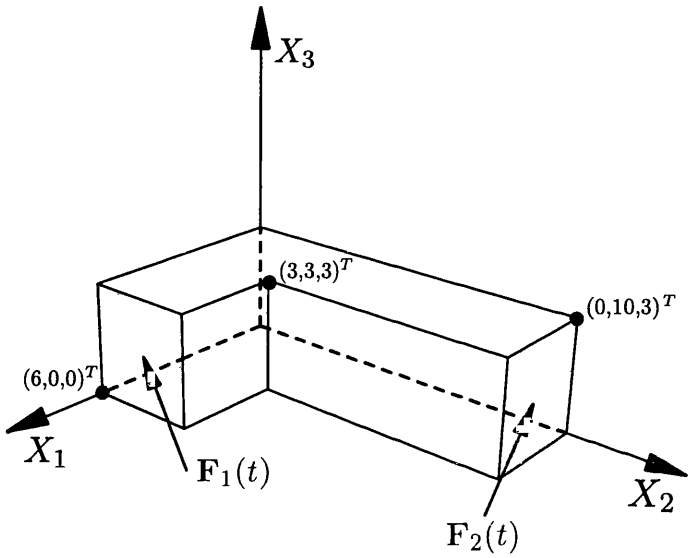

Figure 8.28: L-shaped block, initial configuration

8.4.3 Bending column (3D)

This example is an extension of the two-dimensional column presented previously. The problem is shown to demonstrate the performance of the method in three-dimensional bending dominated scenarios. As in the two-dimensional case, a rubber-like material column is clamped on its bottom face ($X_3 = 0$ m). An initial uniform velocity $\boldsymbol{V}_0 = 10\left(\frac{\sqrt{3}}{2}, \frac{1}{2}, 0\right)^T$ m/s is imposed and the bar is left oscillating freely in time (see Figure 8.33). A neo-Hookean material is chosen with Young's modulus $E = 1.7 \times 10^7$ Pa, density $\rho_0 = 1.1 \times 10^3$ kg/m^3 and Poisson's ratio $\nu = 0.45$.

Figure 8.34 shows the evolution in time of the pressure distribution for the deformed configuration. The solution exhibits a smooth distribution of pressure and absence of locking. In addition, Figure 8.35 compares the solution at the instant $t = 0.45$ s for three different mehes, $h = 1/3$ m, $h = 1/6$ m and $h = 1/12$ m. It can be seen that, as the mesh is refined, the obtained solution better captures the deformation and pressure distribution. Figure 8.36 shows the time history of the vertical displacement (X_3 direction) at point $\boldsymbol{X} = (1, 1, 6)^T$ m and stress component

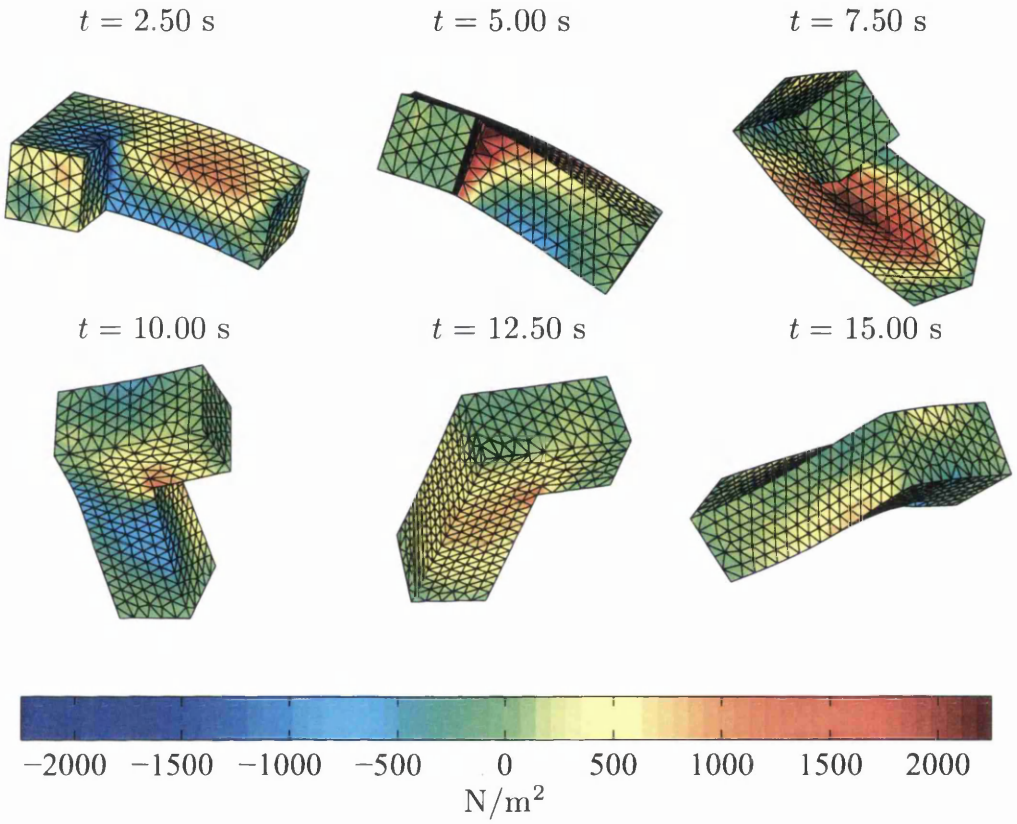

Figure 8.29: L-shaped block, evolution in time of deformation and pressure distribution. Neo-Hookean material with material properties $\mu = 1.925 \times 10^4$ Pa, $\lambda = 2.885 \times 10^4$ Pa, $\rho_0 = 1.0 \times 10^3 \text{kg/m}^3$. JST spatial discretisation using a tetrahedral mesh of 1178 nodes, $\kappa^{(4)} = 1/128$ and $\alpha_{CFL} = 0.4$.

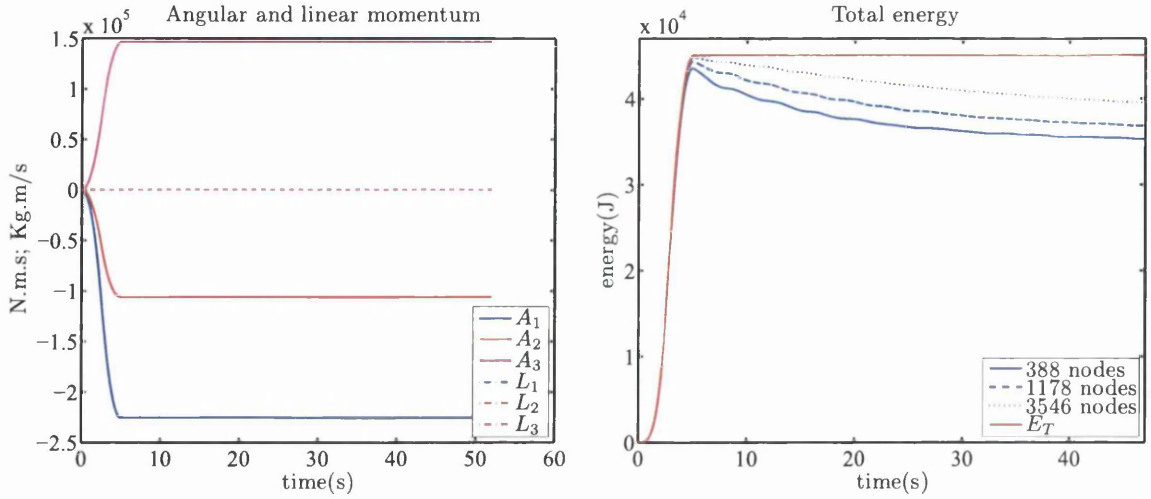

(a) (b)

Figure 8.30: L-shaped block neo-Hookean material with material properties $\mu = 1.925 \times 10^4$ Pa, $\lambda = 2.885 \times 10^4$ Pa, $\rho_0 = 1.0 \times 10^3 \text{kg/m}^3$. JST spatial discretisation using $\kappa^{(4)} = 1/128$ and $\alpha_{CFL} = 0.4$. (a) Conservation of the total linear momentum $\boldsymbol{L} = [L_1, L_2, L_3]^T$ and angular momentum $\boldsymbol{A} = [A_1, A_2, A_3]^T$ for a mesh of 1178 nodes; (b) comparison on the preservation of the total energy when using three different tetrahedral meshes: 388, 1178 and 3546 nodes.

P_{33} history at point $\boldsymbol{X} = (0, 0, 0)^T$ for the same meshes. These figures illustrate the convergence of the solution as the mesh is refined.

Next, the example is extended to show the performance of the method when plasticity is involved. Figure 8.37 compares at time step $t = 0.45$ s the previous neo-Hookean solution against two solutions using Von-Mises hyperelastic-plastic material with yield stress $\bar{\tau}_y^0 = 2 \times 10^9$ Pa and yield stress $\bar{\tau}_y^0 = 1 \times 10^9$ Pa, respectively, and isotropic hardening modulus $H = 0.5 \times 10^9$ Pa (the rest of the material parameters are the same as those of the previous neo-Hookean example). As can be observed, the pressure distribution is smooth and the occurrence of plasticity is perfectly depicted in the clamped end of the column. As expected, the column with lowest yield stress shows a higher deflection.

8.4.4 Taylor impact case

A copper bar of initial length 0.0324 m and initial radius 0.0032 m has a velocity of 227 m/s and impacts against a rigid wall at time $t = 0$ s (see Figure 8.38). A Von-Mises hyperelastic-plastic material with isotropic hardening is chosen to simulate the material. The material parameters are Young's modulus $E = 1.17 \times 10^{11}$ Pa, density $\rho_0 = 8.930 \times 10^3$ kg/m^3, Poisson's ratio $\nu = 0.35$, yield stress, $\bar{\tau}_y^0 = 4 \times 10^8$ Pa and hardening modulus $H = 1 \times 10^8$ Pa. Figure 8.39 shows the results obtained using a discretisation of one quarter of the domain and relevant boundary conditions. The

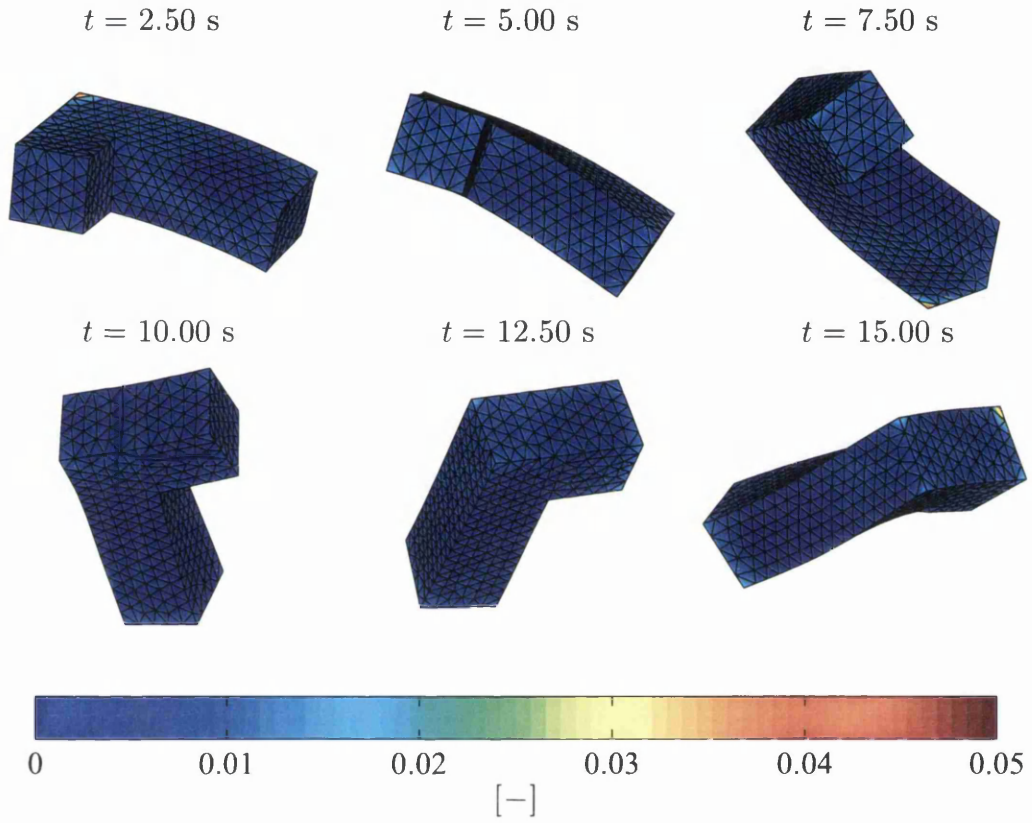

Figure 8.31: L-shaped block, distribution of the normalised norm of the vector resulting from the difference between the modified edge forces, and the original edge forces, $\frac{||(\boldsymbol{f}_k - \hat{\boldsymbol{f}}_k)||}{||\boldsymbol{f}_k||}$. The plot shows the average at the nodes from its surrounding edge values. Neo-Hookean material with material properties $\mu = 1.925 \times 10^4$ Pa, $\lambda = 2.885 \times 10^4$ Pa, $\rho_0 = 1.0 \times 10^3 \text{kg/m}^3$. JST spatial discretisation using a tetrahedral mesh of 1178 nodes, $\kappa^{(4)} = 1/128$ and $\alpha_{CFL} = 0.4$.

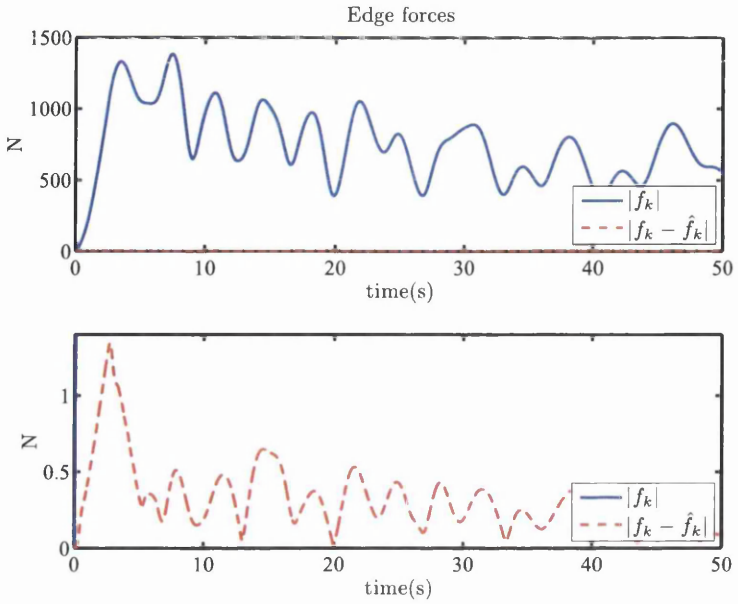

Figure 8.32: L-shaped block, evolution of the L^2 norm of the edge forces (blue) against the L^2 norm of the modification of the edge forces (red). The bottom plot shows a zoomed version of the above plot. Neo-Hookean material with material properties $\mu = 1.925 \times 10^4$ Pa, $\lambda = 2.885 \times 10^4$ Pa, $\rho_0 = 1.0 \times 10^3 \text{kg/m}^3$. JST spatial discretisation using a tetrahedral mesh of 1178 nodes, $\kappa^{(4)} = 1/128$ and $\alpha_{CFL} = 0.4$.

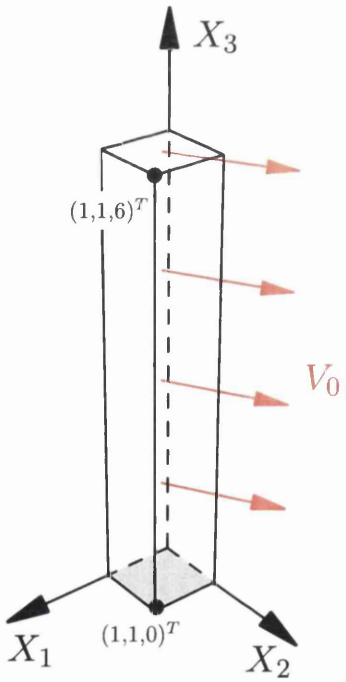

Figure 8.33: Three dimensional bending column. Initial configuration.

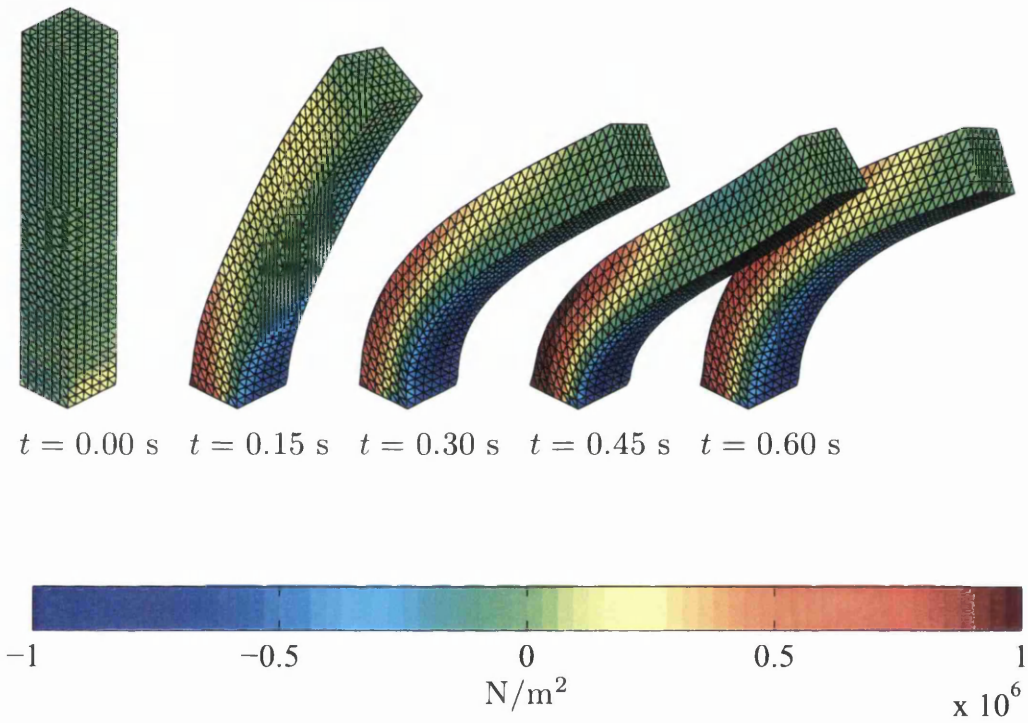

Figure 8.34: Three dimensional bending column. Evolution in time of the pressure distribution in the deformed configuration. Initial uniform velocity $\boldsymbol{V}_0 = 10\left(\frac{\sqrt{3}}{2}, \frac{1}{2}, 0\right)^T$ m/s. Neohookean material with Young's modulus $E = 1.7 \times 10^7$ Pa, density $\rho_0 = 1.1 \times 10^3$ kg/m^3 and Poisson's ratio $\nu = 0.45$. JST spatial discretisation with $h = 1/6$ m, $\kappa^{(4)} = 1/128$ and $\alpha_{CFL} = 0.4$.

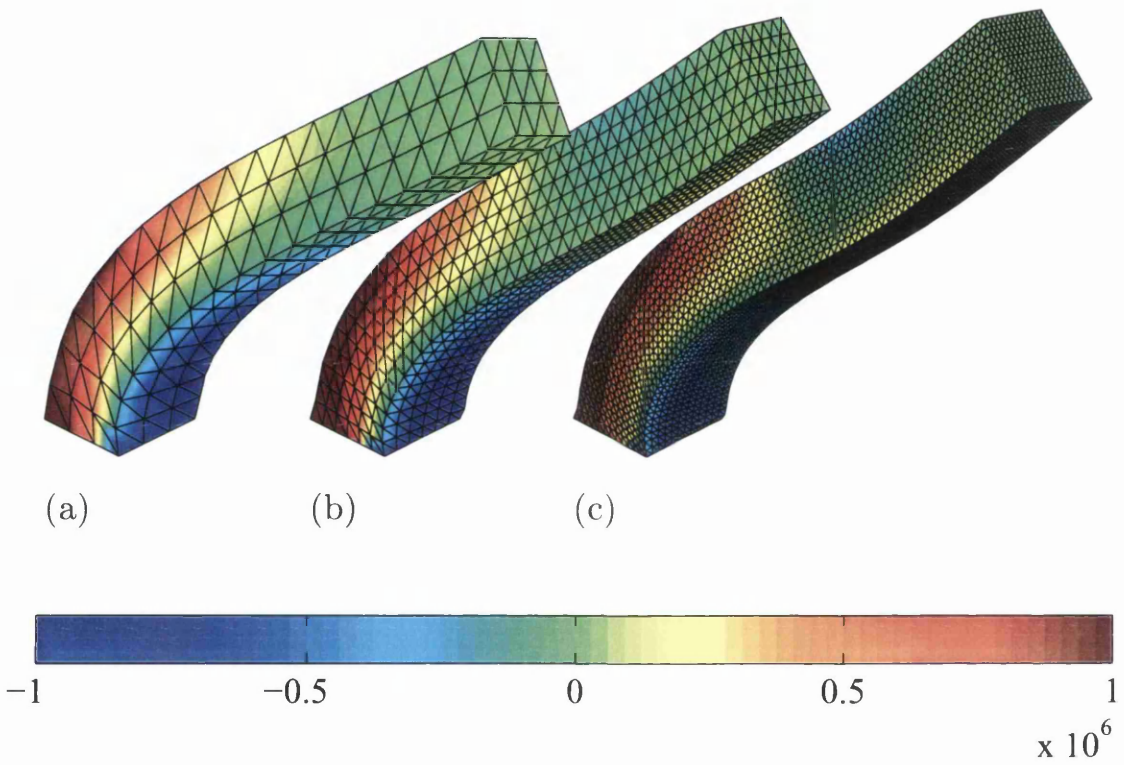

Figure 8.35: Three dimensional bending column. Comparison of the deformation and pressure distribution for three different meshes: $h = 1/3$ m (a), $h = 1/6$ m (b) and $h = 1/12$ m (c). Initial uniform velocity $\boldsymbol{V}_0 = 10\left(\frac{\sqrt{3}}{2}, \frac{1}{2}, 0\right)^T$ m/s. Neohookean material with Young's modulus $E = 1.7 \times 10^7$ Pa, density $\rho_0 = 1.1 \times 10^3$ kg/m^3 and Poisson's ratio $\nu = 0.45$. JST spatial discretisation with $\kappa^{(4)} = 1/128$ and $\alpha_{CFL} = 0.4$.

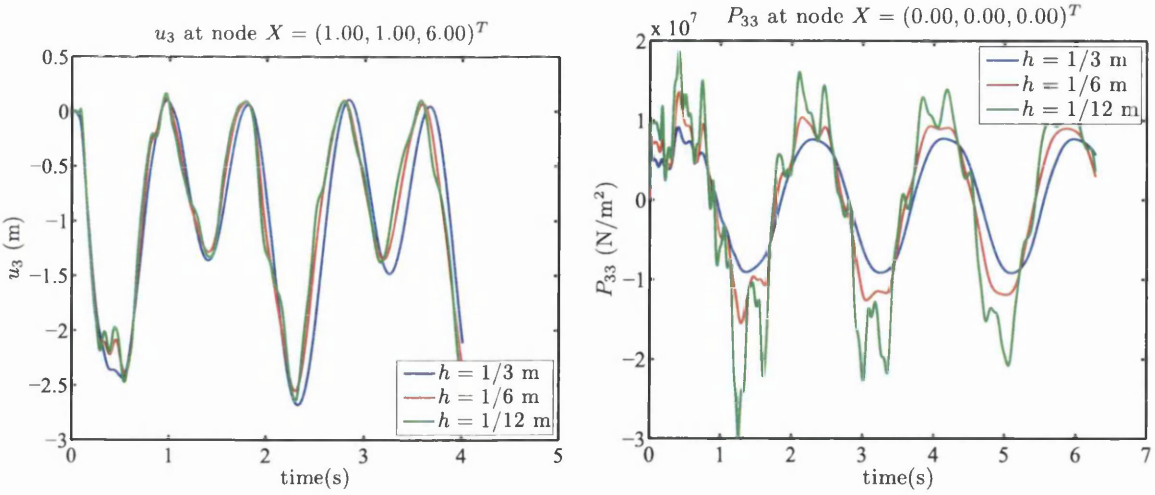

(a) (b)

Figure 8.36: Three dimensional bending column. (a) Time history of the vertical displacement at node $\boldsymbol{X} = (1, 1, 6)^T$ m; (b) time history of the stress P_{33} at node $\boldsymbol{X} = (1/3, 1/3, 3)^T$ m. Initial uniform velocity $\boldsymbol{V}_0 = 10\left(\frac{\sqrt{3}}{2}, \frac{1}{2}, 0\right)^T$ m/s. Neo-hookean material with Young's modulus $E = 1.7 \times 10^7 Pa$, density $\rho_0 = 1.1 \times 10^3$ kg/m^3 and Poisson's ratio $\nu = 0.45$. JST spatial discretisation with $h = 1/3$ m (blue), $h = 1/6$ m (red) and $h = 1/12$ m (green), $\kappa^{(4)} = 1/128$ and $\alpha_{CFL} = 0.4$.

artificial dissipation can be reduced to $\kappa^{(4)} = 1/4096$ due to the presence of physical plastic dissipation in the material. The final radius at time $t = 80\mu s$ is shown in Table 8.4 as compared to numerical results using other methodologies [24]. As it is well known, the standard displacement based FEM solution with linear tetrahedrals suffer from volumetric locking, which is clearly seen in the first result in table 8.4 . The proposed formulation is able to circumvent this issue.

As it can be seen in Figure 8.39, the solution presents certain asymmetry in the plastic strain distribution. This is due to the use of one quarter of the domain in the simulation and, specifically, due to the refinement imposed by the mesh generator at the sharp corners. A more symmetric solution is obtained in Figure 8.40 which shows the solution obtained using a discretisation of the full domain.

8.4.5 Twisting column

This example proves the robustness of the method when dealing with problems involving large deformations. A squared section column of 1 m side length and 6 m height is clamped on its bottom and subjected to an initial angular velocity. This angular velocity is imposed in the central vertical axis of the column (see Figure 8.41) which, combined with the clamped boundary condition of its bottom, results into a twist of the material. Figure 8.42 shows the deformed configuration and pressure distribution for different time instants, using the JST method with a regular mesh of

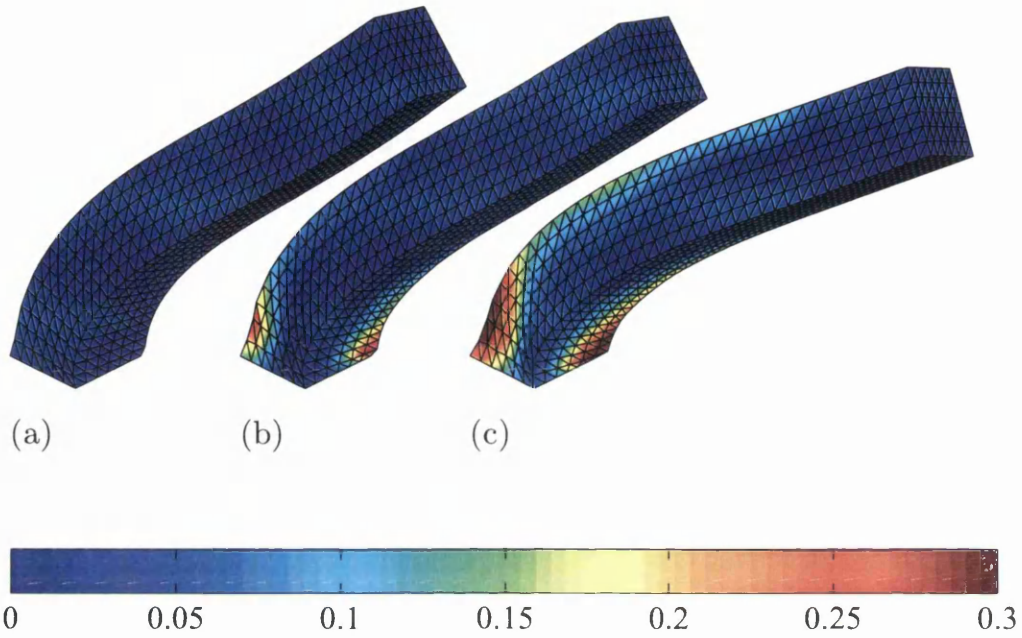

Figure 8.37: Three dimensional bending column. Initial uniform velocity $\boldsymbol{V}_0 = 10(\cos(30), \sin(30), 0)^T$ m/s. Comparison of the plastic strain distribution for two different materials: hyperelastic constitutive model (a), Von-Mises hyperelastic plastic constitutive models (b), (c) at time $t = 0.45$ s. Young's modulus $E = 1.7 \times 10^7$ Pa, density $\rho_0 = 1.1 \times 10^3$ kg/m^3 and Poissons ratio $\nu = 0.45$. Yield stress, $\bar{\tau}_y^0 = 2 \times 10^9$ Pa (b), $\bar{\tau}_y^0 = 1 \times 10^9$ Pa (c), hardening modulus $H = 0.5 \times 10^8$ Pa. JST spatial discretisation with $h = 1/6$ m, $\kappa^{(4)} = 1/128$ and $\alpha_{CFL} = 0.4$.

Method	final radius (mm)
FEM tetrahedrals	5.55
FEM hexahedras	6.95
FEM average nodal pressure	6.99
Proposed approach (JST)	6.98

Table 8.4: Taylor test. Final radius at $t = 80\mu s$ of the proposed method compared to other methodologies and experimental results.

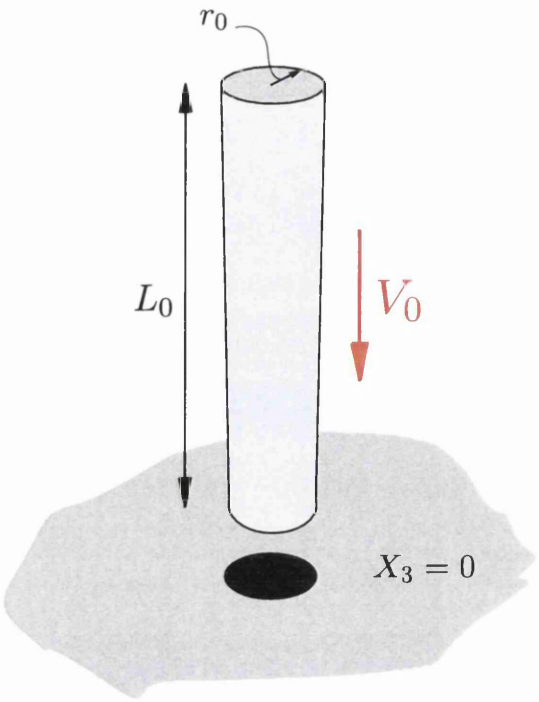

Figure 8.38: Setup of the Taylor test problem

$h = 1/6$ m and $\kappa^{(4)} = 1/128$. It can be seen that the method is capable of capturing the deformation process very accurately, while providing a smooth distribution of pressures. This simulation can be run for long physical times without appearance of instabilities, proving therefore the robustness of the numerical method.

The same example is simulated using a Von-Misses hyperelastic-plastic material, as presented in section 3.3. The elastic material properties are kept the same while the plastic properties are given by a yield stress of $\bar{\tau}_y^0 = 4 \times 10^6$ Pa and hardening modulus of $H = 3 \times 10^6$ Pa. Figure 8.43 shows the deformation process and plastic strain distribution. It can be seen how the column is subjected to larger strains, due to the plasticity effects, but still the method is capable of accurately capturing the deformation process.

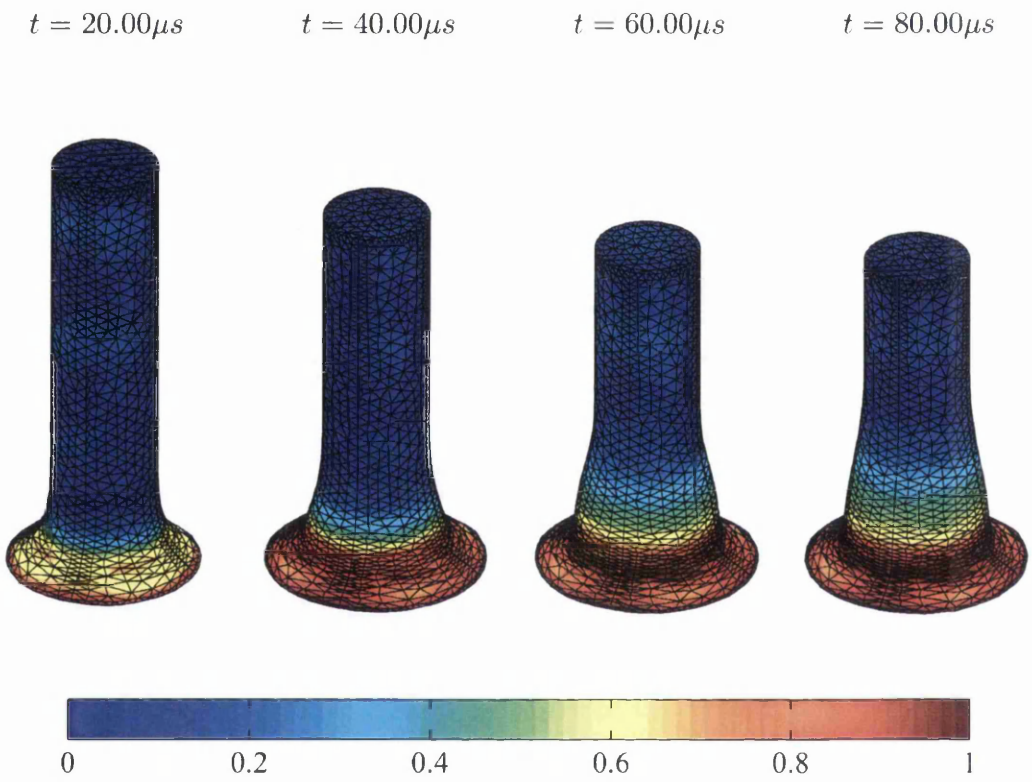

Figure 8.39: Taylor copper bar impact test. Comparison of plastic strain distribution at different time instants. Simulation using one quarter of the domain. Initial velocity $v = 227$ m/s. Young's modulus $E = 117$GPa, density $\rho_0 = 8.930 \times 10^3$ kg/m^3, Poissons ratio $\nu = 0.35$, yield stress, $\bar{\tau}_y^0 = 4 \times 10^8$ Pa and hardening modulus $H = 1 \times 10^8$ Pa. JST spatial discretisation with 1361 nodes per sector, $\kappa^{(4)} = 1/4096$ and $\alpha_{CFL} = 0.4$.

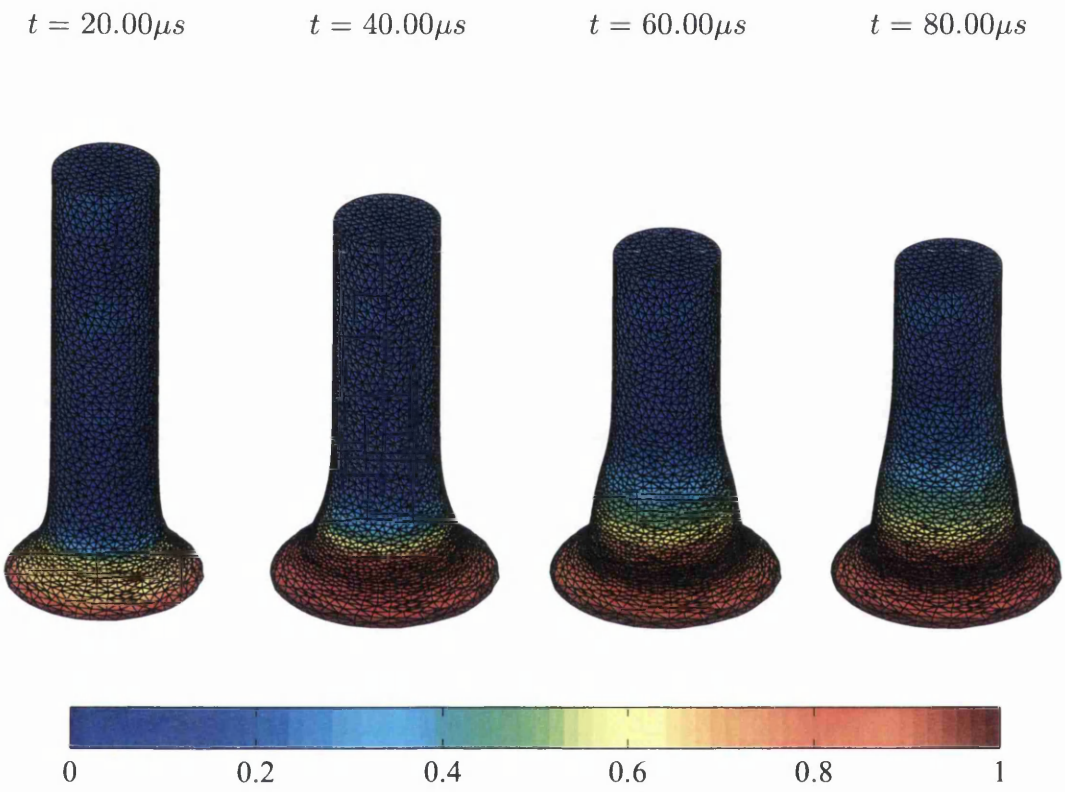

Figure 8.40: Taylor copper bar impact test. Comparison of plastic strain distribution at different time instants. Simulation using the full domain. Initial velocity $v = 227$ m/s. Young's modulus $E = 117$GPa, density $\rho_0 = 8.930 \times 10^3$ kg/m^3, Poissons ratio $\nu = 0.35$, yield stress, $\bar{\tau}_y^0 = 4 \times 10^8$ Pa and hardening modulus $H = 1 \times 10^8$ Pa. JST spatial discretisation with 7347 nodes, $\kappa^{(4)} = 1/4096$ and $\alpha_{CFL} = 0.4$.

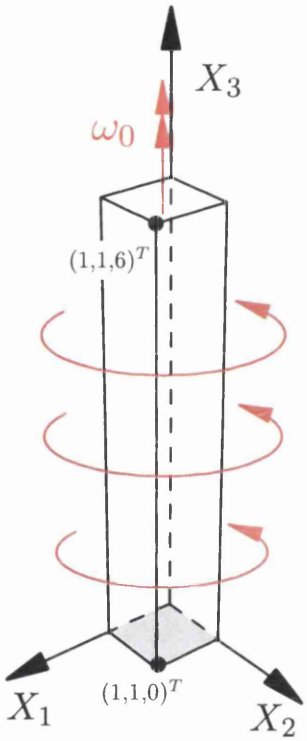

Figure 8.41: Setup of the column twist problem.

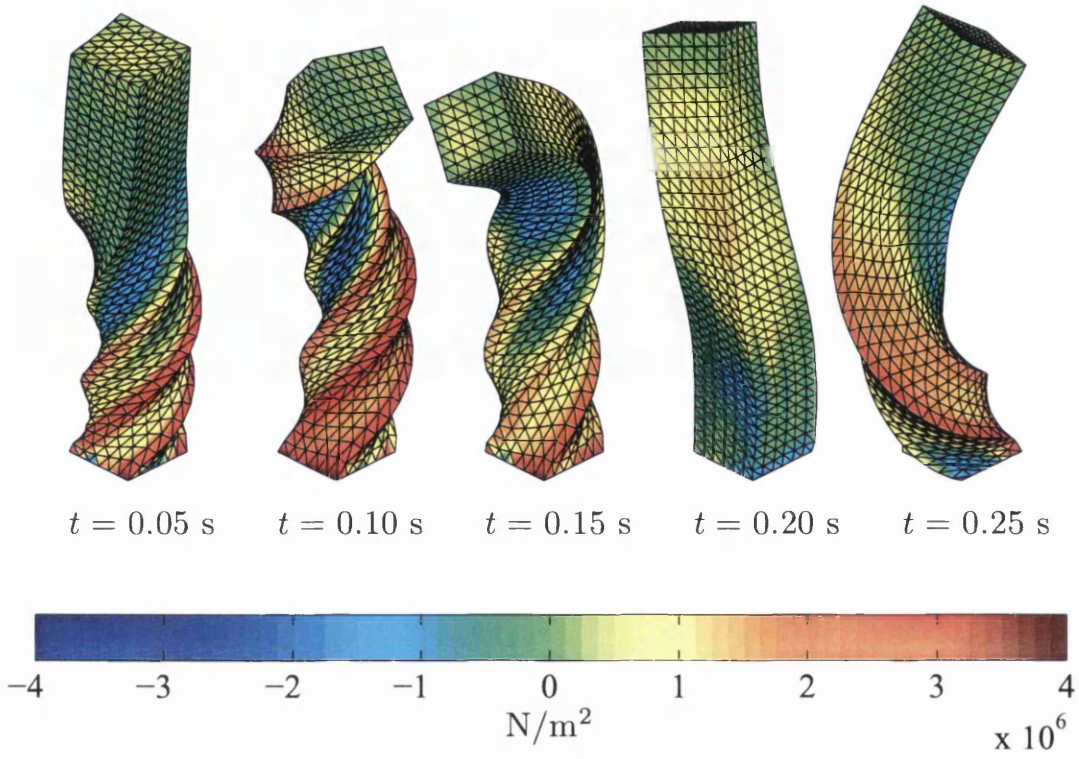

Figure 8.42: Twisting column. Evolution in time of the pressure distribution in the deformed configuration. Initial angular momentum $\boldsymbol{\omega}_0 = (0, 0, 105)^T$ rad/s imposed at the vertical axis. Neo-Hookean material with Young's modulus $E = 1.7 \times 10^7$ Pa, density $\rho_0 = 1.1 \times 10^3$ kg/m^3 and Poisson's ratio $\nu = 0.45$. JST spatial discretisation with $h = 1/6$ m, $\kappa^{(4)} = 1/128$ and $\alpha_{CFL} = 0.4$.

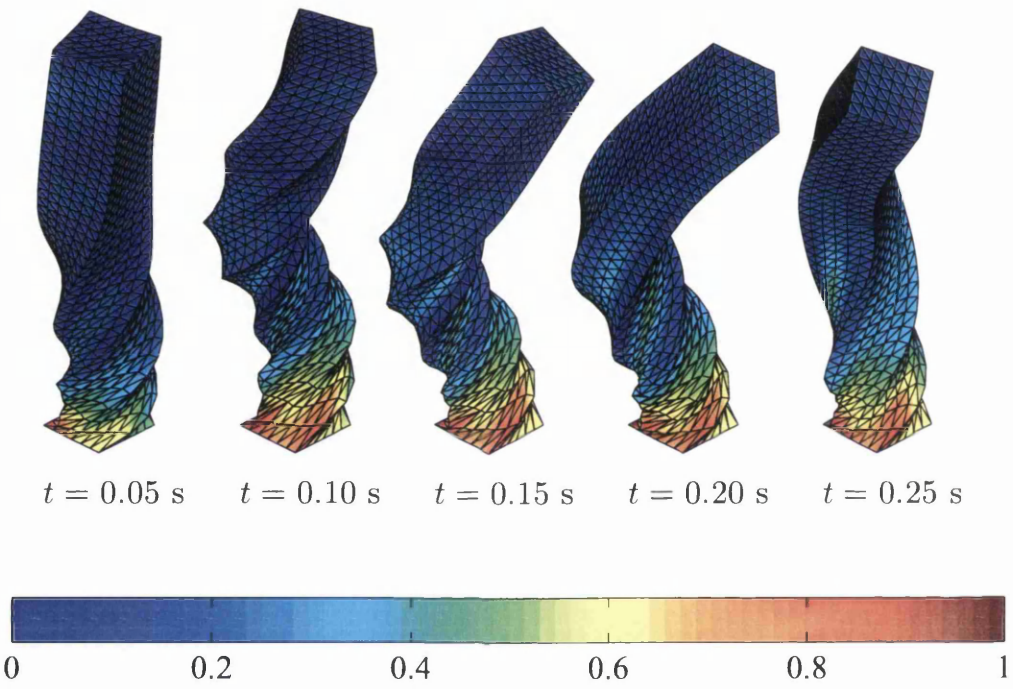

Figure 8.43: Twisting column. Evolution in time of the plastic strain distribution. Initial angular momentum $\boldsymbol{\omega}_0 = (0, 0, 105)^T$ rad/s imposed at the vertical axis. Neo-Hookean material with Von-Misses plasticity, Young's modulus $E = 1.7 \times 10^7$ Pa, density $\rho_0 = 1.1 \times 10^3$ kg/m^3, Poisson's ratio $\nu = 0.45$, yield stress, $\bar{\tau}_y^0 = 4 \times 10^6$ Pa and hardening modulus $H = 3 \times 10^6$ Pa. JST spatial discretisation with $h = 1/6$ m, $\kappa^{(4)} = 1/128$ and $\alpha_{CFL} = 0.4$.

Chapter 9

Conclusions and future work

9.1 Conclusions

This thesis has presented a low order computationally efficient numerical algorithm for solid dynamics. To do so, the mixed conservation law presented in [1] has been discretised using an alternative Finite Volume implemenation for two-dimensional triangular meshes and three-dimensional tetrahedral meshes. This mixed conservation law uses the linear momentum, $\boldsymbol{p}$ and the deformation gradient, $\boldsymbol{F}$, as the problem variables and is presented as an alternative to the displacement based formulations. The semi-discretisation in space has been carried out using a vertex centred Finite Volume with central differences and Jameson-Schmidt-Turkel (JST) type of dissipation. The combination of the central differences and artificial dissipation yields a stable second order method without the need of linear reconstruction. Furthermore, the JST dissipation term provides a built-in discontinuity sensor which preserves the monotonicity of the scheme in the presence of shocks. The definition of a dual mesh (and a set of area vectors) allows the integration of the fluxes using only two loops on edges and one loop on external faces. The combination of these facts with the use of a vertex centred discretisation makes the scheme very cheap in terms of computational cost.

The JST scheme has been adapted to the formulation at hand taking into account its characteristics. Specifically, the compatibility conditions need to be fulfilled, at least in a discrete sense, by the numerical scheme. This is achieved by not including artificial dissipation into the conservation law of the deformation gradient, $\boldsymbol{F}$, which transpires to be not necessary for stability purposes.

The above semi-discretisation in space is combined with a time discretisation using a two stages total variation diminishing (TVD) Runge-Kutta scheme. The scheme is second order in time and ensures that the TVD condition is satisfied, that is, the monotonicity of the scheme is preserved. The overall discretisation is complemented with a numerical correction of the internal tractions and numerical dissipation, which ensure the preservation of the linear and angular momenta. This is achieved through the use of a Lagrange multiplier minimisation procedure, which

requires the computation of three unique parameters for the whole mesh. The computation of these parameters can be embedded in the two loops on edges previously mentioned, therefore with no significant added cost.

In terms of computer implementation, the whole numerical scheme has been implemented from scratch using the numerical software *Matlab* for one, two and three dimensional meshes. A crucial part of this implemenation has been the coding of a preprocessor, which is needed for building the dual mesh and related area vectors.

In order to asses the numerical scheme, a set of benchmark problems have been tested for one, two and three dimensions. The problems have been chosen to prove the order of accuracy and robustness of the numerical method. Crucially, numerical results demonstrate second order convergence for both stresses and velocities, with excellent behaviour in bending dominated scenarios. Implementation of plasticity, or other constitutive models, proves to be straightforward. The obtained solutions compare well with other alternative methodologies, such as cell centred Finite Volume or stabilised Petrov Galerkin. Despite providing more dissipative solutions, the JST method constitutes an important alternative, as compared to other schemes, due to its computational efficiency.

9.2 Future work

Further work is needed to improve the method presented in this thesis. To start with, an alternative implementation combining the upwinding technique, as presented in [1] and the edge-based implementation presented in the current thesis can result in an improved methodology. In this scheme, Riemann solvers would be used in order to propagate the solution in time, which would result in a less dissipative scheme. This would be at the expense of a higher computational cost, since the scheme would require linear reconstruction and use of limiters in the presence of shocks. Nevertheless, the combination of the edge based methodology with the accurate Riemann solvers can provide a very competitive scheme for solid dynamics.

The presented formulation can also be enhanced by use of fractional step methods, as presented in [43] for a Petrov-Galerkin discretisation of the same solid dynamics formulation. This approach allows extending the use of the discretisation presented in this thesis to nearly or fully incompressible materials, which, otherwise would be computationally very expensive due to time step limitations. By using the fractional step methodology, the time step is then limited by the shear wave speed, therefore reducing substantially the computational cost. The approach uses a predictor-corrector algorithm, where the incompressibility constraint is solved implicitly through a Poisson type problem and which can be easily implemented within the existing framework.

So far, just few constitutive models have been used with the presented formulation, which include hyperelastic materials and elastoplastic materials with isotropic

hardening. Furthermore, thermomechanical problems have been simulated by using a Mie-Grüneisen equation of state. The library of constitutive models can be further extended by including visco-elasticity, visco-plasticity or high energy materials.

The presented scheme can also be improved in terms of the conservation of angular momentum. Alternatives approaches could be studied such that the corrections to the internal tractions (as presented in section 6.3) are no longer needed. To do so, the constitutive model could be computed by means of the symmetric second Piola-Kirchhoff stress tensor, $\boldsymbol{S}$, as a function of the deformation gradient, $\boldsymbol{F}$, and recover the first Piola-Kirchhoff through the gradient of the displacements, $\nabla_0 \boldsymbol{x}$. That is, $\boldsymbol{P} = \nabla_0 \boldsymbol{x} \boldsymbol{S}(\boldsymbol{F})$. This approach, combined with the adequate time integrator, would ensure the exact conservation of the angular momentum, as it is the case for the Finite Element Method [106].

The numerical dissipation as presented in this thesis uses a set of geometrical weights that affects the conservation of linear momentum. This dissipation has to be corrected a posteriori in order to ensure that the linear momentum is preserved (see section 6.3). This could be circumvented by defining a new set of symmetric geometrical weights, such that they still keep the second order of the central differences. One approach could be given by calculating the Laplacian (necessary for the second and fourth order differences) from the standard Finite Element shape functions.

The presented formulation can also be extended in order to include additional variables. An interesting approach would be the inclusion of the conservation laws for the determinant of the deformation, J and the cofactor of the deformation, $\boldsymbol{H}$ (see section 2.6 and appendix C). It has been proven in [43], that the discretisation of the additional conservation law for the J, allows simulating materials with a high degree of incompressibility. The conservation law for the J, combined with thermo-mechanical constitutive models, would also allow simulating Lagrangian gas dynamics problems as it is usually done in hydrocodes. The use of a mixed conservation involving $\boldsymbol{F}$, J and $\boldsymbol{H}$ would allow the implementation of polyconvex constitutive models (as for example Mooney-Rivlin type of materials).

The scheme can also have applications in fluid-structure interaction (FSI). This could be tackled through the use of an Arbritary-Lagrangian-Eulerian (ALE) description of the motion (see for example [87]). In this approach, the structural domain would be described using the presented Lagrangian formulation, while the fluid domain would be modelled using a moving Eulerian reference frame. The discretisation of the fluid equations could easily be carried out using the JST scheme presented in this thesis, as this, in fact, was its original purpose (see [5]). The treatment of the contact between fluid and solids (key in FSI) would be carried out using Riemann solvers, standard in Finite Volume techniques [38]. The scheme would result into an interesting monolithic Finite Volume approach for FSI.

In the context of solid dynamics, it is also very important to treat the contact and impact between different bodies. Since low order elements are used, the detection of contact could be done using standard contact tracking techniques [13]. By means

of Riemann solvers at the boundary elements, the information related to the impact could be transferred to the interior elements.

Another interesting feature for the code would be the treatment of dynamic fracture where, by means of Riemann Solvers in the contact between elements, the initiation of fracture could be captured in an accurate manner.

In order to improve the obtained solution, error estimation and mesh adaptivity should also be considered. Since the algorithm has redundancies through the use of the deformation gradient, $\boldsymbol{F}$, this could be use as an error estimator, as compared to the actual gradient of the displacements, $\nabla_0 \boldsymbol{x}$. This same idea could be used with the total energy E, independent variable, as compared to the total numerical energy (summation of the internal and kinetic energies).

The implementation presented is computationally efficient. Even though, this efficiency has not yet been exploited too far: the code is implemented using Matlab, in order to simulate simple "toy" problems. In order to provide an algorithm capable of simulating industrial real life problems, the formulation should be coded using more basic languages, such as C or C++. The code could also be paralellised, so the computer power can be used in a more efficient manner. The parallelisation of the JST scheme has been done in the past as for example in [55].

Appendix A

Mathematical operators

A.1 Gradient and divergence of scalars, vectors and second order tensors

Given a scalar field a, a vector field $\boldsymbol{a}$ and a second order tensor field $\boldsymbol{\mathcal{A}}$, the gradient operator is defined as

$$[\nabla a]_i = \frac{\partial a}{\partial x_i}, \tag{A.1}$$

$$[\nabla \boldsymbol{a}]_{ij} = \frac{\partial a_i}{\partial x_j}, \tag{A.2}$$

$$[\nabla \boldsymbol{\mathcal{A}}]_{ijk} = \frac{\partial \mathcal{A}_{ij}}{\partial x_k}. \tag{A.3}$$

For a vector field $\boldsymbol{a}$ and a tensor field $\boldsymbol{\mathcal{A}}$, the spatial diveregence operator is defined as

$$\operatorname{div} \boldsymbol{a} = \frac{\partial a_i}{\partial x_i}, \tag{A.4}$$

$$[\operatorname{div} \boldsymbol{\mathcal{A}}]_i = \frac{\partial \mathcal{A}_{ij}}{\partial x_j}. \tag{A.5}$$

where repeated indices denote summation. Throughout the thesis, the notation ∇ and div will be used for denoting the gradient and the divergence at the spatial configuration, while ∇_0 and DIV will be used for denoting the gradient and divergence operators at the reference configuration.

A.2 Cross product between tensors

A cross vector product between two point tensors $\boldsymbol{\mathcal{A}}$, $\boldsymbol{\mathcal{B}}$ to give a new two point-tensor denoted $\boldsymbol{\mathcal{A}} \times \boldsymbol{\mathcal{B}}$ is defined as

$$[\boldsymbol{\mathcal{A}} \times \boldsymbol{\mathcal{B}}]_{iI} = \varepsilon_{ijk}\, \varepsilon_{IJK}\, \mathcal{A}_{jJ} \mathcal{B}_{kK}. \tag{A.6}$$

which can be interpreted as a matrix gathering the cross products between the columns of $\boldsymbol{\mathcal{A}}$ and $\boldsymbol{\mathcal{B}}$. The vector cross product between a spatial vector $\boldsymbol{b}$ and a two point tensor $\boldsymbol{\mathcal{A}}$ to give another two-point tensor is defined as

$$[\boldsymbol{b} \times \boldsymbol{\mathcal{A}}]_{iI} = \varepsilon_{ijk}\, b_j \mathcal{A}_{kI}. \tag{A.7}$$

Finally, the vector cross product between a two-point $\boldsymbol{\mathcal{A}}$ and a material vector $\boldsymbol{B}$ to give another two-point tensor is defined as,

$$[\boldsymbol{\mathcal{A}} \times \boldsymbol{B}]_{iI} = \varepsilon_{IJK}\, \mathcal{A}_{iJ} B_K. \tag{A.8}$$

The following properties are satisfied for the above operators

$$\begin{aligned} \boldsymbol{b} \times \boldsymbol{\mathcal{A}} \times \boldsymbol{B} &= -\boldsymbol{\mathcal{A}} \times (\boldsymbol{b} \otimes \boldsymbol{B}), \\ \boldsymbol{\mathcal{A}} \times \boldsymbol{\mathcal{B}} &= \boldsymbol{\mathcal{B}} \times \boldsymbol{\mathcal{A}}, \\ (\boldsymbol{\mathcal{A}} \times \boldsymbol{\mathcal{A}}) : \boldsymbol{\mathcal{A}} &= 6 \det(\boldsymbol{\mathcal{A}}), \\ \operatorname{cof} \boldsymbol{\mathcal{A}} &= \frac{1}{2} \boldsymbol{\mathcal{A}} \times \boldsymbol{\mathcal{A}}, \end{aligned}$$

where

$$\operatorname{cof} \boldsymbol{\mathcal{A}} = \det(\boldsymbol{\mathcal{A}}) \boldsymbol{\mathcal{A}}^{-T}.$$

A.3 CURL of tensors

The CURL operator for a second order two-point tensor $\boldsymbol{\mathcal{A}}$ to give another second order two-point tensor is defined as

$$[\operatorname{CURL}(\boldsymbol{\mathcal{A}})]_{iI} = \varepsilon_{IJK} \frac{\partial \mathcal{A}_{iK}}{\partial X_J}. \tag{A.9}$$

Appendix B

Alternative descriptions of the motion

This chapter will introduce two alternative descriptions of the motion, not considered in the core of the thesis, namely: Updated Lagrangian description and Eulerian description. In the first, the variables are referred to the material configuration while the fluxes to the spatial configuration. In the second, both the variables and fluxes are referred to the spatial configuration. Both descriptions will be applied to the conservation laws introduced in sections 2.4 and 2.6.

The use of an updated Lagrangian type of description has advantages in terms of area conservation, as needed in some applications of fluid structure interaction. An Eulerian description of the motion can be of interest when large deformations are involved, as for example in plastic flow ([72]).

Prior to introducing these two descriptions, the Reynold's transport theorem will be presented. This theorem is necessary for introducing the Eulerian description of the motion and also needed when deducing the Rankine-Hugoniot jump conditions as in section 2.3.3.

B.1 Reynold's Transport Theorem

The Reynold's transport theorem is used for expressing the time derivative of integrals over moving volumes (see [87]). Given a spatial volume v bounded by a smooth surface ∂v whose points at time t move with a material velocity $\boldsymbol{v}$, the total time derivative of the integral across the spatial volume v can be written as

$$\begin{aligned}\frac{d}{dt}\int_v \boldsymbol{\mathcal{U}}\, dv &= \int_V \frac{d}{dt}\left(\boldsymbol{\mathcal{U}} J\right)\, dV = \int_V \frac{d\boldsymbol{\mathcal{U}}}{dt} J\, dV + \int_V \boldsymbol{\mathcal{U}} J \operatorname{div} \boldsymbol{v}\, dV \\ &= \int_v \left(\frac{d\boldsymbol{\mathcal{U}}}{dt} + \boldsymbol{\mathcal{U}} \operatorname{div} \boldsymbol{v}\right)\, dv = \int_v \left(\frac{\partial \boldsymbol{\mathcal{U}}}{\partial t} + \operatorname{div}(\boldsymbol{\mathcal{U}} \otimes \boldsymbol{v})\right)\, dv,\end{aligned}$$

where equation (2.3) has been used. Using the divergence theorem, the following is obtained

$$\frac{d}{dt}\int_v \boldsymbol{\mathcal{U}}\, dv = \int_v \frac{\partial \boldsymbol{\mathcal{U}}}{\partial t}\, dv + \int_{\partial v} (\boldsymbol{\mathcal{U}} \otimes \boldsymbol{v})\boldsymbol{n}\, da, \tag{B.1}$$

which is known as the Reynold's Transport Theorem.

B.2 Updated Lagrangian description

Using the area mapping (2.4) and the volume mapping (2.3), the total Lagrangian conservation law (2.9) is transformed into an updated conservation law Lagrangian as

$$\frac{d}{dt}\int_V \boldsymbol{\mathcal{U}}\, dV + \int_{\partial v} \boldsymbol{\mathcal{G}}_n\, da = \int_v \boldsymbol{\mathcal{T}}\, dv, \tag{B.2}$$

where

$$\begin{aligned} \boldsymbol{\mathcal{G}} &= \boldsymbol{\mathcal{F}}\boldsymbol{H}^{-1}; \quad \boldsymbol{\mathcal{G}}_n = \boldsymbol{\mathcal{G}}\boldsymbol{n}, \\ \boldsymbol{\mathcal{T}} &= J^{-1}\boldsymbol{\mathcal{S}}. \end{aligned}$$

Using the updated Lagrangian framework with the conservation laws of sections 2.4 and 2.6 gives

$$\frac{d}{dt}\int_V \boldsymbol{p} dV = \int_{\partial v} \boldsymbol{\sigma}\boldsymbol{n} da + \int_v \rho \boldsymbol{b} dv, \tag{B.3}$$

$$\frac{d}{dt}\int_V \boldsymbol{F}\, dV = \int_{\partial v} (\boldsymbol{v} \otimes \boldsymbol{H}^{-1})\boldsymbol{n}\, da, \tag{B.4}$$

$$\frac{d}{dt}\int_V J\, dV = \int_{\partial v} \boldsymbol{v}\cdot\boldsymbol{n}\, da, \tag{B.5}$$

$$\frac{d}{dt}\int_V \boldsymbol{H}\, dV = -\int_{\partial v} \boldsymbol{\mathcal{L}}\boldsymbol{n}\, da, \tag{B.6}$$

$$\frac{d}{dt}\int_V E\, dV = \int_{\partial v} \boldsymbol{\sigma}\boldsymbol{n}\cdot\boldsymbol{v}\, da + \int_v \rho\boldsymbol{b}\cdot\boldsymbol{v}\, dv - \int_{\partial v} \boldsymbol{q}\cdot\boldsymbol{n}\, da + \int_v sJ^{-1}\, dv, \tag{B.7}$$

where $[\boldsymbol{\mathcal{L}}]_{iIj} = \varepsilon_{ikl}\,\varepsilon_{IJK}\, v_k [\boldsymbol{F}]_{lK} [\boldsymbol{H}^{-1}]_{Jj}$ and $\boldsymbol{q} = \boldsymbol{H}^{-T}\boldsymbol{Q}$.

B.3 Eulerian description

The Eulerian description is obtained first performing a push forward of the variable $\boldsymbol{\mathcal{U}}$ in equation (B.2) to give

$$\frac{d}{dt}\int_v \boldsymbol{\mathcal{V}}\, dv + \int_{\partial v} \boldsymbol{\mathcal{G}}_n\, da = \int_v \boldsymbol{\mathcal{T}}\, dv, \tag{B.8}$$

where

$$\boldsymbol{\mathcal{V}} = J^{-1}\boldsymbol{\mathcal{U}}.$$

Using now the Reynold's transpor theorem (B.1) on equation (B.8) gives,

$$\int_v \frac{\partial \boldsymbol{\mathcal{V}}}{\partial t}\, dv + \int_{\partial v} \boldsymbol{\mathcal{H}}_n\, da + \int_{\partial v} \boldsymbol{\mathcal{G}}_n\, da = \int_v \boldsymbol{\mathcal{T}}\, dv, \tag{B.9}$$

where $\boldsymbol{\mathcal{H}}_n = (\boldsymbol{\mathcal{V}} \otimes \boldsymbol{v})\boldsymbol{n}$ are the normal convective fluxes. The Eulerian description for the mixed system of conservation laws (B.3,B.4,B.5,B.6,B.7) is

$$\int_v \frac{\partial}{\partial t}(\rho \boldsymbol{v}) dv = \int_{\partial v} \boldsymbol{\sigma}\boldsymbol{n} da - \int_{\partial v} \rho(\boldsymbol{v} \otimes \boldsymbol{v})\boldsymbol{n}\, da + \int_v \rho \boldsymbol{b} dv, \tag{B.10}$$

$$\int_v \frac{\partial}{\partial t}(J^{-1}\boldsymbol{F})\, dv = \int_{\partial v} (\boldsymbol{v} \otimes \boldsymbol{H}^{-1})\boldsymbol{n}\, da - \int_{\partial v} J^{-1}(\boldsymbol{F} \otimes \boldsymbol{v})\boldsymbol{n}\, da, \tag{B.11}$$

$$\int_v \frac{\partial}{\partial t}(J^{-1}J)\, dv = \int_{\partial v} \boldsymbol{v} \cdot \boldsymbol{n}\, da - \int_{\partial v} \boldsymbol{v} \cdot \boldsymbol{n}\, da = 0, \tag{B.12}$$

$$\int_v \frac{\partial}{\partial t}(J^{-1}\boldsymbol{H})\, dv = -\int_{\partial v} \boldsymbol{\mathcal{L}}\boldsymbol{n}\, da - \int_{\partial v} J^{-1}(\boldsymbol{H} \otimes \boldsymbol{v})\boldsymbol{n}, \tag{B.13}$$

$$\begin{aligned}\int_v \frac{\partial}{\partial t}(J^{-1}E)\, dv = &\int_{\partial v} \boldsymbol{\sigma}\boldsymbol{n} \cdot \boldsymbol{v}\, da + \int_v \rho \boldsymbol{b} \cdot \boldsymbol{v}\, dv - \int_{\partial v} \boldsymbol{q} \cdot \boldsymbol{n}\, da \\ &+ \int_v s J^{-1}\, dv - \int_{\partial v} J^{-1} E \boldsymbol{v} \cdot \boldsymbol{n}\, da.\end{aligned} \tag{B.14}$$

If equation (B.12) is replaced by the Eulerian form of the conservation of mass law

$$\int_v \frac{\partial \rho}{\partial t}\, dv = -\int_{\partial v} \rho \boldsymbol{v} \cdot \boldsymbol{n}\, da \tag{B.15}$$

equations (B.10), (B.14) and (B.15) form the Euler equations traditionally used when modelling inviscid flow (see [38, 56, 87]).

Appendix C

Polyconvexity

This chapter gives a brief introduction to polyconvex constitutive laws in solid mechanics. Next, it will present a framework for computing elastodynamics problems in the context of polyconvexity [110], which can be implemented using a Finite Volume Method algorithm as the one of the current thesis (see references [79, 80] for further details).

C.1 Constitutive laws

A polyconvex material is defined through a strain energy function ψ which is a function of $\boldsymbol{F}$ via a convex multi-valued function W as

$$\psi(\boldsymbol{F}) = W(\boldsymbol{F}, \boldsymbol{H}, J), \tag{C.1}$$

where invariance with respect to the rotations in the initial configuration implies that W must be a function of $\boldsymbol{F}$ and $\boldsymbol{H}$ via the symmetric tensor $\boldsymbol{C} = \boldsymbol{F}\boldsymbol{F}^T$ and $\boldsymbol{G} = \boldsymbol{H}\boldsymbol{H}^T$. The three strain measures $\boldsymbol{F}$, $\boldsymbol{H}$ and J have work conjugate stresses $\boldsymbol{\Sigma}_F$, $\boldsymbol{\Sigma}_H$ and $\boldsymbol{\Sigma}_J$ respectively defined as

$$\boldsymbol{\Sigma}_F(\boldsymbol{F}, \boldsymbol{H}, J) = \frac{\partial W}{\partial \boldsymbol{F}}; \quad \boldsymbol{\Sigma}_H(\boldsymbol{F}, \boldsymbol{H}, J) = \frac{\partial W}{\partial \boldsymbol{H}}; \quad \Sigma_J(\boldsymbol{F}, \boldsymbol{H}, J) = \frac{\partial W}{\partial J}. \tag{C.2}$$

The time derivative of the strain energy in terms of $\psi(\boldsymbol{F})$ can be written as

$$\dot{\psi}(\boldsymbol{F}) = \boldsymbol{P} : \dot{\boldsymbol{F}}, \tag{C.3}$$

whereas the time derivative of the strain energy in terms of $W(\boldsymbol{F}, \boldsymbol{H}, J)$ is obtained as

$$\begin{aligned}\dot{W}(\boldsymbol{F},\boldsymbol{H},J) &= \frac{\partial W}{\partial \boldsymbol{F}} : \dot{\boldsymbol{F}} + \frac{\partial W}{\partial \boldsymbol{H}} : \dot{\boldsymbol{H}} + \frac{\partial W}{\partial J}\dot{J} \\ &= \boldsymbol{\Sigma}_F : \dot{\boldsymbol{F}} + \boldsymbol{\Sigma}_H : \dot{\boldsymbol{H}} + \Sigma_J \dot{J} \\ &= \boldsymbol{\Sigma}_F : \dot{\boldsymbol{F}} + \boldsymbol{\Sigma}_H : (\boldsymbol{F} \times \dot{\boldsymbol{F}}) + \Sigma_J \boldsymbol{H} : \dot{\boldsymbol{F}} \\ &= (\boldsymbol{\Sigma}_F + \boldsymbol{\Sigma}_H \times \boldsymbol{F} + \Sigma_J \boldsymbol{H}) : \dot{\boldsymbol{F}}. \end{aligned} \tag{C.4}$$

Comparing equations (C.3) and (C.4) the first Piola-Kirchhoff stress tensor for a polyconvex material is given as

$$\boldsymbol{P} = \boldsymbol{\Sigma}_F + \boldsymbol{\Sigma}_H \times \boldsymbol{F} + \Sigma_J \boldsymbol{H}. \tag{C.5}$$

C.2 System of conservation laws

An alternative system of conservation laws to the one proposed in chapter 4 can be proposed using the variables involved in the polyconvex constitutive model defined in the previous section. By using equations (2.30), (2.58), (2.63) and (2.67) an alternative mixed system of conservation laws can be written as

$$\frac{\partial \boldsymbol{p}}{\partial t} - \mathrm{DIV}\, \boldsymbol{P} = \rho_0 \boldsymbol{b}, \tag{C.6a}$$

$$\frac{\partial \boldsymbol{F}}{\partial t} - \mathrm{DIV}\,(\boldsymbol{v} \otimes \boldsymbol{I}) = \boldsymbol{0}, \tag{C.6b}$$

$$\frac{\partial J}{\partial t} - \mathrm{DIV}(\boldsymbol{H}^T \boldsymbol{v}) = 0, \tag{C.6c}$$

$$\frac{\partial \boldsymbol{H}}{\partial t} - \mathrm{CURL}(\boldsymbol{v} \times \boldsymbol{F}) = \boldsymbol{0}, \tag{C.6d}$$

or, in integral form

$$\frac{d}{dt}\int_V \boldsymbol{p} dV = \int_{\partial V} \boldsymbol{t} dA + \int_V \rho_0 \boldsymbol{b} dV, \tag{C.7a}$$

$$\frac{d}{dt}\int_V \boldsymbol{F}\, dV = \int_{\partial V} \frac{1}{\rho_0} \boldsymbol{p} \otimes \boldsymbol{N}\, dA, \tag{C.7b}$$

$$\frac{d}{dt}\int_V J\, dV = \int_{\partial V} \boldsymbol{v} \cdot (\boldsymbol{H}\boldsymbol{N})\, dA, \tag{C.7c}$$

$$\frac{d}{dt}\int_V \boldsymbol{H}\, dV = -\int_{\partial V} (\boldsymbol{v} \times \boldsymbol{F} \times \boldsymbol{N}) dA, \tag{C.7d}$$

which can be rewritten in short form as

$$\frac{d}{dt}\int_V \boldsymbol{\mathcal{U}}\, dV = -\int_{\partial V} \boldsymbol{\mathcal{F}}_N\, dA + \int_V \boldsymbol{\mathcal{S}}\, dV, \tag{C.8}$$

where

$$\boldsymbol{\mathcal{U}} = \begin{pmatrix} \boldsymbol{p} \\ \boldsymbol{F} \\ J \\ \boldsymbol{H} \end{pmatrix}, \quad \boldsymbol{\mathcal{F}}_N = \begin{pmatrix} -\boldsymbol{t} \\ -\boldsymbol{v} \otimes \boldsymbol{N} \\ -\boldsymbol{v} \cdot (\boldsymbol{H}\boldsymbol{N}) \\ \boldsymbol{v} \times \boldsymbol{F} \times \boldsymbol{N} \end{pmatrix}, \quad \boldsymbol{\mathcal{S}} = \begin{pmatrix} \rho_0 \boldsymbol{b} \\ \boldsymbol{0} \\ 0 \\ \boldsymbol{0} \end{pmatrix}. \tag{C.9}$$

C.3 Hyperbolicity of the system

Following, it will be proved that the system (C.8) is hyperbolic when a polyconvex constitutive model is used. Using equation (2.15) in the system (C.8) gives

$$\begin{pmatrix} Dt\left[\boldsymbol{F}_\alpha^R, \boldsymbol{H}_\alpha^R, J_\alpha^R\right] \\ \boldsymbol{v}_\alpha^R \otimes \boldsymbol{N} \\ \boldsymbol{v}_\alpha^R \times \boldsymbol{F} \times \boldsymbol{N} + \boldsymbol{v} \times \boldsymbol{F}_\alpha^R \times \boldsymbol{N} \\ \boldsymbol{v}_\alpha^R \cdot (\boldsymbol{H}\boldsymbol{N}) + \boldsymbol{v} \cdot (\boldsymbol{H}_\alpha^R \boldsymbol{N}) \end{pmatrix} = c_\alpha \begin{pmatrix} -\rho_0 \boldsymbol{v}_\alpha^R \\ -\boldsymbol{F}_\alpha^R \\ \boldsymbol{H}_\alpha^R \\ -J_\alpha^R \end{pmatrix}. \tag{C.10}$$

Considering the cases where $c_\alpha \neq 0$, the second equation gives

$$\boldsymbol{F}_\alpha^R = -\frac{1}{c_\alpha} \boldsymbol{v}_\alpha^R \otimes \boldsymbol{N}, \tag{C.11}$$

which implies $\boldsymbol{v} \times \boldsymbol{F}_\alpha^R \times \boldsymbol{N} = \boldsymbol{0}$. Replacing this result into the third equation of (C.10) renders

$$\boldsymbol{H}_\alpha^R = \frac{1}{c_\alpha} \boldsymbol{v}_\alpha^R \times \boldsymbol{F} \times \boldsymbol{N} = -\frac{1}{c_\alpha} \boldsymbol{F} \times (\boldsymbol{v}_\alpha^R \otimes \boldsymbol{N}) \tag{C.12}$$

and this in turn implies $\boldsymbol{H}_\alpha^R \boldsymbol{N} = \boldsymbol{0}$ which replaced into the last equation results into

$$J_\alpha^R = -\frac{1}{c_\alpha} \boldsymbol{v}_\alpha^R \cdot (\boldsymbol{H}\boldsymbol{N}) = -\frac{1}{c_\alpha} \boldsymbol{H} : (\boldsymbol{v}_\alpha^R \otimes \boldsymbol{N}). \tag{C.13}$$

Using equations (C.11), (C.12) and (C.13) into the first equation, the following result is obtained

$$Dt\left[\boldsymbol{v}_\alpha^R \otimes \boldsymbol{N},\, \boldsymbol{F} \times (\boldsymbol{v}_\alpha^R \otimes \boldsymbol{N}),\, \boldsymbol{H} : (\boldsymbol{v}_\alpha^R \otimes \boldsymbol{N})\right] = \rho_0 c_\alpha^2 \boldsymbol{v}_\alpha^R,$$

which can be rewritten in a weak manner premultiplying it by a generic virtual velocity $\delta\boldsymbol{v}$ to obtain

$$(\delta\boldsymbol{v} \otimes \boldsymbol{N}) : D\boldsymbol{P}\left[\boldsymbol{v}_\alpha^R \otimes \boldsymbol{N},\, \boldsymbol{F} \times (\boldsymbol{v}_\alpha^R \otimes \boldsymbol{N}),\, \boldsymbol{H} : (\boldsymbol{v}_\alpha^R \otimes \boldsymbol{N})\right] = \rho_0 c_\alpha^2 \delta\boldsymbol{v} \cdot \boldsymbol{v}_\alpha^R,$$

which has to be fulfilled for any value of $\delta\boldsymbol{v}$. Using the definition of $\boldsymbol{P}$ according to the polyconvex constitutive model (equation (C.5)) gives

$$
\begin{aligned}
&(\delta\boldsymbol{v}\otimes\boldsymbol{N}) : D\boldsymbol{P}\left[\boldsymbol{v}_\alpha^R\otimes\boldsymbol{N},\, \boldsymbol{F}\times(\boldsymbol{v}_\alpha^R\otimes\boldsymbol{N}),\, \boldsymbol{H} : (\boldsymbol{v}_\alpha^R\otimes\boldsymbol{N})\right] = \\
&= (\delta\boldsymbol{v}\otimes\boldsymbol{N}) : D(\boldsymbol{\Sigma}_F)\left[\boldsymbol{v}_\alpha^R\otimes\boldsymbol{N},\, \boldsymbol{F}\times(\boldsymbol{v}_\alpha^R\otimes\boldsymbol{N}),\, \boldsymbol{H} : (\boldsymbol{v}_\alpha^R\otimes\boldsymbol{N})\right] \\
&+ (\delta\boldsymbol{v}\otimes\boldsymbol{N}) : D(\boldsymbol{\Sigma}_H\times\boldsymbol{F})\left[\boldsymbol{v}_\alpha^R\otimes\boldsymbol{N},\, \boldsymbol{F}\times(\boldsymbol{v}_\alpha^R\otimes\boldsymbol{N}),\, \boldsymbol{H} : (\boldsymbol{v}_\alpha^R\otimes\boldsymbol{N})\right] \\
&+ (\delta\boldsymbol{v}\otimes\boldsymbol{N}) : D(\Sigma_J\boldsymbol{H})\left[\boldsymbol{v}_\alpha^R\otimes\boldsymbol{N},\, \boldsymbol{F}\times(\boldsymbol{v}_\alpha^R\otimes\boldsymbol{N}),\, \boldsymbol{H} : (\boldsymbol{v}_\alpha^R\otimes\boldsymbol{N})\right]. \qquad \text{(C.14)}
\end{aligned}
$$

The first term of the right hand side of (C.14) can be further expanded in the following manner

$$
\begin{aligned}
&(\delta\boldsymbol{v}\otimes\boldsymbol{N}) : D(\boldsymbol{\Sigma}_F)\left[\boldsymbol{v}_\alpha^R\otimes\boldsymbol{N},\, \boldsymbol{F}\times(\boldsymbol{v}_\alpha^R\otimes\boldsymbol{N}),\, \boldsymbol{H} : (\boldsymbol{v}_\alpha^R\otimes\boldsymbol{N})\right] \\
&=(\delta\boldsymbol{v}\otimes\boldsymbol{N}) : \left(\frac{\partial^2 W}{\partial\boldsymbol{F}\partial\boldsymbol{F}} : (\boldsymbol{v}_\alpha^R\otimes\boldsymbol{N}) + \frac{\partial^2 W}{\partial\boldsymbol{F}\partial\boldsymbol{H}} : (\boldsymbol{F}\times(\boldsymbol{v}_\alpha^R\otimes\boldsymbol{N})) + \frac{\partial^2 W}{\partial\boldsymbol{F}\partial J}(\boldsymbol{H} : (\boldsymbol{v}_\alpha^R\otimes\boldsymbol{N}))\right),
\end{aligned}
$$

proceeding in the same manner for the second term gives

$$
\begin{aligned}
&(\delta\boldsymbol{v}\otimes\boldsymbol{N}) : D(\boldsymbol{\Sigma}_H\times\boldsymbol{F})\left[\boldsymbol{v}_\alpha^R\otimes\boldsymbol{N},\, \boldsymbol{F}\times(\boldsymbol{v}_\alpha^R\otimes\boldsymbol{N}),\, \boldsymbol{H} : (\boldsymbol{v}_\alpha^R\otimes\boldsymbol{N})\right] \\
&=((\delta\boldsymbol{v}\otimes\boldsymbol{N})\times\boldsymbol{F}) : \left(\frac{\partial^2 W}{\partial\boldsymbol{H}\partial\boldsymbol{F}} : (\boldsymbol{v}_\alpha^R\otimes\boldsymbol{N}) + \frac{\partial^2 W}{\partial\boldsymbol{H}\partial\boldsymbol{H}} : (\boldsymbol{F}\times(\boldsymbol{v}_\alpha^R\otimes\boldsymbol{N})) + \frac{\partial^2 W}{\partial\boldsymbol{H}\partial J}(\boldsymbol{H} : \boldsymbol{v}_\alpha^R\otimes\boldsymbol{N}\right.
\end{aligned}
$$

and finally the last term,

$$
\begin{aligned}
&(\delta\boldsymbol{v}\otimes\boldsymbol{N}) : D(\Sigma_J\boldsymbol{H})\left[\boldsymbol{v}_\alpha^R\otimes\boldsymbol{N},\, \boldsymbol{F}\times(\boldsymbol{v}_\alpha^R\otimes\boldsymbol{N}),\, \boldsymbol{H} : (\boldsymbol{v}_\alpha^R\otimes\boldsymbol{N})\right] \\
&=((\delta\boldsymbol{v}\otimes\boldsymbol{N}) : \boldsymbol{H})\left(\frac{\partial^2 W}{\partial J\partial\boldsymbol{F}} : (\boldsymbol{v}_\alpha^R\otimes\boldsymbol{N}) + \frac{\partial^2 W}{\partial J\partial\boldsymbol{H}} : (\boldsymbol{F}\times(\boldsymbol{v}_\alpha^R\otimes\boldsymbol{N})) + \frac{\partial^2 W}{\partial J\partial J}\boldsymbol{H} : \boldsymbol{v}_\alpha^R\otimes\boldsymbol{N}\right).
\end{aligned}
$$

The results above can be rewritten as

$$
\begin{pmatrix} (\delta\boldsymbol{v}\otimes\boldsymbol{N}) : & ((\delta\boldsymbol{v}\otimes\boldsymbol{N})\times\boldsymbol{F}) : & (\delta\boldsymbol{v}\otimes\boldsymbol{N}) : \boldsymbol{H} \end{pmatrix} \boldsymbol{\mathcal{H}}_W \begin{pmatrix} : (\boldsymbol{v}_\alpha^R\otimes\boldsymbol{N}) \\ : (\boldsymbol{F}\times(\boldsymbol{v}_\alpha^R\otimes\boldsymbol{N})) \\ \boldsymbol{H} : \boldsymbol{v}_\alpha^R\otimes\boldsymbol{N} \end{pmatrix} = \rho_0 c_0^2 \delta\boldsymbol{v}\cdot\boldsymbol{v}_\alpha^R, \qquad \text{(C.15)}
$$

where $\boldsymbol{\mathcal{H}}_W$ is the Hessian defined as

$$
\boldsymbol{\mathcal{H}}_W = \begin{pmatrix} \frac{\partial^2 W}{\partial\boldsymbol{F}\partial\boldsymbol{F}} & \frac{\partial^2 W}{\partial\boldsymbol{F}\partial\boldsymbol{H}} & \frac{\partial^2 W}{\partial\boldsymbol{F}\partial J} \\ \frac{\partial^2 W}{\partial\boldsymbol{H}\partial\boldsymbol{F}} & \frac{\partial^2 W}{\partial\boldsymbol{H}\partial\boldsymbol{H}} & \frac{\partial^2 W}{\partial\boldsymbol{H}\partial J} \\ \frac{\partial^2 W}{\partial J\partial\boldsymbol{F}} & \frac{\partial^2 W}{\partial J\partial\boldsymbol{H}} & \frac{\partial^2 W}{\partial J\partial J} \end{pmatrix}
$$

and therefore hyperbolicity will be ensured if the strain energy is polyconvex. Consider the particular strain energy, which is polyconvex in $\boldsymbol{F}$ and J,

$$
W(\boldsymbol{F}, J) = \frac{1}{2}(\boldsymbol{F} : \boldsymbol{F} - 3) - \mu\ln J + \frac{\lambda}{2}(J-1)^2,
$$

the Hessian is given by

$$\mathcal{H}_W = \begin{pmatrix} 2\mu\mathcal{I} & \mathbf{0} & \mathbf{0} \\ \mathbf{0} & \mathbf{0} & \mathbf{0} \\ \mathbf{0} & \mathbf{0} & \frac{\mu}{J^2} + \lambda \end{pmatrix},$$

where

$$\mathcal{I}_{iIjJ} = \delta_{ij}\delta_{IJ}$$

Using this particular Hessian in (C.15) gives

$$\mu\delta\boldsymbol{v}\cdot\boldsymbol{v}_\alpha^R + \left(\frac{\mu}{J^2}+\lambda\right)(\boldsymbol{h}\cdot\delta\boldsymbol{v})\left(\boldsymbol{h}\cdot\boldsymbol{v}_\alpha^R\right) = \rho_0 c_\alpha^2 \delta\boldsymbol{v}\cdot\boldsymbol{v}_\alpha^R, \tag{C.16}$$

which is the characteristic equation of the system for this particular strain energy. The first two wave families are obtained setting $\boldsymbol{v}_\alpha^R = \boldsymbol{n}$. Replacing in (C.16) gives

$$\mu\delta\boldsymbol{v}\cdot\boldsymbol{n} + \left(\frac{\mu}{J^2}+\lambda\right)(h\boldsymbol{n}\cdot\delta\boldsymbol{v})(h\boldsymbol{n}\cdot\boldsymbol{n}) = \rho_0 c_p^2\delta\boldsymbol{v}\cdot\boldsymbol{n},$$

and finally

$$c_{1,2} = \pm c_p; \qquad c_p = \sqrt{\frac{\mu}{\rho_0} + \frac{h^2}{\rho_0}\left(\frac{\mu}{J^2}+\lambda\right)}.$$

On the other hand, the third to sixth wave families are obtained using two arbitrary vectors orthogonal to $\boldsymbol{n}$, that is $\boldsymbol{v}_\alpha^R = \boldsymbol{t}_i$, $i = \{1,2\}$. Replacing in (C.16) gives

$$\mu\delta\boldsymbol{v}\cdot\boldsymbol{t}_\alpha = \rho_0 c_s^2\delta\boldsymbol{v}\cdot\boldsymbol{t}_\alpha$$

and the wave speeds are given by

$$c_{3,4} = c_{5,6} = \pm c_s; \qquad c_s = \pm\sqrt{\frac{\mu}{\rho_0}}$$

and it can be seen that the system is always hyperbolic. Finally, the right eigenvectors are given by

$$\mathcal{U}_R^{1,2} = \begin{pmatrix} \boldsymbol{n} \\ \pm\frac{1}{c_p}\boldsymbol{n}\otimes\boldsymbol{N} \\ \pm\frac{1}{c_p}\boldsymbol{F}\times(\boldsymbol{n}\otimes\boldsymbol{N}) \\ \pm\frac{1}{c_p}\boldsymbol{H}:(\boldsymbol{v}_\alpha^R\otimes\boldsymbol{N}) \end{pmatrix}; \quad \mathcal{U}_R^{3,4} = \begin{pmatrix} \boldsymbol{t}_1 \\ \pm\frac{1}{c_p}\boldsymbol{t}_1\otimes\boldsymbol{N} \\ \pm\frac{1}{c_p}\boldsymbol{F}\times(\boldsymbol{t}_1\otimes\boldsymbol{N}) \\ 0 \end{pmatrix}; \quad \mathcal{U}_R^{5,6} = \begin{pmatrix} \boldsymbol{t}_2 \\ \pm\frac{1}{c_p}\boldsymbol{t}_2\otimes\boldsymbol{N} \\ \pm\frac{1}{c_p}\boldsymbol{F}\times(\boldsymbol{t}_2\otimes\boldsymbol{N}) \\ 0 \end{pmatrix}.$$

Appendix D

Vertex centred finite volume and Galerkin Finite Element

D.1 Preliminaries

In this appendix, the vertex centred Finite Volume will be compared to the Finite Element Galerkin formulation. In D.2, the Finite Element discretisation of a conservation law will be briefly summarised. In D.3 this discretisation will be reordered in order to prove that, for an interior node, is equivalent to a Finite Volume discretisation using central differences and a median dual mesh. Finally, in D.4 the weights used for the boundary contribution in section 5.4 will be explained from a Finite Element point of view. The comparison will be carried out for a two dimensional case, but this same procedure can be easily extended to three dimensions.

D.2 Finite Element discretisation of a conservation law

A conservation law of the type of equation (2.9) can be written in variational form as [52,87],

$$\int_V \delta\boldsymbol{\mathcal{V}} \cdot \frac{\partial \boldsymbol{\mathcal{U}}}{\partial t}\, dV - \int_V \nabla_0 \delta\boldsymbol{\mathcal{V}} : \boldsymbol{\mathcal{F}}(\boldsymbol{\mathcal{U}})\, dV + \int_{\partial V} \delta\boldsymbol{\mathcal{V}} \cdot \boldsymbol{\mathcal{F}}_{\boldsymbol{N}}\, dA = \mathbf{0} \qquad \text{(D.1)}$$

where $\delta\boldsymbol{\mathcal{V}}$ are a set of test functions satisfying homogeneous boundary conditions on the Dirichlet Boundaries Γ_D. By choosing a specific discretisation, the following discretised variational formulation is obtained

$$\int_V \delta\boldsymbol{\mathcal{V}}^h \cdot \frac{\partial \boldsymbol{\mathcal{U}}^h}{\partial t}\, dV - \int_V \nabla_0 \delta\boldsymbol{\mathcal{V}}^h : \boldsymbol{\mathcal{F}}(\boldsymbol{\mathcal{U}}^h)\, dV + \int_{\partial V} \delta\boldsymbol{\mathcal{V}}^h \cdot \boldsymbol{\mathcal{F}}_{\boldsymbol{N}}\, dA = \mathbf{0} \qquad \text{(D.2)}$$

where $\delta\boldsymbol{\mathcal{V}}^h$ and $\boldsymbol{\mathcal{U}}^h$ are, respectively, the discretised test functions and solution. The Galerkin discretisation is obtained using the same interpolation functions both for the discretised solution $\boldsymbol{\mathcal{U}}^h$ and the test functions $\delta\boldsymbol{\mathcal{V}}^h$ as

$$\delta\boldsymbol{\mathcal{V}}^h = \sum_{a=1}^{n} N_a \delta\boldsymbol{\mathcal{V}}_a, \tag{D.3}$$

$$\boldsymbol{\mathcal{U}}^h = \sum_{b=1}^{n} N_b \boldsymbol{\mathcal{U}}_b, \tag{D.4}$$

by using these relations, equation (D.1) can be written as

$$\sum_{a=1}^{n} \delta\boldsymbol{V}_a \cdot \left(\int_V N_a \frac{\partial \boldsymbol{\mathcal{U}}^h}{\partial t}\, dV - \int_V \boldsymbol{\mathcal{F}}(\boldsymbol{\mathcal{U}}^h) \nabla_0 N_a\, dV + \int_{\partial V} N_a \boldsymbol{\mathcal{F}}_{\boldsymbol{N}}\, dA \right) = 0 \tag{D.5}$$

and since the equation above has to be satisfied for all $\delta\boldsymbol{V}_a$, the following is verified,

$$\int_V N_a \frac{\partial \boldsymbol{\mathcal{U}}^h}{\partial t}\, dV - \int_V \boldsymbol{\mathcal{F}}(\boldsymbol{\mathcal{U}}^h) \nabla_0 N_a\, dV + \int_{\partial V} N_a \boldsymbol{\mathcal{F}}_{\boldsymbol{N}}\, dA = \mathbf{0}. \tag{D.6}$$

D.3 Interior nodes

For an interior node a, equation D.6 is reduced into

$$\int_V N_a \frac{\partial \boldsymbol{\mathcal{U}}^h}{\partial t}\, dV - \int_V \boldsymbol{\mathcal{F}}(\boldsymbol{\mathcal{U}}^h) \nabla_0 N_a\, dV = \mathbf{0} \tag{D.7}$$

Using (D.4) and a linear interpolation of fluxes

$$\boldsymbol{\mathcal{F}}(\boldsymbol{\mathcal{U}}^h) = \sum_b \boldsymbol{\mathcal{F}}(\boldsymbol{\mathcal{U}}_b) N_b, \tag{D.8}$$

equation (D.7) can be extended as

$$\begin{aligned} \sum_{b \in \Lambda_a} \frac{\partial \boldsymbol{\mathcal{U}}_b}{\partial t} \int_V N_a N_b\, dV &= \sum_{e \ni a} \left(\int_{V_e} \sum_{c \in e} \boldsymbol{\mathcal{F}}(\boldsymbol{\mathcal{U}}_c) N_c \nabla_0 N_a\, dV \right) \\ \sum_{\alpha \in \Lambda_a} \frac{\partial \boldsymbol{\mathcal{U}}_b}{\partial t} \int_V N_a N_b\, dV &= \sum_{e \ni a} \frac{A_e}{3} \left(\sum_{c \in e} \boldsymbol{\mathcal{F}}(\boldsymbol{\mathcal{U}}_c) \right) \nabla_0 N_a^e. \end{aligned} \tag{D.9}$$

Assuming the use of linear shape functions, for a given shape function N_a, evaluated at an element e formed by nodes a, b and c (see Figure D.1a), the following holds

$$\int_V \nabla_0 N_a^e\, dV = \int_{V_e} \nabla_0 N_a^e\, dV = \int_{\partial V_e} N_a^e \boldsymbol{N}\, dA = \frac{l_b^e}{2} \boldsymbol{N}_b^e + \frac{l_c^e}{2} \boldsymbol{N}_c^e = \frac{1}{2} \left(\boldsymbol{N}_b^e l_b^e + \boldsymbol{N}_c^e l_c^e \right), \tag{D.10}$$

where l_b^e, $\boldsymbol{N}_b^e$ are the length and normal vector of the edge opposite to node b at element e (see Figure D.1b). Taking into account

$$\boldsymbol{N}_a^e l_a^e + \boldsymbol{N}_b^e l_b^e + \boldsymbol{N}_c^e l_c^e = \int_{\partial V_e} \boldsymbol{N}\, dA = \boldsymbol{0} \tag{D.11}$$

and using $\int_{V_e} \nabla_0 N_a^e\, dV = A_e \nabla_0 N_a^e$, the gradient within an element e can be written as

$$\nabla_0 N_a^e = -\frac{l_a^e}{2A_e} \boldsymbol{N}_a^e. \tag{D.12}$$

This result can be replaced into (D.9) to give

$$\sum_{b\in\Lambda_a} \frac{\partial \boldsymbol{\mathcal{U}}_b}{\partial t} \int_V N_a N_b\, dV = \sum_{\substack{e\ni a \\ b,c\in e}} -\frac{l_a^e}{6} \left(\boldsymbol{\mathcal{F}}(\boldsymbol{\mathcal{U}}_a) + \boldsymbol{\mathcal{F}}(\boldsymbol{\mathcal{U}}_b) + \boldsymbol{\mathcal{F}}(\boldsymbol{\mathcal{U}}_c)\right) \boldsymbol{N}_a^e \tag{D.13}$$

$$= \sum_{\substack{e\ni a \\ b,c\in e}} -\frac{l_a^e}{6} \left(\boldsymbol{\mathcal{F}}(\boldsymbol{\mathcal{U}}_a) + \boldsymbol{\mathcal{F}}(\boldsymbol{\mathcal{U}}_b)\right) \boldsymbol{N}_a^e - \frac{l_a^e}{6} \left(\boldsymbol{\mathcal{F}}(\boldsymbol{\mathcal{U}}_a) + \boldsymbol{\mathcal{F}}(\boldsymbol{\mathcal{U}}_c)\right) \boldsymbol{N}_a^e \tag{D.14}$$

where the following has been taken into account

$$\sum_{e\ni a} l_a^e \boldsymbol{N}_a^e = \boldsymbol{0}. \tag{D.15}$$

The above can be rewritten as a sum over nodes b connected to a in the following manner

$$\sum_{b\in\Lambda_a} \frac{\partial \boldsymbol{\mathcal{U}}_b}{\partial t} \int_V N_a N_b\, dV = \sum_{\substack{b\in\Lambda_a \\ e_1,e_2\ni ea}} -\frac{1}{6} \left(\boldsymbol{\mathcal{F}}(\boldsymbol{\mathcal{U}}_a) + \boldsymbol{\mathcal{F}}(\boldsymbol{\mathcal{U}}_b)\right) (l_a^{e_1} \boldsymbol{N}_a^{e_1} + l_a^{e_2} \boldsymbol{N}_a^{e_2}). \tag{D.16}$$

It is easily proved that the following identity holds (see Figures D.2a and D.2b)

$$l_a^{e_1} \boldsymbol{N}_a^{e_1} + l_a^{e_2} \boldsymbol{N}_a^{e_2} = l_{ab}^1 \boldsymbol{N}_{ab}^1 + l_{ab}^2 \boldsymbol{N}_{ab}^2 = 3\boldsymbol{C}^{ab}, \tag{D.17}$$

where l_{ab}^i and $\boldsymbol{N}_{ab}^i$ stands for the medial i that goes from the midpoint of edge ab to the opposed vertex in element e_i and $\boldsymbol{C}^{ab}$ is given by equation (5.6). Replacing this result in (D.16) renders

$$\sum_{b\in\Lambda_a} \frac{\partial \boldsymbol{\mathcal{U}}_b}{\partial t} \int_V N_a N_b\, dV = \sum_{b\in\Lambda_a} -\frac{1}{2} (\boldsymbol{\mathcal{F}}(\boldsymbol{\mathcal{U}}_a) + \boldsymbol{\mathcal{F}}(\boldsymbol{\mathcal{U}}_b)) \boldsymbol{C}^{ab}, \tag{D.18}$$

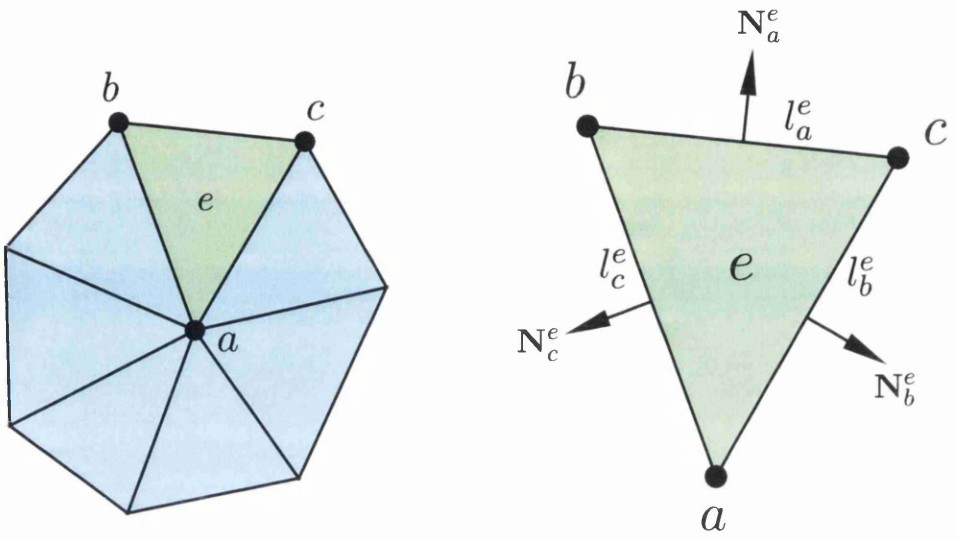

(a) (b)

Figure D.1: Set of triangular elements e to which the node a belongs (a) and notation for the normal vectors and lengths of the edges of a triangular element (b).

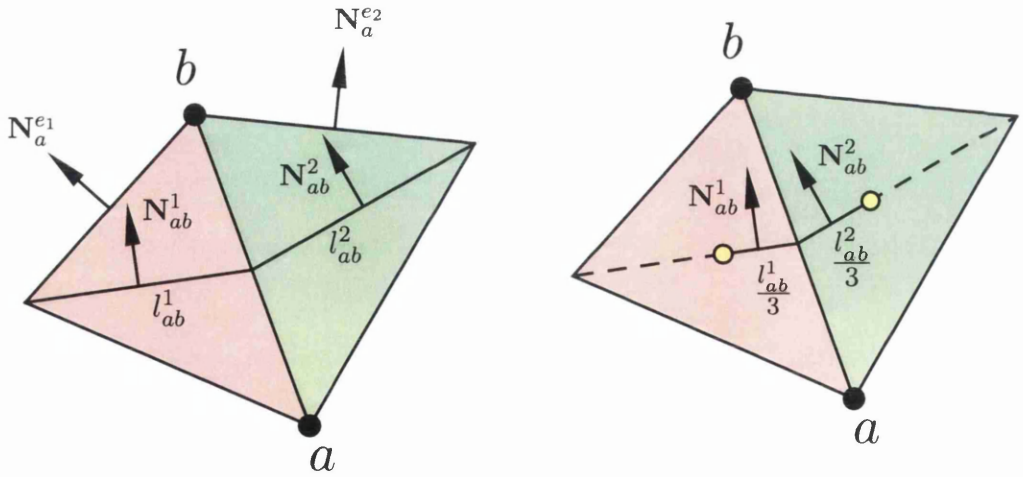

(a) (b)

Figure D.2: Normal vectors and lengths of the median line connecting the midpoint of edge ab with the opposite vertexes of its surrounding elements (a) and segments of these median lines corresponding to the dual mesh (b).

Finally, by using a lumped mass matrix, the above is written as

$$\frac{\partial \boldsymbol{\mathcal{U}}_a}{\partial t} = \frac{1}{V_a} \sum_{\alpha \in \Lambda_a} -\frac{1}{2}(\boldsymbol{\mathcal{F}}(\boldsymbol{\mathcal{U}}_a) + \boldsymbol{\mathcal{F}}(\boldsymbol{\mathcal{U}}_b))\boldsymbol{C}^{ab} \tag{D.19}$$

where

$$V_a = \int_V N_a \, dV \tag{D.20}$$

which is identical to the interior contribution of (5.7) for the Finite Volume Method.

D.4 Boundary contribution

Using the linear interpolation of fluxes (equation (D.8)), the boundary contribution of equation (D.6) is written as

$$\int_{\partial V} N_a \boldsymbol{\mathcal{F}}_{\boldsymbol{N}}(\boldsymbol{\mathcal{U}}^h) \, dA = \sum_b \boldsymbol{\mathcal{F}}(\boldsymbol{\mathcal{U}}_b) \int_{\partial V} N_a N_b \boldsymbol{N} \, dA \tag{D.21}$$

$$\int_{\partial V} N_a \boldsymbol{\mathcal{F}}_{\boldsymbol{N}}(\boldsymbol{\mathcal{U}}^h) \, dA = \sum_b m_{ab} \boldsymbol{\mathcal{F}}(\boldsymbol{\mathcal{U}}_b) \boldsymbol{N}_{ab} \tag{D.22}$$

where m_{ab} are the components of the mass matrix $\boldsymbol{m}$. As recommended in [91], a combination of consistent mass matrix and lump mass matrix coefficients is used at the boundaries (see as well [8]). This gives, for a two dimensional case,

$$\frac{1}{2}\left(\boldsymbol{m}^C + \boldsymbol{m}^L\right) = \frac{l_{ab}}{12} \begin{pmatrix} 5 & 1 \\ 1 & 5 \end{pmatrix} \tag{D.23}$$

therefore

$$\int_{\partial V} N_a \boldsymbol{F}_{\boldsymbol{N}}(\boldsymbol{\mathcal{U}}^h) \, dA = \sum_{\alpha \in \Lambda_a^B} \frac{5\boldsymbol{\mathcal{F}}(\boldsymbol{\mathcal{U}}_a) + \boldsymbol{\mathcal{F}}(\boldsymbol{\mathcal{U}}_b)}{6} \boldsymbol{N}_{e\alpha} \frac{l_{e\alpha}}{2} \tag{D.24}$$

For the three dimensional case, the coefficients are obtained as

$$\frac{1}{2}\left(\boldsymbol{m}^C + \boldsymbol{m}^L\right) = \frac{A_{abc}}{24} \begin{pmatrix} 6 & 1 & 1 \\ 1 & 6 & 1 \\ 1 & 1 & 6 \end{pmatrix} \tag{D.25}$$

which gives,

$$\int_{\partial V} N_a \boldsymbol{F}_{\boldsymbol{N}}(\boldsymbol{\mathcal{U}}^h) \, dA = \sum_{\alpha \in \Lambda_a^B} \sum_{c \in (\Lambda_a^B \bigcap \Lambda_b^B)} \frac{2\boldsymbol{\mathcal{F}}(\boldsymbol{\mathcal{U}}_a) + \boldsymbol{\mathcal{F}}(\boldsymbol{\mathcal{U}}_b) + \boldsymbol{\mathcal{F}}(\boldsymbol{\mathcal{U}}_c)}{4} \boldsymbol{N}_{abc} \frac{A_{abc}}{3} \tag{D.26}$$

Appendix E

Geometrical Weights

The geometrical weights are obtained as proposed in [48] by means of a Lagrange multiplier minimisation procedure. A set of numerical weights θ_{ab} are proposed such that the second order differences cancel for a linear field. This is,

$$\boldsymbol{L}(\boldsymbol{X}_a) = \sum_{b \in \Lambda_a} \theta_{ab}(\boldsymbol{X}_b - \boldsymbol{X}_a) = \boldsymbol{0}. \tag{E.1}$$

The minimisation procedure consists in finding the values θ_{ab} closest as possible to 1, such that satisfy equation (E.1). This is achieved defining the geometrical weights as

$$\theta_{ab} = 1 + \Delta\theta_{ab}$$

and minimising for $\Delta\theta_{ab}$. To do so, the following functional is defined

$$\Pi(\Delta\theta_{ab}, \boldsymbol{\lambda}) = \frac{1}{2}\sum_{b \in \Lambda_a}(\Delta\theta_{ab})^2 + \boldsymbol{\lambda} \cdot \sum_{b \in \Lambda_a}(1 + \Delta\theta_{ab})(\boldsymbol{X}_b - \boldsymbol{X}_a) \tag{E.2}$$

where the first part is a cost function that will ensure that the weights are as closest to unity as possible, whereas the second part is the actual constraint, where $\boldsymbol{\lambda}$ is the Lagrange multiplier. The minimisation of this function with respect to $\boldsymbol{\lambda}$ and $\Delta\theta_{ab}$ gives the following system of equations

$$\boldsymbol{K}_a\boldsymbol{\lambda} = \boldsymbol{b}_a, \tag{E.3}$$

where

$$\begin{aligned}
\boldsymbol{K}_a &= \sum_{b \in \Lambda_a}(\boldsymbol{X}_b - \boldsymbol{X}_a) \otimes (\boldsymbol{X}_b - \boldsymbol{X}_a), \\
\boldsymbol{b}_a &= \sum_{b \in \Lambda_a}(\boldsymbol{X}_b - \boldsymbol{X}_a).
\end{aligned}$$

Once the Lagrange multiplier $\boldsymbol{\lambda}$ is obtained, the geometrical weights are obtained as

$$\theta_{ab} = 1 - \boldsymbol{\lambda} \cdot (\boldsymbol{X}_b - \boldsymbol{X}_a). \tag{E.4}$$

And since this is a total Lagrangian framework, these geometrical weights will need to be calculated once per simulation (pre-processing).

Bibliography

[1] C. H. Lee, A. J. Gil, and J. Bonet. Development of a cell centred upwind Finite Volume algorithm for a new conservation law formulation in structural dynamics. *Computers & Structures*, 118:13 – 38, 2013. Special Issue: UK Association for Computational Mechanics in Engineering.

[2] C. H. Lee, A. J. Gil, and J. Bonet. Development of a stabilised Petrov-Galerkin formulation for conservation laws in Lagrangian fast solid dynamics. *Computer Methods in Applied Mechanics and Engineering*, 268:40 – 64, 2014.

[3] I. A. Karim, C. H. Lee, A. J. Gil, and J. Bonet. A two-step Taylor Galerkin formulation for fast dynamics. *Engineering Computations*, 31:366–387, 2013.

[4] N.C. Nguyen and J. Peraire. Hybridizable Discontinuous Galerkin Methods for partial differential equations in continuum mechanics. *Journal of Computational Physics*, 231(18):5955 – 5988, 2012.

[5] A. Jameson, W. Schmidt, and E. Turkel. Numerical solution of the Euler equations by Finite Volume methods using Runge-Kutta time-stepping schemes. *AIAA 5th Computational Fluid Dynamics Conference*, 81:1259, 1981.

[6] D. J. Benson. Computational methods in Lagrangian and Eulerian hydrocodes. *Computer Methods in Applied Mechanics and Engineering*, 99(23):235 – 394, 1992.

[7] J. O. Hallquist. *LS-DYNA theoretical manual.* Livermore Software Technology Corporation, 1998.

[8] T. J. R. Hughes. *The Finite Element Method. Linear Static and Dynamic Finite Element Analysis.* Dover Publications, 2000.

[9] Hibbitt, Karlsson, and Inc. Sorensen. *ABAQUS Explicit.* ABAQUS/Explicit: User's Manual. 1996.

[10] J. Bonet and R. D. Wood. *Nonlinear Continuum Mechanics for Finite Element Analysis.* Cambridge University Press, 2nd edition, 2008.

[11] G. A. Holzapfel. *Nonlinear solid mechanics: a continuum approach for engineering.* Wiley, 2000.

[12] F. M. Capaldi. *Continuum Mechanics. Constitutive Modeling of Structural and Biological Materials.* Cambridge University Press, 2012.

[13] T. A. Laursen. *Computational contact and impact mechanics*, volume 38. Springer, 2003.

[14] E. J. Kubatko, C. Dawson, and J. J. Westerink. Time step restrictions for Runge - Kutta discontinuous galerkin methods on triangular grids. *Journal of Computational Physics*, 227(23):9697 – 9710, 2008.

[15] P. George and H. Borouchaki. *Delaunay Triangulation and Meshing.* Hermes, 1998.

[16] P.J. Frey and P. George. *Mesh Generation. Application to Finite Elements.* Hermes Science, 2000.

[17] C. H. Lee. *Development of an upwind Finite Volume Algorithm for a New Conservation Law Formulation in Structural Dynamics.* PhD thesis, Department of Civil Engineering. University of Wales. Swansea, 2011.

[18] H. M. Hilber, T. J. R. Hughes, and R. L. Taylor. Improved numerical dissipation for time integration algorithms in structural dynamics. *Earthquake Engineering & Structural Dynamics*, 5(3):283–292, 1977.

[19] W. L. Wood, M. Bossak, and O. C. Zienkiewicz. An alpha modification of Newmark's method. *International Journal for Numerical Methods in Engineering*, 15(10):1562–1566, 1980.

[20] D. D. Adams and W. L. Wood. Comparison of Hilber-Hughes-Taylor and Bossak α methods for the numerical integration of vibration equations. *International Journal for Numerical Methods in Engineering*, 19(5):765–771, 1983.

[21] J. Chung and G. M. Hulbert. A time integration algorithm for structural dynamics with improved numerical dissipation: The generalized α method. *Journal of Applied Mechanics*, 60(2):371–375, June 1993.

[22] A.F. Bower. *Applied Mechanics of Solids.* Taylor & Francis, 2011.

[23] K. Washizu. *Variational Methods in Elasticity and Plasticity.* 01. Elsevier Science & Technology, 1974.

[24] J. Bonet and A. J. Burton. A simple average nodal pressure tetrahedral element for incompressible and nearly incompressible dynamic explicit applications. *Communications in Numerical Methods in Engineering*, 14(5):437–449, 1998.

[25] J. Bonet, H. Marriott, and O. Hassan. Stability and comparison of different linear tetrahedral formulations for nearly incompressible explicit dynamic applications. *International Journal for Numerical Methods in Engineering*, 50(1):119–133, 2001.

[26] C.R. Dohrmann, M. W. Heinstein, J. Jung, S. W. Key, and W. R. Witkowski. Node-based uniform strain elements for three-node triangular and four-

node tetrahedral meshes. *International Journal for Numerical Methods in Engineering*, 47(9):1549–1568, 2000.

[27] J. Bonet, H. Marriott, and O. Hassan. An averaged nodal deformation gradient linear tetrahedral element for large strain explicit dynamic applications. *Communications in Numerical Methods in Engineering*, 17(8):551–561, 2001.

[28] S. K. Lahiri, J. Bonet, and J. Peraire. A variationally consistent mesh adaptation method for triangular elements in explicit Lagrangian dynamics. *International Journal for Numerical Methods in Engineering*, 82(9):1073–1113, 2010.

[29] M. W. Gee, C. R. Dohrmann, S. W. Key, and W. A. Wall. A uniform nodal strain tetrahedron with isochoric stabilization. *International Journal for Numerical Methods in Engineering*, 78(4):429–443, 2009.

[30] M. A. Puso and J. Solberg. A stabilized nodally integrated tetrahedral. *International Journal for Numerical Methods in Engineering*, 67(6):841–867, 2006.

[31] M. Aguirre, A. J. Gil, J. Bonet, and A. Arranz-Carreño. A vertex centred Finite Volume Jameson-Schmidt-Turkel (JST) algorithm for a mixed conservation formulation in solid dynamics. *Journal of Computational Physics*, 259(0):672 – 699, 2014.

[32] S. K. Lahiri, J. Bonet, J. Peraire, and L. Casals. A variationally consistent fractional time-step integration method for incompressible and nearly incompressible Lagrangian dynamics. *International Journal for Numerical Methods in Engineering*, 63(10):1371–1395, 2005.

[33] G. Scovazzi. Stabilized shock Hydrodynamics: II. Design and physical interpretation of the SUPG operator for Lagrangian computations. *Computer Methods in Applied Mechanics and Engineering*, 196(46):967 – 978, 2007.

[34] G. Scovazzi, M.A. Christon, T.J.R. Hughes, and J.N. Shadid. Stabilized shock Hydrodynamics: I. a Lagrangian method. *Computer Methods in Applied Mechanics and Engineering*, 196(46):923 – 966, 2007.

[35] G. Scovazzi, E. Love, and M.J. Shashkov. Multi-scale Lagrangian shock Hydrodynamics on Q1/P0 finite elements: Theoretical framework and two-dimensional computations. *Computer Methods in Applied Mechanics and Engineering*, 197(912):1056 – 1079, 2008.

[36] G. Scovazzi, J.N. Shadid, E. Love, and W.J. Rider. A conservative nodal Variational Multiscale Method for Lagrangian shock Hydrodynamics. *Computer Methods in Applied Mechanics and Engineering*, 199(4952):3059 – 3100, 2010.

[37] G. Scovazzi. Lagrangian shock Hydrodynamics on tetrahedral meshes: A stable and accurate Variational Multiscale approach. *Journal of Computational Physics*, 231(24):8029 – 8069, 2012.

[38] E. F. Toro. *Riemann Solvers and Numerical Methods for Fluid Dynamics.* Springer, 1999.

[39] R. J. Leveque. *Finite-Volume Methods for Hyperbolic Problems.* Cambridge University Press, 2004.

[40] H. Versteeg and W. Malalasekera. *An Introduction to Computational Fluid Dynamics. The Finite Volume Method.* Pearson/Prentice Hall, 2007.

[41] T.J.R. Hughes, L.P. Franca, and M. Mallet. A new Finite Element formulation for computational fluid dynamics: I. Symmetric forms of the compressible Euler and Navier-Stokes equations and the second law of thermodynamics. *Computer Methods in Applied Mechanics and Engineering*, 54(2):223 – 234, 1986.

[42] T. J. R. Hughes. Multiscale phenomena: Green's functions, the Dirichlet-to-Neumann formulation, subgrid scale models, bubbles and the origins of stabilized methods. *Computer Methods in Applied Mechanics and Engineering*, 127(14):387 – 401, 1995.

[43] A. J. Gil, C. H. Lee, J. Bonet, and M. Aguirre. A stabilised Petrov-Galerkin formulation for linear tetrahedral elements in compressible, nearly incompressible and truly incompressible fast dynamics. *Computer Methods in Applied Mechanics and Engineering*, 276(0):659 – 690, 2014.

[44] B. Cockburn and C. W. Shu. The Runge–Kutta Discontinuous Galerkin Method for Conservation Laws V: Multidimensional Systems. *Journal of Computational Physics*, 141(2):199 – 224, 1998.

[45] A. Jameson, T.J. Baker, and N. P. Weatherill. Calculation of inviscid transonic flow over a complete aircraft. *AIAA 24h Aerospace Sciences Meeting*, 1986.

[46] D.J. Mavriplis. Multigrid solution of the Navier-Stokes equations on triangular meshes. *AIAA Journal*, 26:824–831, 1989.

[47] R.D. Rausch, J.T. Batina, and H.T.Y. Yang. Spatial adaption procedures on unstructured meshes for accurate unsteady aerodynamic flow computations. *AIAA Paper*, 91-1106, 1991.

[48] N.T. Frink. Recent progress toward a three-dimensional Navier-Stokes solver. In *AIAA Paper 94-0061*, 1994.

[49] T.J. Barth. On unstructured grids and solvers. *VKI, Computational Fluid Dynamics, Volume 2 66 p (SEE N90-27993 22-34)*, 2, 1990.

[50] D. J. Mavriplis. Unstructured grid techniques. *Annual Review of Fluid Mechanics*, 29(1):473–514, 1997.

[51] K. Morgan and J. Peraire. Unstructured grid Finite-Element methods for fluid mechanics. *Reports on Progress in Physics*, 61:569–638, 1998.

[52] Charles Hirsch. *Numerical Computation of Internal & External Flows. Volume 1: Fundamentals of Computational Fluid Dynamics*, volume 1. Elsevier, 2007 edition, 2007.

[53] R. C. Swanson and Eli Turkel. On central-difference and upwind schemes. *Journal of Computational Physics*, 101(2):292 – 306, 1992.

[54] P. Jorgenson and E. Turkel. Central difference TVD schemes for time dependent and steady state problems. *Journal of Computational Physics*, 107(2):297 – 308, 1993.

[55] K. A. Sørensen, O. Hassan, K. Morgan, and N. P. Weatherill. A multigrid accelerated hybrid unstructured mesh method for 3D compressible turbulent flow. *Computational Mechanics*, 31:101–114, 2003.

[56] J. Blazek. *Computational fluid dynamics: principles and applications.* Elsevier, 2nd edition, 2005.

[57] T. Barth. Aspects of unstructured grids and Finite-Volume solvers for the Euler and Navier-Stokes equations. *AGARD R-787, Special Course on Unstructured Grid Methods for Advection Dominated Flows, Brussels, Belgium*, pages 6.1–6.61, 1992.

[58] F.T. Johnson, E.N. Tinoco, and N.J. Yu. Thirty years of development and application of CFD at Boeing commercial airplanes, Seattle. *AIAA Computational Fluid Dynamics Conference*, (AIAA 2003-3439), June 23–26 2003.

[59] B. Courbet, C. Benoit, V. Couaillier, F. Haider, M.C. Le Pape, and S. Pron. Space discretization methods. *Aerospace Lab Journal*, 2011.

[60] Y.D. Fryer, C. Bailey, M. Cross, and C.-H. Lai. A Control Volume procedure for solving the elastic stress-strain equations on an unstructured mesh. *Applied Mathematical Modelling*, 15(1112):639 – 645, 1991.

[61] C. Bailey and M. Cross. A Finite Volume procedure to solve elastic solid mechanics problems in three dimensions on an unstructured mesh. *International Journal for Numerical Methods in Engineering*, 38(10):1757–1776, 1995.

[62] A.K. Slone, C. Bailey, and M. Cross. Dynamic solid mechanics using Finite Volume Methods. *Applied Mathematical Modelling*, 27(2):69 – 87, 2003.

[63] G. A. Taylor, C. Bailey, and M. Cross. A vertex-based Finite Volume Method applied to non-linear material problems in computational solid mechanics. *International Journal for Numerical Methods in Engineering*, 56(4):507–529, 2003.

[64] S. K. Sambasivan, M. J. Shashkov, and D. E. Burton. A Finite Volume cell-centered Lagrangian hydrodynamics approach for solids in general un-

structured grids. *International Journal for Numerical Methods in Fluids*, 72(7):770–810, 2013.

[65] J. A. Trangenstein and P. Colella. A higher-order Godunov method for modeling finite deformation in elastic-plastic solids. *Communications on Pure and Applied Mathematics*, 44(1):41–100, 1991.

[66] G. H. Miller and E. G. Puckett. A high-order Godunov method for multiple condensed phases. *Journal of Computational Physics*, 128(1):134 – 164, 1996.

[67] H. S. Tang and F. Sotiropoulos. A second-order Godunov method for wave problems in coupled solid-water-gas systems. *Journal of Computational Physics*, 151(2):790 – 815, 1999.

[68] B. P. Howell and G. J. Ball. A Free-Lagrange Augmented Godunov Method for the Simulation of Elastic-Plastic Solids. *Journal of Computational Physics*, 175(1):128 – 167, 2002.

[69] G. Kluth and B. Després. Discretization of hyperelasticity on unstructured mesh with a cell-centered Lagrangian scheme. *Journal of Computational Physics*, 229(24):9092 – 9118, 2010.

[70] Pierre-Henri Maire, Rémi Abgrall, Jérome Breil, Raphael Loubère, and Bernard Rebourcet. A nominally second-order cell-centered Lagrangian scheme for simulating elastic-plastic flows on two-dimensional unstructured grids. *Journal of Computational Physics*, 235(0):626 – 665, 2013.

[71] C. W. Shu and S. Osher. Efficient implementation of essentially non-oscillatory shock-capturing schemes. *Journal of Computational Physics*, 77(2):439 – 471, 1988.

[72] T. Belytschko, W. Kam Liu, and B. Moran. *Nonlinear Finite Elements for Continua and Structures.* Wiley, 2000.

[73] X. Oliver and C. Agelet. *Mecánica de medios continuos para ingenieros.* Edicions UPC, 2000.

[74] O. Gonzalez and A. Stuart. *A First Course in Continuum Mechanics.* Cambridge University Press, 2008.

[75] J. Marsden and T. Hughes. *Mathematical Foundations of Elasticity.* Dover Publications, 1983.

[76] M. E. Gurtin, E. Fried, and L. Anand. *The mechanics and thermodynamics of continua.* Cambridge University Press, 2010.

[77] P. Wriggers. *Nonlinear Finite Element methods.* Springer, 2008.

[78] J. Donea. Recent advances in computational methods for steady and transient transport problems. *Nuclear Engineering and Design*, 80(2):141 – 162, 1984.

[79] J. Bonet, A. J. Gil, C. H. Lee, M. Aguirre, and R. Ortigosa. A first order hyperbolic framework for large strain computational solid dynamics - Part I total Lagrangian isothermal elasticity. *Computer Methods in Applied Mechanics and Engineering*, 2014. Under review.

[80] J. Bonet, A. J. Gil, and R. Ortigosa. A computational framework for polyconvex large strain elasticity. *Computer Methods in Applied Mechanics and Engineering*, 2014. Submitted.

[81] C. M. Dafermos. *Hyperbolic conservation laws in continuum physics, 2nd edition*, volume 44. Springer Netherlands, 2nd edition, 2009.

[82] J.C. Simo. Algorithms for static and dynamic multiplicative plasticity that preserve the classical return mapping schemes of the infinitesimal theory. *Computer Methods in Applied Mechanics and Engineering*, 99(1):61 – 112, 1992.

[83] M. A. Meyers. *Dynamic behavior of materials.* John Wiley & Sons, Ltd, 1994.

[84] M. Arienti, E. Morano, and J.E. Shepherd. Shock and detonation modeling with the Mie-Grüneisen equation of state. Technical report, Graduate Aeronautical Laboratories, California Institute of Technology, 2004.

[85] Stefan Hiermaier. *Structures under crash and impact: continuum mechanics, discretization and experimental characterization.* Springer, 2008.

[86] Olivier Heuzé. General form of the Mie-grüneisen equation of state. *Comptes Rendus Mecanique*, 340(10):679 – 687, 2012.

[87] J. Donea and A. Huerta. *Finite Element Methods for Flow Problems.* John Wiley & Sons, Ltd, 2003.

[88] P. L. Roe. Approximate Riemann solvers, parameter vectors, and difference schemes. *Journal of Computational Physics*, 43(2):357 – 372, 1981.

[89] S. Osher and F. Solomon. Upwind difference schemes for hyperbolic systems of conservation laws. *Mathematics of Computation*, 38(158):pp. 339–374, 1982.

[90] A. Delis, I. Nikolos, and M. Kazolea. Performance and comparison of Cell-Centered and Node-Centered unstructured Finite Volume discretizations forshallow water free surface flows. *Archives of Computational Methods in Engineering*, 18:57–118, 2011. 10.1007/s11831-011-9057-6.

[91] H. Luo, J.D. Baum, and R. Löhner. An improved Finite Volume scheme for compressible flows on unstructured grids. *AIAA paper*, 95-0348, 1995.

[92] T.H. Pulliam. Artificial dissipation models for the Euler equations. *AIAA Journal*, 24:1931–1940, 1986.

[93] J. Peraire, J. Peiro, and K. Morgan. A 3D Finite Element multigrid solver for the Euler equations. In *Aerospace Sciences Meetings.* American Institute of Aeronautics and Astronautics, January 1992.

[94] M. Torrilhon. Locally divergence-preserving upwind Finite Volume schemes for magnetohydrodynamic equations. *SIAM Journal on Scientific Computing*, 26(4):1166–1191, 2005.

[95] J.D. Hoffman and S. Frankel. *Numerical methods for engineers and scientists.* CRC press, 2001.

[96] A. Jameson. Solution of the Euler equations for two dimensional transonic flow by a multigrid method. *Applied Mathematics and Computation*, 13:327–355, 1983.

[97] A. Jameson. Artificial diffusion, upwind biasing, limiters and their effect on accuracy and multigrid convergence in transonic and hypersonic flows. In *AIAA 11th Computational Fluid Dynamics Conference*, 1993.

[98] R. Courant, K. Friedrichs, and H. Lewy. On the Partial Difference Equations of mathematical physics. *IBM Journal of Research and Development*, 11(2):215 –234, March 1967.

[99] R.D. Richtmyer and K.W. Morton. *Difference methods for initial-value problems.* Interscience tracts in pure and applied mathematics. Interscience Publishers, 1967.

[100] R. J. Leveque. *Finite Difference Methods for Ordinary and Partial Differential Equations.* SIAM, 2007.

[101] L. N. Trefethen. *Finite Difference and Spectral Methods for Ordinary and Partial Differential Equations.* Unpublished text, 1996.

[102] E. Kreyszig. *Advanced Engineering Mathematics.* John Wiley & Sons, Ltd, 9th edition, 2006.

[103] W. Hundsdorfer and J. G. Verwer. *Numerical solution of time-dependent advection-diffusion-reaction equations.* Springer, 2003.

[104] M. Baldauf. Stability analysis for linear discretisations of the advection equation with Runge-Kutta time integration. *Journal of Computational Physics*, 227(13):6638 – 6659, 2008.

[105] S.K. Sambasivan, M. Shashkov, D. E. Burton, and M. A. Christon. Mimetic theory for cell-centered Lagrangian Finite Volume formulation on general unstructured grids. Technical report, Los Alamos National Laboratory, 2012.

[106] J.C. Simo and N. Tarnow. The discrete energy-momentum method. Conserving algorithms for nonlinear elastodynamics. *Zeitschrift für angewandte Mathematik und Physik ZAMP*, 43(5):757–792, 1992.

[107] X.N. Meng and T.A. Laursen. Energy consistent algorithms for dynamic finite deformation plasticity. *Computer Methods in Applied Mechanics and Engineering*, 191(1516):1639 – 1675, 2002.

[108] L. Noels, L. Stainier, and J. P. Ponthot. An energy-momentum conserving algorithm for non-linear hypoelastic constitutive models. *International Journal for Numerical Methods in Engineering*, 59(1):83–114, 2004.

[109] S. Dong. BDF-like methods for nonlinear dynamic analysis. *Journal of Computational Physics*, 229(8):3019 – 3045, 2010.

[110] Q. Tiehu. Symmetrizing nonlinear elastodynamic system. *Journal of Elasticity*, 50(3):245–252, 1998.